UNIVERSITÉ DE STRASBOURG

ÉCOLE DOCTORALE DES SCIENCES DE LA VIE ET DE LA SANTÉ

IGBMC – CNRS UMR 7104 – Inserm U 1258

THÈSE présentée par :

Arthur MICHAUT

soutenue le : **21 septembre 2018**

pour obtenir le grade de : **Docteur de l'université de Strasbourg**

Discipline/ Spécialité : Biologie du développement

Biomécanique de l'élongation de l'axe antéro-postérieur chez l'embryon de poulet

Biomechanics of anteroposterior axis elongation in the chicken embryo

THÈSE dirigée par :
M. RIVELINE Daniel	Directeur de recherche, IGBMC
M. POURQUIÉ Olivier	Professeur, Harvard Medical School
Mᵐᵉ GUEVORKIAN Karine	Chargée de recherche, Institut Curie

RAPPORTEURS :
M. HEISENBERG Carl-Philipp	Professeur, IST Austria
M. NASSOY Pierre	Directeur de recherche, Institut d'Optique d'Aquitaine

EXAMINATEURS :
M. GROS Jérôme	Assistant Professeur, Institut Pasteur
M. VERMOT Julien	Directeur de recherche, IGBMC

Abstract

In vertebrates, the elongation of the anteroposterior axis is a crucial step during embryonic development as it results in the establishment of the basic body plan. A previous study highlighted the importance of the presomitic mesoderm (PSM) in elongation and showed that a gradient of random cell motility along the anteroposterior axis is necessary for proper elongation of the chicken embryo (Bénazéraf et al., 2010). It was proposed that a gradient of random cell motility, downstream of a morphogen gradient, results in a biased posterior movement of PSM cells and drives axis extension. To date, the potential interaction between well-established molecular signaling and physical mechanisms involved in axis elongation remains largely unexplored. In particular, several mechanical questions need to be addressed. First, can the cell motility gradient lead to PSM extension? Second, is the force generated by PSM extension capable of promoting axis elongation? Third, how is PSM extension mechanically coupled with the elongation of all embryonic tissues?

In order to tackle these questions, a better description of the mechanical properties of embryonic tissues is required. Moreover, to assess specific tissues' contribution to elongation, a quantitative analysis of their force production is needed. In this Ph.D. thesis, we report an experimental investigation of the chicken embryo mechanics. In particular, we measure how the viscoelastic properties of both the PSM and the neural tube vary along the anteroposterior axis. We also demonstrate that isolated PSM explants are capable of autonomous elongation and we measure their contribution to the total force production in the embryo.

Acknowledgements

I would like to acknowledge all the people who helped me, supervised me and supported me during these four years in both Strasbourg and Boston. I would like to thank deeply Karine Guevorkian and Olivier Pourquié for offering me the opportunity to work on this Ph.D. project under their supervision. I am extremely grateful for their trust, the experience they brought me and their support during these four years. I am thankful to Daniel Riveline for his co-supervision during my fourth year and the time he dedicated to my mid-Ph.D. meeting.

I want to thank Carl-Philipp Heisenberg, Pierre Nassoy, Jérôme Gros and Julien Vermot for accepting being part of my Ph.D. committee and for offering me their time and consideration.

I want to acknowledge all the people who helped me and participated in this Ph.D. project. In particular, I thank Olivier Henry for his dedication in introducing me to microfabrication. An important part of this Ph.D. project would not have been possible without him. I am also grateful to Aditi Chakrabarti for her help with the cantilever calibration and for very interesting scientific conversations. I would like to thank Jun Chung for his ideas and help for designing the mica cantilever. I am grateful to L. Mahadevan for the time he dedicated during my mid-Ph.D. meeting and many other interesting meetings. I am also extremely thankful to Françoise Brochard-Wyart for her advice and for very stimulating meetings. I thank Gilles Charvin as well, for his help with 3D printing and interesting conversations. I also want to thank Bertrand Bénazéraf and Thibaut Divoux for their valuable advice.

I would like to thank all the members of the Pourquié lab in both Strasbourg and Boston for their help during all my Ph.D. I especially want to thank Alexis Hubaud who has been of a great support during the last three years, and Adrian Ranga for his enthusiasm and his excellent ideas. I would also like to thank Charlène Guillot for her advice and for introducing me to many biological techniques. I thank Masayuki Oginuma too for passing on so much of his experience to me. Many thanks to Daniel Sieiro Mosti, Fengzhu Xiong, Jyoti Rao, Margarete Diaz Cuadros and Marie Knockaert for their time and valuable comments on my Ph.D. thesis.

I am also extremely grateful to Annie Stephenson, Charlotte Lesur, Colm Kelleher, Sébastien Uzel and Yi-Jang Lin for their kind help in proofreading my thesis.

I want to thank my previous professors and supervisors without whom I would not have followed the path to this Ph.D. First, I want to thank my biology professors Mathieu Vartanian, Cécile van der Rest and Bruno Anselme, who sparked my interest in biology and science in general. I want to thank them deeply for their inspiring lectures and the confidence they brought me. During my time in the ENS de Lyon, I benefited a lot from the time spent by Cendrine Moskalenko and Sébastien Manneville to help me shape my career project.

I would like to thank my previous supervisors, who introduced me to research. I was really pleased to have my first research experience with Grégoire Danger and Robert Pascal. I really enjoyed my time with them in Marseille and Montpellier. I loved working under Matthew Turner's supervision at Warwick University. I had a great time in his lab, where I learned so much from Jack Cohen in particular. Finally, I want to acknowledge both François Graner and Alexandre Kabla who introduced me to my current field of research. I am extremely grateful to François, thanks to whom I found my Ph.D., for his wonderful supervision. I also deeply thank Alexandre for all the time and effort he devoted to my applications, and for everything he

taught me during my time in Cambridge.

Last but not least, I want to thank my family and friends for their constant support. Without them, nothing would have been possible. I especially thank Clara, Clothilde, Juliette, Katy, Louise & Paul (for being my second home in Paris), Antoine, Lucie, Michiels, Éric, Félix, Hugo, Théophile, Carole & Jib & Élise (for their help with MT180) and Charlotte & Chad (for being my second home in Boston). I am also grateful to my grandparents and Valérie for this adventurous trip to Liège! Finally, I dedicate this thesis to my parents for the love and confidence they gave me during all these years.

Contents

List of Figures

List of Tables

List of Abbreviations

AFM	Atomic Force Microscopy
AP	AnteroPosterior
CE	Convergent Extension
DMEM	Dulbecco's Modified Eagle Medium
ECM	ExtraCellular Matrix
EMT	Epithelial-Mesenchymal Transition
FBS	Fetal Bovine Serum
FGF	Fibroblast Growth Factor
FRET	Förster Resonance Energy Transfer
HH	Hamburger-Hamilton
HN	Hensen's Node
MAPK	Mitogen-Activated Protein Kinase
ML	MedioLateral
MLCI	MedioLateral Cell Intercalation
NT	Neural Tube
PBS	Phosphate-Buffered Saline
PDMS	PolyDiMethylSiloxane
PM	Paraxial Mesoderm
PMZ	Posterior Marginal Zone
PS	Primitive Streak
PSM	PreSomitic Mesoderm
SLS	Standard Linear Solid
TFM	Traction Force Microscopy

List of Symbols

γ	surface tension	$\text{N} \cdot \text{m}^{-1}$
ϵ	strain	dimensionless
ΔP	aspiration pressure	Pa
ΔP_c	critical pressure	Pa
η	dynamic viscosity	$\text{Pa} \cdot \text{s}$
κ_d	drop curvature	μm^{-1}
κ_p	curvature within the pipette	μm^{-1}
σ	stress	Pa
τ	rounding time	s
τ_c	cellular elastic time	s
τ_t	tissular elastic time	s
E	Young's modulus	Pa
G	shear modulus	Pa
K	bulk modulus	Pa
k_f	friction coefficient	$\text{N} \cdot \text{s} \cdot \text{m}^{-3}$
L	aspired tongue length	μm
R_p	pipette radius	μm
v_p	viscocapillary velocity	$\mu\text{m} \cdot \text{min}^{-1}$
x	radius of fusion neck	μm

Chapter 1

Introduction

The goal of this Ph.D. thesis is to present a physical investigation of the elongation of the chicken embryo during its early development. In particular, we studied experimentally the elongation of the anteroposterior axis during somitogenesis. In the introduction of this thesis, we will present key developmental processes and important physical concepts and methods involved in vertebrate elongation. We will first review the morphogenetic events involved in the extension of the embryo from the onset of gastrulation to secondary neurulation. Then, we will present physical methods for measuring the mechanical properties of biological tissues.

1.1 Elongation of the anteroposterior axis in vertebrate embryos

Vertebrates diverged from cephalochordates by acquisition of a metamerized skeleton. The repetitive units of the axial skeleton first form as embryonic structures (called somites) along the anteroposterior (AP) axis and then differentiate into vertebrae. The basic body plan along the AP axis is established at a stage when embryos from different species share a high degree of anatomical similarities (the phylotypic stage). As proposed in the hourglass model, the anatomical structures of various species present distinct morphologies at early stages, then, converge towards a similar morphological organization at the phylotypic stage (see Figure 1.1), and finally, diverge again (Duboule, 1994, Raff, 1996).

During early development, vertebrates derive their periodic organization along the AP axis by a rhythmic head-to-tail segmentation of the presomitic mesoderm (PSM) into somites. Somites will give rise to both axial skeleton and axial skeletal muscles. This stage of development, referred to as somitogenesis, is characterized by a simultaneous elongation of the body axis and its segmentation. The total number of somites depends on both the segmentation rate and the elongation rate (Gomez and Pourquié, 2009). While the mechanism underlying somitogenesis appears conserved across vertebrates, the rhythm of somite production and their total number exhibit a tremendous variation. The timing of somitogenesis with respect to development also varies across species. For instance, it happens between 2 and 4 days after fertilization in the chicken embryo (for a total of 55 pairs of somites), 8 to 15 days in the mouse embryo (for a total of 65 pairs of somites) and 5 to 8 weeks in the human embryo (for a total of 38-39 pairs of somites) (Gomez et al., 2008, O'Rahilly and Müller, 2003). The subsequent steps of development gradually diverge between species and eventually lead to the specific traits of each species.

In order to study the formation of the vertebrate axis, the chicken is a convenient model for several reasons. First, birds like mammals are amniotes and homeotherms and their development is highly similar at least for early stages. Second, as the
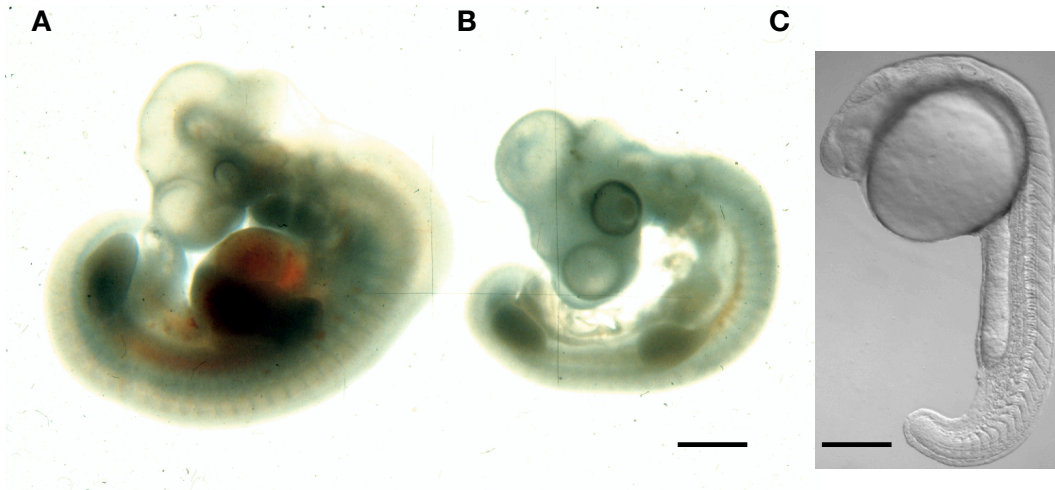
FIGURE 1.1 – Phylotypic stage in vertebrates. **A**: Human embryo stage Carnegie 16 (6 weeks after fertilization, 33-35 pairs of somites). **B**: Chicken embryo stage Hamilton-Hamburger 21 (3.5 day of incubation, 43-44 pairs of somites). **C**: Zebrafish embryo 24 hours after fertilization (26+ pairs of somites), adapted from Dray et al., 2013. Scale bars: 1 mm (**A**, **B**), 200 µm (**C**).

embryo develops in an egg, it is much more accessible than mammalian embryos. Third, during somitogenesis, the embryo is a mostly flat structure facilitating its imaging all across the embryonic body and throughout long periods of development. Even though it is less transparent than zebrafish (*Danio rerio*), it can easily be separated from the underlying yolk and culture *in vitro* which allows both imaging and manipulation. Lastly, its large dimensions, comparable to the frog (*Xenopus laevis*) embryo, make it more amenable to physical manipulations than mammalian and fish embryos. As a result, the chicken embryo is a good compromise for imaging (between zebrafish and frog embryos) and offers comparable opportunities for physical approaches as amphibians do. For these reasons, the experimental work presented in this thesis has been conducted on the chicken embryo. In this introduction, we will present the early steps of development in vertebrates and the mechanisms of embryonic body extension.

1.1.1 Overview of development in the chicken embryo

Before addressing the problem of axis elongation during embryonic development, we briefly introduce key developmental steps in the chicken embryo.
In the chicken embryo, after fertilization within the oviduct, the first cleavages of the egg-cell happen before the albumen and the shell encapsulate it (Eyal-Giladi and Kochav, 1976). As a result, by the time the egg is laid, the embryo consists of a disk of 60,000 cells on top of the yolk, referred to as the blastoderm (Pokhrel et al., 2017). The blastoderm is formed of an inner single epithelial cell disk called *area pellucida* which will give rise to the embryonic tissues, surrounded by a darker multilayered ring of cells called *area opaca* (see Figure 1.2). Once the egg is laid, normal development happens at 37°C. A cavity between the blastoderm and the yolk, called the subgerminal space, is formed. Cells leave the blastoderm to form islands of cells below the blastoderm. These islands will be part of a layer called hypoblast. From stage XI to XIII (early staging table from Eyal-Giladi and Kochav, 1976), cells from
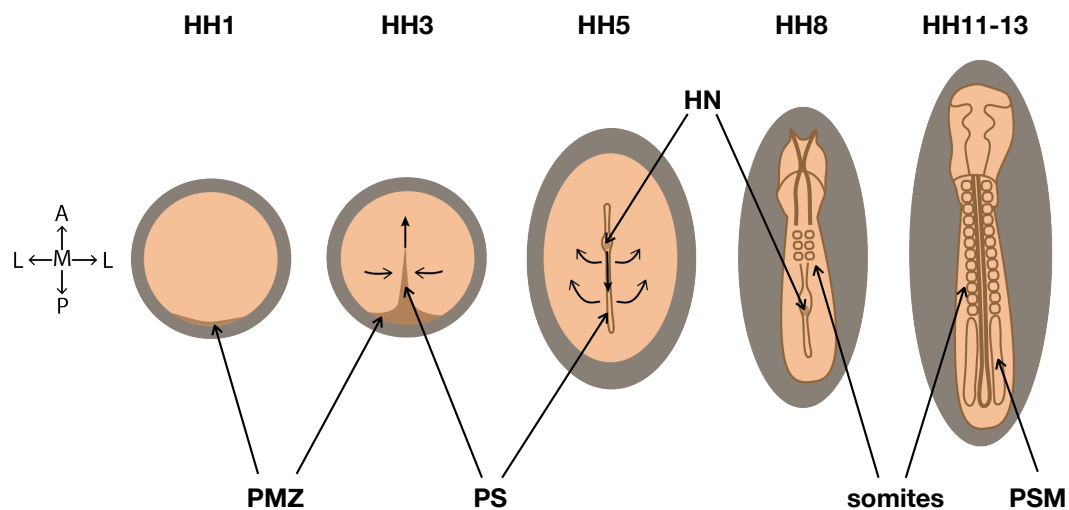
FIGURE 1.2 – Schematic of the early embryonic stages in the chicken embryo. Gray: *area opaca*, beige: *area pellucida*. The polarity is given by the arrows on the left: A: anterior, P: posterior, L: lateral, M: medial. PMZ: posterior marginal zone, PS: primitive streak, HN: Hensen's node, PSM: presomitic mesoderm. Arrows overlaying the tissues show morphogenetic movements. Developmental stages HH1, HH3, HH5, HH8, HH11-13 are given by the Hamburger-Hamilton staging table (Hamburger and Hamilton, 1951).

a denser zone at the posterior edge of the *area pellucida*, the posterior marginal zone (PMZ), migrate anteriorly to complete the hypoblast. The upper layer is then called the epiblast and the cavity between the hypoblast and the epiblast is named the blastocoele.

After formation of this first two layers, the AP axis becomes visible during gastrulation which results in the formation of the three germ layers: the ectoderm, the mesoderm and the endoderm. Gastrulation happens along an elongated structure called primitive streak (PS). The PS starts forming along the AP axis at the midline (*i.e.* along the diameter of the disk along the AP axis) at Hamburger-Hamilton stage 3 (Hamburger and Hamilton, 1951). In the PS region, epiblast cells internalize into the blastocoele to form the endoderm and the mesoderm. The internalization, referred to as ingression, takes place by epithelial-mesenchymal transition (EMT). Cells remaining in the epiblast become the ectoderm. During ingression, endoderm cells gradually displace the hypoblast (Lawson and Schoenwolf, 2003), while mesoderm cells migrate between the forming endoderm and the epiblast. The PS first extends in a posterior-to-anterior fashion, before regressing and initiating the anterior-to-posterior elongation at stage HH5 (see Figure 1.2). During PS extension the cephalic mesoderm is internalized (Psychoyos and Stern, 1996). Tissues along the body axis are formed after the onset of PS regression (Jouve et al., 2002). The neural plate and the notochord are formed axially, at the anterior of the regressing PS. The neural tube is generated by a gradual folding of the neural plate until the secondary neurulation (27-somite stage). These axial tissues are lined on both sides by the paraxial mesoderm. The paraxial mesoderm is divided into a segmented region (the somites) and an unsegmented region (the PSM). All these tissues are generated by progenitor cells located at the posterior end of the AP axis. As a result, there is a differentiation gradient along the AP axis, with newly added cells at the posterior end and more

"mature" cells towards the anterior end. After four days of development, the paraxial mesoderm is fully segmented and the future organs keep developing following the body plan established during somitogenesis.

1.1.2   Convergent extension: a central mechanism of axis elongation during embryonic development

Historically, morphogenetic processes associated with elongation have been extensively studied in amphibians. In this system, convergent extension (CE) has been described as a major mechanism of elongation. We will discuss in this introduction, that while CE remains a key mechanism in a number of morphogenetic processes, other mechanisms have been described.

CE is a mechanism of deformation of a tissue by contraction along a direction, resulting in extension along the orthogonal direction (Keller et al., 2000). Importantly, this mechanism does not rely on proliferation, and therefore, it can drive morphogenetic changes on timescales shorter than cell cycle. In practice, this process comprises a convergence step in which cells on both sides of the midline converge orthogonally towards the extension axis. Next, an intercalation step at the midline takes place. During the intercalation step, cells exchange neighbors resulting in an extension along the midline (see Figure 1.3 A). This process notably happens in the *Xenopus* mesoderm. Keller and Danilchik, 1988 demonstrated that CE could drive mesoderm extension along the AP axis in cultured explants (see Figure 1.3 B).

In order to migrate towards the midline, cells need to be polarized. This polarization is mediated by an evolutionarily conserved signaling pathway: the planar cell polarity (PCP) pathway. A molecular polarity is established at the cellular level through the asymmetric localization of various proteins (*i.e.* Frizzled and Dishevelled, Seifert and Mlodzik, 2007). In vertebrates, but not in invertebrates, the PCP signaling pathway also includes β-catenin independent Wnt activity. Polarized cells exhibit protrusions preferentially along the convergence axis. In *Xenopus*, bipolar protrusions along the convergence axis have been shown to exert pulling forces driving convergence and intercalation at the midline (Keller et al., 2000).

In summary, a coordinated convergence of cells along an axis can drive elongation of the tissue along the orthogonal axis. Therefore, CE is a mode of elongation by deformation which does not involve any volumetric growth. However, more recent studies in other models than amphibians showed that elongation can happen without CE. In particular other modes of elongation can be based on volume growth along a direction (by cell growth, decrease in cell density or extracellular matrix production). In the rest of this introduction, we will present how these different modes of elongation are involved during vertebrate embryonic development.

1.1.3   Initiation of anteroposterior elongation during gastrulation

Before gastrulation, vertebrate embryos do not exhibit an elongated shape along the AP axis. Anamniotes embryos (*e.g.* amphibians and fish) have a spherical geometry, while birds and human embryos are made of a flat disc of cells and mouse embryos exhibit a cup shape. Gastrulation is the first important morphogenetic process which results in dramatic tissular movements. Some of these movements will initiate elongation along the AP axis. However, both gastrulation and early AP elongation differ between vertebrates species.

In chicken, after 6-7 hours of incubation (HH2), the PS extends anteriorly from the
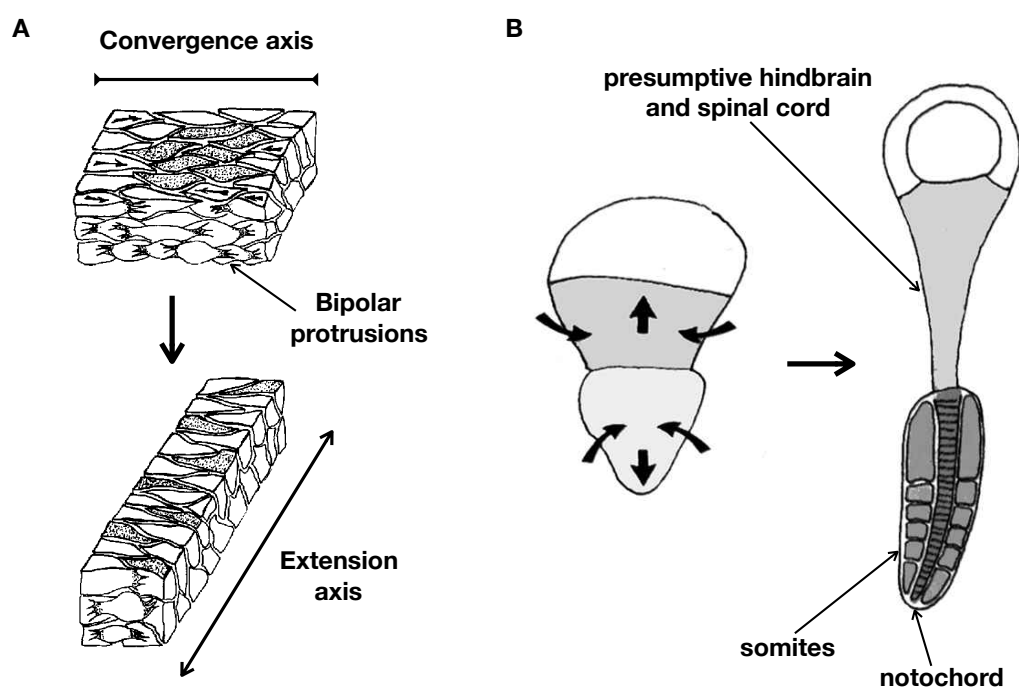
FIGURE 1.3 – Schematic of convergent extension adapted from Keller et al., 2000. **A**: Convergent extension mediated by cell intercalation. **B**: Elongation of a *Xenopus* mesoderm explant by convergent extension.

A   **B**
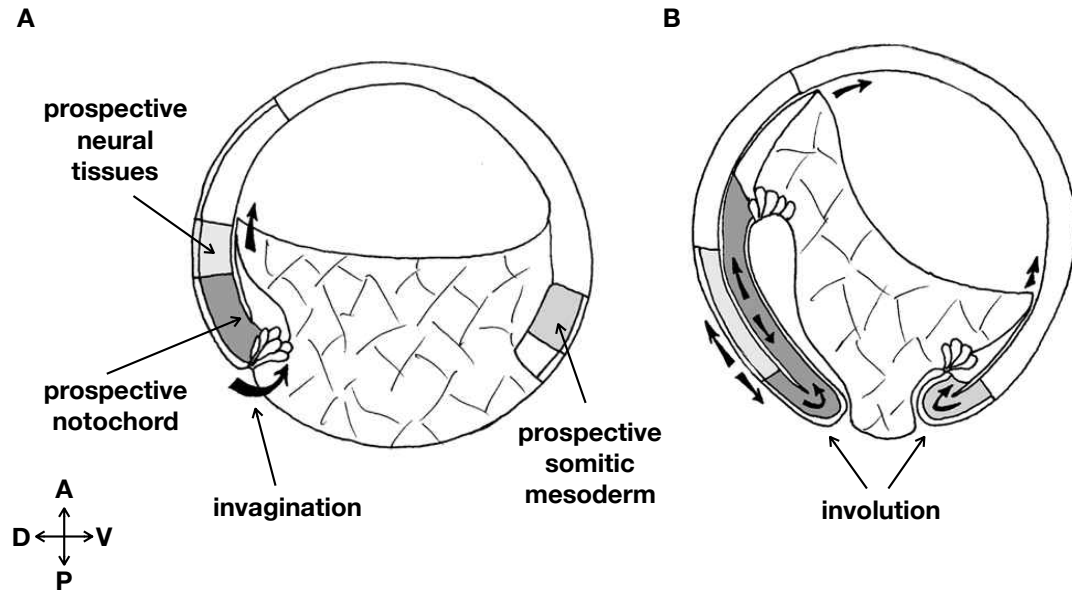
FIGURE 1.4 – Schematic of gastrulation in *Xenopus* in saggital view, at stages early gastrula (**A**) and late gastrula (**B**). The polarity is given by the arrows on the left: A: anterior, P: posterior, D: dorsal, V: ventral. Adapted from Keller et al., 2000.

PMZ until HH4 (18-19 hours after incubation). When fully extended, the PS forms a groove. In anamniotes, due to the spherical geometry of the early embryo, gastrulation happens around a ring: the blastopore in amphibians and the germ ring in zebrafish. In addition to the geometry, cell internalization during gastrulation is distinct between species. In anamniotes, cells invaginate towards the inner cells and then internalize in a coherent flow, a process called involution (see Figure 1.4). In sharp contrast with anamniotes, it has been recently shown that no involution is present in birds (Voiculescu et al., 2014). Cells internalize individually by EMT, which is referred to as ingression. Ingressing cells are sparsely scattered across the epiblast before the formation of the PS. Then, as the PS extends anteriorly and lateral cells converge towards the midline, the frequency of cell ingression increases as they get closer to the PS.

Despite distinct structures and mechanisms, AP movements are initiated in both amniotes and anamniotes during gastrulation. We review here the morphogenetic processes resulting in the early formation of the AP axis.

Initiation of anteroposterior elongation in amniotes

Determination of the primitive streak

Unlike the *Drosophila* or *Xenopus* egg, in which maternal components set the polarity and cell fate very early in development, it has been shown that any portion of the blastoderm can give rise to a complete axis in duck (Lutz, 1950) and in chicken (Spratt and Haas, 1960). Spratt and Haas cut the blastoderm in various shapes and showed that the isolated pieces could give rise to a normal embryonic axis (see Figure 1.5). The competency of the embryo to form ectopic PS is retained until the very beginning of PS formation. It was later demonstrated that an epiblast isolated from the hypoblast could generate up to three separated streaks in the same epiblast, irrespective of the former polarity introduced by the PMZ (Bertocchini and Stern, 2002).
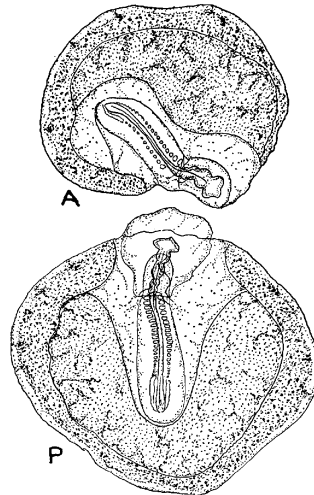
FIGURE 1.5 – Whole blastoderm competency to give rise to embryonic body (adapted from Spratt and Haas, 1960). Living embryos 48 hours after *aera opaca* removal and blastoderm separated into two halves (A: anterior half, P: posterior half).

In Bertocchini's and Stern's study, it was proposed that signals from the PMZ inducing the streak (Vg1 and Wnt) are inhibited by a factor secreted by the hypoblast, Cerberus. The anterior displacement of the hypoblast by the forming endoderm, disrupts the local Cerberus-mediated inhibition of the streak. Taken together, these experiments demonstrate the late specification of the different layers in the chicken embryo and show the importance of the PMZ in positioning of the streak.

Extension of the primitive streak
In birds, at stage HH2, the epiblast in the PMZ thickens and extends towards the anterior of the epiblast. This extension is accompanied by two large counter-rotating circular flows first described by Gräper, 1929 and Wetzel, 1929 called *polonaise* movements. The iron and carbon particles used 90 years ago to follow the tissue movements have been replaced more recently by injection of fluorescent cell trackers (the lipophilic dye DiI) or cell electroporation with a fluorescent protein (Cui et al., 2005 and Chuai et al., 2006) (see Figure 1.6). These more detailed observations indicated that the flow of cells is coherent and symmetric. Chuai et al., 2006 mosaically labeled epiblast cells by electroporation in order to obtain flow maps with a cellular resolution. This gave the possibility to image cell division and show that daughter cells stayed in the same region, which demonstrates the coherence of the flow. Besides, DiI injection labeled larger groups of cells, including cells from deeper layers (especially in the PMZ), and showed that a subset of deeper cells posterior to the forming streak already initiated a posterior elongation by migrating posteriorly. These rotating movements are important for the right patterning of the future embryonic body (Hatada and Stern, 1994 and Psychoyos and Stern, 1996). However, for a long time, it was unclear whether the rotating flows were driving the streak extension or if they were a consequence of it. A wide variety of models tried to account for these morphogenetic events, as summarized by Chuai and Weijer, 2008.

- **Locally Restricted Cell Division**
  Following the observation of polarized mitosis in the streak, it was proposed that polarized cell division in the streak could drive its extension (Wei and Mikawa, 2000). However, it was later suggested that the polarized division
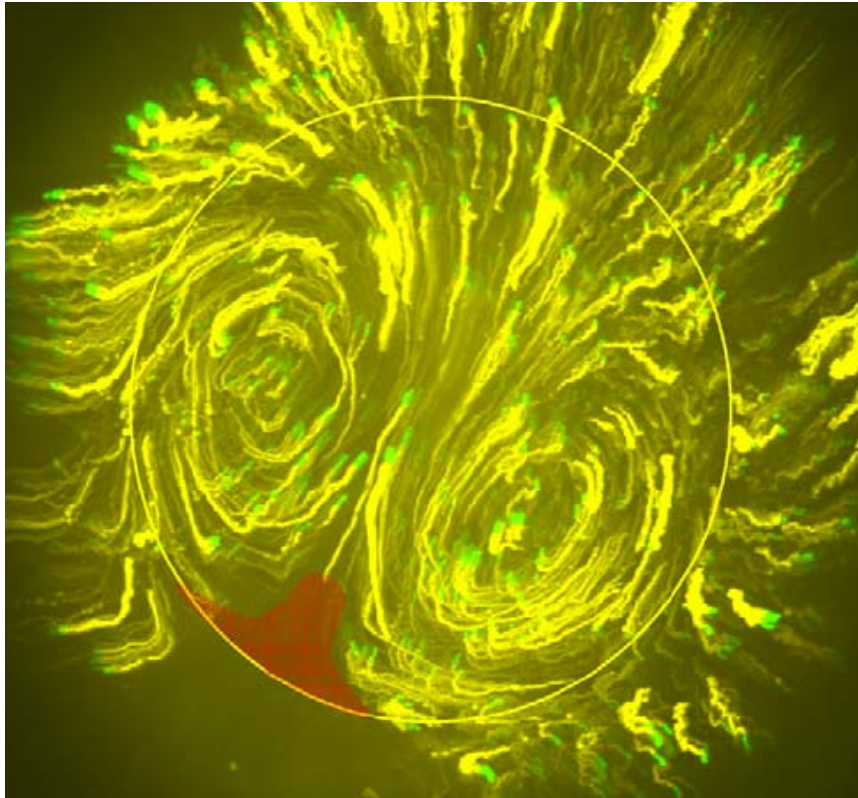
FIGURE 1.6 – Time-lapse of *polonaise* movements imaged by DiI injection (adapted from Chuai and Weijer, 2008). The PMZ is indicated by the red area.

could be the consequence of extension and not its cause. Indeed, the measured cell cycle (6.5 hours) is too slow to explain extension (Chuai and Weijer, 2008). In addition, inhibition of cell division by aphidicolin (which does not interfere with the cytoskeleton), abolished the counter-rotating flows but did not fully prevent the streak from elongating (Cui et al., 2005). These experiments suggest that cell division is implicated in *polonaise* movements but is not driving extension.

- **Chemotaxis**
An appealing hypothesis to explain the extreme regularity of the rotating patterns was that cells were migrating along a "chemotactic dipole". A combination of chemoattractant and chemorepellent molecules would generate a chemical field patterning the movements (Sandersius et al., 2011). This hypothesis was motivated by the fact that several members of the FGF family, which can act as chemoattractants or chemorepellents, have been shown to be indispensable to streak formation (Chuai et al., 2006). However, the wide spectrum of actions of the FGF family (especially on cell ingression) makes it difficult to be conclusive on the mechanism of streak formation. In addition, the chemotaxis model does not explain how migrating cells can generate the global extracellular matrix (ECM) flow which has been shown to follow the cellular flow (Zamir et al., 2008).

- **Spatially Organized Cell-Cell Intercalation**
A concurrent idea was that CE in the epiblast mediated by mediolateral cell intercalation (MLCI) drives PS extension. The idea was first dismissed by Chuai

et al., 2006 because the Wnt-PCP pathway appears dispensable to streak extension. Indeed, Disheveled mutants or inhibition of myosin-II phosphorylation by blebbistatin treatment did not prevent streak formation. However, Voiculescu et al., 2007 brought contradictory evidence that showed extensive cell-cell intercalation from cells along the PS axis. In addition, they showed that, in contrast with results from Chuai et al., inhibition of Wnt-PCP arrested extension.

Benefiting from a substantial improvement of imaging techniques and the development of transgenic lines, new studies now favor the cell-cell intercalation model over the chemotaxis-based ones. Using light sheet microscopy, Rozbicki et al., 2015 produced maps of contraction and expansion and cell-cell rearrangements along the PS (see Figure 1.7 A). The authors showed that pre-patterned myosin cables along the mediolateral (ML) axis in the posterior region align the cells and are involved in a pulling mechanism contracting the tissue towards the midline. The contraction towards the midline was proposed to drive both an important ingression into the PS and an intercalation along the AP axis which passively extends it (see Figure 1.7 B). In addition, the authors confirmed that blebbistatin does not impair this process. However, they showed that unconventional myosins (myosin-I and myosin-V) have a strong effect on the PS extension.

While the intercalation model explains how epiblast cells converge towards the midline where they intercalate and extend the PS, it does not explicitly provide an explanation for the origin of *polonaise* movements. As reported by Cui et al., 2005, inhibition of cell division abolishes *polonaise* movements but leaves the streak extension unperturbed. This result suggests that *polonaise* movements are not a direct driver of extension, but might be a consequence of it. The role of cell division in these movements was recently elucidated (Firmino et al., 2016). The authors described how mitosis differs during gastrulation compared to earlier stages. Unlike in most epithelia, cell division leads to an important tissue rearrangement in the gastrulating chicken embryo. After cell division, neighboring cells quickly intercalate between daughter cells and daughter cells intercalate between other neighbors (see Figure 1.7 C). As a result, most of the neighbor exchanges in the epiblast are due to cell division. Cell division mediated rearrangement is due to lower levels of actomyosin which soften cell-cell junctions. It was therefore proposed that cell division actively fluidizes the epiblast. While it was previously thought that the extension of the streak could alone drive *polonaise* movements (Voiculescu et al., 2007, Voiculescu et al., 2014 and Rozbicki et al., 2015), Firmino et al., 2016 suggested that forces generated by streak extension might not be sufficient if the epiblast resists too much. In the case of cell division inhibition, the epithelium is in a locked conformation and only pulling movements towards the streak are present. However, upon epithelium fluidization by cell division mediated rearrangements, forces generated by streak extension can propagate across the whole epithelium and drive *polonaise* movements.

Unlike birds, the murine PS does not involve extensive large-scale movements (Williams et al., 2012). Time-lapse analysis did not reveal CE movements. In addition, the streak does not present the characteristic denser and bent structure of the avian embryos. It is rather a region that undergoes preferential ingression, starting from the posterior tip and propagating towards the anterior as gastrulation proceeds. Like in birds, the EMT process happens in individual cells and no involution is present. Ingression of cells drives convergent movements by simply filling the space left by ingressed cells which maintain the epithelium integrity. Consequently,
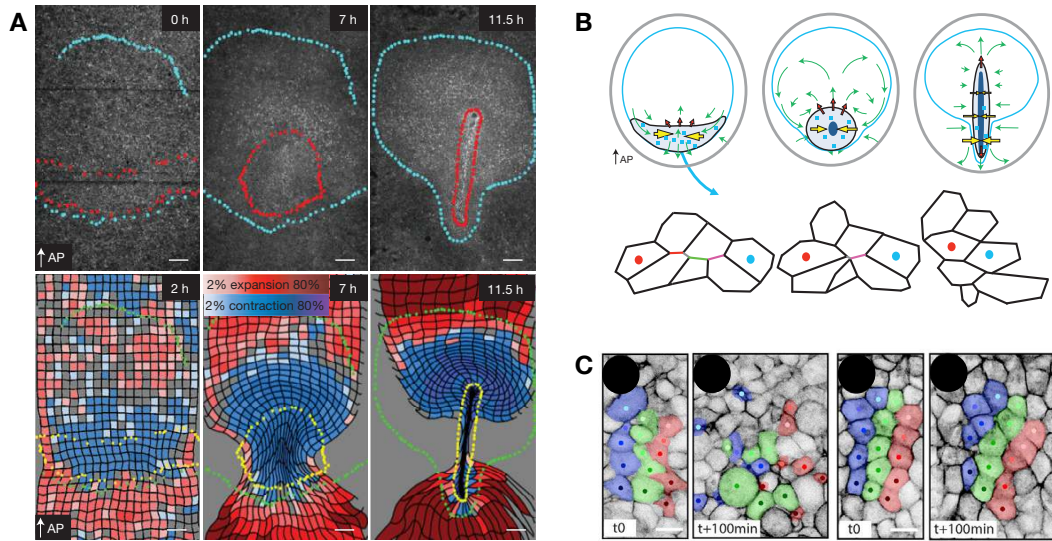
FIGURE 1.7 – Mechanism of extension of the primitive streak. **A**: Top panels: back-tracking of the PS region (in red) showing its gradual contraction along the ML axis and extension along the AP axis. Bottom panels: expansion and contraction maps (adapted from Rozbicki et al., 2015). **B**: Model of the PS extension. Yellow arrows: active forces, magenta arrows: passive forces, green arrows: tissue flow (adapted from Rozbicki et al., 2015). **C**: Cell division mediated tissue rearrangement during gastrulation (left panels), and lack of rearrangement upon aphidicolin treatment (adapted from Firmino et al., 2016).

these convergent movements are passive and do not trigger any extension by cell intercalation.

Regression of the primitive streak

After its full extension at stage HH4 (19 hours after incubation), the PS starts regressing as its anterior end initiates an anterior-to-posterior movement, which reduces the length of the streak over time. This movement will last until the 20-somite stage when the PS disappears and is replaced by the tail bud (Schoenwolf, 1979).

An important structure appears at the beginning of regression in a region anterior to the PS anterior tip: the Hensen's node (HN). This is the equivalent of the blastopore dorsal lip in amphibians and the embryonic shield in zebrafish. All these structures share the feature of being an organizer as defined by Spemann and Mangold, 1924. In their famous experiment, Spemann and Mangold showed that ectopic grafting of the dorsal lip of the blastopore could generate a new axis in amphibians. Grafted cells could induce differentiation of dorsal structures in ventral tissues by secreting inductive signals. In zebrafish, it was also shown that the embryonic shield (a thickened dorsal region at the leading edge of the blastoderm) could generate a new axis upon ectopic grafting (Shih and Fraser, 1996). In chicken, ectopic grafting of the HN also generates axial tissues of a new axis (but limited paraxial tissues). Moreover, there is a balance between induction and self-differentiation of the graft depending on the ages of the donor and the host (Dias and Schoenwolf, 1990 and Storey et al., 1992).

The mechanical mechanism by which the PS regresses has not been described in
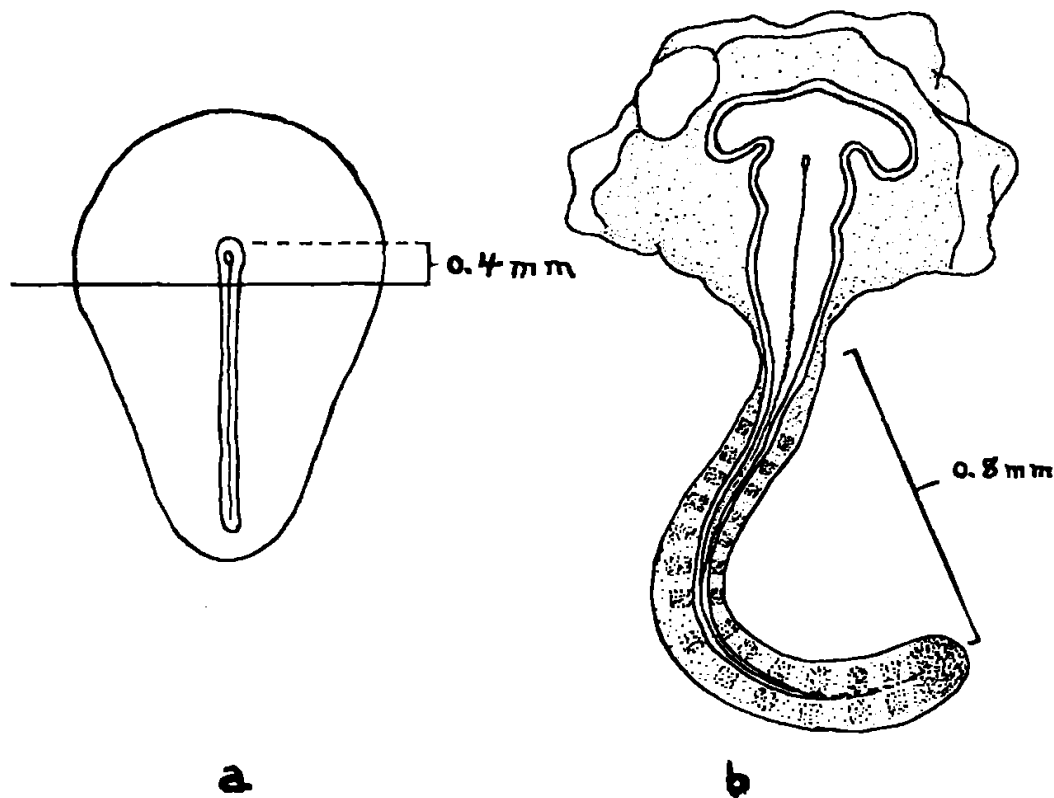
FIGURE 1.8 – Ablation of the posterior primitive streak during regression (Figure 7 from Spratt, 1947). **a**: Schematic of the ablation, the region anterior to the solid line is culture *in vitro*. **b**: anterior region after 20 hours cultured *in vitro*, a "tail piece" containing the midline structures (notochord, neural tube and somites) has grown out of the edge.

details yet. In comparison to its extension, PS regression remains unclear. Movements of regression were described in detail by Spratt, 1947 who showed that the entire streak was regressing in a coherent movement. Spratt notably reported that the anterior region of the streak could exhibit posterior movements even when it was physically separated from its posterior region. In this case, the embryo develops a head and axial tissues forming a "tail-piece" (see Figure 1.8). The HN is dispensable to PS regression in both chicken (Charrier et al., 1999) and mouse (Davidson et al., 1999). Charrier et al., 1999 carried out excisions in the region of the HN at the 5-somite stage (HH8-9). They showed that the node was key for the formation of various midline structures and the survival of these structures. Depending on the ablated region, some midline structures (notochord, floor plate *i.e.* the ventral midline of the neural tube) would be interrupted but would form more posteriorly, suggesting that the HN progenitors can be recruited again after excision. Although this study does not rule out a role of the node at the beginning of the regression movement (HH4), it suggests the HN is not involved in the regression mechanism. In the mouse too, ablation of the node does not affect body extension (Davidson et al., 1999). Although node ablated embryos are shortened and miss the notochord, the neural tube formed by *de novo* recruitment of neural ectoderm.

The physical mechanism driving the regression remains unclear. Driving forces might depend on myosin-II activity as blebbistatin treatment blocks regression (Chuai

et al., 2006). One possibility is that the neural plate folding anteriorly to streak might exert pushing forces. This region undergoes important CE movements by cell intercalation (Nishimura et al., 2012). CE depends on junction rearrangement driven by contractile and polarized actomyosin cables along the ML axis. The authors showed that contractility along the ML axis depends on Rho kinase activity. However, they did not describe the dynamics of PS regression in parallel with CE. In addition to CE in the neural plate, ECM in the mesoderm exhibits two counter-rotating flows converging towards the midline under the neural plate (Zamir et al., 2006). Taken together these studies suggest a likely pushing mechanism mediated by the CE movements in the tissues anterior to the streak in both the neural plate and the mesoderm. However, a detailed study of the mechanical coupling of these two processes is still needed.

In summary, while PS extension is well explained by CE, the mechanism of PS regression remains unclear. Polarization and contraction along the ML axis result in ingression and intercalation at the midline. This intercalation drives PS extension and *polonaise* movements, which are facilitated by active fluidization of the epiblast. More experimental investigation is needed to describe the putative role of CE during PS regression.

Initiation of anteroposterior elongation in anamniotes

In both zebrafish and amphibians, pre-gastrula embryos exhibit a spherical geometry. At early stages, cells at the surface of the animal pole (*i.e.* the anterior pole) spreads collectively downward to the vegetal pole (*i.e.* the posterior pole). During this movement, called epiboly, the spreading cells in surface engulf the deeper tissues. The epiboly movement is essentially driven by cell intercalation from deeper cells into the outer layer (radial intercalation). As epiboly takes place, internalization proceeds around a ring (the germ ring margin in zebrafish and the blastopore in amphibians) at the border of the advancing epibolic cells.
Therefore, the region of internalization does not appear along an AP oriented structure. Nonetheless, important extension movements happen internally. Two kinds of extension movements have been described (as reviewed by Tada and Heisenberg, 2012): directed collective migration and CE. A wide range of progenitors undergo directional collective migration towards the animal pole once they involuted (the zebrafish prechordal plate and lateral mesendoderm progenitors, and the *Xenopus* head mesendoderm). CE movements mediated by MLCI are restricted to the notochord in zebrafish and *Xenopus*, while CE happens also by collective migration towards the midline without cell intercalation (mesendoderm progenitors at the midgastrula).

We have described that gastrulation presents very distinct morphogenetic movements depending on animal models. The first source of differences comes from the geometry. In amniote embryos, gastrulation happens along a line, whereas the spherical geometry of anamniotes leads to gastrulation around a ring. The internalization process can also happen as a coherent flow of cells (anamniotes) or as individual cell ingression (amniotes). Regarding AP elongation, movements in anamniotes are continuous over gastrulation, while two distinct steps can be identified in amniotes. Amniote elongation starts first with posterior-to-anterior movements (PS extension), and next continues with anterior-to-posterior movements (PS regression). These posterior movements will be continued during the following steps of
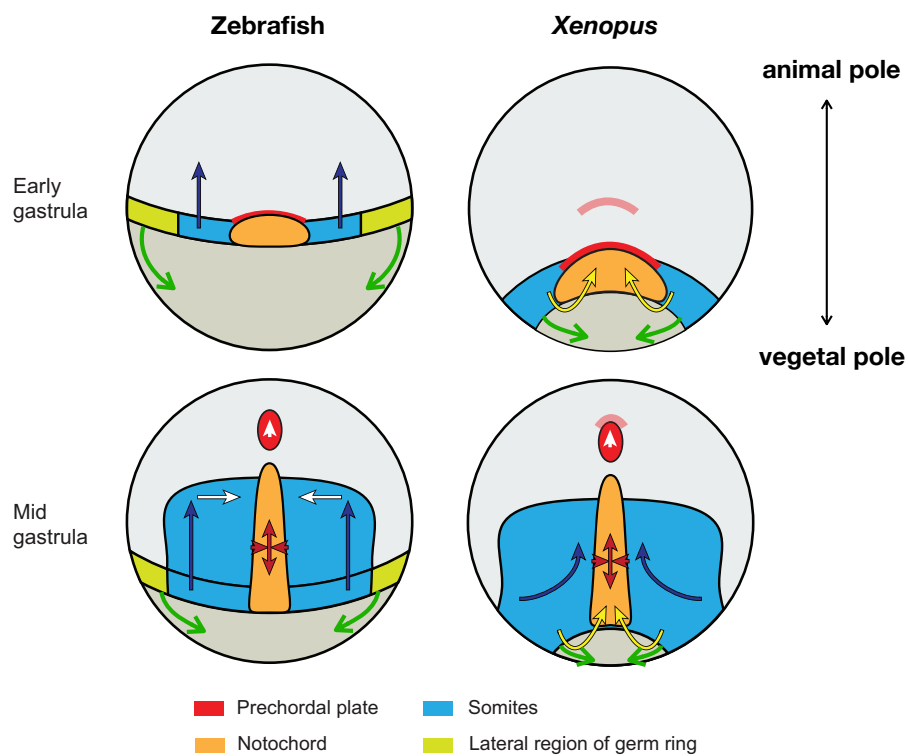
FIGURE 1.9 – Schematics of gastrulation in anamniotes in dorsal view (adapted from Tada and Heisenberg, 2012). Green arrows: epiboly movements, black arrows: internalization movements, white arrows: collective migration, red arrows: convergent extension by mediolateral intercalation, yellow arrows: involution movements
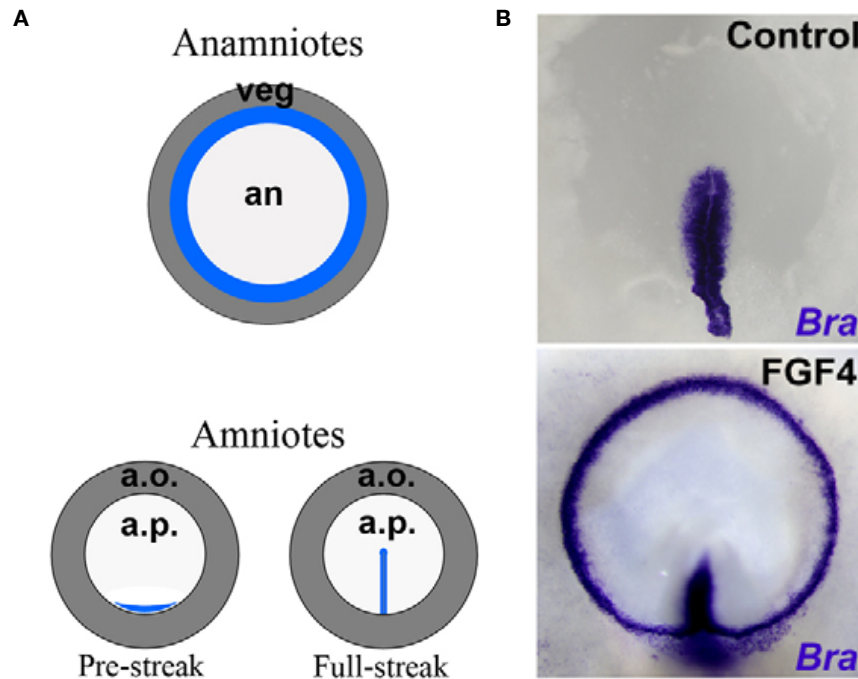
FIGURE 1.10 – Evolutionary relation between the blastopore and the primitive streak (adapted from Alev et al., 2013). **A**: Schematics of gastrulation in anamniotes and amniotes. veg: vegetal pole, an: animal pole, a.o.: *area opaca*, a.p.: *area pellucida*. **B**: "Circumblastoporal" mesoderm induction by global FGF4 activation in the chicken embryo. *Bra*: *in situ* staining of *Brachyury*.

development.

Despite these differences, gastrulation is evolutionarily related among vertebrates. Indeed, a global activation of the fibroblast growth factor-4 (FGF4) pathway has been shown to lead to mesoderm induction along a circle, in a similar fashion to anamniotes in the chicken embryo (Alev et al., 2013, see Figure 1.10). Alev et al. proposed that the streak evolved then secondarily by restricting the FGF4 zone to the PMZ.

We have shown how the AP axis is first physically established during gastrulation. After the end of gastrulation, the AP axis is further extended and the embryonic structures form along the axis.

1.1.4   Elongation after gastrulation

When gastrulation ends is debated in chicken embryos. According to some authors, gastrulation ends after full PS extension (Stern, 2004). However, mesoderm ingression continues during PS regression resulting in the formation of the somitic and lateral plate material of the body and tail. This has led other authors to propose that gastrulation continues until the end of axis elongation (Gont et al., 1993). During PS regression, general convergence movements are observed leading to the narrowing and elongation of the embryonic body. After the 10-somite stage, elongation continues without any further narrowing. Therefore, in this section, we will focus on the developmental window from the end of the convergence movements (10-somite stage) to the 25-somite stage, when body axis extension becomes negligible (Denans et al., 2015).

In other vertebrates, elongation dynamics differ throughout developmental stages. In zebrafish, we can consider two different phases of extension. From the 1-somite stage to the 15-somite stage, the embryonic tissues essentially converge towards the AP axis but still wrap the egg cell. From the 15-somite stage onward, the tail of the embryo gradually separates from the egg cell and start extending. In *Xenopus laevis*, during neurulation, until the stage 22 (12-somite stage), the embryo's aspect ratio stays roughly constant, then the axis starts extending.

As somitogenesis progresses, the anatomical structures of the different vertebrates species become more and more similar. Different species converge towards the phylotypic stage. However, the mechanisms by which they elongate are diverse. We review here these different mechanisms. Ray Keller previously published an important review of elongation mechanisms during embryogenesis which encompasses some of the mechanisms presented here (Keller, 2006).

Convergent extension mechanism

CE has been extensively studied in amphibians, with an important contribution from Ray Keller's laboratory. Explant cultures of mesodermal and neural tissues showed that these tissues were mostly contributing to the extension of the axis. After involution of the mesoderm, it extends internally along the AP axis. If it is dissected out from the rest of the embryo and cultured as explants, it undergoes autonomous CE (Keller et al., 2000). This autonomous extension of the internal tissues has been quantified by measuring the maximum force they could exert (stalling force) and the stiffening of the tissues during development. Moore et al., 1995 showed that the dorsal mesoderm is exerting the highest pushing forces ($\sim$ 500 nN). Neural tissues extend as well but they are less stiff than the dorsal mesoderm. These CE movements are driven by two kinds of processes: radial intercalation (deep layers of cells intercalating into outer layers) and MLCI (lateral cells intercalating towards the midline). MLCI initially involves bipolar protrusive activity oriented along the ML axis, which exerts traction of the cells with respect to one another and forces them to intercalate. Later, a boundary of the proto-notochord is visible by a loss of the bipolar activity on the lateral region, while the bipolar behavior is kept in the midline until the proto-notochord is a two-cell wide structure. In surface, the neural plate also exhibits CE movements by monopolar protrusive activity leading to directed migration towards the midline (Keller et al., 2000).

Moore et al., 1995 showed that the involuting tissues were stiffening much more along the AP axis (more than a 3-fold increase between the early and late gastrula stages) than along the ML axis (about a 1.5-fold increase between the early and late gastrula stages). This polarized stiffening creates a scaffold along which the embryo extends.

CE has an important contribution to zebrafish extension too. It was recently shown that convergent movements towards the midline persist longer than it was previously thought (Steventon et al., 2016). Up to the 12-somite stage, lateral cells enter the midline by directed migration directly into the forming somites without going through the tailbud. CE also happens all along the axis up to the 24-somite stage. It mainly takes place in the unsegmented region but also in the somitic region, which extends the axis before a second phase of extension continues by volumetric growth. CE-dependent elongation has been shown to be present in mice as well. The early axis extension depends on CE movement in the neural plate (Williams et al., 2014). At stage 2-4 somites (E8) while the epithelium is highly proliferative, it does not exhibit any oriented division which could explain axis extension. Vangl2 and Ptk7

dependent ML polarization and protrusive activity was shown to drive MLCI and consequently CE movements. At stage 5-7 somites (E8.5), Ptk7-dependent CE activity was also noticed in the anterior PSM (Yen et al., 2009). Inhibition of CE behavior impaired the compaction of the PSM and the subsequent somites, and left the mesoderm as a thin and wide layer of cells.

CE is a major elongation mechanism. While it appears restricted to early somitogenesis stages in the chicken embryo (see PS regression above), it can persist longer in other vertebrates. Several cell movements drive CE: MLCI, radial intercalation and directed migration.

Osmotic swelling mechanisms

In *Xenopus*, the notochord has been shown to be an important component of the axis extension and stiffening processes (Adams et al., 1990). The authors showed that isolated notochords can be extended upon increase of the osmotic pressure. The notochord can undergo repeated cycles of stiffening, extension, bending and softening by varying the osmotic strength of the medium. During development, large vacuoles filled with proteoglycans appear in notochord cells making them sensitive to osmotic pressure. Then, the notochord swells but it is constrained by a sheath of fibrillar ECM deposited at a precise $54°$ angle along the notochord. The angle is a compromise to maximize both the flexural stiffness and straightening. The notochord is, therefore, a stiff scaffold to the elongating AP axis. However, more recent investigations showed that force production by the notochord was negligible compared to neural and mesodermal tissues (Zhou et al., 2015). Thus, the role of notochord stiffening is likely to be restricted to a scaffolding role without any active pushing contribution. In zebrafish too, the notochord swells during axis extension (Ellis et al., 2013). Vacuole formation is essential to proper axis elongation. If vacuole formation is inhibited zebrafish axis are 35% shorter.

In summary, the notochord appears to be important in axis elongation in anamniotes. However, in amniotes, the notochord is relatively less prominent than in anamniotes. Indeed, while in zebrafish, the notochord and the neural tube have an equivalent diameter (40 µm), in chicken, the notochord is only a third of the neural tube (respectively 50 µm and 150 µm).

Cell motility based mechanisms

In the chicken embryo, a mechanism involving the profile of motility of the PSM cells along the AP axis has been proposed to explain elongation of the posterior tissues by Bénazéraf et al., 2010. This mechanism will be presented in detail in Chapter 2. Nonetheless, we briefly review the proposed model here. The authors showed that the posterior PSM is essential to proper elongation of the axis. It has been previously shown that a gradient of Wnt, FGF8 coupled with mitogen-activated protein kinase (MAPK) along the axis plays a key role in elongation (Delfini et al., 2005, Bénazéraf and Pourquié, 2013). Bénazéraf et al., 2010 further demonstrated that the graded profile of cell motility, downstream of the FGF8/MAPK gradient, controls elongation. Indeed, PSM cells do not show any directed migration but high random motility in the posterior region and low random motility in the anterior region. Furthermore, cell density is low in the PSM compared to neighboring tissues and it exhibits an AP gradient. The decrease of cell motility in the anterior PSM is linked

with its epithelialization, which results in compaction that could be involved in elongation too. Moreover, cell proliferation was shown to play a limited role in axis short term elongation, further suggesting that the addition of cells is not part of the extension mechanism. Unlike, other models in which elongation is driven by stiff, dense and epithelial tissues, the proposed model of chicken embryo elongation relies on a tissue with a low density and an important cell random motility. To account for elongation, the authors proposed a model in which the gradient of cell motility creates a posterior bias in the average movement of cells, which with their high motility exert a pushing pressure on the posterior boundary. A theoretical continuum model has recently been proposed to quantitatively detail how the pattern of motility can drive axis extension (Regev et al., 2017).

In zebrafish, cell motility has also been shown to play a key role in elongation. Similarly to the chicken embryo, inhibition of cell division has little effect on elongation (Zhang et al., 2008). Inhibition of the Wnt or the FGF pathways also leads to dramatic elongation defects. The effect of these pathways on tissue flows has recently been investigated. Taking advantage of the high-quality imaging offered by zebrafish, Lawton et al., 2013 could produce all-cell velocity maps in 3D during elongation. Cells in the axial dorsal region exhibit a fast and coherent flow directed towards the tail. Then, they enter the progenitor zone where they mix and swirl around to enter the PSM. Cells quickly slow down in the PSM. The authors did not uncouple the cell-autonomous movements from the mean tissue flow. Therefore, the motility profile cannot be directly compared to the chicken one. An important difference with the chicken PSM is that the density is higher and fairly constant along the axis in the zebrafish PSM. Therefore, the compaction in the anterior chicken PSM is absent in zebrafish. A consequence of the tissue higher density is that it is prone to tissue jamming which happens in the case of Wnt inhibition (Lawton et al., 2013). Wnt inhibition has a dramatic effect by disrupting bilateral symmetry. The authors showed that Wnt inhibition leads to a loss of flow coherence in the axial dorsal region but does not slow down the cells. The perturbed flow creates cell jamming and disrupts the smooth mixing of cell in the progenitor zone. As a result, the flux of cells entering the PSM is highly chaotic and triggers axis asymmetry. Regarding FGF inhibition, the disruption of flow coherence is even stronger but surprisingly leads to a less severe phenotype as axis elongation is only reduced. Lawton et al. explained this result by the fact that the loss of flow coherence all along the axis results in a reduced flux of cells which avoided cell jamming. This study explains how the tissue flow is important to proper axis elongation but it does not provide a mechanism accounting for extension and force transmission.
Another study from Scott Holley's laboratory investigated the role of ECM in elongation (Dray et al., 2013). When interactions with the fibronectin network are disrupted (by targeting their cellular receptors integrin $\alpha5$ and integrin αV using morpholinos), fibronectin orientation was abnormal and trunk elongation was notably impaired. Surprisingly, the authors could only find a very limited impact on the cell motility profile. However, they showed that notochord growth was disconnected from the paraxial mesoderm and, consequently buckled. Elongation could be rescued by restoring integrin activity only in the PSM, and therefore ECM connections between the PSM and the notochord.
In summary, axis extension in zebrafish seems to rely both on a smooth coherent flow in the dorsal axial posterior zone and a tight inter-tissue mechanical adhesion to propel the tissues coherently (see Figure 1.11).
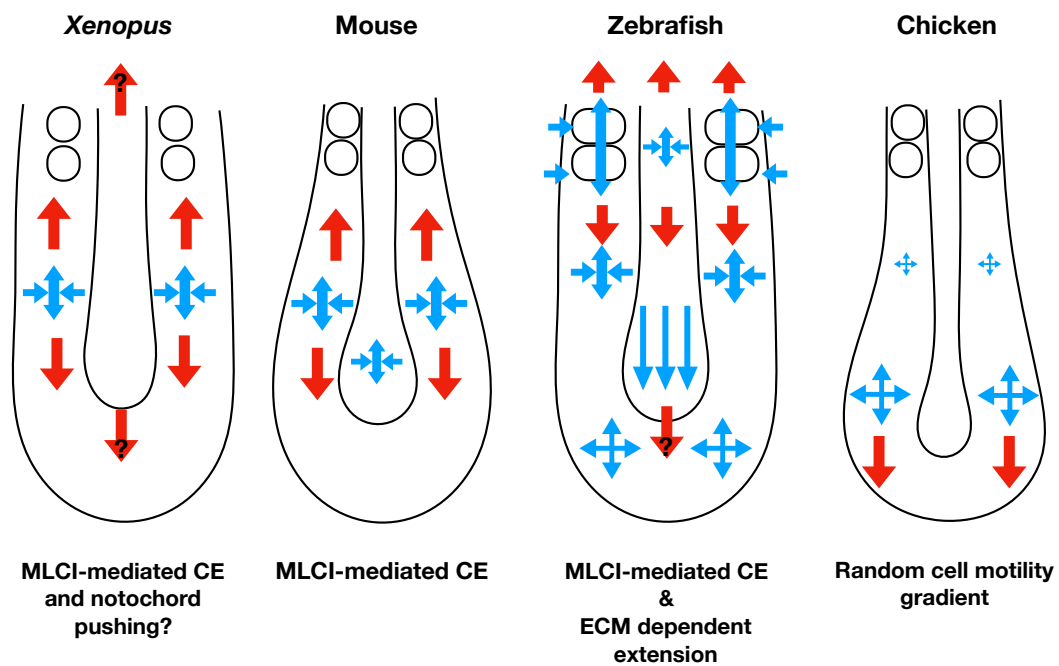
FIGURE 1.11 – Axis extension models. Blue arrows: morphogenetic movements. Red arrows: exerted forces. Convergent extension is crucial in *Xenopus* mesoderm, in mice mesoderm and neural plate and in zebrafish PSM, somites and neural tube. Notochord role is key in zebrafish and debated in *Xenopus*. Cell flow is important to symmetrical elongation in zebrafish but its role in force production remains unclear. A random cell motility gradient is proposed to drive elongation in chicken.

Conclusion

The extension of the AP axis in vertebrates generates similar anatomical structures during somitogenesis. However, the mechanisms involved in AP extension are varied between animal models, owing to different initial geometries and to important differences in tissue architecture.

CE movements have been extensively investigated. Their molecular basis and their physical mechanism of action are now well described. However, CE does not seem to be involved in late phases of axis elongation in the chicken embryo. Proposed mechanisms (coupled extension of axial and paraxial tissues in zebrafish and cell motility gradient in chicken) still lack a detailed mechanical description. Mechanical measurements of the tissue properties and the force production are therefore necessary. We will review methods of such measurements in the rest of this introduction.

1.2   Mechanics of biological tissues

As the description of embryo patterning by morphogens reached high levels of detail, it became clear that a better understanding of how these molecular determinants could trigger physical actions was required. In parallel, the mechanics of living systems has been a developing topic of interest among physicists in past decades, especially in the soft matter community. Living systems exhibit novel properties compared to non-living soft systems, owing to their out-of-equilibrium nature (Marchetti et al., 2013).

In order to better understand the role of mechanics in morphogenesis, two kinds of measurements can be carried out. First, tissue mechanical properties must be described to understand how tissues respond to internal or external stress: do they resist, flow, buckle or wrinkle? Second, stress production, at different scales, needs to be assessed to unravel how embryos deform themselves or their environment. These two kinds of properties are coupled during morphogenetic events. For instance, the elastic resistance of a tissue to a stress produces another stress in response. In addition, these two kinds of properties should not be seen as respectively passive and active properties. Indeed, the mechanical properties can arise from active processes, as tissues can actively stiffen during development.
In the following, we introduce physical quantities and their definition and we review the techniques developed to measure them. An important review of these techniques has been recently presented (Sugimura et al., 2016). We first focus on mechanical properties, and then, on stress production.

1.2.1   Mechanical properties measurement

Measuring mechanical properties involves imposing a deformation or a stress to a material and measuring its response. The response can be instantaneous and will not evolve over time. This behavior characterizes solid materials: if the imposed stress (respectively deformation) is constant over time, the deformation (respectively stress) will be constant too, and the relation between the two is quantified by the elasticity. Alternatively, the response can evolve over time. This is the behavior of liquid materials. For instance, if a stress is imposed, the deformation will vary over time at a certain rate controlled by viscosity. However, in biological samples, the response is often not as simple as these two classical kinds of properties in material science. Biological systems often share properties of both a solid and a liquid, they are viscoelastic materials. Solid or liquid properties of viscoelastic systems arise at different timescales. Below, we define in more details the diverse mechanical properties and review the methods to measure them.

In the following sections, we will describe the relations between stress and deformation. Let us define these terms more precisely:

- in a continuous material, the stress σ is define as the force f applied across an area A: $\sigma = \frac{f}{A}$. Therefore, it has the dimension of a pressure.

- the deformation, also referred to as the strain ϵ, is the relative change in size of an object. If we consider the simple case of the change of a length $\Delta\ell$ from an initial length ℓ_0: $\epsilon = \frac{\Delta\ell}{\ell_0}$. This is the Cauchy strain (or engineering strain). Another definition of the strain can be given as the true strain (also called the natural strain) $\epsilon_{true} = \ln\left(\frac{\ell_0+\Delta\ell}{\ell_0}\right) = \ln(1 + \epsilon)$. It is often used when large

deformations are involved. Here, we stay in the domain of small deformations, so we will only use the Cauchy strain definition.

The stress and the strain are quantities that can vary in a material depending on the direction of space. For instance, a material during a uniaxial stretch is under a stress along the stretch axis and no stress along orthogonal axes to the stretch axis. The material will classically extend along the stretch axis and thin down along orthogonal axes to the stretch axis. Therefore, the strain is not constant along all directions either. A mathematical description of this dependency on the directions of space is given by the tensorial notation. This notation gathers the components of the stress (or the strain) along the principal directions of the coordinates system. We briefly introduce here the tensorial notation in the cartesian coordinates system in three dimensions. This notation will not be extensively used in this thesis, but will rather be used to introduce simple deformations such as the shear deformation. The stress tensor $\bar{\bar{\sigma}}$ (respectively the strain tensor $\bar{\bar{\epsilon}}$) gathers all the components of the stress σ_{ij} (respectively the strain ϵ_{ij}) along a direction $\vec{j}$ applied on an infinitesimal surface defined by the orthogonal direction $\vec{i}$:

$$\bar{\bar{\sigma}} = \begin{pmatrix} \sigma_{xx} & \sigma_{xy} & \sigma_{xz} \\ \sigma_{yx} & \sigma_{yy} & \sigma_{yz} \\ \sigma_{zx} & \sigma_{zy} & \sigma_{zz} \end{pmatrix} \tag{1.1}$$

and,

$$\bar{\bar{\epsilon}} = \begin{pmatrix} \epsilon_{xx} & \epsilon_{xy} & \epsilon_{xz} \\ \epsilon_{yx} & \epsilon_{yy} & \epsilon_{yz} \\ \epsilon_{zx} & \epsilon_{zy} & \epsilon_{zz} \end{pmatrix} \tag{1.2}$$

Depending on the mechanical properties of the material the stress and strain are related by different stress-strain relations. For instance, if the material is elastic, the relation does not depend on time. Thus, to a variation of the stress (respectively the strain) corresponds an instantaneous variation of the strain (respectively the stress). In addition, if the deformation is in the regime of linear elasticity (often for small deformations), the strain and the stress are proportional. The coefficient of proportionality is classically referred to as the stiffness, which can be described by different quantities depending on the kind of deformation (see below).
While an elastic material stores an energy during a deformation, a viscous material dissipates it along the deformation. There is no instantaneous deformation and there is a relation between the strain rate $\dot{\epsilon}$ and the stress ($\dot{\epsilon}$ being the time derivative of the strain).

Elastic properties measurement

In material science, different kinds of assays have been developed to measure the elastic properties of a sample. Depending on the kind of deformations, the stress-strain relation can be expressed by different mechanical quantities. In the case of a classical uniaxial stretch, the stress-strain relation is expressed by the Young's modulus E. If we simplify the problem to a two-dimensional description, with a stretch along the $\vec{x}$ axis, there is no shear so the stress tensor is:

$$\bar{\bar{\sigma}} = \begin{pmatrix} \sigma_{xx} & 0 \\ 0 & 0 \end{pmatrix} \tag{1.3}$$

and the strain tensor:

$$\bar{\bar{\sigma}} = \begin{pmatrix} \epsilon_{xx} & 0 \\ 0 & \epsilon_{yy} \end{pmatrix} \tag{1.4}$$

with $\epsilon_{xx} > 0$ and $\epsilon_{yy} < 0$ (if $\nu > 0$, where ν is the Poisson ratio, which describes the response of the material in the transverse direction). The stress-strain relation then reads:

$$\begin{cases} \epsilon_{xx} & = & \frac{1}{E}\sigma_{xx} \\ \epsilon_{yy} & = & -\frac{\nu}{E}\sigma_{xx} \end{cases} \tag{1.5}$$

Since the strain and the Poisson coefficient are dimensionless, the Young's modulus has the same dimension as the stress (*i.e.* a pressure).

In the case of an isotropic compression by a pressure p, the stress tensor reads:

$$\bar{\bar{\sigma}} = \begin{pmatrix} \sigma_{xx} & 0 & 0 \\ 0 & \sigma_{yy} & 0 \\ 0 & 0 & \sigma_{zz} \end{pmatrix} = \begin{pmatrix} -p & 0 & 0 \\ 0 & -p & 0 \\ 0 & 0 & -p \end{pmatrix}. \tag{1.6}$$

Then, the response of the material is described by the bulk modulus K: $\bar{\bar{\sigma}} = K\bar{\bar{\epsilon}}$. K is related to E and ν by: $K = \frac{E}{3(1-2\nu)}$.

In the case of a simple two-dimensional shear μ, the stress tensor reads:

$$\bar{\bar{\sigma}} = \begin{pmatrix} 0 & \sigma_{xy} \\ \sigma_{yx} & 0 \end{pmatrix} = \begin{pmatrix} 0 & \mu \\ \mu & 0 \end{pmatrix}. \tag{1.7}$$

Then, the response of the material is described by the shear modulus G: $\bar{\bar{\sigma}} = 2G\bar{\bar{\epsilon}}$. G is related to E and ν by: $G = \frac{E}{2(1+\nu)}$.

Compression and indentation methods

Biological samples are often in limited supply and not homogeneous on very large scales. Thus, compared to classical samples in material science, traditional macroscopic mechanical tests are difficult to perform. Furthermore, samples can be challenging to manipulate. For instance, pulling on a sample requires to find a way of sticking the sample to a probe in physiological condition without breaking it. As a result, compression is a straightforward strategy for measuring elasticity, as it does not require any attachment to the sample. A nanonewton force apparatus has been developed by the laboratories of Lance Davidson and Ray Keller (Davidson and Keller, 2007). It consists of an indenter linked to a force sensor (made of a calibrated optic fiber). The sample is submitted to uniaxial compression to measure the stress-strain relation. Uniaxial compression has notably been used to measure the stiffening of *Xenopus* dorsal tissue during development (Zhou et al., 2009). As often with embryonic tissues, Zhou et al., 2009 noticed their sample exhibited a viscoelastic behavior (see below) as the sample response showed different timescales: short times it flowed like a liquid but at long times the deformation saturated like a solid. The authors, therefore, defined the strain as the maximum strain. Measured stiffness increased over 6-fold during development (from 13 to 85 Pa), with the paraxial mesoderm being the major contributor to the stiffness (the individual tissue contribution was assessed by iteratively removing tissues). Moreover, the authors showed that ECM had no effect on the tissue stiffness while the actomyosin network had a major impact on it.

Atomic force microscopy (AFM) has been extensively used to measure the mechanical properties of individual cells. Atomic force microscopes are made of a flexible beam (cantilever) which deflection is monitored by shining a laser on it. They are typically used to probe the topography of a sample with a nanometer precision. By calibrating the stiffness of the cantilever, they can be used as pN to nN force sensors. Thanks to their fine tip, subcellular properties can be measured. For instance, the role of the cytoskeleton contractility in the cortical tension has been assessed by AFM (Krieg et al., 2008). AFM can also be used to measure tissular properties, by using a colloidal tip of various sizes. For instance, the elasticity of spinal cord slices has been measured with a 40 μm diameter colloidal tip (Koser et al., 2015). The turgor pressure in plant apical meristem was also measured (Beauzamy et al., 2015).

Stretching methods

Certain tissues due to their geometry are more amenable to stretching. Suspended cell monolayers can be specifically cultured on a uniaxial stretching apparatus prior to mechanical assay (Harris et al., 2012). The suspended monolayer, freed from its substrate, can be stretched. A biaxial stretcher made of a hollow ring below a cell monolayer that can aspirate it on its sides and stretch the monolayer in the center has also been devised (Benham-Pyle et al., 2015). It was used to show that quiescent cells could re-enter their cell cycle upon stretching.

Regarding embryonic tissues, explants from *Xenopus* are large enough to be fixed by their two ends and subsequently stretched. For instance, two dissected explants of the involuting margin zone (constricting region during the blastopore closure) can "sandwich" the stretching apparatus (Shook et al., 2018). This method uses the Keller's sandwich technique to culture flat explants. Isolated explants would curl up if cultured alone, but if two similar explants are cultured by bringing in contact their mesodermal layer (*i.e.* the "sandwich"), they stay flat (Keller and Danilchik, 1988). The authors measured the sandwich's stiffness to be around 10 to 20 Pa. The cylinder geometry of the gut and its important length makes it also an ideal tissue to stretch uniaxially. A glass fiber cantilever has been used as force sensor at the end of a chicken embryo mid-gut to measure stiffness in the order of 1 kPa (Chevalier et al., 2016). A similar stretcher has been used to measure the stiffness of the gut tube and the mesentery to be around respectively 20 kPa and 300 kPa (Nerurkar et al., 2017).

Aspiration methods

As pulling on the bulk of the sample by a stretch is often challenging, another way of pulling on a sample is to aspirate it in a capillary. Aspiration by micropipettes has historically been used to measure both elastic and viscous properties (see below) of single cells (Jones et al., 1999, Theret et al., 1988). The relation between the length of the aspirated material (deformation) and the applied pressure yields the Young's modulus, E. These studies measured $E \approx 400$ Pa (Theret et al., 1988) for endothelial cells and $E \approx 650$ Pa for chondrocytes (Jones et al., 1999). It has also been used on multicellular scales to measure the mechanical properties of cellular aggregates of epithelial cells with $E \approx 700$ Pa (Guevorkian et al., 2010). More details about the theory of pipette aspiration will be presented in Chapter 4.

Viscous properties measurement

Viscosity is a measurement of how a fluid flows. Microscopically, there is a friction between the internal components of the fluid that controls the flow dynamics (the components being either small molecules, macromolecules, cellular organelles

or even cells). For a newtonian fluid, there is a linear relation between the stress σ and the strain rate, $\dot{\epsilon}$ (we use the dot notation as the time derivative throughout this thesis):

$$\sigma = \eta\dot{\epsilon} \tag{1.8}$$

where η is the dynamic viscosity.

The viscosity can be measured by tracking the passive diffusion of spherical beads in the sample of interest. The Stokes-Einstein relation can then be used to relate the beads diffusion coefficient D to the viscosity η:

$$k_B T = 6\pi\eta DR \tag{1.9}$$

where k_B is the Boltzmann constant, T the temperature and R the bead radius. The diffusion coefficient can be measured by plotting the bead mean squared displacement $\langle\Delta r^2(t)\rangle$ with respect to time, where $\Delta\overrightarrow{r}(t) = \overrightarrow{r}(t) - \overrightarrow{r}(0)$, with the bead position $\overrightarrow{r}(t)$ at time t. If the movement is diffusive, the relation is linear and $\langle\Delta r^2(t)\rangle = 6Dt$ (for a tridimensional diffusion). In this way, the cytosol of the *Drosophila* blastula has been measured to be around 3 Pa·s (Bambardekar et al., 2015). However, this method relies on the assumption that the movement of the beads is solely driven by thermal fluctuations, while the activity of the cytoskeleton might also be involved. In addition, the movement of the beads is not necessarily diffusive (it can be subdiffusive in case of important crowding or superdiffusive in case of directional movements) in which case D cannot be measured.

Pipette aspiration has also been used on cells exhibiting a liquid behavior. The flow rate into the pipette can be measured to calculate the viscosity. The viscosity of blood granulocytes has been measured to be roughly in the order of magnitude of hundreds of Pa·s depending on the temperature (Evans and Yeung, 1989). The viscosity of cellular aggregates has also been measured by this method to be $\eta \approx 2 \times 10^5$ Pa·s (Guevorkian et al., 2010).

The five orders of magnitude between the Drosophila cytosol and the cellular aggregate can be explained by the fact that probed fluids show very distinct natures. The passive microrheology experiment probes the drag with the macromolecules, while the flow of the whole cytoplasm of a blood cell involves friction by the rearrangement of the cell organelles, and the cellular aggregates viscosity rises from the cell-cell rearrangement.

Viscoelastic properties measurement

Biological samples often exhibit a more complex mechanical behavior than a pure elasticity or a pure viscosity, they are viscoelastic materials. Such materials can be described by rheological models. These models are built by associating different elastic (spring) and viscous (dashpot) elements. For instance let us consider the two most simple viscoelastic models: the Maxwell model and the Kelvin-Voigt model.

The Maxwell model is the association in series of a spring element and dashpot element (see Figure 1.12). We note the strain and stress of respectively the spring and the dashpot elements: ϵ_S, σ_S and respectively ϵ_D, σ_D. The whole element is under the same total stress $\sigma_T = \sigma_S = \sigma_D$ while the total strain ϵ_T is the sum of the strains of the two elements: $\epsilon_T = \epsilon_S + \epsilon_D$. The stress-strain relation and respectively the stress-strain rate relation can be written for the spring element of spring constant k,

Maxwell model **Kelvin-Voigt model**
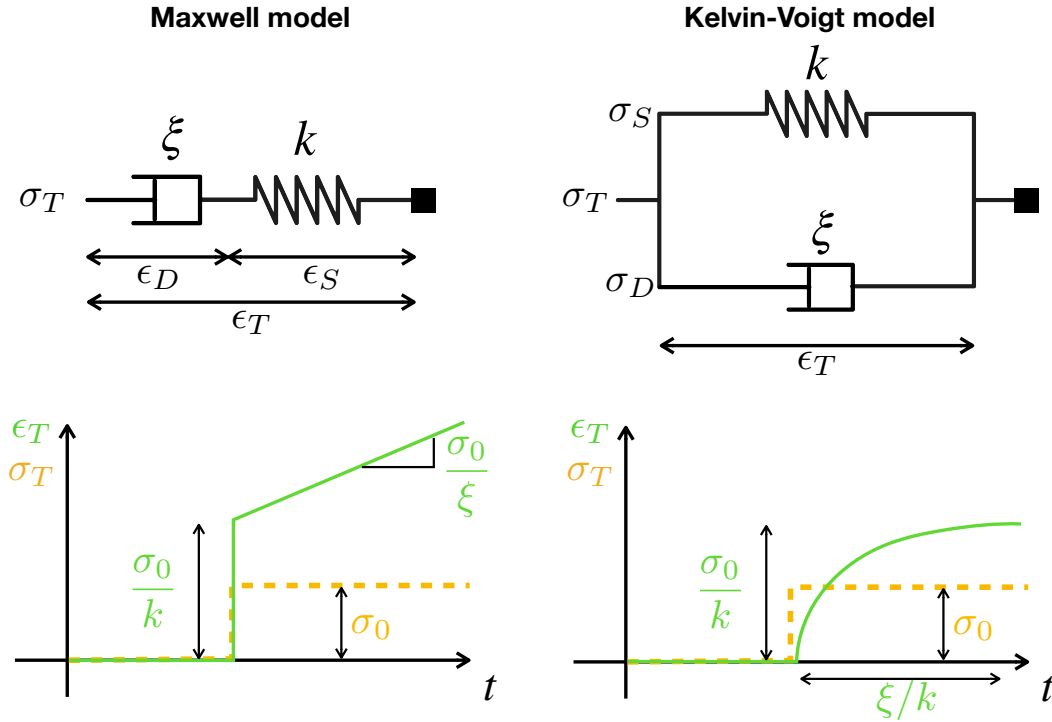
FIGURE 1.12 – Schematics and temporal evolution of the Maxwell and Kelvin-Voigt models.

respectively for the dashpot element of viscosity ξ:

$$\begin{cases} \epsilon_S &= \frac{\sigma_S}{k} &= \frac{\sigma_T}{k} \\ \dot{\epsilon}_D &= \frac{\sigma_D}{\xi} &= \frac{\sigma_T}{\xi} \end{cases} \tag{1.10}$$

Thus, the temporal evolution is given by the differential equation: $\dot{\epsilon}_T = \frac{\dot{\sigma}_T}{k} + \frac{\sigma_T}{\xi}$. In the case of the response to a sudden stress σ_0 at time t_0, $\dot{\sigma}_T(t) = \sigma_0 \delta(t - t_0)$, where δ is the Dirac function. By integration, we have: $\epsilon_T(t) = \frac{\sigma_0}{k} + \frac{\sigma_0}{\xi} t$. Therefore, a Maxwell material is a solid at short times (instantaneous jump of amplitude $\frac{\sigma_0}{k}$) and a liquid a long times (viscous creep of rate $\frac{\sigma_0}{\xi}$).

An equivalent kind of derivation can be done with a Kelvin-Voigt model, which is made of a dashpot element and a spring element in parallel, giving the relation:

$$\sigma_T(t) = k\epsilon_T + \xi\dot{\epsilon}_T \tag{1.11}$$

The temporal evolution after a sudden stress σ_0 is given by $\epsilon_T(t) = \frac{\sigma_0}{k}\left(1 - \exp(\frac{t}{\tau})\right)$, where the characteristic time is $\tau = \frac{\xi}{k}$. Thus, the deformation of a Kelvin-Voigt material saturates at long times, which is a solid-like behavior.

Materials can even be more complex by associating different Maxwell or Kelvin-Voigt models in series or parallel. If there is a sufficient number of Kelvin-Voigt models in series, the material is characterized by a wide spectrum of characteristic times. As the spectrum of characteristic times becomes wide the temporal evolution converges to a power law. Creep experiments on single cells have been shown to be well described by power laws (Balland et al., 2006). The compliance $J(t) = \frac{\epsilon(t)}{\sigma(t)}$ follows a power law: $J(t) = At^\alpha$. In this study, single cells are stretched between

two parallel microplates, or beads tethered to the membrane are optically trapped and submitted to oscillatory displacements. In both techniques, the cell response exhibits a stereotypical power exponent of $\alpha \approx 0.2$, while the prefactor A is variable. In suction experiments of *Xenopus* gastrula into a microchannel, the dynamics of aspiration has also been described by a power law with a typical exponent of 0.25, which is insensitive to the applied pressure (Dassow et al., 2010).

Viscoelastic materials are often probed by oscillatory assays. So if we consider an oscillatory strain of angular frequency ω and amplitude ϵ_0 in the form of $\epsilon(t) = \epsilon_0 e^{i\omega t}$, we have the temporal evolution of the stress for a Kelvin-Voigt model using the constitutive equation 1.11:

$$
\begin{aligned}
\sigma(t) &= k\epsilon_0 e^{i\omega t} + i\xi\omega\epsilon_0 e^{i\omega t} \\
&= (k + i\xi\omega)\,\epsilon(t) \\
&= E^*\epsilon(t)
\end{aligned}
\tag{1.12}
$$

where we define the dynamic modulus $E^* = k + i\xi\omega$. Its real and imaginary components E' and E'' are respectively called the storage and loss moduli. In the Kelvin-Voigt model, we have $E' = k$ and $E'' = \xi\omega$, so we see the first is related to the elastic properties of the material and the second to its viscous properties.
More generally, if the strain follows $\epsilon(t) = \epsilon_0 e^{i\omega t}$, the stress will also have the same oscillatory form with a delay, as we saw there was a lag time between in the sudden stress and the maximum deformation for the Kelvin-Voigt model. So $\sigma(t) = \sigma_0 e^{i(\omega t + \delta)}$, where δ is the phase shift and σ_0 the stress amplitude. For a purely elastic material, $\delta = 0$ and for a purely viscous material, $\delta = \frac{\pi}{2}$. Analogous to the Kelvin-Voigt model, we can define the dynamic modulus E^*:

$$
\begin{aligned}
E^* &= \frac{\sigma(t)}{\epsilon(t)} \\
&= \frac{\sigma_0 e^{i(\omega t + \delta)}}{\epsilon_0 e^{i\omega t}} \\
&= \frac{\sigma_0}{\epsilon_0} e^{i\delta}
\end{aligned}
\tag{1.13}
$$

The storage and loss moduli then read: $E' = \frac{\sigma_0}{\epsilon_0}\cos\delta$ and $E'' = \frac{\sigma_0}{\epsilon_0}\sin\delta$.

Oscillatory assays have been used to measure cytoplasm properties by active microrheology. In these experiments, beads injected in the cell cytoplasm are actively moved by either magnetic or optical tweezers. In brief, these tweezers rely on generating traps by a magnetic field or a laser beam. The beads movements with respect to the imposed position of the trap are measured and the force applied by the trap is known as the trap stiffness can be calibrated. By imposing oscillatory movements to the trap at different frequencies, the frequency profile of the storage and loss moduli can be measured. Fabry et al., 2001 showed that cell cytoplasm exhibited the properties of soft glassy materials with storage and loss moduli following power laws. Furthermore, at short timescales (frequency ranging from 0.3 to 100 Hz), cytoplasm behaves more as a weak elastic gel than a viscous liquid (Guo et al., 2014).

1.2.2 Stress production measurement

Biological tissues are active materials. Their metabolism generates a sustained flux of energy that maintains them out of equilibrium. Consequently, biological systems have the ability to internally produce forces that might deform their shape. The force production is not necessarily independent from their mechanical properties, so biological systems exhibit a complex behavior of interactions between the stress production and active response of the mechanical properties.

The force production takes place at the molecular and cellular level. At the molecular level, directed polymerization of cytoskeleton (*e.g.* actin bundles in lamelipodia), and action of molecular motors (*e.g.* actomyosin contractility, action of dynein on anti-parallel microtubules of the spindle during cytokinesis) exert forces. At the cellular level, osmotic pressure and mass gain produce stress on the cell environment. However, stress production has physical consequences at very different scales. The spatial distribution of individual sources of production might create mechanical states of stress on a large scale.

We review below various methods to measure the stress production at different scales.

Measurement at the cellular level

Laser-microsurgery has been extensively used to sever subcellular regions and monitor the dynamics of relaxation of the system. The anisotropy of the opening after laser "drilling" can reveal the stress tensor within the cell (Ma et al., 2009). If a quasistatic state is assumed, the initial velocity of the opening yields the magnitude of the stress. If we consider a cytoskeleton filament undergoing a tension T, just after the severing, it recoils at an initial speed v_0 and the tension is balanced by the drag viscosity η. The recoil velocity quickly decreases as the tension is dissipated by the viscous drag. Thus, we can write: $T = \eta v_0$. However, in practice, the drag viscosity is challenging to estimate. Consequently, this technique is mostly used to measure relative values of the tension T/η which can be compared in the same system assuming η does not vary too much. This method has been mostly used to measure junction tension anisotropy which will be discussed below (section 1.2.2).

A recent technique has been developed to measure tension in individual cytoskeleton molecules. This technique is based on an engineered molecular spring integrated in cytoskeleton molecules, for which the state of extension is measured by Förster resonance energy transfer (FRET) (Grashoff et al., 2010). The FRET effect relies on the coupled emission of fluorescent light by two fluorophores close enough in space. Upon excitation of a first fluorophore, if the second is close enough a part of its energy can be transferred to the second without emission. The second will then emit the received energy at a lower wavelength than the first fluorophore's one. So, the ratio of the two emissions quantifies the FRET effect. This effect precisely depends on the distance between the two fluorophores. Taking advantage of this spatial dependency, FRET force sensors are designed by genetically inserting two fluorophores at each end of a molecular spring. When the spring is under no tension, there is no extension, so the fluorophores are close and the FRET effect is strong. As the tension increases, the spring is stretched and the FRET effect decreases. Several FRET sensors have been developed with different spring constant ranging from 1-5 pN to 8-12 pN.
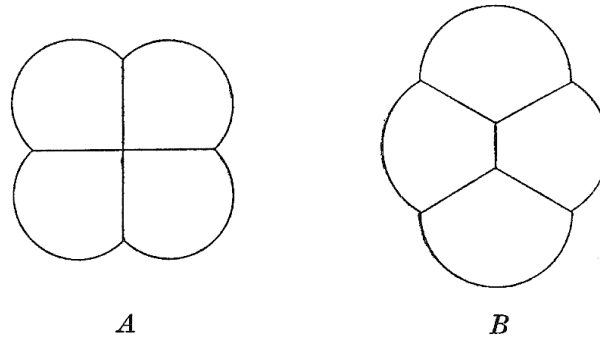
Fig. 172.   A, an unstable arrangement of four cells or bubbles.   B, the normal and
stable configuration, showing the polar furrow.

FIGURE 1.13 – Illustration of cells or bubbles arrangement by Thompson, 1942.

Another technique called traction force microscopy (TFM) has been extensively used to measure forces produced by cells with a subcellular precision which yields maps of force application. The rationale of this technique is to culture cells on a substrate of known stiffness and to image the deformation of the substrate by means of embedded fluorescent trackers. Substrates are classically soft gels (polyacrylamide or agarose gels) with embedded fluorescent beads. The stress distribution (of the order of magnitude around 100 Pa) within a collective migrating cell monolayer could be mapped in this way (Trepat et al., 2009). The 3D components of the traction of Dictyostelium cells over time were measured too (Delanoë-Ayari et al., 2010). However, a limitation of this method is that deformation can propagate far in the gel, so it is difficult to correlate the strain state of the gel with a complex field of force sources. A solution to this limitation has been to mechanically uncouple the deformation trackers. Cells are cultured on a substrate made of flexible micropillars, each micropillar being an independent force sensor from its neighbors (Gupta et al., 2015). Recent efforts also led to the development of 3D TFM in ECM-like networks which are highly non-linear and therefore complicate the strain-stress relation (Steinwachs et al., 2016).

Measurement at the tissular level

Surface tension
A century ago, D'Arcy Thompson noticed in his *On growth and forms* that as cells pack together, they share common geometrical arrangements with foam (Thompson, 1942, second edition, see Figure 1.13). He hypothesized that the physics of bubbles and foam could be extended to biological tissues. In particular, he noted that the Plateau rules on angles and shapes of interfaces in a foam (Plateau, 1873) are valid in biological tissues. This analogy had a fruitful legacy in the field of tissue biophysics. As foam structure is controlled by a balance between surface tension at bubble interfaces and pressure in bubbles, it was hypothesized that surface tension could be also present in biological tissues and dictate their structure.
The first strong evidence that surface tension might play a role in biological tissues was brought by Townes and Holtfreter, 1955, when they saw that reaggregated cells from different cell types segregate (cell sorting), as two non-miscible fluids would do. Later, it was proposed by Steinberg, 1970 that cell sorting could be driven by different patterns of adhesion molecules between cell types, as he noticed that cells

expressing similar levels of cadherin cluster together. This led him to formulate the differential adhesion hypothesis. The hypothesis was soon debated by Harris, 1976, who criticized, in particular, the lack of consideration of the thermodynamic activity of the cells and proposed a differential surface contraction hypothesis. It was then shown *in silico* that differential adhesion energies between cell types could drive cell sorting (Graner and Glazier, 1992). However, finite elements simulations later showed that cell sorting could still occur even though both cells types share the same interfacial energy, which is in sharp contradiction with the differential adhesion hypothesis (Brodland and Chen, 2000). What drives cell sorting is the interfacial energy between cells of different types and interfacial energy with the medium. This result led Brodland, 2002 to propose the differential interfacial tension hypothesis, which incorporates cell junction contractility to the interfacial energy. It was later confirmed *in vitro* that differential contractility is a major ingredient of differential interfacial tension which could drive cell sorting of zebrafish embryonic cells (Krieg et al., 2008). However, recently, this result was mitigated by investigations that highlighted the fact that interfacial tension contribution is highly dependent on osmotic pressure. What was previously observed *in vitro* could not be verified *in vivo*, as osmolarity conditions do not lead to sufficient tension to drive cell sorting (Krens et al., 2017). If this recent result does not rule out the role of surface tension in general, it highlights the sensibility of the phenomenon with respect to the culture conditions.

Surface tension theory

Physically, the surface tension γ is defined by the variation of a system energy $\mathcal{E}$ when its interface surface area A is varied:

$$\gamma = \frac{\partial \mathcal{E}}{\partial A} \tag{1.14}$$

It is therefore an energy per unit of surface area (or a force per unit of length). This surface energy arises once an interface with another material is generated, so it can be related to the bond density energies. To create an interface on a unit surface between a material i and a material j, bonds of energy e_{ij} are gained and bonds (on half the unit surface) of energies e_{ii} and e_{jj} are lost. So, the surface tension γ_{ij} between the material i and j reads:

$$\gamma_{ij} = \frac{e_{ii} + e_{jj}}{2} - e_{ij} \tag{1.15}$$

If $\frac{e_{ii}+e_{jj}}{2} < e_{ij}$, γ_{ij} is negative, the interface is more favorable than the isolated materials. If $\frac{e_{ii}+e_{jj}}{2} > e_{ij}$, γ_{ij} is positive, the interface is not favorable and introduces an energy cost. As a result, the surface of the interface tends to be minimized, hence the spherical geometry of an isolated bubble. Surface tension is constant all across a foam because surface tension is only a property of the two materials (air and soapy water). A consequence of the constant tension in a foam is the Plateau's rule stating that all junctions at a vertex meet with the same angle (120° in the case of a three-junction vertex).

The analogy of bubbles packing has been recently revisited by studying the contact angles of cellular junction in the *Drosophila* ommatidium (Hayashi and Carthew, 2004). It was noticed that the contact angles at a junction were violating the Plateau's rule, suggesting that tension is not constant all across the tissue. This prompted Käfer et al., 2007 to propose a 2D mathematical description of the junction tension.
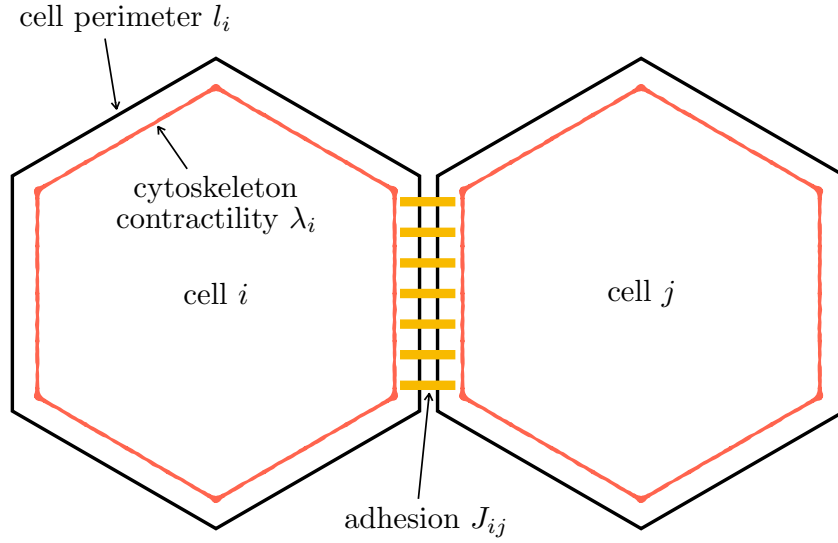
FIGURE 1.14 – Schematic of parameters controlling the interfacial tension. According to Käfer et al., interfacial tension arises from a balance between adhesion energy at the interface and cell perimeter elasticity controlled by cytoskeleton contractility.

The interfacial tension is a balance between the junction adhesion pattern and contractility at the junction of both cells. This can be written by:

$$\gamma_{ij} = -J_{ij} + 2\lambda_p(l_i - l_{0i}) + 2\lambda_p(l_j - l_{0j}) \tag{1.16}$$

where J_{ij} is the adhesion at the junction between the cells i and j, λ_p is the perimeter modulus, l_{0i} (respectively l_{0j}) the target perimeter of cell i (respectively j) and l_i, l_j the actual perimeters of cells i and j (see Figure 1.14). Therefore, a strong adhesion J_{ij} reduces the interfacial tension, while a strong contractility λ_p increases it.

However, as the adhesion can depend on the junction, the contractility can vary depending on the type of interface. Therefore, the mathematical description was later modified as follows (Krieg et al., 2008):

$$\begin{aligned} \gamma_{ij} &= -J_{ij} + T_{ij} + T_{ji} + 2\lambda_p(l_i - l_{0i}) + 2\lambda_p(l_j - l_{0j}) \\ &= -J_{ij} + T_{ij}^c + T_{ji}^c \end{aligned} \tag{1.17}$$

where T_{ij} is an increment to the cortical tension of the cell i at the junction with the cell j, and we define the new cortical tension of the cell i at the junction with the cell j: $T_{ij}^c = T_{ij} + 2\lambda_p(l_i - l_{0i})$.
The tissular surface tension can be then derived using an analogous reasoning as equation 1.15. The tissular surface tension γ_{IJ}^T in a tissue containing two cell types I and J is:

$$\gamma_{IJ}^T = \gamma_{IJ} - \frac{\gamma_{II} + \gamma_{JJ}}{2} \tag{1.18}$$

Note that γ_{IJ} are interfacial energies contributing positively to the system energy, in contrast the bond energy from equation 1.15, hence the sign difference.
The tissular surface tension γ_{IM}^T of a tissue with the medium M reads, considering
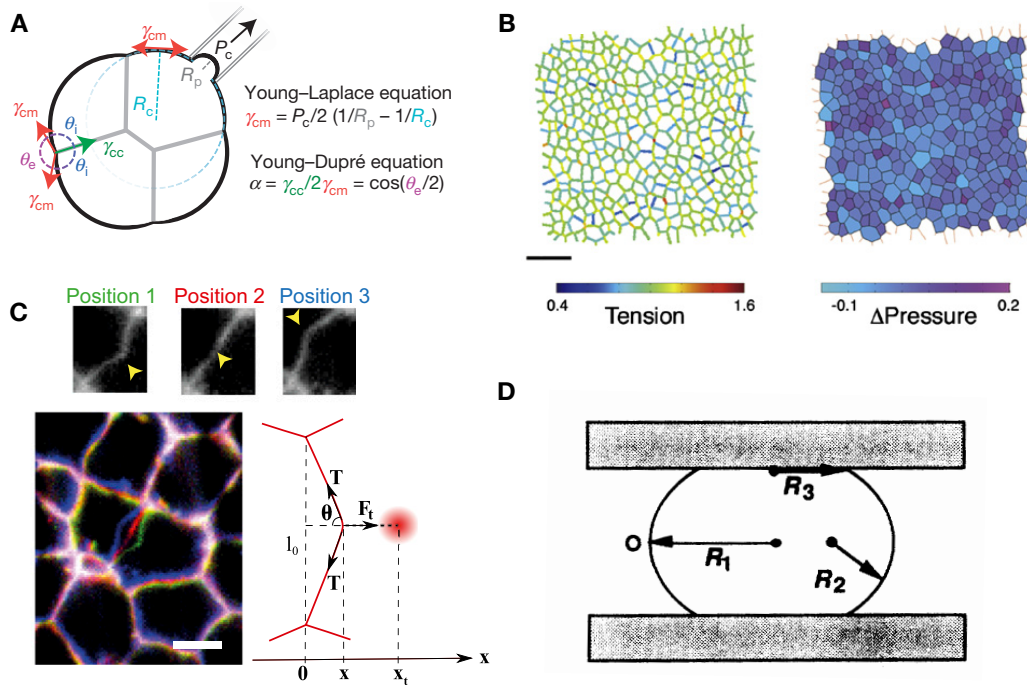
FIGURE 1.15 – Junction and tissular tension measurement method. **A**: Cell-medium tension measured by pipette aspiration (adapted from Maître et al., 2015). **B**: Junction tensions inference (adapted from Ishihara and Sugimura, 2012). **C**: Junction tension measured by optical trapping (adapted from Bambardekar et al., 2015). **D**: Tissular tension measured by parallel plate compression trapping (adapted from Foty et al., 1994).

that $\gamma_{MM} = 0$ and using equation 1.17:

$$\begin{aligned}
\gamma_{IJ}^T &= \gamma_{IM} - \frac{\gamma_{II}}{2} \\
&= T_{IM}^c - T_{II}^c + \frac{J_{II}}{2}
\end{aligned} \tag{1.19}$$

Note that we assumed there is no adhesion from the medium ($J_{IM} = 0$) and no contractility from the medium onto the cell ($T_{MI}^c = 0$).

Experimental measurement of the junction tension and the surface tension

The cortical tension and the tissular tension can be measured by micropipette aspiration (see Figure 1.15 A). When a cell or a spherical tissue is aspirated within a pipette, the curvature within the pipette increases with the applied aspiration pressure, following the Laplace law: $\kappa_p \gamma = P_d - P_p$, with κ_p the curvature within the pipette, P_d the pressure inside the aspirated material and P_p the pressure inside the pipette. There is a critical pressure beyond which the curvature is maximal and the relation cannot be satisfied anymore. The material then starts flowing. Measuring this critical pressure is then a way of calculating the surface tension (for more details, see theory section 4.1.1). This method has been used on single cells with the pioneering work from Evans and Yeung, 1989 in which neutrophils exhibited a cortical tension of 35

$\mu N \cdot m^{-1}$. The technique has been recently applied to early mouse embryo (8-cell stage) to measure the cortical tension increase throughout the compaction (Maître et al., 2015). The cell-medium tension γ_{cm} could then be measured to increase from 200 to 400 $\mu N \cdot m^{-1}$ in the course of 10 hours. In parallel, the cell-cell tension γ_{cc} could be calculated by measuring the angles at the vertices. γ_{cc} decreased from 300 to 200 $\mu N \cdot m^{-1}$ over the same period leading to the early embryo compaction. Finally, the tissue tension was also measured to be 6 $mN \cdot m^{-1}$ using the same technique on cellular aggregates (Guevorkian et al., 2010).

In addition to aspiration, compression can be used to measure the cortical or tissular tension. On isolated cells, AFM indentation has been carried out on zebrafish embryonic dissociated cells (Krieg et al., 2008). The cell is assumed to be a contractile shell under pressure. Then, the force F of indentation by a spherical probe of radius R_b at depth δ is related to the tension γ (Rosenbluth et al., 2006):

$$F = \left(2\gamma \left(\frac{1}{R_c} + \frac{1}{R_b} \right) + 2\pi R_b \right) \delta \tag{1.20}$$

where R_c is the cell radius.
Krieg et al., 2008 showed that ectoderm cells had the highest cortical tension (80 $\mu N \cdot m^{-1}$), while the endoderm cells had the weakest one (30 $\mu N \cdot m^{-1}$). As explained above, these measurements favored the differential interfacial tension hypothesis over the differential adhesion hypothesis, even though its importance in case of cell sorting during zebrafish gastrulation was later questioned (Krens et al., 2017).
Regarding tissular tension, the parallel plates compression method pioneered by Foty et al., 1994 has become a standard measurement. However, its strong limitation is that it relies on a spherical geometry of the tissue. This method is based on writing the Laplace law that relates a compressive pressure on the tissue and its curvature. The spherical geometry offers the opportunity to measure the curvature from a side imaging. Assuming the tissue incompressibility, the force F applied to compress the tissue can be related to the tension γ and the tissue radii R_1, R_2 and R_3 (see Figure 1.15 D):

$$\gamma = \frac{F}{\pi R_3^2} \left(\frac{1}{R_1} + \frac{1}{R_2} \right)^{-1} \tag{1.21}$$

The technique was later used to investigate the magnitude of different contributions to the tissular surface tension in cellular aggregates (Stirbat et al., 2013a). By dramatically inhibiting the cortical contractility, the authors could obtain an estimate of the adhesion component, since equation 1.19 simplifies to $\gamma \approx \frac{J}{2}$ (as $T_{IM}^c \approx 0$ and $T_{II}^c \approx 0$). While, without contractility inhibition $\gamma \approx 4.7$ $mN \cdot m^{-1}$, the authors could estimate $\frac{J}{2} \approx 1.5$ $mN \cdot m^{-1}$. The technique was also used on embryonic tissues that were previously left rounding up in spheres, in chicken (Mombach et al., 2005) and zebrafish (Schötz et al., 2008). Surface tension of chicken embryonic neural aggregates was measured to increase from 1.6 to 4.0 $mN \cdot m^{-1}$ between day 6 and 9 of development. Surface tension in zebrafish ectoderm and mesoderm were measured to be respectively $\gamma \approx 0.8$ $mN \cdot m^{-1}$ and $\gamma \approx 0.4$ $mN \cdot m^{-1}$.

The aforementioned principle of laser ablation has been used to measure junction tension. These techniques measure only relative values over the viscous drag, which is often difficult to measure. However, anisotropy of the tensions within the

tissue could be measured in *Drosophila* (Rauzi et al., 2008) and *C.elegans* (Mayer et al., 2010). Recently, Bambardekar et al., 2015 showed that the cellular junctions could be directly trapped with an optical tweezer (see Figure 1.15 C). Conventional optical tweezers are used to trap beads with a higher refraction index than the surrounding medium within a focused laser beam (Svoboda and Block, 1994). In this case, the junction itself could be trapped. Bambardekar et al., 2015 measured the stiffness of their optical trap and submitted the junction to oscillatory deflection. This mismatch between the trap position and the actual position of the deflected junction revealed the force balance between the trap and the junction tension. This method gave a measurement of the force resulting from the junction tension to be on average 44 pN in the early *Drosophila* embryo.

A non-destructive method to measure patterns of junction tensions is force inference from microscopy data. The method relies on writing the force balance, using junction angle measurements, at each vertex between the contribution of the pressure of each cell and the contribution of the tension of each junction. The tensions and the pressures can be inferred by a bayesian approach minimizing force balance errors across the tissue (Ishihara and Sugimura, 2012, Ishihara et al., 2013) (see Figure 1.15 B). By considering the junction curvature, another set of equations satisfying the Laplace law can be written and can lead to an over-determined problem enabling a direct resolution (Brodland et al., 2014). This method yields maps of pressure and tension across a tissue without any physical manipulation which allows studies to be conducted over time without introducing any perturbation. However, this is a relative method: measured tensions are ratios with respect to the mean tension and measured pressures are differences to the mean pressure. Also, this method assumes that junctions geometry is only determined by tensions and pressures. It cannot be applied if the junction has a complex geometry (*e.g.* if it is deformed by transverse elements of cytoskeleton or subcellular components).

Other methods such as tissue rounding or tissue fusion proposed by Gordon et al., 1972 have been used to measure ratios of surface tension over tissue viscosity. They are based on monitoring the surface minimization dynamics driven by surface tension and resisted by viscosity. These techniques coupled with another measurement of the viscosity can also give values for the surface tension, as it will be presented in more details in Chapter 3.

In summary, surface tension spans over two orders of magnitude between cell cortical tension ($\sim 30\ \mu\mathrm{N}\cdot\mathrm{m}^{-1}$) and tissular tension ($\sim 5\ \mathrm{mN}\cdot\mathrm{m}^{-1}$), as summarized Table 1.1.

Bulk stress

After considering the stress production along cell-cell interfaces or at the tissue surface, we now turn to stress production at the tissue scale. A stress at such a scale can have multiple origins. The propagation of junction tensions throughout the tissue can result in a mean state of stress. Alternatively, stress can arise from compression of a tissue by another one.

Laser ablation has been used at the tissue level as well. In this way, the anisotropy of the stress within the tissue could be measured by comparing the relative opening of severed lines depending on the direction of ablation (Campinho et al., 2013). The stress tensor can directly be obtained by ablating a circle and fitting an ellipse on the relaxed tissue (Bonnet et al., 2012) (see Figure 1.16 A). However, laser ablation only

TABLE 1.1 – Junction and tissular tension

Quantity	Method	Sample	Value	Reference
Cell-medium tension	pipette aspiration	neutrophils	$35\,\mu\mathrm{N}\cdot\mathrm{m}^{-1}$	Evans and Yeung, 1989
Cell-medium tension	pipette aspiration	8-cell stage mouse embryo	$200\text{-}400\,\mu\mathrm{N}\cdot\mathrm{m}^{-1}$	Maître et al., 2015
Cell-medium tension	AFM indentation	zebrafish dissociated cells	$30\text{-}80\,\mu\mathrm{N}\cdot\mathrm{m}^{-1}$	Krieg et al., 2008
Junction tension	pipette aspiration	8-cell stage mouse embryo	$200\text{-}300\,\mu\mathrm{N}\cdot\mathrm{m}^{-1}$	Maître et al., 2015
Junction adhesion	parallel plate compression	epithelial stem cell (F9) aggregate	$1.5\,\mathrm{mN}\cdot\mathrm{m}^{-1}$	Stirbat et al., 2013a
Tissular tension	parallel plate compression	zebrafish embryonic rounded tissue	$430\text{-}800\,\mu\mathrm{N}\cdot\mathrm{m}^{-1}$	Schötz et al., 2008
Tissular tension	parallel plate compression	chicken embryonic rounded tissue	$1.4\text{-}4.0\,\mathrm{mN}\cdot\mathrm{m}^{-1}$	Mombach et al., 2005
Tissular tension	parallel plate compression	epithelial stem cell (F9) aggregate	$4.7\,\mathrm{mN}\cdot\mathrm{m}^{-1}$	Stirbat et al., 2013a
Tissular tension	pipette aspiration	epithelial murine sarcoma (S180) aggregate	$6\,\mathrm{mN}\cdot\mathrm{m}^{-1}$	Guevorkian et al., 2010
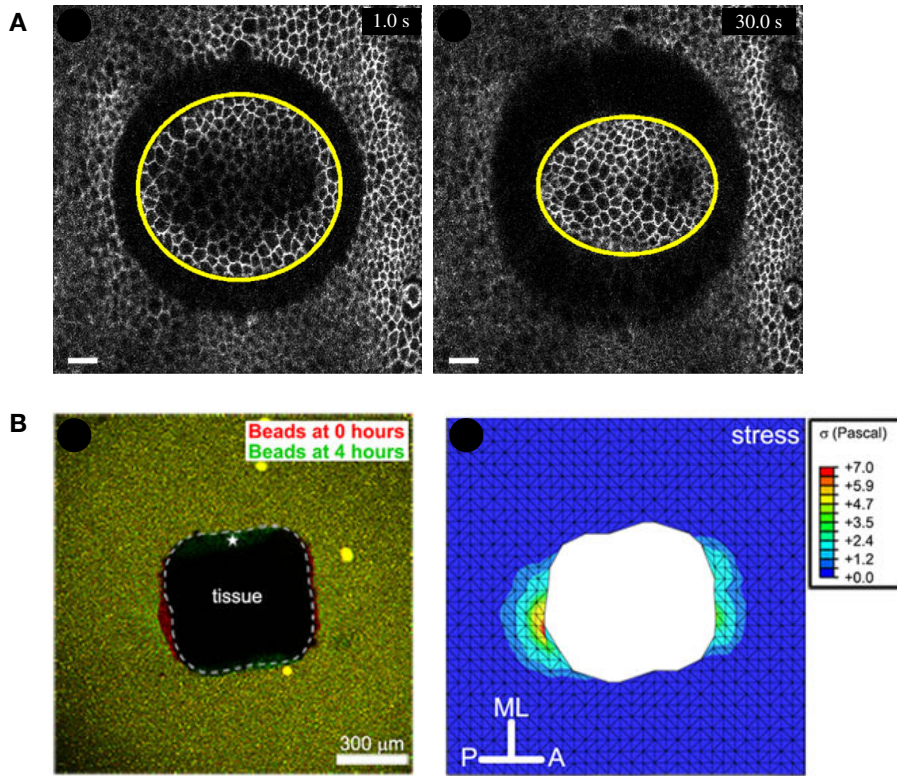
FIGURE 1.16 – Bulk stress measurement methods. **A**: 2D stress tensor measured by laser ablation (adapted from Bonnet et al., 2012). **B**: Extension stress measured by a gel sensor (adapted from Zhou et al., 2015).

reveals 2D stresses, therefore this method is only suitable for epithelial systems.

A recent method has offered the possibility to measure the 3D stress tensor *in vivo* (Campàs et al., 2013). The authors injected oil drops functionalized with cell-binding molecules (RGD peptide or E-cadherin antibody) in cellular aggregates and mice embryo. Injected drops were of the typical size of a cell ($\sim$ 20 µm) and were deformed by cells. Confocal 3D reconstruction of the drop shape allowed the authors to access the anisotropy of the stress. Along the same idea, using compressible gel spheres instead of oil drops was recently proposed to measure the isotropic components of the stress (Mohagheghian et al., 2018).

The aforementioned methods measure the tensile stress within the tissue. A gel probe has been devised by Zhou et al., 2015 to measure extension stress of a *Xenopus* explant undergoing CE (see Figure 1.16 B). A tissue explant was embedded in a calibrated gel which deformation was imaged by means of fluorescent beads. They could measure a maximum stress produced by the explant extension of 7 Pa.

1.2.3 Mechanical properties in the chicken embryo

A detailed description of the chicken embryo mechanical properties is still missing. Only a few embryonic structures have been previously investigated. Average elasticity over the whole axis has previously been measured (Agero et al., 2010). The authors submitted the whole embryo to a uniaxial stretch by the mean of a calibrated glass fiber, and then assumed the embryo is composed of three mechanically

homogeneous regions (*area opaca*, *area pellucida* and midline structures). By tracking the strain field in the different regions, they could find the best combination of stiffnesses satisfying the stress-strain relation all over the embryonic body. They found that the stiffness was 11.9 kPa in the *area opaca*, 2.1 kPa in the *area pellucida* and 2.4 kPa in the midline structures.

The stress principal directions in the neural plate and around it during head folding (HH5-7) were measured by circular hole punching through the blastoderm (using a glass pipette) (Varner et al., 2010).

In addition, more local measurements have been carried out on specific tissues. The heart has been probed by micropipette aspiration (Majkut et al., 2013) and microindentation (Zamir and Taber, 2004). Majkut et al., 2013 showed that the heart exhibits a solid behavior and it stiffens from 0.4 to 2 kPa between day 1 and day 6 of incubation. Zamir and Taber, 2004 studied the effect of pre-stress on indentation models. Depending on the assumptions on pre-stress, they found very different stiffness (from 3 to 70 Pa). As it was mentioned above, the gut stiffness has also been investigated by uniaxial extension (Savin et al., 2011, Chevalier et al., 2016 and Nerurkar et al., 2017): the gut tube stiffness was measured to be around $E \approx 20$ kPa. Moreover, compression of the gut tube in the 8-day and 10-day old embryo yielded shear moduli of different layers: $G \approx 700$ Pa for the inner layer (endoderm) and $G \approx 80$ Pa for the outer layer (mesenchyme) (Shyer et al., 2013).

In summary, a wide variety of methods exists to measure mechanical properties and stress production within embryonic tissues. However, to date, only stiffness measurements have been carried out on the chicken embryo and numerous tissues have not been investigated yet.

1.3   Aims of the Ph.D.

In this chapter, we have presented various mechanisms of elongation of the AP axis at different stages in vertebrates. While different animal models present structural similarities during axis elongation, elongation mechanisms vary. CE mechanism is central to many morphogenetic processes but it does not play a major role in the formation of the posterior tissues of the trunk in the chicken embryo. After the 10-somite stage, elongation is driven by the PSM, a loosely packed mesenchymal tissue. An original model has been proposed to account for this elongation. A gradient of random cell motility downstream of a morphogen gradient (FGF8/MAPK) along the AP axis controls elongation. It has been proposed that a graded random cell motility along the PSM generates a biased movement of cells towards the posterior boundary and elongates the axis. While the genetic, molecular and cellular descriptions of this process have been previously studied, the physical mechanism remains to be investigated in detail. Mechanical data quantifying how PSM cells can deform their environment are still missing.

1.3.1   Aim 1: measuring the mechanical properties of the presomitic mesoderm and its neighboring tissues

The first aim of this Ph.D. is to experimentally investigate the mechanical properties of the posterior embryonic tissues in the chicken embryo. These mechanical data are needed to refine the theoretical model of elongation. In particular, we want

to measure the elastic properties of the posterior tissues to confirm an important assumption of the model, that the PSM is confined mediolaterally by the neural tube and the lateral plate. Therefore, we need to assess the relative stiffness of these tissues. In addition, the theoretical model explicitly depends on the tissular viscosity, thus, its profile along the axis needs be measured. Furthermore, in the model, cell motility and viscosity are independent parameters. However, these properties might be mutually dependent *in vivo*, as cellular movements can be involved in tissue fluidity. How these two properties are connected remains unclear.

In order to tackle this aim, we will present rounding and fusion experiments which provide us with a ratio of surface tension over viscosity (Chapter 3). Chapter 4 will be dedicated to pipette aspiration experiments which yield elasticity, viscosity and surface tension data.

1.3.2 Aim 2: measuring stress production by the posterior tissues during axis elongation

The second aim of this Ph.D. is to measure the stress production of different tissues during the extension of the AP axis, in order to, first, confirm the driving role of the PSM, second, compare the stress production data with the prediction from the theoretical model. In Chapter 5, a cantilever-based method to measure the stress production will be presented.

Chapter 2

Role of the presomitic mesoderm in anteroposterior elongation

In this second introductory chapter, we will focus in more details on the role of the presomitic mesoderm (PSM) in body extension during somitogenesis. Here, we will focus on avian embryos only. We will first describe the architecture of the PSM by reviewing what is known about its dimensions, cellular density and extracellular matrix (ECM) composition. We will then introduce experimental data on the role of the PSM in elongation. We will finally discuss the current theoretical model which accounts for the role of the PSM in elongation.

2.1 Structure of the posterior tissues

As shown in Figure 2.1, tissues posterior to the head and the heart are mostly composed of:

- two axial tissues: the neural tube (NT) on the dorsal side, and the notochord on the ventral side;

- the paraxial mesoderm on each side of the axial tissue, which is subdivided in somites and an unsegmented tissue, the PSM;

- the lateral plate, flanking the paraxial mesoderm on its lateral side.

On the dorsal side of these tissues lies the ectoderm (a multilayered structure) and on the ventral side lies the endoderm (a monolayer of cells). In the posterior-most region of the axis, the rest of the regressing primitive streak constitutes a zone of progenitor cells which generate the aforementioned axial, paraxial and lateral tissues.

2.1.1 Temporal evolution of posterior tissues structure

A detailed quantitative description of the posterior tissues during axis elongation has been recently published (Bénazéraf et al., 2017). Confocal imaging of transgenic quails offered an unprecedented picture with a cellular resolution of the tissues dimensions and movements over time. The authors presented volume and density measurements showing that the PSM is the largest and least dense tissue over all the posterior tissues. Cell density was calculated by measuring the average distance between nuclei in a given region. The PSM exhibits an AP gradient in cell density along the AP axis, which is maintained over time: posterior PSM has a very low density (less than 1382 cells / 100 μm^3), while anterior PSM exhibits an intermediate density (between 1382 and 2388 cells / 100 μm^3), compared to the high density of the neural tube and the lateral plate (more than 2388 cells / 100 μm^3). The neural
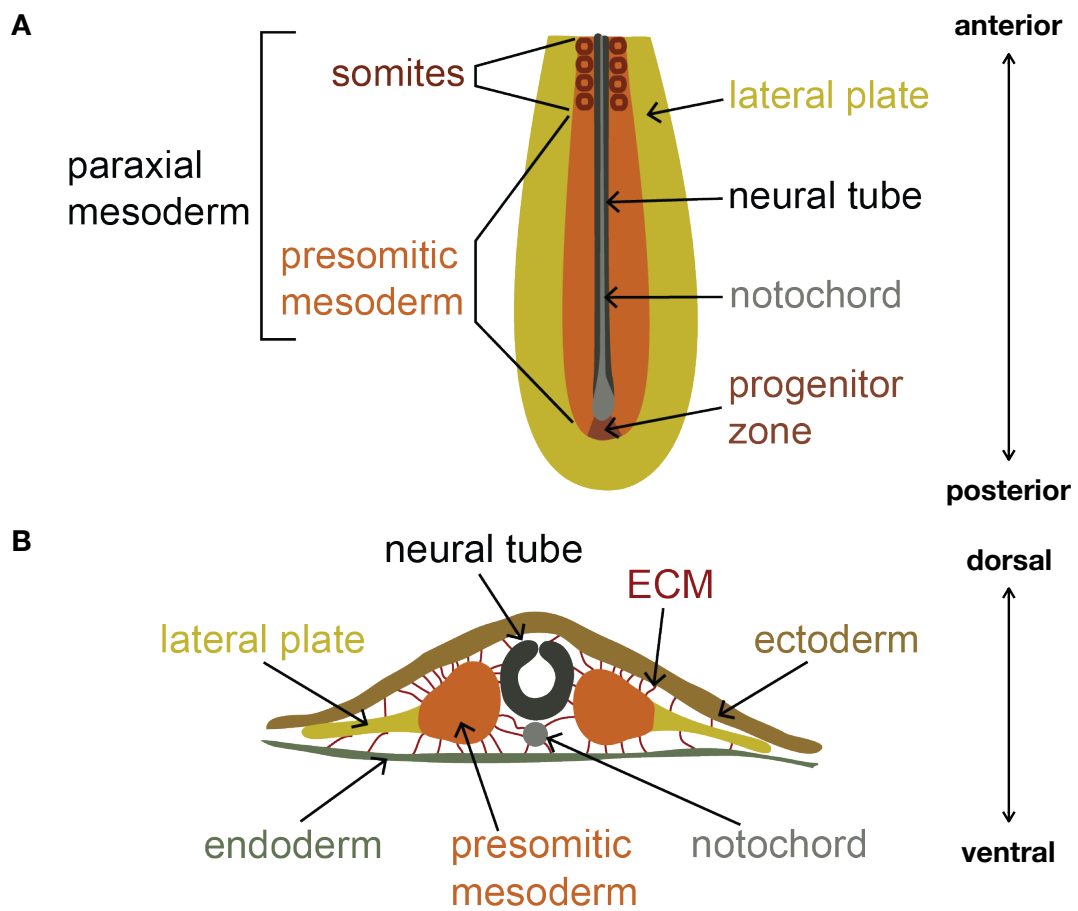
FIGURE 2.1 – Schematic of the posterior tissues of the chicken embryo. **A**: Longitudinal section of the posterior embryo. **B**: Transverse section of the posterior embryo. ECM: extracellular matrix.

tube and the lateral plate also exhibit an AP gradient in cell density. The authors ruled out the possibility that density difference could be due to differences in cells size, as the paraxial mesoderm cells have similar sizes as the neural tube and the notochord. This AP pattern of density could be explained by tissue deformation. The authors tracked the nuclei of all cells in order to generate expansion and contraction maps during elongation. They showed that the posterior PSM was expanding, while anterior PSM was contracting, which correlates with the density pattern. Moreover, the contraction is not due to mediolateral cell intercalation, but rather to a coherent lateral-to-medial tissue flow. As a result, the extension of the PSM exhibits a complex profile along the AP axis. The authors quantified tissues' extension by plotting their relative speed with respect to the last formed somite in different regions. By looking at the component along the AP axis of this relative speed, they could see that anterior PSM has a negative speed (*i.e.* it is getting closer to the last somite), whereas the speed increases, and becomes positive in the posterior region (*i.e.* it is moving further away from the last somite). Another striking observation was that the neighboring tissues have very different patterns of relative speed with respect to the last somite, which means that the extension is not coherent between different tissues and that they slide with respect to each other. These sliding movements are especially important in the anterior PSM region, where the notochord moves posteriorly at the highest speed, while the neural tube moves slowly posteriorly and the PSM moves anteriorly. However, in the posterior region, the extension movements converge to the same speed across all tissues. This extension, in the long run, leads to volume growth of different tissues. As the density pattern stays constant during elongation, proliferation of cells might explain the difference in volume expansion. Because of its larger width, the PSM is the tissue that shows the larger volume expansion. Interestingly, it is also the tissue with the shortest cell cycle (8.75 hours) which could explain part of its volume expansion. The PSM progenitor region has a slightly slower cell cycle (11.49 hours), but has a constant volume which can be explained by the flux of cells leaving the region to enter other tissues. Regarding proliferation, the notochord is a peculiar tissue with an extremely slow cell cycle (28.06 hours), which is associated with a slight volume constriction: the notochord does not grow in volume during elongation but it thins down along the AP axis.

2.1.2 Extracellular matrix in the presomitic mesoderm

ECM is an important substrate for cell motility and it is key for axis elongation in zebrafish (Dray et al., 2013). In addition, ECM plays a functional role in the maturation of the PSM. In particular, fibronectin central role in somitogenesis has been demonstrated in birds and many vertebrates. Rifes et al., 2007 showed that if PSM explants are isolated by means of wide-spectrum ECM digesting enzymes such as pancreatin or dispase, explants are not able to segment into somites if cultured *in vitro*. However, if fibronectin is not digested during the dissection, using collagenase, for instance, 2 somites can be formed in 6 hours. It was previously known that PSM could produce somites if it is cultured with the ectoderm (Palmeirim et al., 1998), even when previously isolated with pancreatin. This is due to the fact that fibronectin is mostly expressed in the ectoderm. Rifes et al., 2007 further demonstrated the essential role of fibronectin by itself, as the somite formation in the pancreatin-isolated PSMs could be partially rescued when cultured in fibronectin supplemented medium. So, regarding somitogenesis, the role of the ectoderm is to produce the bulk of fibronectin. The receptor of fibronectin, integrin $\alpha 5\beta 1$, is mainly expressed in the PSM. Therefore, the ectoderm and the PSM
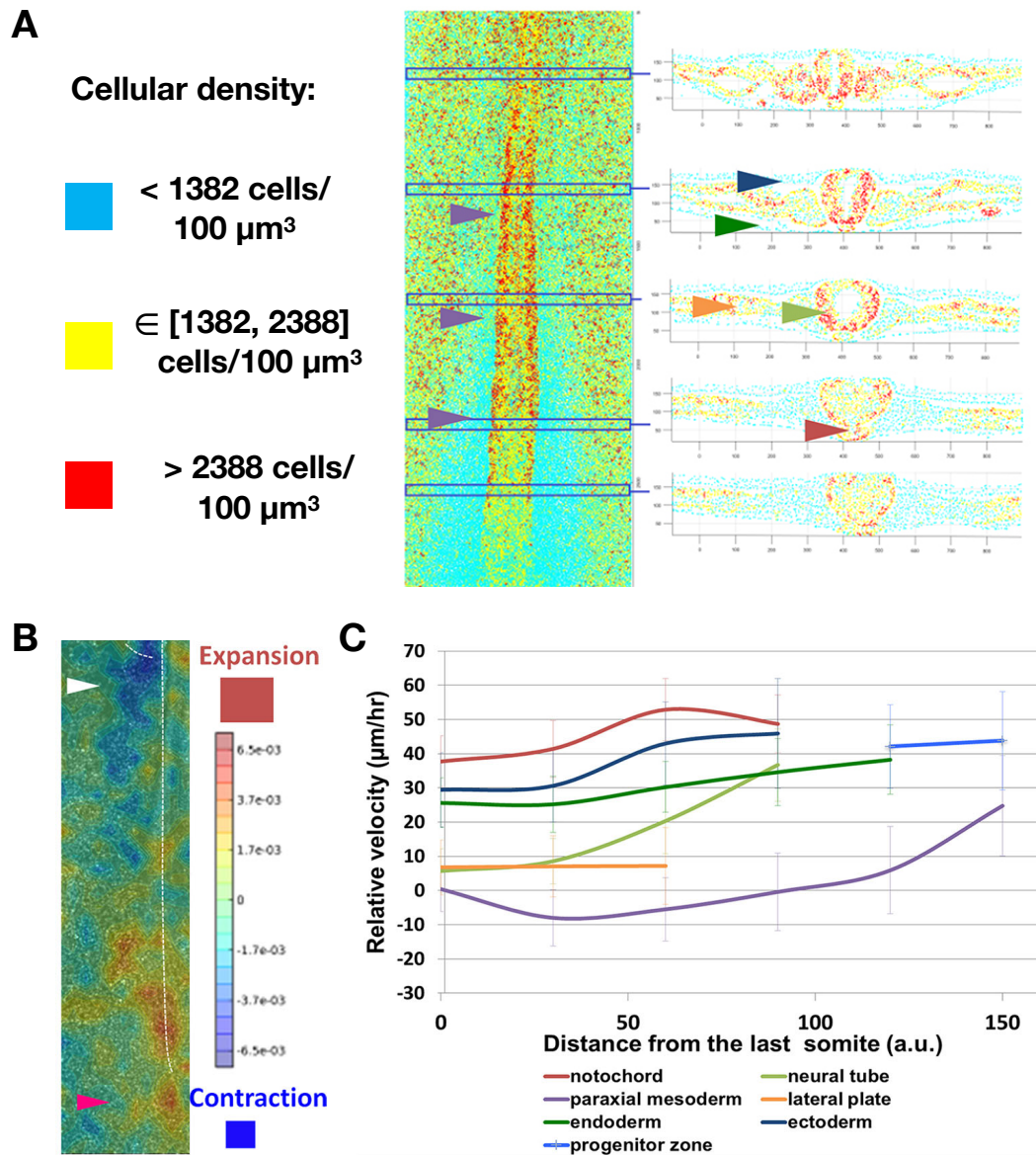
FIGURE 2.2 – Quantitative description of the posterior tissues. Cellular density (**A**), tissue expansion/constriction (**B**) and tissue relative movements (**C**). Adapted from Bénazéraf et al., 2017.
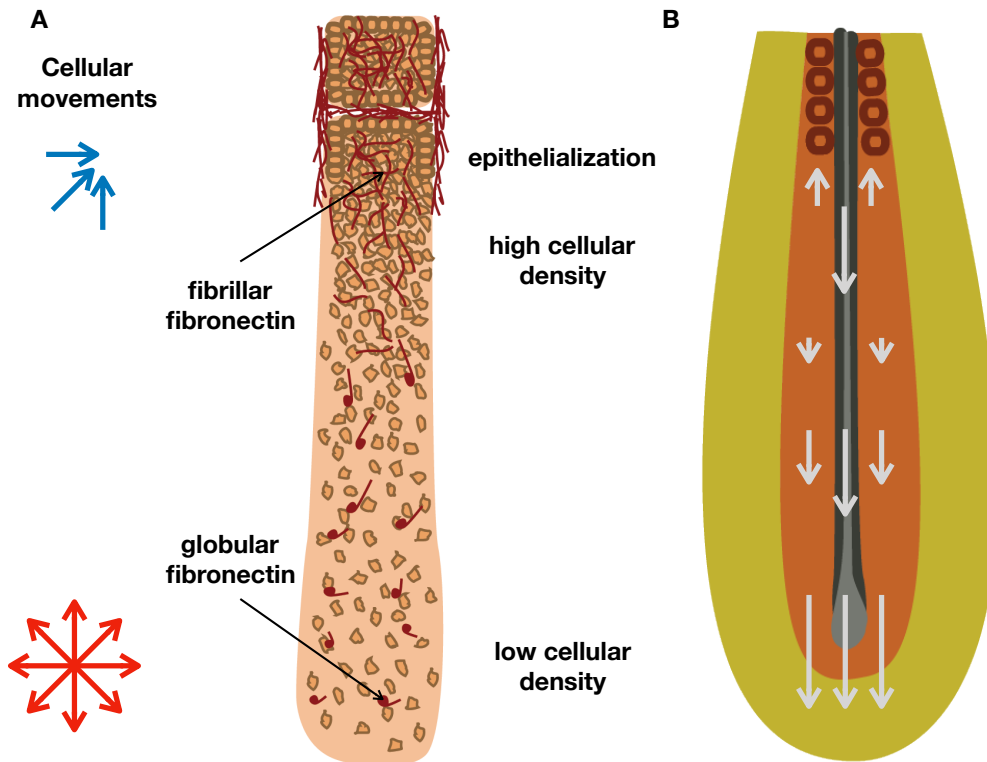
FIGURE 2.3 – Schematics of the cellular and tissular movements. **A**: Cellular density and movements along in the PSM. Red arrows represent isotropic expansion in the posterior PSM, blue arrows represent constriction by lateral-to-medial convergence in anterior PSM. **B**: Relative tissular movements. Arrows represent the AP component of the relative speed with respect to the last formed somites.

collaborate in the assembly of a dense fibronectin network, which is required for somite formation. The mechanism explaining the role of fibronectin in somitogenesis has been described in more details (Martins et al., 2009). Fibronectin is involved in the gradual epithelialization of anterior PSM, by promoting the polarization of mesenchymal cells which is required for their egression to the epithelial layer. In addition to its structural role, fibronectin could be indispensable to somitogenesis through its signaling role. Indeed, fibronectin is involved in the upregulation of N-cadherin which is important for the formation of the somite cleavage cleft (Chal et al., 2016).

ECM was described in detail by 3D reconstruction of immunostained embryos (Rifes and Thorsteinsdóttir, 2012). The authors studied the two major components of ECM: fibronectin and laminin. They showed that the internal surfaces of the ectoderm and the endoderm were mostly composed of the laminin organized as patches. These patches gradually merge together as the tissues mature towards the anterior of the PSM. Fibronectin is secreted in its globular conformation by the ectoderm. By interaction with integrin at the surface of the PSM, it takes its fibrillar conformation and forms a denser and more complex network in anterior PSM. As a result, these ECM molecules are found at the surface of the PSM and not in its core.

Conclusion

In summary, the PSM exhibits a highly regionalized structure along the AP axis (see Figure 2.3 A). In the posterior region, the low density is associated with high random cell motility which expands the tissue. As the PSM matures, globular fibronectin deposited by the ectoderm is gradually assembled in a denser fibrillar network. This ECM assembly, coupled with a decrease in the cell motility, leads to constriction of the PSM, mainly through a lateral-to-medial coherent flow. In parallel to this constriction, the PSM epithelializes. This complex cellular behavior along the AP axis leads to a peculiar pattern of extension of the tissue compared to its neighboring tissue (see Figure 2.3 B). While all the tissues in the posterior region extend away from the last pair of formed somites at the same speed, the PSM extension gradually slows down in a posterior-to-anterior gradient. There is a zero extension point in the PSM along the AP axis, anteriorly to which the PSM extension is negative, *ie* it moves anteriorly towards the last formed somite. In contrast, the notochord moves away from the pair of last formed somites at a constant speed all along the AP axis. The NT moves also away from the pair of last formed somites but at a slower speed than the notochord and with a slight AP gradient. As a result, all tissues extends coherently in the posterior region, and then gradually individualize themselves from each other as they mature, which leads to inter-tissue sliding.

2.2   Role of the presomitic mesoderm in elongation

Various experimental studies have emphasized the central role of the PSM in embryo elongation during somitogenesis. Firstly, the gradient of cell motility along the AP axis was shown to be key in elongation. Secondly, a metabolic gradient is important for the proper elongation. Lastly, in order to sustain elongation, posterior ingression of new cells is required.

2.2.1   The cell motility profile in the PSM drives elongation

Up to now, the main mechanism to account for elongation of the posterior body in the chicken embryo has been proposed by Bénazéraf et al., 2010. The authors quantified the impact of various tissues on the speed of elongation by laser ablation. Posterior PSM ablation leads to a striking decrease of the speed of elongation (about two thirds slower) whereas ablation of the progenitor zone, the posterior lateral plate, or the anterior PSM, has a weak effect on elongation (at least during the first 8 hours post-ablation). This suggests that addition of new cells coming from the progenitor zone has a limited role in the short-term extension mechanism. On the contrary, the posterior PSM seems to have a direct impact on the elongation mechanism. The authors showed that this region is characterized by a higher motility than in the anterior PSM. Furthermore, they showed that cells lose their posterior-ward directionality when the movement of fibronectin is subtracted from the cell tracks. All along the PSM, the cell movements with respect to their local environment is not directional (see Figure 2.4). However, a posterior-to-anterior gradient of the amplitude of the random movements is kept even after subtracting the ECM movement. In addition, the distribution of the cell protrusions does not show any favored directionality. Taken together, this suggests that the PSM extension is not the result of a directed motion of the PSM cells, but it is the consequence of a long-range tissue flow in which cells exhibit a random walk-like motility.
The authors then investigated how the gradient of random cell motility plays a role
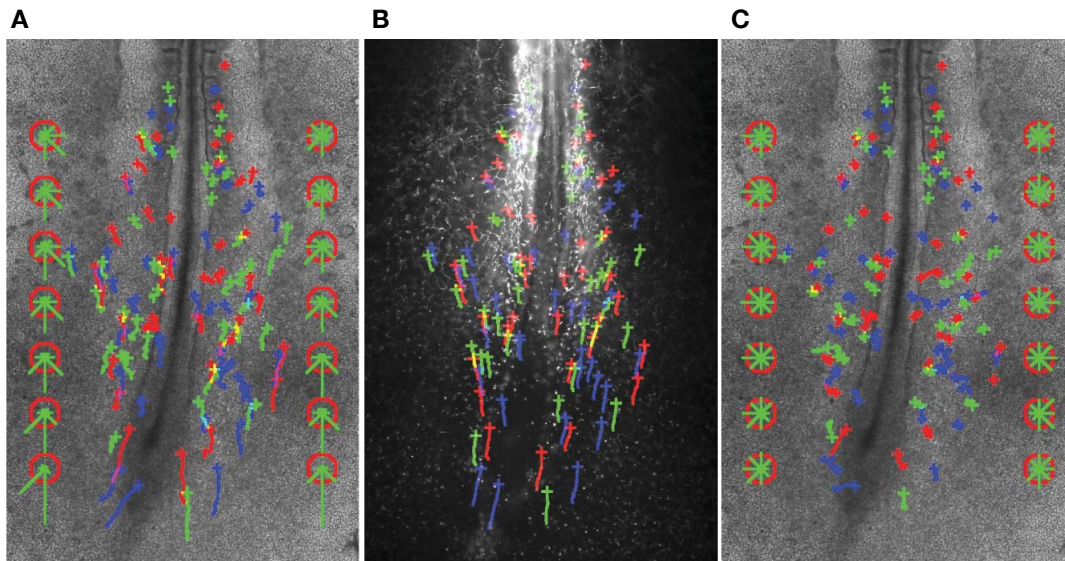
FIGURE 2.4 – Cellular and ECM movements along the axis (adapted from Bénazéraf et al., 2010). **A**: Individual cellular trajectories and average directionality (green bars in the red octagons represent cell average directionality). **B**: ECM movements. **C**: Cellular trajectories with respect to local ECM movements.

in elongation by modulating cell motility in various ways. The motility gradient is downstream of an FGF8 gradient along the PSM (Delfini et al., 2005). FGF8 is a secreted morphogen which acts on several pathways including the mitogen-activated protein kinase (MAPK) pathway, which controls cell motility. The motility gradient can be disrupted in several ways: cell motility is decreased by either inhibiting FGF signaling, or Rho-kinase activity or myosin-II phosphorylation. All these treatments strongly reduce elongation speed. Upregulating FGF8 all along the axis also disrupts the motility gradient (in this case by having highly motile cells all along the axis) and leads to a PSM that fails to constrict in anterior and, surprisingly, to a slow elongation too. This suggests that cell motility plays an important role in elongation. A high motility in the posterior region is not sufficient but a graded profile along the axis seems necessary.

The authors controlled that a potential posterior bias of cell proliferation downstream of the FGF gradient is not implicated in the elongation mechanism, and showed that proliferation inhibition did not decrease elongation rate. These results suggest that the gradient of random cell motility controls elongation, while cell proliferation and cell ingression from the progenitor zone do not play a major role at short times.

2.2.2 A gradient of cell metabolism controls PSM elongation and segmentation

In parallel to the cell motility gradient, a metabolic activity gradient has been shown to be involved in both axis elongation and segmentation by Oginuma et al., 2017. The authors demonstrated that the FGF gradient along the AP axis regulates a gradient of metabolic activity: a high lactate production which reveals a high glycolytic activity is present in the posterior region and gradually decreases towards the anterior region. Inhibition of FGF activity triggers a downregulation of the rate-limiting glycolytic enzymes. In contrast, respiration activity, revealed by cytochrome

c oxydase activity, anti-correlates with the glycolytic activity gradient, in an anterior-to-posterior gradient. The authors then showed that this metabolic pattern along the axis controls elongation and segmentation of the axis. The inhibition of the glycolytic activity by 2-deoxy-D-glucose (2DG) leads to axis truncation but has no effect on segmentation. Conversely, inhibition of respiration by sodium azide blocks axis segmentation but leaves axis elongation unchanged compared to the control situation. It was also shown that glycolytic activity controls the cell motility gradient. The reduction of elongation speed upon 2DG treatment is also associated with a decrease of cell motility in the posterior region, confirming the role of cell motility in elongation (see section 2.2.1). The authors also proposed a phenotypic analogy to the Warbug effect in cancer as high glycolytic activity is linked to an acidification of the extracellular environment. Therefore, the extracellular pH gradient (low in the posterior region and higher in the anterior region) is flattened upon glycolytic activity inhibition. In addition, abolishing solely the pH gradient by culturing the embryo on alkaline plates also reduces posterior cell motility and axis elongation rate. These results suggest the acidification of the extracellular environment plays a role in the cell motility, as it was shown in tumors by ECM remodeling (Gardner, 2015).

In summary, the role of the metabolic activity in axis elongation also highlights its connections with the cell motility gradient and emphasizes the importance of the acidification of the extracellular environment to promote cell motility.

2.2.3 Cell ingression sustains elongation

The speed of elongation is not constant throughout development. It quickly increases from the 1-somite stage to the 10-somite stage, then it gradually decreases until the 25-somite stage, when it dramatically drops (Denans et al., 2015). However, the somites production rate is roughly constant throughout somitogenesis, which leads to a variable length of the PSM throughout development and sets the total number of somites. Understanding what regulates axis extension speed and its termination gives valuable information about the mechanism of elongation.

Denans et al., 2015 showed that there is a strong correlation between the expression of posterior *Hox* genes and the elongation rate. *Hox* genes are a family of genes known to control the identity of the different tissues along the AP axis across bilaterians. *Hox* genes are characterized by their collinearity (the sequential order of the genes along the genome parallels their sequential territories of expression along the AP axis), by the timing of their activation and by their posterior dominance (genes specifying posterior domains repress the activity of anterior genes) (Noordermeer and Duboule, 2013). It was already shown that the sequential activation of *Hoxb* genes controls the timing of ingression. Overactivation of posterior-most *Hoxb* genes leads to a delayed ingression of cells from the epiblast (Iimura and Pourquié, 2006). The posterior dominance of *Hoxb* genes was confirmed regarding cell ingression.

It was later presented that a subset of more posterior *Hox* genes (*Hoxa9*, *Hoxc9*, *Hoxd10*, *Hoxd11*, *Hoxc11*, *Hoxa13*, *Hoxb13*, or *Hoxc13*) controlled cell ingression at later stages through the Wnt/βcatenin pathway (see Figure 2.5). Overactivation of these posterior *Hox* genes downregulated Wnt and slowed down elongation. The downregulation of Wnt consequently downregulates *Brachyury*, which is known to control mesoderm cell ingression. However, since the Wnt and FGF signaling pathways are tightly linked, downregulation of Wnt by *Hoxb* genes also led to downregulation of FGF in the posterior region and consequently a weaker cell motility. As a

result, it is still difficult to disentangle the contributions of the PSM cell motility and the PSM progenitors ingression on the elongation rate from these experiments.

Conclusion

The experimental data previously presented emphasize the crucial role of the cell motility gradient along the PSM. Both a high motility in the posterior region and its gradual decrease towards the anterior region are important to extend the axis. The high motility seems to be linked to an expansion of the posterior region which might be necessary to propel forward the posterior-most part of the embryo. On the other hand, a lower motility is required for anterior constriction, which might be another component of axis extension. Indeed, the elongation rate being measured by tracking the movement of the progenitor zone with respect to the last formed pair of somites, if anterior PSM fails to condense, the last formed somite might not be pushed as efficiently.

The fact that the PSM is a highly proliferative tissue might appear in contradiction with the lack of effect of proliferation inhibition. However, it is possible that proliferation has only a long-term effect on elongation which keeps the cellular density constant in the long run, while at short times the volume growth by cell proliferation does not provide the driving force.

2.3 The random motility gradient mechanical model

In order to test if the motility bias introduced by the random motility gradient can physically extend the PSM, a mechanical model has recently been proposed by Regev et al., 2017. A continuum theory was developed to describe the extension of the PSM. The PSM is assumed to be a continuum material confined between two rigid walls against which it slides with a friction ξ. It is assumed to be homogeneous along the ML axis at a given position along the AP axis. The density of motile cells ρ can be described hydrodynamically by balancing the equations of mass and momentum. In this 1D model, the density depends only on the position x along the axis and the time t (see Figure 2.6 A). In an Eulerian description, the density $\rho(x,t)$ varies by advection (with the velocity field v), diffusion (with the constant $\mathcal{D}$) and degradation (with a characteristic time τ). The degradation accounts for cells becoming non-motile, therefore leaving the pool of moving cells involved in PSM expansion.

$$\rho_t + (\rho v)_x = (\mathcal{D}\rho_x)_x - \frac{\rho}{\tau} \tag{2.1}$$

In addition, the active pressure of the motile cells p is balanced by material viscosity η and the wall friction ξ. In first approximation, the pressure can be proportional to the density: $p \sim \alpha\rho$ (like an ideal gas).

$$(-p + \eta v_x)_x = \xi v \tag{2.2}$$

The following boundary conditions are set by the model. Far from the posterior region, there is no more motile cell: $\rho(\infty) = 0$ and $v(\infty) = 0$. At the posterior boundary ($s(t)$), a flux of motile cells $\mathcal{R}$ is injected and a pressure F resists the advancing PSM. Therefore, the mass balance and the momentum balance can be written at the moving boundary $x = s(t)$. The flux of injected cells is defined by a function of the difference between the local density $\rho(s)$ and the maximum density ρ_0: $\mathcal{R}(\rho_0 - \rho(s))$. At the boundary, the velocity field is the velocity of the moving
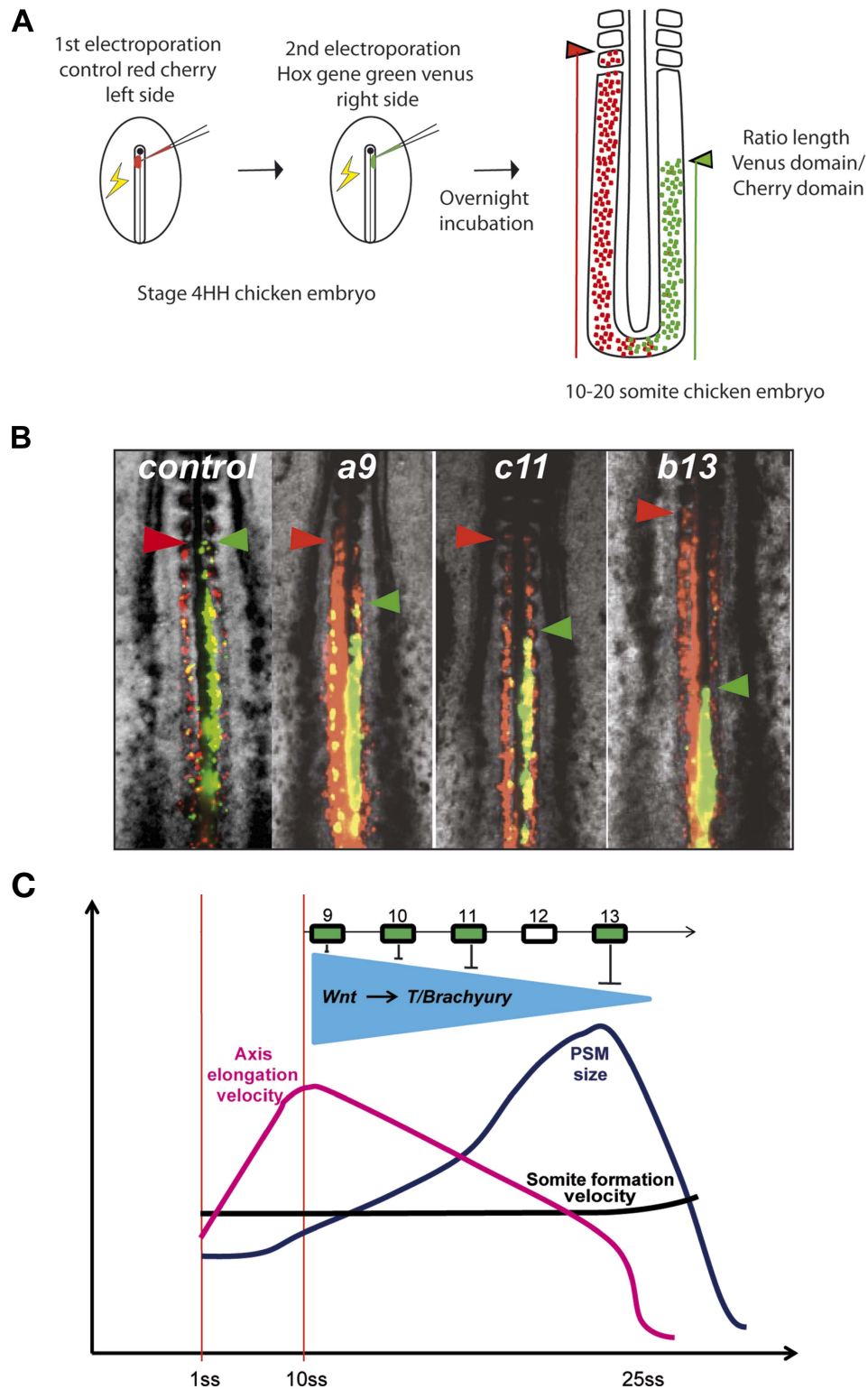
FIGURE 2.5 – Inhibition of cell ingression by posterior *Hox* genes (adapted from Denans et al., 2015). **A**: Schematic of the experiment quantifying the ingression inhibition. **B**: Differential ingression rate between control electroporated cells and posterior *Hox* gene electroporated cells. **C**: Schematic of elongation dynamics.

boundary: $v = \dot{s}$ (where $\dot{s}$ is the temporal derivative of $s(t)$). Thus, the flux is balanced by the diffusion and the advection:

$$\mathcal{R} \left(\rho_0 - \rho(s) \right) |_{x=s(t)} = \left(-\mathcal{D} \rho_x(s) + \rho(s) \dot{s} \right) |_{x=s(t)} \tag{2.3}$$

And the force balance writes:

$$\left(-\alpha \rho + \eta v_x \right) |_{x=s(t)} = -F \tag{2.4}$$

Using these boundary conditions, equations 2.1 and 2.2 can be solved self consistently by injecting experimental values for $\mathcal{D} \approx 0.1 \ \mu m^2 \cdot s^{-1}$, $\tau \approx 2 \times 10^4$ s and $\eta \approx 10^4$ Pa $\cdot$ s (where the viscosity value comes from preliminary measurements using pipette aspiration). F, $\alpha \rho_0$ and ξ are fitting parameters so the profiles of velocity $v(x)$ and the cell diffusion $D(x) = \mathcal{D} \rho(x) / \rho_0$ are in best agreement with the experimental data. These two profiles have been measured in the embryo by tracking the cells and fitting their mean squared displacement $\langle \Delta r^2(t) \rangle$ where $\Delta \overrightarrow{r}(t) = \overrightarrow{r}(t) - \overrightarrow{r}(0)$, with the cell position $\overrightarrow{r}(t)$ at time t. Since cells are diffusing at constant D within a flow of velocity v, the 2D mean squared displacement can be written as:

$$\langle \Delta r^2(t) \rangle = 4Dt + v^2 t^2 \tag{2.5}$$

These measured profiles and their fit by the continuum model are displayed Figure 2.6 B, C. The fitted parameters values are: $F \approx 1.5$ mPa, $\alpha \rho_0 \approx 1.3$ Pa and $\xi \approx 0.7$ Pa $\cdot$ s $\cdot$ m^{-2}. The resisting pressure F is negligible compared to the PSM active pressure at the posterior limit $\alpha \rho_0$, indicating that the growth is favored.

2.4 Limits of the random motility gradient model

All these experiments taken together demonstrate the key role of the PSM, especially its posterior region, and of the pattern of cell motility along the axis in elongation. However, a realistic physical mechanism remains to be demonstrated.
We presented how a theoretical model could account for PSM expansion. However, we still have to show if the assumptions this model relies on are justified. In particular, the model assumes that the PSM is confined mediolaterally by two rigid walls (*i.e.* infinitely stiffer). Therefore, the relative stiffness of the PSM and its neighboring tissues needs to be assessed. Additionally, the theoretical model uses as an input parameter a constant viscosity of the PSM along the axis. The precise pattern of viscosity along the axis has to be measured. Furthermore, a pushing pressure is predicted by the theory, it also has to be compared with experimental measurements.

Posterior tissues' coordination during elongation is not explained by the model yet. Several hypotheses can be devised. If the PSM is the sole tissue pushing, the extension of the axial tissues needs to be explained. Is the PSM pushing the extraembryonic boundary which is physically connected to the axial tissues and pulls on them (see Figure 2.7 A)? Is the PSM laterally dragging the axial tissues? On the contrary, if the PSM is not the only growing tissue, its central role needs to be accounted for. Is the growth of the axial tissues dependent on the PSM activity? We could envision a convergent extension mechanism in the axial tissues, driven by the lateral compression of the PSM (see Figure 2.7B). However, if the growth of the axial tissues is independent of the PSM, we could hypothesize that the central role of the PSM is to push the extra-embryonic boundary forward and to make room for
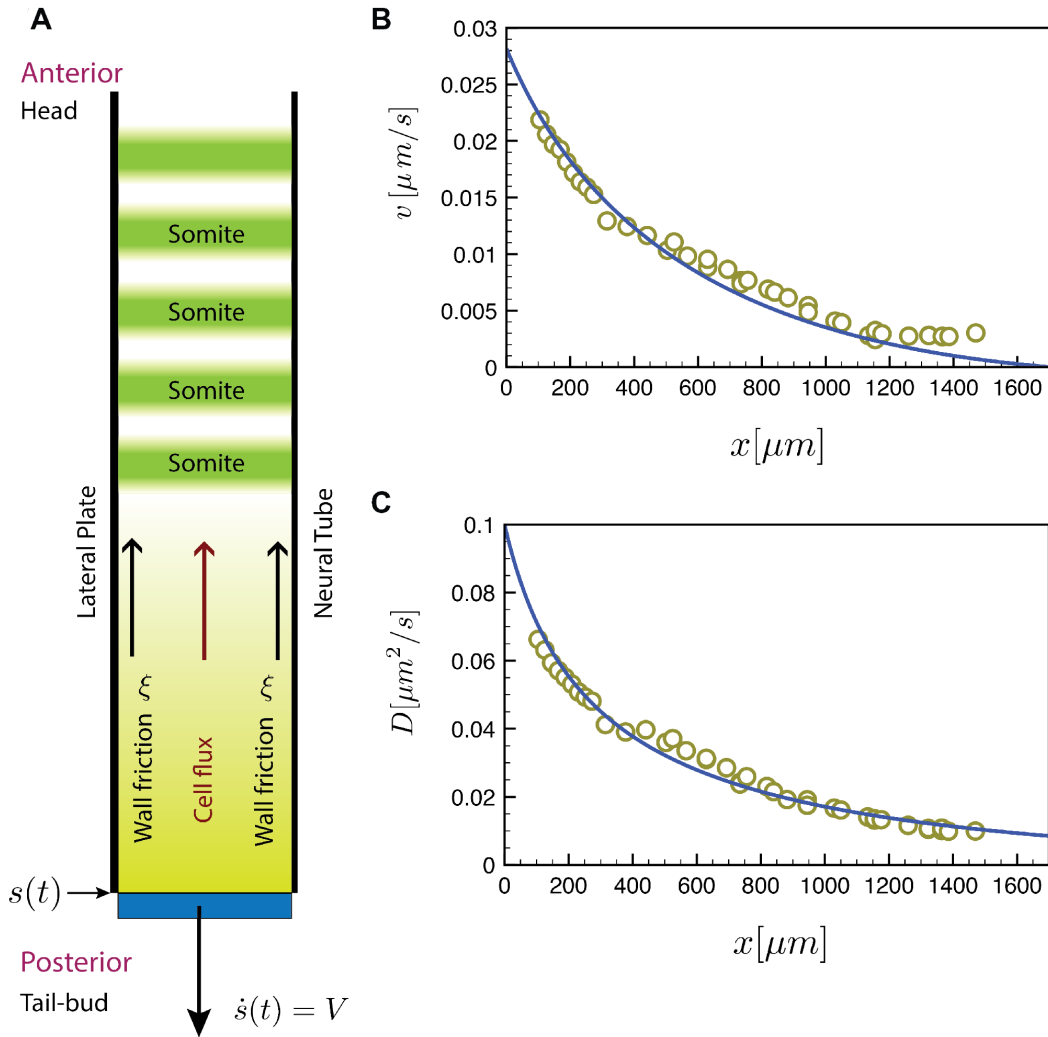
FIGURE 2.6 – Continuum model of random cell motility (adapted from Regev et al., 2017). **A**: Schematic of the continuum model. Experimental flow velocity (**B**) and cell diffusion (**C**) along the axis away from the posterior limit of the PSM. Solid line: continuum model prediction.
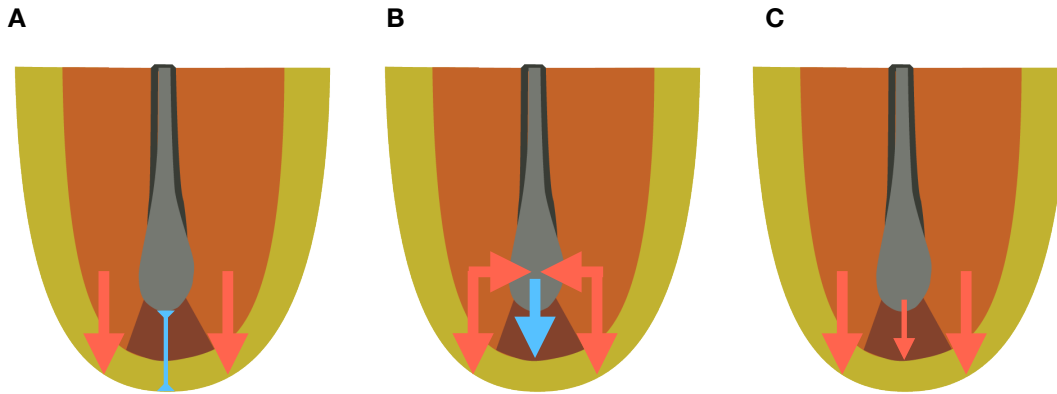
FIGURE 2.7 – Multi-tissue elongation models. **A**: PSM growth only model. The PSM is the only tissue growing and actively pushes the posterior boundary. The axial tissues are pulled by the posterior boundary. **B**: PSM mediated convergent extension of the axial tissues model. The PSM is actively pushing the posterior boundary and compressing the axial tissues, which undergo convergent extension leading to their growths. **C**: Axial tissues independent growth model. Axial tissues push independently of the PSM activity but they generate a force too weak to displace the boundary in the absence of the PSM push. Red arrows: active forces, blue arrows: passive forces.

the axial growing tissues, which would not be able to generate enough pressure to push the boundary forward by themselves (see Figure 2.7 C). In order to test these hypotheses, the independent elongation of isolated tissues must be measured, together with the forces produced by elongation. The mechanical coupling between the various tissues must also be assessed.

In this thesis, we will present experimental results which aim at providing an experimental validation to our theoretical model. In particular, we want to provide the model with measurements of mechanical properties in order to, first, confirm the assumption of a mediolateral confinement of the PSM by rigid walls, second, refine the viscosity pattern along the axis, and lastly, compare the pushing pressure prediction with experimental data.
In Chapter 3, we will present experiments which allowed us to measure a ratio of surface tension over viscosity along the PSM. In Chapter 4, we will show the results of independent measurements of elasticity, viscosity and surface tension, in both the PSM and the NT. And finally, in Chapter 5, we will assess the contribution of the PSM to the total force of elongation. In this last chapter, the force measurements will also give us hints about the different models which can explain the multi-tissue coordination during elongation.

Chapter 3

Viscocapillary properties of the presomitic mesoderm along the anteroposterior axis

In this chapter, we present measurements of the ratio of surface tension over viscosity along the AP axis. To do so, we monitor the shape of dissected PSM explants when cultured *in vitro*. We also investigate the role of cell motility on these mechanical properties.

3.1   Tissue viscocapillary velocity measured by rounding and fusion dynamics

In their seminal work, Gordon et al., 1972 showed how monitoring the shape of cellular aggregates cultured *in vitro* could be used to measure the ratio of surface tension over viscosity γ/η. This quantity has the dimension of a velocity, as γ is a force per unit of length and η is a pressure multiplied by a time. Therefore, we will refer to this ratio as viscocapillary velocity v_p as it was referred to by Stirbat et al., 2013a. Gordon et al. presented several experiments to measure viscocapillary velocity of cellular aggregates. They all shared in common that the studied aggregates exhibit a liquid nature at long times: they tend to minimize their surface area over volume ratio. This phenomenon is led by surface tension and resisted by viscosity. In this chapter, we will focus on two experiments described by Gordon et al.: aggregate rounding and aggregate fusion.
Gordon et al. analyzed rounding data previously published on reaggregated heart cells from 4-day old chicken embryo and estimated that $v_p \approx 0.6\,\mu\text{m} \cdot \text{min}^{-1}$ (Phillips and Steinberg, 1969). The rounding experiment was later used on reaggregated neural cells from the retina of 9-day old chicken embryo and a 10-fold slower viscocapillary velocity was measured $v_p = 0.06 \pm 0.01\,\mu\text{m} \cdot \text{min}^{-1}$ (Mombach et al., 2005).
The fusion experiment has been studied in more details by Gordon et al. They measured a viscocapillary velocity ranging from 0.42 to 1.14 $\mu\text{m} \cdot \text{min}^{-1}$. More recent fusion experiments carried out on embryonic mouse carcinoma cellular aggregate yielded 0.46 to 0.68 $\mu\text{m} \cdot \text{min}^{-1}$ (Marmottant et al., 2009 and Stirbat et al., 2013a). $v_p = 0.16\,\mu\text{m} \cdot \text{min}^{-1}$ has been reported for fusion of murine sarcoma aggregates (Douezan and Brochard-Wyart, 2012).

In order to measure viscocapillary velocity of the PSM, we carried out rounding and fusion experiments on dissected PSM explants, which were monitored by microscopy.

A

B
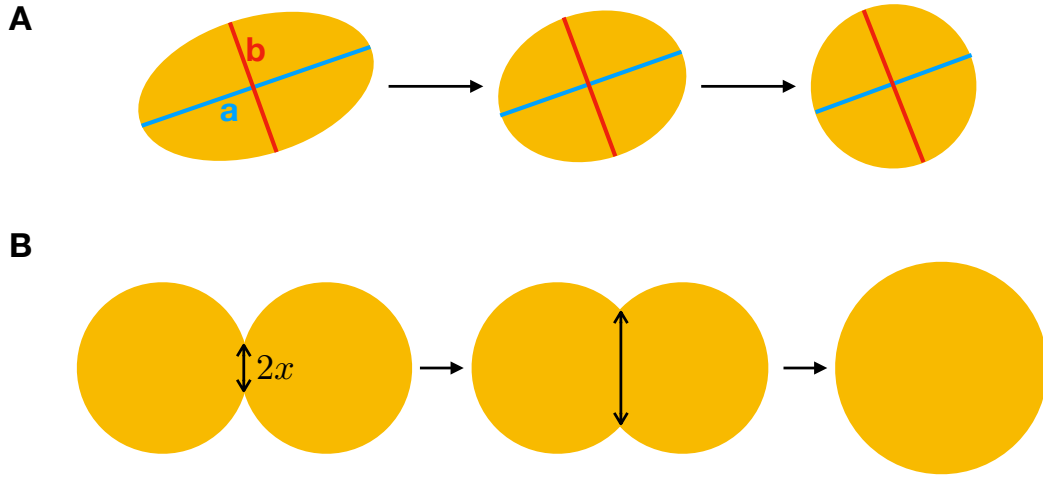
FIGURE 3.1 – Schematic of rounding and fusion experiments. **A**: Rounding experiment. A piece of tissue in the shape of an ellipsoid of revolution of major axis *a* and minor axis *b* rounds up over time. **B**: Fusion experiment. Two spheroids meet and a fuse by a neck, which radius *x* grows over time.

3.1.1 Tissue rounding theory

If a rounding tissue is assumed to be an ellipsoid of revolution, the rounding dynamics can be described by the temporal evolution of its aspect ratio a/b, where a and b are respectively the lengths of the major and minor axis (see Figure 3.1 A). The aspect ratio has been previously shown to follow an exponential decay (Gordon et al., 1972):

$$\frac{a(t)}{b(t)} - 1 = \left(\frac{a_0}{b_0} - 1\right) \exp\left(\frac{-t}{\tau}\right) \tag{3.1}$$

where $a_0 = a(0)$, $b_0 = b(0)$ and the typical decay time τ is given by:

$$\tau = \alpha \frac{\eta}{\gamma} R_f \tag{3.2}$$

with the $\alpha \approx 0.95$ if the tissue aggregate is much larger than the medium viscosity, η the explant viscosity, γ surface tension and R_f the explant final radius.

3.1.2 Fusion of tissues theory

Gordon et al. also studied the case of the fusion of two spherical cellular aggregates. In a similar way as the rounding experiment, surface tension tends to minimize the surface area over volume ratio and drives the fusion of the two aggregates into a larger aggregate. The cellular rearrangement also resists this fusion. Therefore, the same balance of surface tension and viscosity sets the dynamics of fusion. The fusion of two viscous drops of same initial radius R_0 has been studied by Frenkel, 1945. The squared radius of the fusion neck x^2 grows linearly with time, at short times (see Figure 3.1 B). Therefore, using Frenkel's formula, Gordon et al. could measure viscocapillary velocity of cell aggregates. Later, corrections were brought by Eshelby, 1949 and Stirbat et al., 2013a. In the end, the dynamics of fusion at short times is dictated by:

$$x^2 = \frac{R_0 \gamma}{\eta} t \tag{3.3}$$

3.2 Experimental protocol

3.2.1 Preparation of presomitic mesoderm explants

For multiple experiments that will be presented in this thesis, explants of PSM were dissected out of the embryo. As shown in Figure 2.1, the PSM lies dorsoventrally, between the ectoderm and the endoderm, and mediolaterally between the neural tube and the lateral plate. Therefore, dissecting out the PSM requires to detach it from the ectoderm and the endoderm and to cut it away from the neural tube and the lateral plate. The adhesion between the PSM and the ectoderm is fairly loose, whereas the endoderm is strongly connected to the mesoderm. To isolate the PSM, after collecting embryos (stage 12-14 somites) and transferring them in phosphate-buffered saline (PBS), three different strategies were tested:

- the ectoderm was carefully lifted apart from the PSM by means of a fine glass fiber. The connections with neural tube and lateral plate were cut. The PSM was then carefully cut apart from the endoderm. However, each of these steps was destructive, especially the latest, and most of the times a layer of mesodermal cells was left sticking to the endoderm. This technique was not suitable for mechanical measurements as the PSM structure was extremely altered.

- a similar protocol was used after loosening the tissues by a 1-minute treatment by pancreatin (a porcine pancreas extract containing a mixture of proteolytic enzymes and lipases). After washing away pancreatin, the endoderm could be carefully removed. The PSM was then cut on its sides and lifted apart from the ectoderm. This protocol allowed us to successfully isolate PSM explants without altering too much their structure. However, an important variability in the pancreatin activity was noticed between enzyme batches which led to very variable PSM conditions. Indeed, Figure 3.2 A and B show two representative examples of PSM conditions after pancreatin-based dissection. In addition, pancreatin digests a very wide spectrum of ECM proteins, especially fibronectin (see Figure 3.2 C, D) which might alter the PSM mechanical properties.

- the same protocol was modified by replacing pancreatin by collagenase type IV as shown by Rifes et al., 2007. PBS with Ca^{2+} and Mg^{2+} ions, as the collagenase catalytic activity depends on them, was also used. The collagenase was used for a 10-minute treatment prior to dissection. This protocol led to a much more reproducible PSM mechanical state.

We divided the PSM into three regions (anterior, medial and posterior) as shown in Figure 3.3 A. We typically dissected out explants ranging from 150 to 400 µm long for rounding experiments, and 100 µm long for fusion experiments (so explants rapidly round up as spheroids).

3.2.2 Explants culture and imaging

After dissection, explants were transferred to an imaging slide (8-well Labtek) in Dulbecco's Modified Eagle Medium (DMEM-F12) enriched with 10% fetal bovine
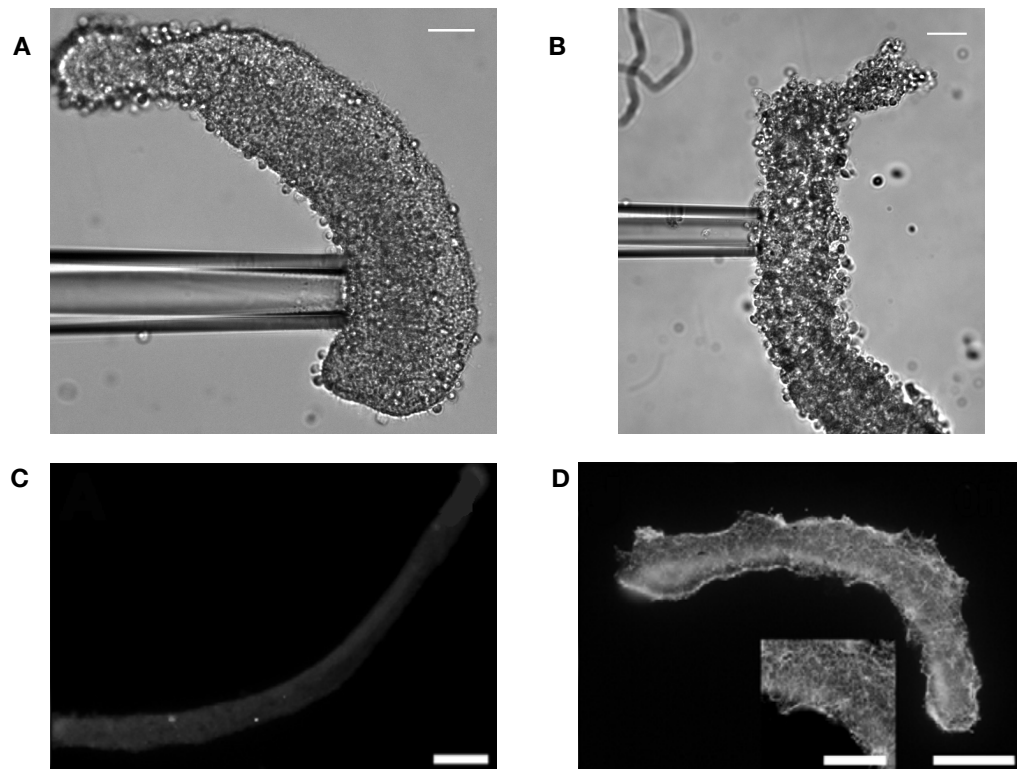
FIGURE 3.2 – PSM dissection. Healthy (**A**) and damaged (**B**) PSM both dissected following the pancreatin-based protocol. Note the large number of round dead cells on **B**. **C**: Fibronectin immunostaining on PSM dissected following the pancreatin-based protocol: fibronectin is almost completely digested. **D**: Fibronectin immunostaining on PSM dissected following the collagenase-based protocol: fibronectin is abundant. **C**, **D**: adapted from Rifes et al., 2007. Scale bars: 50 μm (**A**, **B**), 100 μm (**C**, **D**).

serum (FBS) at 37 °C with 7.5% CO_2. The imaging slide was a glass substrate dish which was previously coated with $0.3 \, mg \cdot mL^{-1}$ PolyEthyleneGlycol-PolyLysin in HEPES solution (10 mM), to prevent any adhesion of the cells to the glass (Douezan and Brochard-Wyart, 2012). The explants were imaged with a 6-min interval under an inverted wide-field microscope (Zeiss Axioobserver Z1, objective 10X 0.3 numerical aperture) and the incubation conditions (7.5% CO_2, 37 °C) were maintained constant throughout the experiment.

3.3 Rounding dynamics along the anteroposterior axis

3.3.1 Analyzing rounding dynamics

Analysis procedure

After placing dissected explants in culture, we observed that they were rounding over time with different dynamics depending on the region they were dissected from. Posterior explants rounded faster than anterior explants (see Figure 3.3). To quantify the rounding dynamics, we automatically segmented each explant using the CellProfiler software (Carpenter et al., 2006) and fitted the shape with an ellipse using the normalized central moments calculation. The major and minor axes, a and b, were measured to compute the aspect ratio a/b over time. As expected from the relation 3.1, the aspect ratio follows an exponential decay over time (see Figure 3.4 A). The typical time of this decay τ was computed for all explants by fitting the slope of the semilog plots (with a_0 and b_0 kept fixed):

$$\log \left(\frac{\frac{a(t)}{b(t)} - 1}{\frac{a_0}{b_0} - 1} \right) = \frac{-t}{\tau} \tag{3.4}$$

Three typical rounding experiments of explants along the AP axis are presented Figure 3.4 B and Movies 1, 2 and 3. The rounding dynamics is graded along the axis with a faster dynamics towards the posterior of the body. On average, $\tau = 456 \pm 234$ min in anterior, $\tau = 149 \pm 114$ min in medial and $\tau = 68 \pm 26$ min in posterior.

Special case of anterior explants

A phenomenon complicated the analysis in anterior-most explants. Inter-somitic clefts are prepatterned in the anterior PSM up to 4 future somites (Palmeirim et al., 1997). Therefore, for a majority of anterior explants ($n = 32/36$) somite formation took place during the rounding process. In this case, cleavage was initiated during 2-3 hours, then failed and the explants subsequently rounded up. A typical sequence of snapshots of this process is presented in Figure 3.5 A. For these peculiar situations, the aspect ratio was either constant or increased during the cleavage process. We, therefore, fitted the exponential decay only after the end of the cleavage phase (see Figure 3.5 B).

3.3.2 A graded viscocapillary velocity along the anteroposterior axis

In order to verify the relation 3.2, we plotted τ against the final radius of the rounded explant R_f. We were limited by the accessible range of R_f, because the starting explants could not be too small as they would be already almost round. They could not be longer than a third of the PSM as they would encompass more
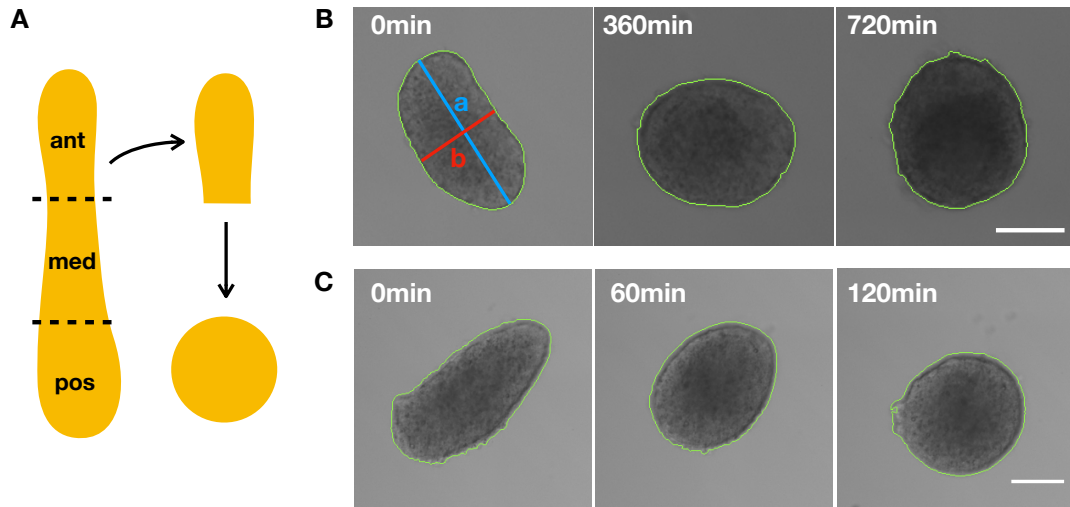
FIGURE 3.3 – Explant rounding dynamics. **A**: Schematic of explant dissection. Snapshots during anterior (**B**) and posterior (**C**) explant rounding. Green lines show segmented contour. Blue line shows the major axis of length *a* of the fitted ellipse. Red line shows the minor axis of length *b* of the fitted ellipse. Scale bars: 100 µm.
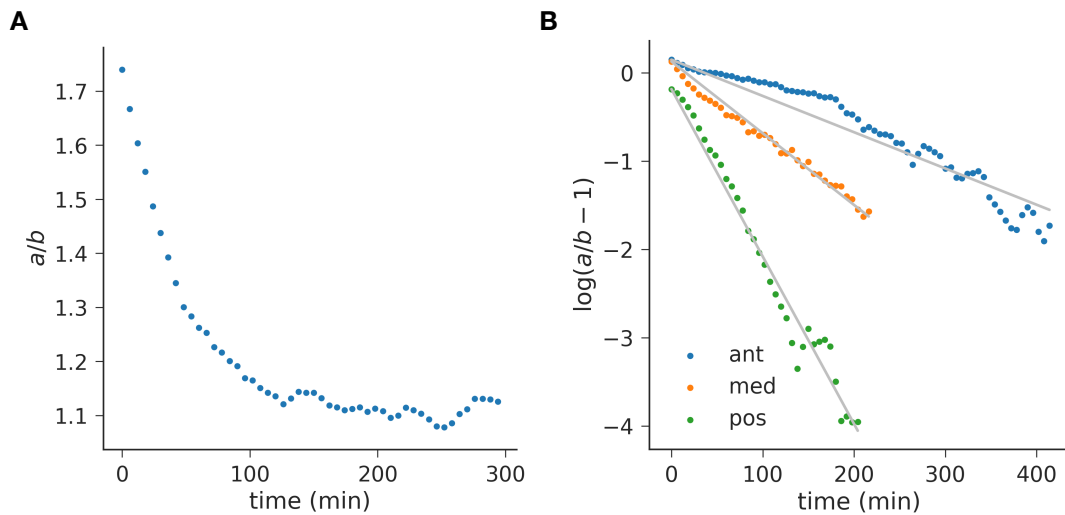
FIGURE 3.4 – Measurement of the rounding dynamics along the anteroposterior axis. **A**: Typical exponential decay of the aspect ratio a/b for a medial explant. **B**: Semilog plots of a/b along the anteroposterior axis (ant: anterior, med: medial, pos: posterior). Solid lines: linear fits with a_0/b_0 fixed.
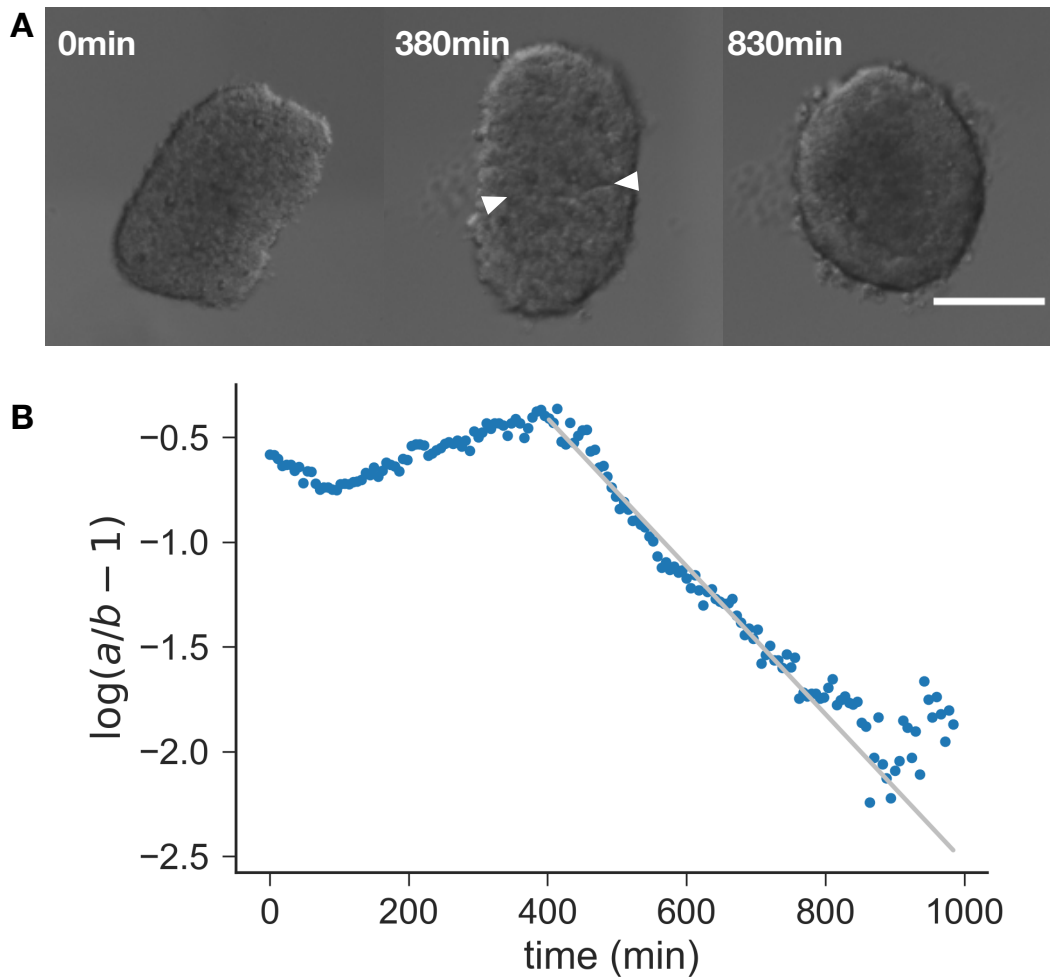
FIGURE 3.5 – Somitogenesis in anterior explants. **A**: Snapshots of a time-lapse of an anterior explant. The explant starts cleaving (arrowheads indicate the cleavage plan), then fuses again and rounds up. Scale bar: 100 µm. **B**: Quantification of the rounding dynamics. The aspect ratio a/b increases during the first 400 min (extension), and then exhibits an exponential decay (rounding).

than one region. For this reason, R_f was limited to less than a 2-fold range (from 70 µm to 130 µm). Despite data variability, we could see that there was a general trend of increasing τ with respect to R_f (see Figure 3.6 A, B). Thus, we considered that the linear dependency is verified.

We next investigated how viscocapillary velocity varied along the AP axis. Figure 3.6 C shows that the posterior region rounds up nearly 8 times faster than the anterior region ($v_p = 0.21 \pm 0.08\,\mu\text{m} \cdot \text{min}^{-1}$ in anterior and $v_p = 1.57 \pm 0.53\,\mu\text{m} \cdot \text{min}^{-1}$ in posterior, see Table 3.1). We observed intermediate rounding dynamics in the medial region, with a wide dispersion: some explants were already anterior-like, some were still posterior-like ($v_p = 0.92 \pm 0.44\,\mu\text{m} \cdot \text{min}^{-1}$). This decreasing viscocapillary velocity as the PSM matures can be explained by two non-mutually exclusive hypotheses:

- surface tension decreases from posterior to anterior. Since the PSM epithelializes during its maturation, this possibility seems unlikely;

- viscosity increases from posterior to anterior. As the ECM is deposited along the AP axis and cellular density increases, this hypothesis seems more plausible.

Therefore, if we assume that surface tension stays at least constant, or even increases during PSM maturation, viscosity needs to increase to an even greater extent to explain the graded dynamics of rounding.

3.3.3 Effect of cell motility

As motility of PSM cells is a key driver of elongation, we next investigated the effect of motility on rounding dynamics. Cell motility is likely to impact tissular viscosity as cell-cell rearrangement is an important determinant of tissue fluidity. We, therefore, investigated the rounding dynamics of explants incubated with two different drugs known to inhibit cell motility *in vivo*: blebbistatin and the MAPK inhibitor PD0325901 (Bénazéraf et al., 2010).
Blebbistatin is an inhibitor of myosin-II phosphorylation which decreases actomyosin contractility. Consequently, cell motility is impaired, but so is cortical tension. Therefore, we could expect that the explant surface tension would be lowered by blebbistatin, and thus viscocapillary velocity (if viscosity stays constant). We incubated explants with 20 µM blebbistatin. Surprisingly, viscocapillary speed showed a weak but significant increase in anterior explants (Student t-test's p-value: 0.039) and no change in medial and posterior explants (Student t-test's p-values respectively: 0.81 and 0.19). We verified that the blebbistatin treatment was effective. First, we observed that cell protrusive activity was blocked and thus explants exhibited a characteristic smooth surface. Second, as it will be shown in Chapter 4, we measured that surface tension was significantly lowered upon blebbistatin treatment, also confirming blebbistatin activity.
One likely hypothesis to explain these results is that inhibiting actomyosin contractility decreases viscosity and surface tension to similar extents in medial and posterior regions. However, viscosity might be decreased to a greater extent than surface tension in the anterior region, hence v_p increase. We also noticed that the somitic cleft formation was always absent in blebbistatin-treated explants. As such, another potential explanation for a higher v_p is that somitic cleft formation in control explants slows down the rounding process.
Next, we studied the effect of the FGF/MAPK gradient. 2 µM PD0325901 treatments also led to a significant increase of viscocapillary velocity in anterior (+45%,
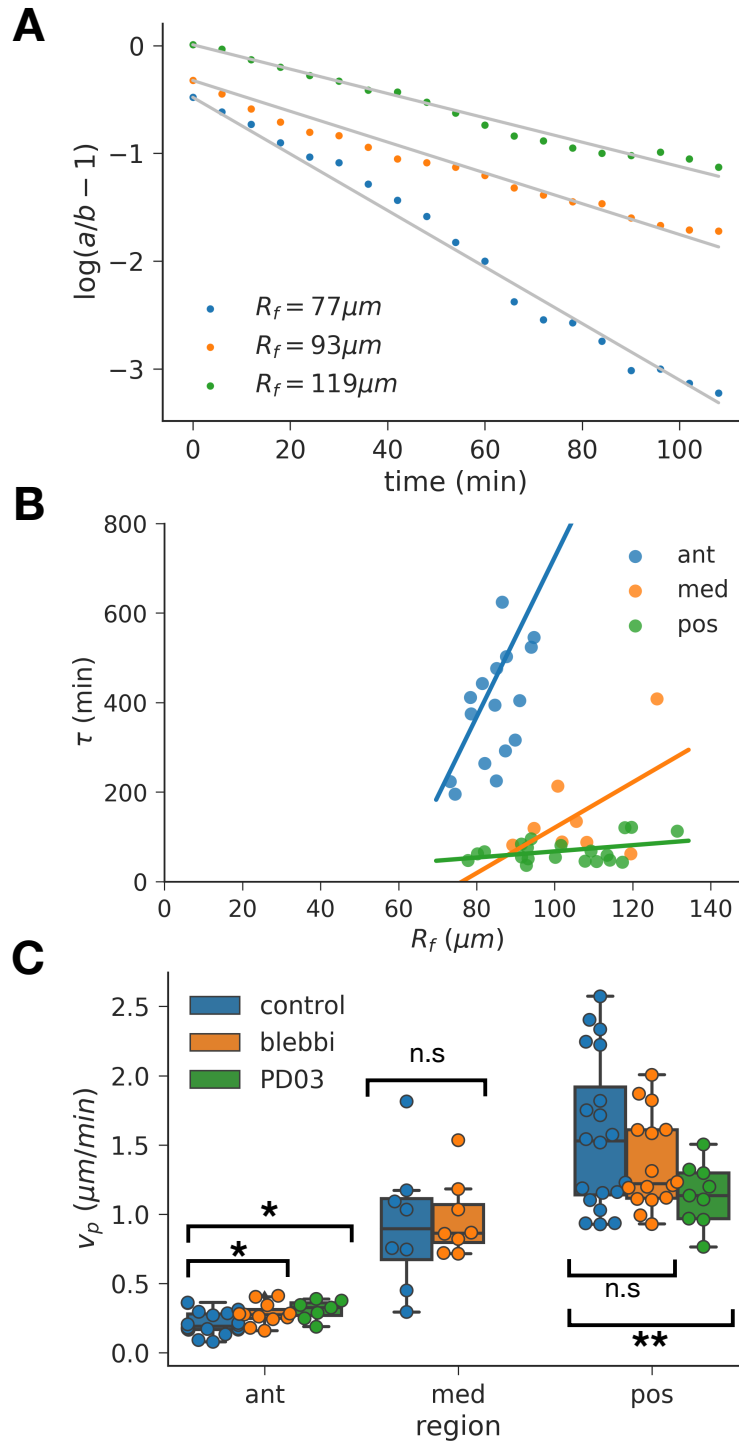
FIGURE 3.6 – Viscocapillary velocity along the anteroposterior axis.
A: Semilog plots of a/b for posterior explants of various final radii.
Solid lines: linear fits with a_0/b_0 fixed. **B**: Decay time τ with respect
to the final radius R_f. **C**: Viscocapillary velocity along the axis (ant:
anterior, med: medial, pos: posterior), and for different conditions
(blebbi: 20 μM blebbistatin, PD03: 2 μM PD0325901). Student's t-test
p-value p: n.s: $p > 0.05$, ⋆: $p < 0.05$, ⋆⋆: $p < 0.01$.

TABLE 3.1 – Viscocapillary velocity along the anteroposterior axis measured by rounding dynamics (mean and standard deviation, in µm / min).

	Anterior	Medial	Posterior
Control	0.21 ± 0.08	0.91 ± 0.44	1.56 ± 0.53
Blebbistatin	0.28 ± 0.07	0.96 ± 0.25	1.36 ± 0.32
PD0325901	0.30 ± 0.06		1.13 ± 0.21

Student t-test's p-value: 0.014). In posterior explants, we noticed an important reduction of v_p upon FGF/MAPK inhibition (-28%, Student t-test's p-value: 0.005). FGF/MAPK inhibition should have a greater effect on cell motility in posterior explants. Therefore, the posterior reduction of v_p suggests that cell motility inhibition increases viscosity (assuming the effect on surface tension is low). However, it is difficult to anticipate the impact of the FGF/MAPK inhibition on surface tension, therefore the interpretation of these results remains unclear while we do not have independent measurements of surface tension and viscosity.

3.3.4 Fusion dynamics yields a similar viscocapillary velocity

In order to confirm the values of viscocapillary velocity obtained by rounding experiments, we carried out a fusion experiment. We dissected out explants of similar sizes with aspect ratios close to 1, so they could rapidly round up. We incubated them in DMEM-F12 enriched with 10% FBS at 37 °C with 7.5% CO_2 for an hour until they were spheroids. We then brought them in contact by pairs and imaged their fusion in same culture conditions (see Figure 3.7 and Movies 4, 5). The neck of fusion was manually measured using the Fiji software (Schindelin et al., 2012). We fitted the square of the neck radius x^2 with respect to time during the linear regime (the first half of the experiment) and extracted viscocapillary speed. Figure 3.8 C shows that fusion experiments gives similar AP gradient to rounding experiments ($v_p = 0.16 \pm 0.05$ µm · min^{-1} in anterior and $v_p = 0.99 \pm 0.15$ µm · min^{-1} in posterior). We also monitored the fusion of anterior with posterior explants, as potential differences in surface tension might lead to the engulfment of one region by the other. Surprisingly, these explants from different regions failed to fuse.

3.4 Conclusion

In this chapter, we presented viscocapillary velocity measurements from two distinct methods which lead to similar orders of magnitude. Our data show that the PSM exhibits a graded viscocapillary velocity along the axis. Anterior PSM explants exhibit viscocapillary velocities comparable to previous rounding or fusion experiments carried out on cellular aggregates. However, the posterior region of the PSM shows significantly higher viscocapillary velocities which suggests an important tissue fluidity (or a high, although unlikely, surface tension) compared to previously studied tissues. This pattern can potentially be explained by a low viscosity in the posterior PSM which gradually increases as the PSM matures towards the anterior PSM.

We also showed that drugs which are known to decrease cell motility in the posterior PSM result in a non-trivial profile of velocity change: increase in anterior
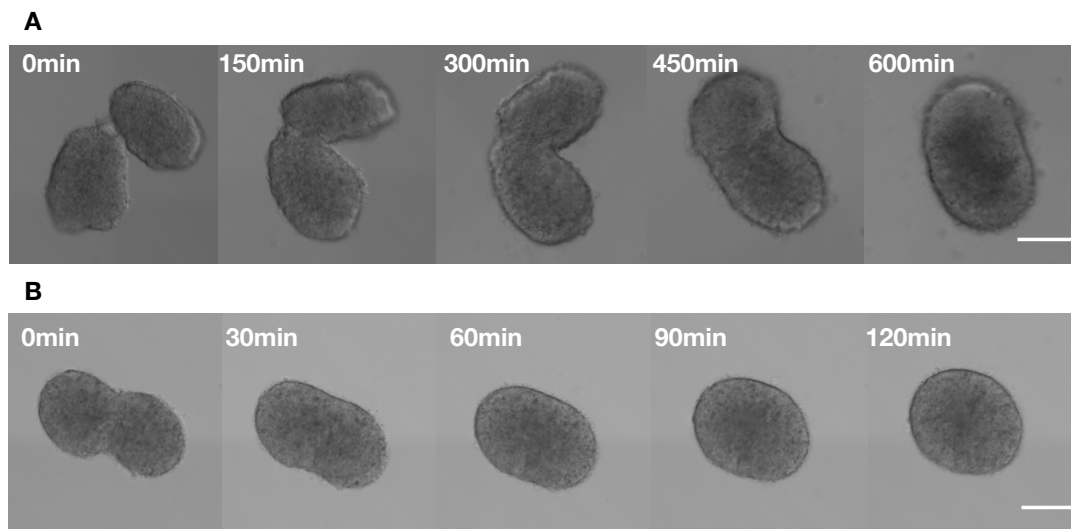
FIGURE 3.7 – Fusion experiment along the anteroposterior axis. Snapshots of time-lapses of fusing explants. **A**: Two anterior explants fusing. **B**: Two posterior explants fusing. Scale bars: 100 μm.
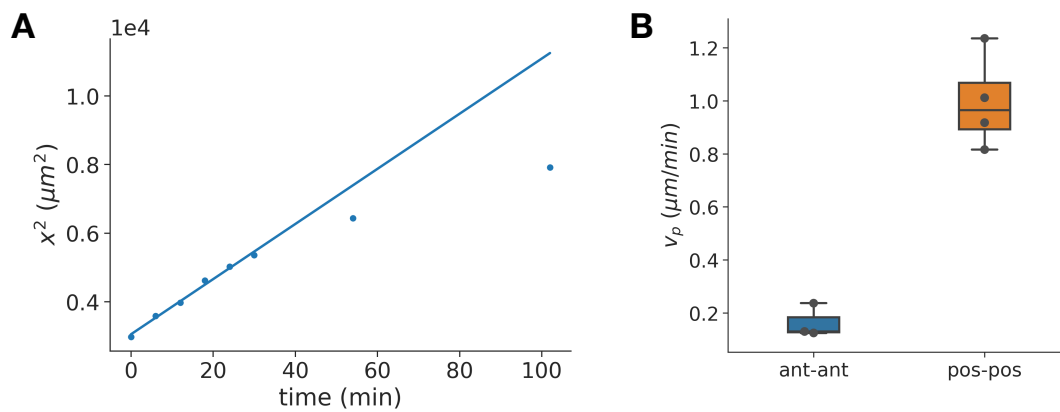
FIGURE 3.8 – Viscocapillary velocity along the anteroposterior axis measured by fusion. **A**: Neck radius dynamics during the fusion of two posterior explants. **B**: Viscocapillary velocity measured by fusion of pairs of anterior explants (ant-ant) and posterior explants (pospos).

and decrease in posterior (for FGF/MAPK inhibition) or no-impact in posterior (for myosin-II phosphorylation inhibition). In order to further investigate the impact on viscosity and surface tension, these properties must be measured independently which is the aim of the next chapter.

Chapter 4

Viscoelastic properties of the axial and paraxial tissues along the anteroposterior axis

In this chapter, we present tissue viscoelasticity and surface tension independently measured by microaspiration. Historically, the micropipette aspiration technique has been used to measure membrane tension of red blood cells (Evans, 1973). Viscoelastic properties of different cell types have also been measured by pipette aspiration (Hochmuth, 2000). More recently it was used to measure junction tension in early mouse embryos (Maître et al., 2015). The viscoelastic properties measured by pipette aspiration were used as a diagnostic tool for oocyte viability (Yanez et al., 2016). Viscoelastic and surface tension were also probed at the tissue level by aspiration of cellular aggregates (Guevorkian et al., 2010, Guevorkian et al., 2011). Viscosity of bacterial aggregates involved in meningitis and septicemia was recently measured by pipette aspiration (Bonazzi et al., 2018).

4.1 Micropipette aspiration technique

The micropipette aspiration technique enables the measurement of the strain response over time within a transparent capillary. In this technique, the opening of a micropipette is brought into contact with the material of interest. Next, a suction pressure is applied, causing the material to be aspirated into the pipette. The length of the aspirated tongue is measured by microscopy. A typical pipette aspiration setup for probing biological tissues is shown in Figure 4.1 A. In this setup, biological samples are placed in a culture medium under a microscope. Depending on the suction pressure precision needed, pressure can be controlled by means of a pump or simply by adjusting the hydrostatic pressure.

4.1.1 Micropipette aspiration theory

The theory of pipette aspiration has been extensively developed for single cells. An important review of the various mechanical properties that can be measured by pipette aspiration has been published by Hochmuth, 2000. In particular, certain cell types behave as a solid while others exhibit the properties of a liquid surrounded by a cortical elastic shell. The difference between liquid and solid behaviors lies in the dynamics of aspiration after a critical length of aspiration.
The length of aspiration L of a solid cell quickly saturates to a constant value soon after application of the pressure, for all pressures. This is the case of endothelial
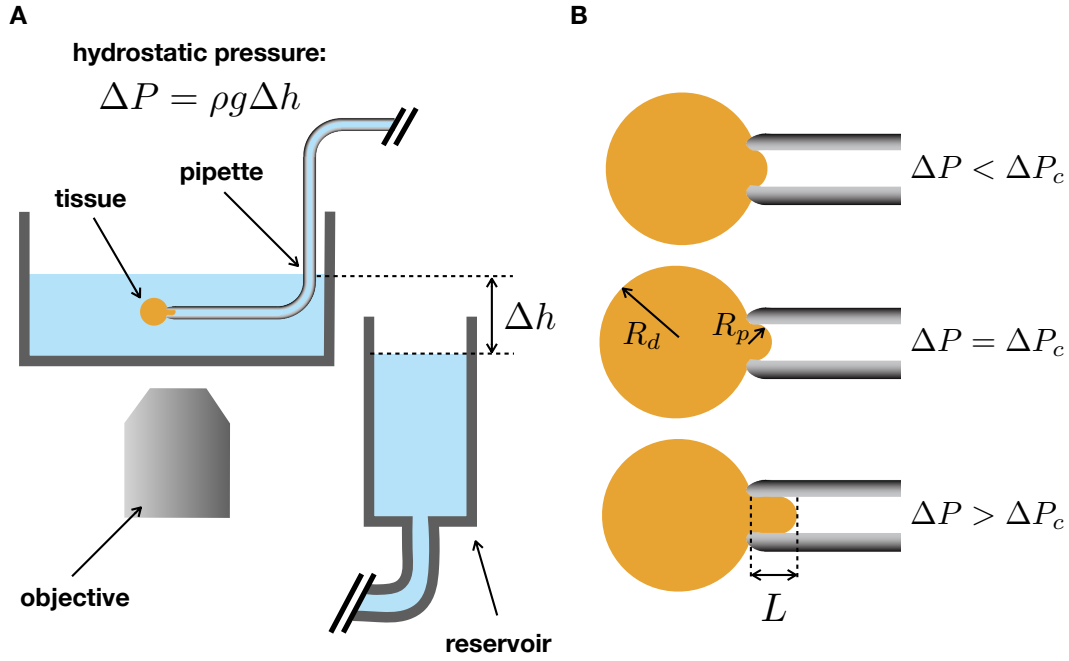
FIGURE 4.1 – Micropipette aspiration principle. **A**: Schematic of the aspiration experimental setup. **B**: Schematic of a viscous spherical drop aspirated under different regimes of pressure, $\Delta P < \Delta P_c$: the curvature within the pipette increases with the pressure, $\Delta P = \Delta P_c$: the curvature within the pipette is maximal $(2/R_p)$, $\Delta P > \Delta P_c$: the curvature within the pipette is maximal and stays constant, and the drop flows into the pipette.

cells or chondrocytes (Theret et al., 1988, Jones et al., 1999). The relation between L and the applied pressure is set by cell elasticity, which is quantified by the Young's modulus, E. These studies measured $E \approx 400$ Pa for endothelial cells and $E \approx 650$ Pa for chondrocytes.

A liquid-like cell has a more complex dynamics. For small pressures, the length also saturates at lengths smaller than the pipette radius R_p (see Figure 4.1 B), whereas at higher pressures, L is not a constant overtime anymore: the cell flows in the pipette at a rate controlled by cell viscosity. For instance, neutrophils have been shown to exhibit such a behavior (Evans and Yeung, 1989). Therefore, there is a critical pressure ΔP_c above which cells flow. ΔP_c is related to cortical tension. So, both the cytoplasm viscosity η and the cortical tension γ can be measured. In the case of neutrophils, $\eta = 200$ Pa $\cdot$ s and $\gamma = 35$ mN $\cdot$ m^{-1}.

We will review below the theories leading to these measurements.

Elasticity measurement

Following the cylinder geometry of a pipette we can write the stress σ:

$$\sigma = \frac{f}{\pi R_p^2} \tag{4.1}$$

where f is the applied force and πR_p^2 the pipette cross section. The strain ϵ scales like: $\epsilon \sim \frac{L}{R_p}$. Therefore, we can write that the Young's modulus E follows:

$$E = \frac{\sigma}{\epsilon} \sim \frac{f}{\pi R_p L} \tag{4.2}$$

However, this scaling law needs to be completed by a detailed theoretical study as prefactors can arise from the geometry of the pipette contact. The first theoretical study of cell elasticity measurement by pipette aspiration was published by Theret et al., 1988. They studied the stain-stress relation assuming the sample is an isotropic and incompressible elastic half-space. Two distinct analytical models with different boundary conditions were proposed (see Figure 4.2 A). The *force model* assumes that the stress is constant over the annular region where the tip of the pipette wall is in contact with the material. The *punch model* assumes that the material is always in contact with the annular region. This is not the case in the force model for which there is a typical bending of the material upon aspiration see Figure 4.2 B. Both models relate the length of aspiration to Young's modulus by the same relation, with a different prefactor Φ:

$$\frac{L}{R_p} = \frac{3\Phi}{2\pi} \frac{\Delta P}{E} \tag{4.3}$$

where Φ is a function of the wall thickness. For the force model, there is a strong dependency (Φ decreases from 2.3 to 1.4 as the wall thickness increases), while for the punch model, the dependency is very weak ($\Phi \approx 2.1$ for most of the wall thickness). As a result, $\frac{L}{R_p} \approx \frac{\Delta P}{E}$, for the punch model. The authors discussed that the contact profile described by the punch model was more realistic.

Aoki et al., 1997 later confirmed that the punch model was in better agreement with experimental data. By means of numerical simulations, they investigated the errors brought by several geometrical parameters such as the sample thickness and the sample total radius. They found that the sample total radius did not affect much the stress-strain relation. However, the stiffness is significantly underestimated if the sample thickness is lower than 1.5-2R_p.

Viscosity measurement

We can also derive a scaling law for viscosity by writing the stress-strain rate relation:

$$\eta = \frac{\sigma}{\dot{\epsilon}} \sim \frac{f}{\pi R_p \dot{L}} \tag{4.4}$$

where $\dot{\epsilon}$ and $\dot{L}$ are the time derivatives of respectively ϵ and L.

The first theory for measuring cytoplasm viscosity has been proposed in two companion papers from Evans and Yeung (Yeung and Evans, 1989 and Evans and Yeung, 1989). The cytoplasm was treated as a newtonian fluid. Viscosity was later expressed following a linearized relation by Needham and Hochmuth, 1990:

$$\eta = \frac{R_p \left(\Delta P - \Delta P_c \right)}{\dot{L} m \left(1 - R_p / R_d \right)} \tag{4.5}$$

where ΔP is the applied pressure, ΔP_c the critical pressure, $\dot{L}$ the flow rate, $m = 6$ a fitting parameter and R_d the drop radius. This expression relies on the parameter m which had been estimated to fit experimental data on single cells. Therefore, this

A

$$s_{zz} = \frac{-a^2}{b^2 - a^2} \Delta p \quad \text{(FORCE MODEL)}$$

or $u_z = 0$ (PUNCH MODEL)

$s_{rz} = 0$

Π

$s_{zz} = \Delta p$

$s_{zz} = 0$

Ω

r

z

B

force model

punch model

u_z/a

r/a
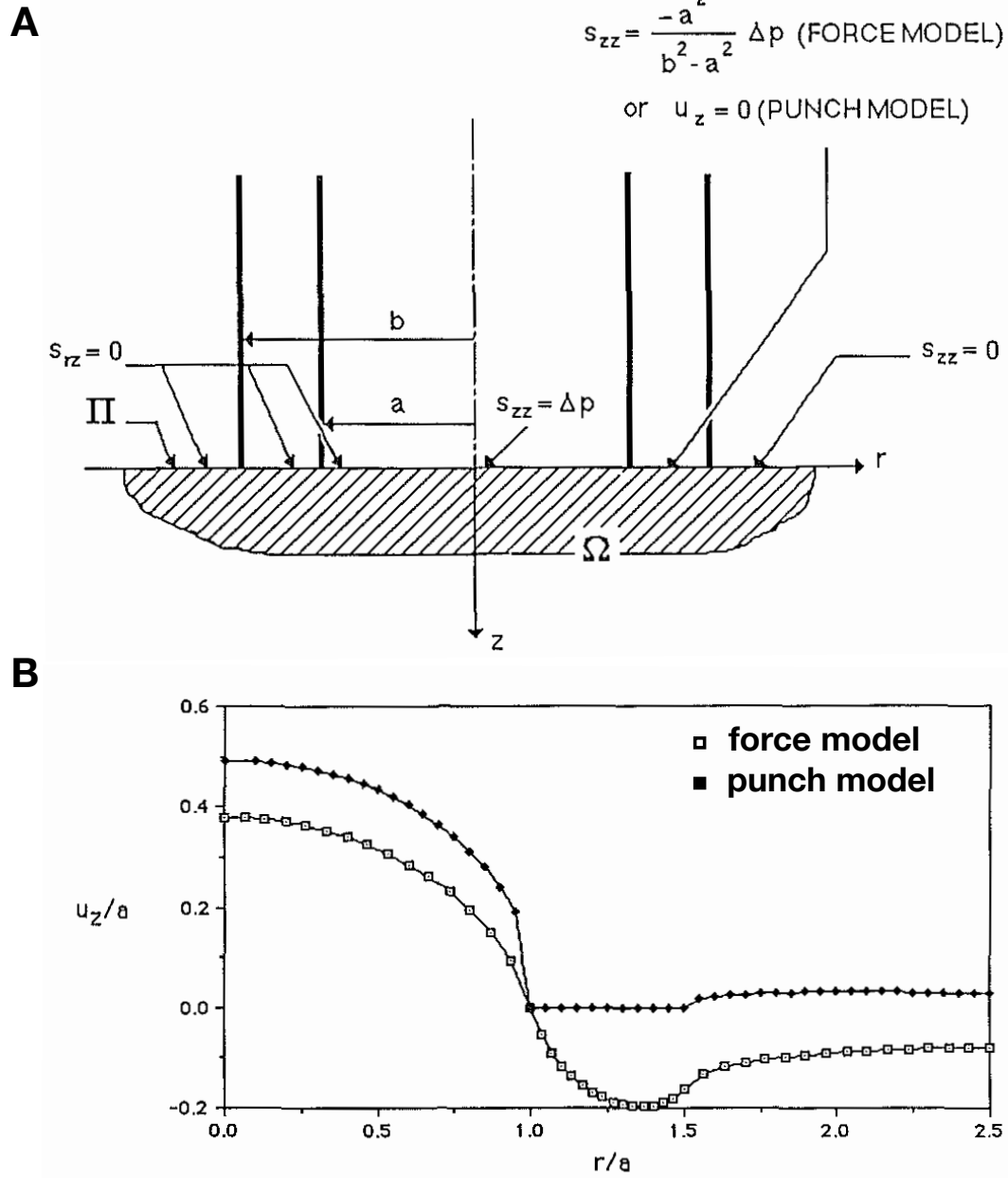
FIGURE 4.2 – Theory of elasticity measurement by pipette aspiration. **A**: Schematic of the boundary conditions of the force model and the punch model. s_{zz} is the normal stress along the pipette axis, u_z is the sample interface displacement along the pipette axis, a the inner radius of the pipette (in this thesis, a is noted R_p) and b the outer radius of the pipette. Adapted from Theret et al., 1988. **B**: Sample interface displacement for the force and the punch models. Adapted from Theret et al., 1988.

expression lacks some generality. More generally, Dagan et al., 1982 showed the geometry brought a $1/3\pi$ prefactor to the scaling law 4.4:

$$\eta = \frac{f}{3\pi^2 R_p \dot{L}} \tag{4.6}$$

Surface tension measurement

As presented above, liquids must overcome surface tension in order to flow. Consequently, surface tension is related to a critical pressure defined as the pressure when the flow starts. Yeung and Evans, 1989 derived the relation between surface tension and this critical pressure applying the Laplace law.
We consider here the case of a drop of liquid sucked in at the end of a pipette. As the aspirating pressure ΔP is increased, the curvature of the liquid inside the pipette κ_p increases over a finite range. At $\Delta P = 0$, the surface of the drop is not deformed and the curvature is the curvature of non-deformed drop κ_d. Then, as ΔP is increased, κ_p reaches a maximum value set by the pipette radius R_p, above which the surface would not be hemispherical anymore. This maximum of κ_p is reached at the critical pressure ΔP_c. We can relate ΔP_c to the surface tension of the liquid γ by writing twice the Laplace law across the drop interface: inside the pipette and outside the pipette. For $\Delta P \in [0, \Delta P_c]$:

$$\begin{cases} \kappa_d \gamma &= P_d - P_0 \\ \kappa_p \gamma &= P_d - P_p \end{cases} \tag{4.7}$$

where P_d, P_p, P_0 are respectively the pressure inside the drop, the pressure inside the pipette and the atmospheric pressure. By equalizing P_d in both expression we have $\kappa_d \gamma + P_0 = \kappa_p \gamma + P_p$ which leads to the following expression of the surface tension:

$$\gamma = \frac{\Delta P}{\kappa_p - \kappa_d} \tag{4.8}$$

with $\Delta P = P_0 - P_p$.
At $\Delta P = \Delta P_c$, the radius of curvature of the interface inside the pipette is R_p, so we can write the two curvatures as $\kappa_d = 2/R_d$ and $\kappa_p = 2/R_p$, where R_d is the radius of the drop. Therefore, the surface tension can be related to geometrical variables:

$$\gamma = \frac{\Delta P_c}{2 \left(\frac{1}{R_p} - \frac{1}{R_d} \right)} \tag{4.9}$$

The critical pressure ΔP_c can be measured by slowly increasing the aspirating pressure until κ_p reaches its maximum and the liquid start flowing into the pipette since surface tension cannot resist the increasing pressure any further. This critical pressure can be measured by monitoring the length of the tongue L over time. For $\Delta P < \Delta P_c$, the tongue saturates and $L(t) = \text{constant} < R_p$. At $\Delta P = \Delta P_c$, $L(t) = R_p$. And for $\Delta P > \Delta P_c$, the tongue flows and $L(t) > R_p$ (see Figure 4.1 B).

Measurement of bulk viscoelastic properties

For aspirating pressures above the critical pressure $\Delta P > \Delta P_c$, the applied force $f = \pi R_p^2 \Delta P$ is balanced by the contribution of surface tension f_γ, the friction with the pipette wall f_{friction} and the contribution of the drop bulk mechanical properties

A

B
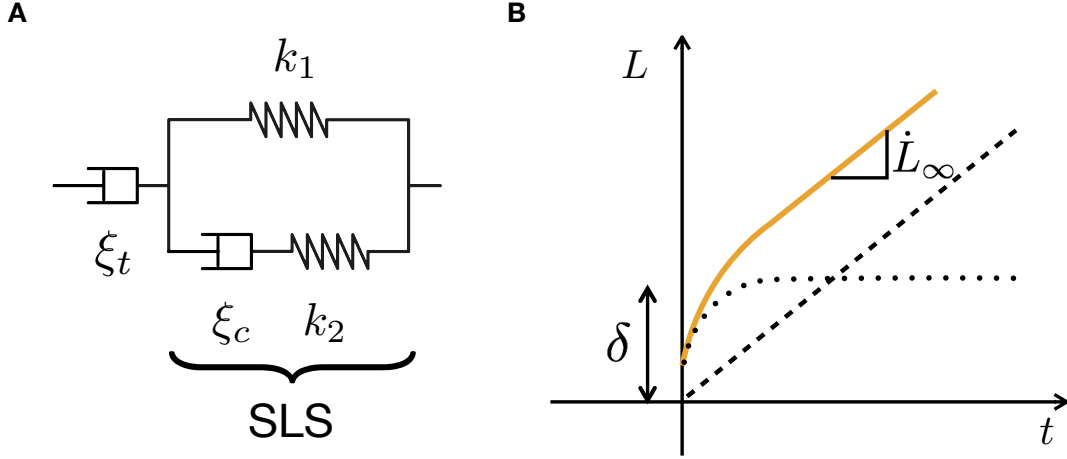
FIGURE 4.3 – The modified Standard Linear Solid model. **A**: Schematic of the modified Standard Linear Solid (SLS) model comprising a dashpot element in series with a SLS element. **B**: Schematic of the strain response of the modified SLS model (solid orange line) to a sudden stress: the sum of the response of the SLS element (dotted line) and the response of the dashpot element (dashed line).

f_{bulk}:

$$f = f_\gamma + f_{\text{friction}} + f_{\text{bulk}} \tag{4.10}$$

We consider here the case for which the friction is negligible (the condition of validity of this assumption will be discussed below). Then, we can write $f_{\text{bulk}} = 0$. In addition, if the drop is large compared to the pipette ($R_p \ll R_d$), the volume variation of the drop during aspiration is small and we can consider R_d constant during the aspiration, and thus ΔP_c (following relation 4.9) is constant too. Therefore, the contribution of tension is constant too, $f_\gamma = \pi R_p^2 \Delta P_c$, and:

$$f_{\text{bulk}} = f - f_\gamma = \pi R_p^2 \left(\Delta P - \Delta P_c \right) \tag{4.11}$$

f_{bulk} is the force applied only to the bulk properties. Depending on the nature of the studied sample, the expression of the force resisting f_{bulk} varies. For a purely viscous drop, the tongue flows at a constant rate $\dot{L}$, for a constant applied pressure. Using the expression 4.6, we have:

$$\pi R_p^2 \left(\Delta P - \Delta P_c \right) = 3\pi^2 \eta R_p \dot{L} \tag{4.12}$$

Therefore, viscosity can be quantified by measuring the critical pressure ΔP_c and the flow rate $\dot{L}$:

$$\eta = \frac{R_p \left(\Delta P - \Delta P_c \right)}{3\pi \dot{L}} \tag{4.13}$$

Biological tissues do not often exhibit rheological properties as simple as those of a viscous fluid. As we will show below, biological tissues studied in this thesis exhibit a viscoelastic response at short times and a purely viscous flow at long times, as described for chicken embryonic tissues (Forgacs et al., 1998) and cellular aggregates (Guevorkian et al., 2010, Stirbat et al., 2013b). Therefore, we consider here a modified version of the standard linear solid (SLS) model (see Figure 4.3 A). The SLS element is made of a spring in parallel of a Maxwell element, so it exhibits an instantaneous response and a saturation at long times. This is the behavior of a viscoelastic

solid which deformation arises after a typical time set by ξ_c, k_1 and k_2. Our modified SLS model has in addition a dashpot in series of the SLS element which leads to a purely viscous flow at long times set by ξ_t. We review here the theory presented by Guevorkian et al., 2010 to measure the mechanical properties of tissues exhibiting such viscoelastic properties at short times and a liquid behavior at long times.

The temporal evolution of the strain ϵ of such a rheological model is therefore the superposition of the SLS model one and the dashpot element one. As a result, the aspiration response $L(t)$ to an instantaneous step of force f_{bulk} is given by:

$$L(t) = \underbrace{\frac{f_{bulk}}{k_1}\left(1 - \frac{k_2}{k_1 + k_2}e^{-t/\tau}\right)}_{\text{SLS element}} + \underbrace{\frac{f_{bulk}}{\xi_t}t}_{\text{dashpot element}} \qquad (4.14)$$

where $\tau_c = \frac{\xi_c(k_1+k_2)}{k_1 k_2}$ and k_1, k_2, ξ_c, ξ_t are defined Figure 4.3 A. (see Appendix B.1 for the derivation of the SLS expression).

We rewrite this relation:

$$L(t) = \delta\left(1 - \beta e^{-t/\tau_c}\right) + \dot{L}_\infty t \qquad (4.15)$$

where we define:

- the amplitude of the short term elastic deformation $\delta = \frac{f_{\text{bulk}}}{k_1} = \frac{\pi R_p^2(\Delta P - \Delta P_c)}{k_1}$;

- the rate of the viscous flow at long times $\dot{L}_\infty = \frac{f_{\text{bulk}}}{\xi_t} = \frac{\pi R_p^2(\Delta P - \Delta P_c)}{\xi_t}$;

- a parameter controlling the amplitude of the instantaneous elasticity $\beta = \frac{k_2}{k_1+k_2}$. $\beta \in [0,1]$, if $\beta = 0$, the model is a Maxwell model with an instantaneous step followed by a viscous flow. If $\beta = 1$, $L(0) = 0$, there is no instantaneous jump, and the elastic response is purely viscoelastic.

We can relate these fitting parameters to the viscoelastic properties of the tissue by comparing them with the equations 4.2 and 4.6: $k_1 = \pi R_p E$ and $\xi_t = 3\pi^2 R_p \eta$. Thus, we can write that elasticity and viscosity depend on the fitting parameters δ and $\dot{L}_\infty$ through the following equations:

$$\begin{cases} E &= \frac{R_p(\Delta P - \Delta P_c)}{\delta} \\ \eta &= \frac{R_p(\Delta P - \Delta P_c)}{3\pi \dot{L}_\infty} \end{cases} \qquad (4.16)$$

Dynamics is controlled by two characteristic times: the raising time of the elastic deformation τ_c and the tissue relaxation time that defines the separation between the elastic and the viscous regimes: $\tau_t = \frac{\delta}{\dot{L}_\infty}$.

Assuming that the mechanical properties do not vary between the aspiration and the retraction, the relations 4.16 can be written in both situations: $E = \frac{R_p(\Delta P - \Delta P_c)}{\delta^a} = \frac{R_p(\Delta P - \Delta P_c)}{\delta^r}$ and $\eta = \frac{R_p(\Delta P - \Delta P_c)}{3\pi \dot{L}_\infty^a} = \frac{R_p(\Delta P - \Delta P_c)}{3\pi \dot{L}_\infty^r}$ where the superscript a and r respectively refer to the aspiration and retraction measurements. Thus, we can compute
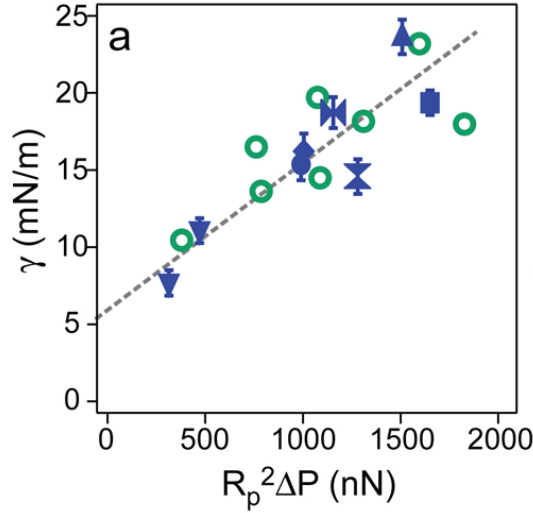
FIGURE 4.4 – Dependency of tension on the force of aspiration in cellular aggregates. Blue: calculated using relation 4.18. Green: calculated using the mean value of η and the measured value of $\dot{L}_\infty^a$ with relation 4.16. Adapted from Guevorkian et al., 2010

ΔP_c in two different ways:

$$\Delta P_c \quad = \quad \Delta P \frac{\delta^r}{\delta^r + \delta^a} \tag{4.17}$$

$$= \quad \Delta P \frac{\dot{L}_\infty^r}{\dot{L}_\infty^r + \dot{L}_\infty^a} \tag{4.18}$$

In this way, for each series of aspiration and retraction, we can measure ΔP_c, and consequently E and η. This value of ΔP_c can also be used to calculate the surface tension γ using the relation 4.9. However, it was shown that for cellular aggregates tension measured using relation 4.18 depended on the force of aspiration (Guevorkian et al., 2010). This can presumably be due to an active response of the tissue during the aspiration. This dependency on tension was linear and tension of the aggregate at rest could be estimated by extrapolation (see Figure 4.4). It was in the same range ($6\,\mathrm{mN \cdot m^{-1}}$) than tension measured by direct measurements of ΔP_c using its definition (the minimal pressure at which the tissue starts flowing). Therefore, if there is an active response during aspiration, as δ and $\dot{L}_\infty$ describe the response at short and long times respectively, relations 4.17 and 4.18 might give different results.

It is also possible to measure ΔP_c by varying the applied pressure ΔP between different aspirations, *only if ΔP_c is constant*, which implies that the surface tension, the pipette radius and the local curvature are constant too. Practically, this can be achieved with a series of successive aspirations of the same drop with the same pipette, at different pressures. In this situation, as shown on the schematic in Figure 4.5 A, plotting δ/R_p against ΔP yields a linear relation (following equation 4.16) which slope is $1/E$ and the intersect with the x-axis ΔP_c. However, if ΔP_c is not constant, this relation is not linear as shown in Figure 4.5 B. In this case, ΔP_c needs to be measured in order to perform a linear regression with respect to the bulk stress $\Delta P - \Delta P_c$ and calculate the mechanical parameters. As mentioned above, there might be an active response to the aspiration force. So in order to measure a constant ΔP_c with this method, only values of δ can be used as the active response might not affect the measurement at short times.
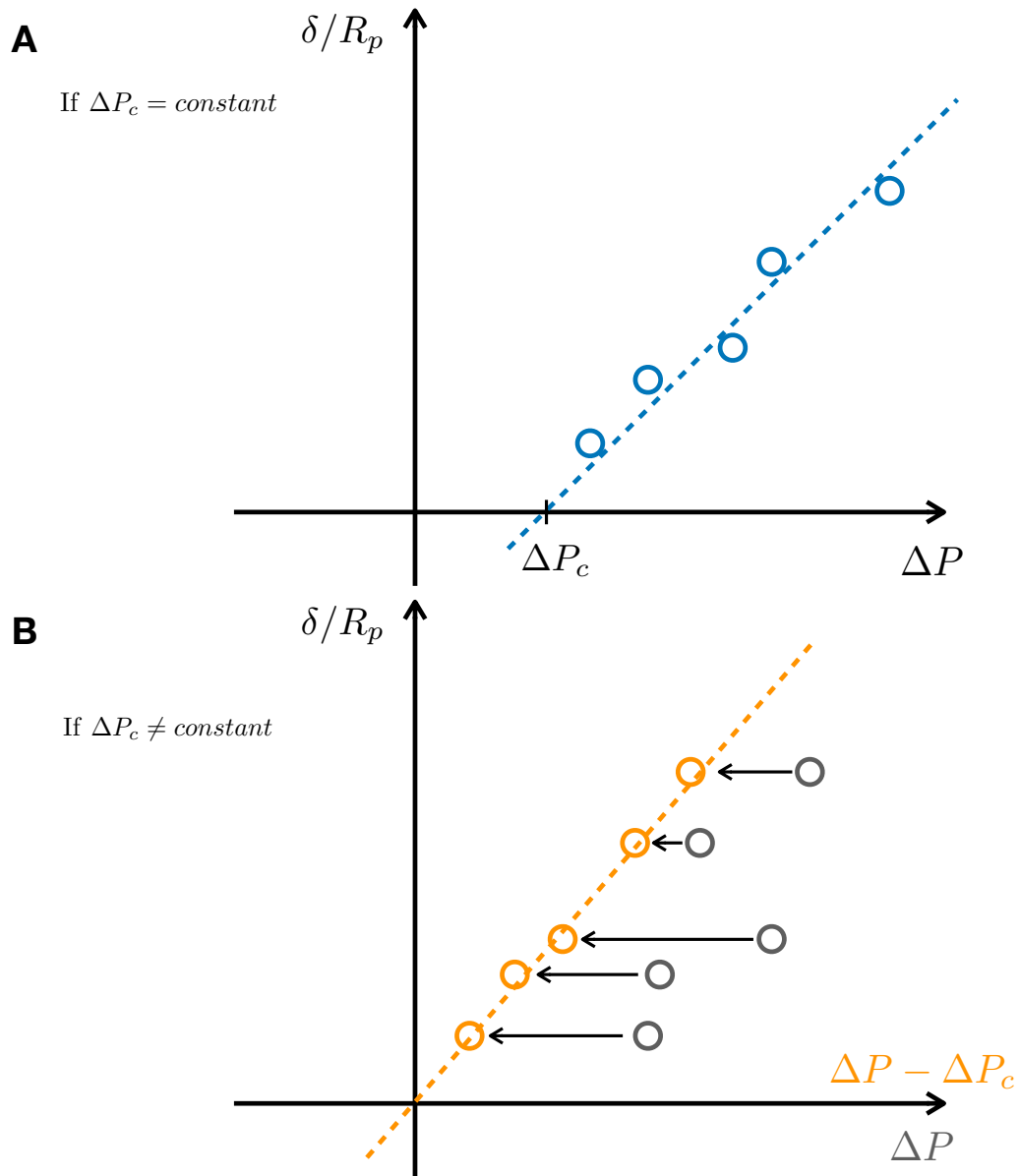
FIGURE 4.5 – Linear dependency of the fitting parameters δ and $\dot{L}_\infty$ with respect to the applied pressure ΔP. **A**: Schematic of the linear dependency of the fitting parameter on ΔP, if ΔP_c is constant. **B**: Schematic of the linear dependency of the fitting parameter on $\Delta P - \Delta P_c$ (orange points), if ΔP_c is not constant. There is no linear relation with ΔP (gray points).

4.1.2   Aspiration setup

We developed a microaspiration setup to measure mechanical properties in the order of a few hundreds of pascals of stiffness. Thereby, a sub-pascal precision offered by a pump-controlled pressure did not appear to be necessary. We chose a hydrostatic pressure-controlled setup instead. In detail, to control the pressure inside the pipette, the pipette is connected to a water reservoir, which can be vertically displaced to adjust the hydrostatic pressure difference ΔP. Indeed,

$$\Delta P = \rho g \Delta h \tag{4.19}$$

where ρ is the water density, $g \approx 9.81$ m $\cdot$ s^{-2} the gravitational constant and Δh the level difference between the reservoir and the medium. The water reservoir is manually displaced with a sub-millimeter precision. The reservoir displacement precision was estimated by measuring how precisely the reservoir could be moved close to a landmark pressure that can be precisely detected, the 0 Pa pressure difference. The zero can be adjusted by finely displacing the reservoir, by means of a precision screw, until the flow within the pipette is totally arrested, which can be monitored by visually tracking the movements of particles in suspension in the pipette. By aiming to slide the reservoir to the zero-position and then measuring the distance away from the actual zero-position, using the precision screw, we could estimate that the reservoir positioning was achieved with a typical 150 µm precision, which corresponds to a 1.5 Pa precision (since 1 mm of vertical displacement leads to 9.8 Pa pressure difference using the hydrostatic relation 4.19). The typical pressures used during the experiments presented in this thesis were in the range of several hundreds of pascals. Therefore, the experimental error on the pressure did not exceed 1%.

Pipettes were positioned under an inverted microscope (imaging from the bottom of the dish) by means of a tridimensional micromanipulator. Pipettes are borosilicate capillaries (1 mm/0.65 mm outer/inner diameter) pulled with a filament-based puller in order to control the diameter at the tip of the pipette. After being pulled, the capillary has an elongated conical shape, thus the diameter at the tip can be varied by manually severing its end at different distances. We prepared pipettes in this way with tip diameter ranging from 30 to 60 µm. Note that the conical shape is extremely elongated, so pipette walls can be considered to be parallel on the lengthscale of the deformation used in this thesis (a couple of pipette radii R_p). Pipettes are next bent using a flame, so we could bring them parallel to the bottom of the dish (see 4.1 A).

4.1.3   Calibration by means of a viscous standard

We calibrated our experimental setup using a commercial polybutene oil (high viscosity reference standard, Cannon) of viscosity $\eta_{ref} = 1.35$ kPa $\cdot$ s, and density $\rho \approx$ 880-920 kg $\cdot$ m^{-3}. Drops of oil were dispersed in pure water and aspirated into a pipette with diameter ranging from 40 to 60 µm (see Figure 4.6).

Friction measurement

We first investigated whether the friction was negligible. If we consider the friction contribution resisting the force of aspiration f, we can write:

$$f = 3\pi^2 \eta R_p \dot{L} + 2\pi k_f R_p L \dot{L} \tag{4.20}$$
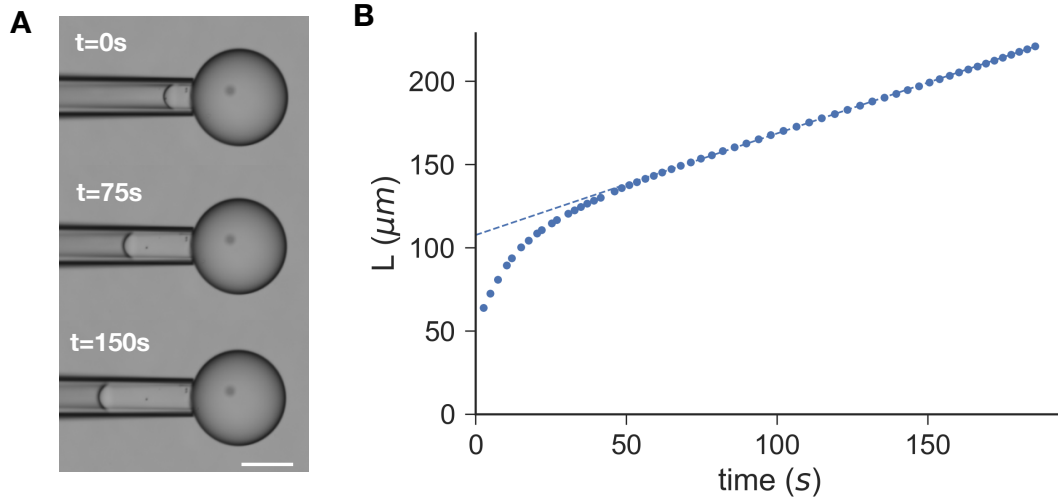
FIGURE 4.6 – Aspiration of an oil drop. **A**: Snapshots of an aspiration within a sodium hydroxide treated pipette at $\Delta P = 2.65$ kPa. Scale bar: 100 µm. **B**: Length L of the aspirated tongue over time.

where k_f is the wall friction coefficient.

A critical lengthscale can be defined as $L_c = 3\pi\eta/2k_f$ that sets the nature of the aspiration. At $L < L_c$, the dynamics is controlled by viscosity: $L(t) \sim t$ and at $L > L_c$, the dynamics is controlled by the wall friction: $L(t) \sim t^{1/2}$. Figure 4.7 A shows that $L(t) \sim t^{1/2}$ suggesting that the friction was not negligible. Therefore, we measured the friction coefficient k_f by monitoring the velocity v of a completely aspirated oil slug of length l (see Figure 4.7 B, C). By balancing the force of friction $2\pi R_p l k_f$ and the force of aspiration $\pi R_p^2 \Delta P$, we can write:

$$v = \frac{R_p}{2l k_f}\Delta P \tag{4.21}$$

By linear regression, we measured k_f and then calculated that $L_c \approx 3$ µm, confirming that the friction was not negligible. In order to enhance the hydrophilic properties of the glass, we treated the pipettes for 10 min by a 1 M sodium hydroxide (NaOH) solution following a protocol of oil capillary extraction (Piroird et al., 2011). In this case, the aspiration curve did not show a $t^{1/2}$ profile suggesting a weak friction (see Figure 4.6). Moreover, the advancing slug experiment could not be precisely carried out, as the slug was moving at a greater speed than the camera frame rate could capture even at very small pressures, which also suggests a very weak friction. While not precisely measured, the slug speed was estimated to be around 100 µm · s^{-1}. Therefore, $L_c \approx 300$ µm, while aspiration experiments never involved aspirated tongues longer than 150 µm. For this reason, friction was then considered negligible for NaOH treated pipettes.

Surface tension and viscosity measurements

For NaOH treated pipettes, several series of aspirations and retractions were carried out in order to measure the critical pressure ΔP_c using the relation 4.18 on the flow rates $\dot{L}_\infty^a$ and $\dot{L}_\infty^r$ (see Figure 4.8). Therefore, for each aspiration we can plot the flow rate with respect to $\Delta P - \Delta P_c$ and calculate tension using its definition 4.9. By linear regression, we measured viscosity to be 1.71 ± 0.05 kPa · s and tension was
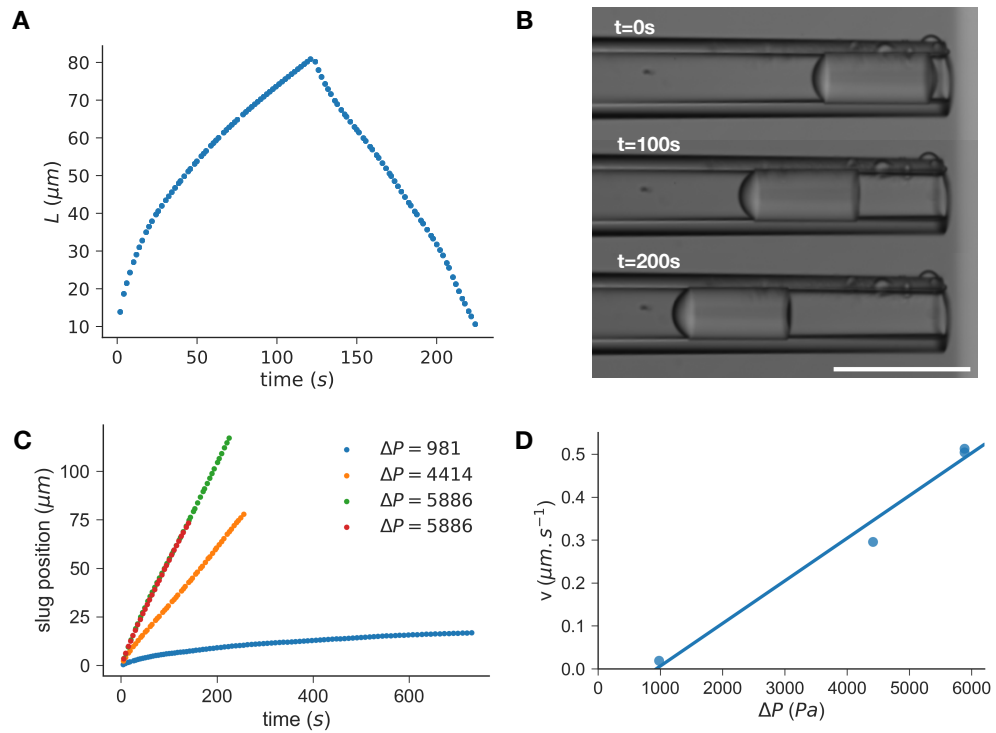
FIGURE 4.7 – Assessment of the friction coefficient. **A**: Dynamics of aspiration within an non-treated pipette. Note the typical $t^{1/2}$ aspiration curve and the acceleration at the end of the retraction suggesting a non-negligible friction. **B**: Snapshots of an advancing fully aspirated oil slug within non-treated pipette at $\Delta P = 5.89$ kPa. Scale bar: 100 μm. **C**: Slug position over time for different applied pressures. **D**: Slug velocity against the applied pressure.

calculated from the ΔP_c measurements: $40 \pm 5 \, \text{mN} \cdot \text{m}^{-1}$.

Surface tension of this oil in water has not been measured by another technique, as the classical pendant drop method was challenging to carry out in water. However, the surface tension of polybutene oils in air is typically in the range of 26-34 $\text{mN} \cdot \text{m}^{-1}$ (Rudnick, 2005). As surface tension of oils is higher in water than in air, the 40 $\text{mN} \cdot \text{m}^{-1}$ value seems reasonable.

The measured value of viscosity is higher than the reference value by 10.9%. The difference could be explained by a residual friction.

4.2 Mechanical properties of presomitic mesoderm explants

The first approach we used to measure the PSM mechanical properties by pipette aspiration was to aspirate freshly dissected PSM explants. Here, we present the results of two different protocols.

4.2.1 Experimental procedure

Micropipette preparation

In order to investigate tissular mechanical properties in the chicken embryo, we probed embryonic tissues on a scale larger than a couple of cells (PSM cell diameter $\sim$ 15 µm (Bénazéraf et al., 2017)). For this reason, the minimum diameter of the pipettes we used was 35 µm. When we aspirated PSM tissues, we had to face an upper limit as well, because PSMs are typically 60-80 µm thick. We, therefore, never used pipettes with a diameter larger than 55 µm.

Prior to aspiration, the pipette tip was gently heated over a filament to fire polish its sharp end which could damage cells. Pipettes were subsequently incubated in 0.3 mg/mL PolyEthyleneGlycol-PolyLysin (PEG-PLL) in HEPES solution (10 mM) for 1 hour, to reduce the adhesion of cells with glass. The very weak adhesion of the embryonic tissue to the pipette wall after coating with PEG-PLL was assessed in several ways. Firstly, the spherical geometry of explants left rounding on glass treated with PEG-PLL as presented in Chapter 3 suggests the adhesion is negligible. Secondly, the retraction of the tissue after aspiration into the pipette was systematically monitored to ensure dead cells left behind were not sticking to the glass. Lastly, the retraction dynamics of the tissue gives an indication about the importance of the friction: in cases where friction is not negligible, retraction curves is slow and exhibit a typical acceleration at the end of the retraction when $L < L_c$, as shown in the calibration experiment (Figure 4.7 A).

Sample preparation

As presented in section 3.2.1, PSM explants were dissected out by means of either pancreatin or collagenase. Full PSM were dissected out for the pancreatin dataset. The PSM orientation was visualized by staining the anterior with a dot of DiI. Regarding the collagenase dataset, only pieces of a maximum of one-third of PSM were dissected out. After dissection, explants were transferred to DMEM-F12 with 10% FBS at 37 °C. The pipette was introduced into the chamber. The air-medium interface was covered with a thin layer of mineral oil to prevent any evaporation. The pressure $\Delta P = 0$ was adjusted. One explant was brought into contact at the end of the pipette by applying a small pressure (typically $\Delta P = 40$ Pa). We ensured the pipette opening was fully closed by the explant by verifying that the flow was
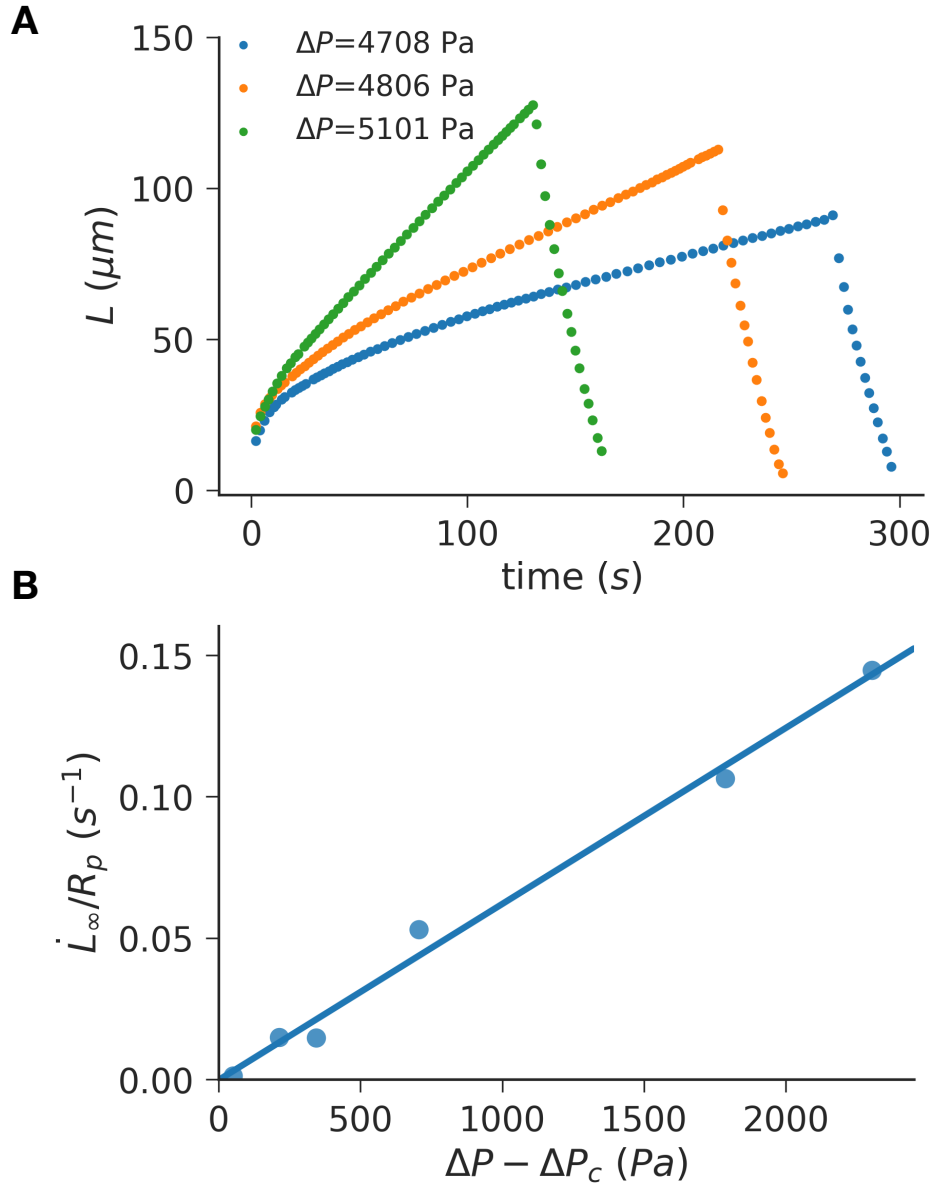
FIGURE 4.8 – Measurement of the oil standard viscosity. **A**: Aspiration and retraction curves of an oil drop at three different pressures. $R_p = 21$ μm. **B**: Linear regression of the scaled aspiration rate by the applied stress.
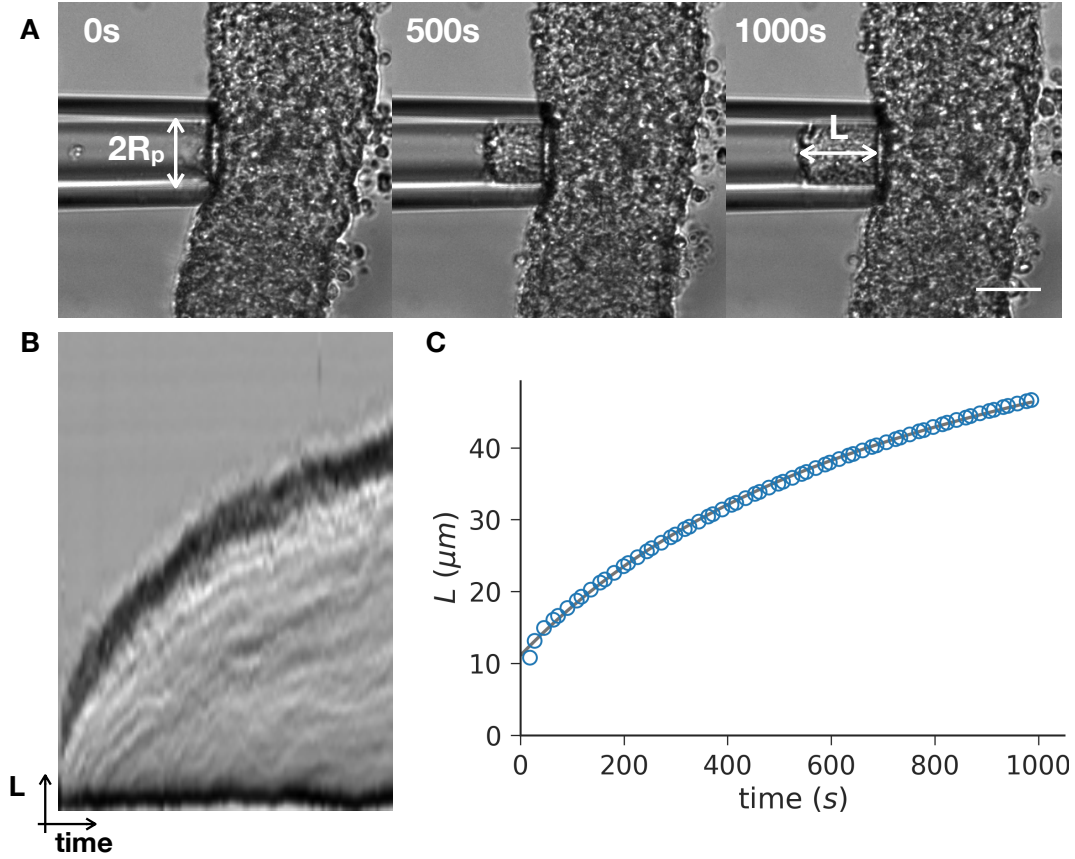
FIGURE 4.9 – Aspiration of a PSM explant. **A**: Series of snapshots of the movie of aspiration. Scale bar 50 μm. **B**: Kymograph along the horizontal direction within the pipette. **C**: Temporal evolution of the length of the aspirated tongue. Circle: tracked data points of the kymograph. Solid line: modified SLS fit.

arrested within the pipette. Next, we applied a step of pressure and recorded the aspiration with a frame interval of 2 s. All aspirations were carried out within two hours following dissection.

4.2.2 Analysis procedure

The profile of the advancing tongue was obtained by plotting a kymograph along a line within the pipette using the Fiji software (Schindelin et al., 2012). Figure 4.9 A, B shows an example of aspiration. In detail, the pixels along a horizontal line within the pipette are displayed vertically on the kymograph, the horizontal axis being the different frames. The end of the advancing tongue was manually traced on the kymograph. Each curve was fitted by means of a non-linear least-squared regression provided by the Python package LMFIT (Newville et al., 2014), which allows constraining the fitted parameters. β was bounded by 0 and 1 and its initial guess was 0.5, δ was set to be positive and its initial guess was R_p, $\dot{L}_\infty$ was set to be positive and its initial guess was $0.01 \; \mu\mathrm{m} \cdot \mathrm{s}^{-1}$, and τ_c was bounded by 0 and the last point of the aspiration and its initial guess was 50 s.

The quality of our analysis was evaluated by comparing the fitting parameters δ and $\dot{L}_\infty$ with a crude linear regression on the viscous part of the plot. In theory, the slope of the linear fit should yield $\dot{L}_\infty$ and the intercept with the y-axis should give

δ. While some experiments showed a good agreement between the two methods, a significant number of experiments were poorly fitted by the modified SLS model because they did not show a significant linear regime. To investigate this issue, we analyzed in detail the aspiration movies and noticed that the leading edge of the tongue was extremely active (see Movies 6, 7). PSM cells present a high protrusive activity, as shown by the wide black profile in Figure 4.9 B. As a result, the edge of the advancing tongue could be difficult to trace. As such, some aspirations had to be discarded, as the tissue lost its cohesiveness.

Furthermore, we noticed that it was difficult to define a linear regime for some aspirations (see Figure 4.10 A). In these cases, the fitted τ_c was large (comparable to the experimental time) and $\dot{L}_\infty$ tended towards 0. We also observed aspirations showing a viscous regime with two distinct linear slopes (see Figure 4.10 B). In these cases, the fitted procedure was inconsistent (sometimes fitting the first slope, sometimes fitting the second slope). We were not able to relate these different behaviors with any specific conditions (region of aspiration, time after dissection, etc.). Nevertheless, these poorly fitted dynamics did not exceed a third of our aspirations (see Figure 4.10 C). For this reason, we decided to discard the "curved" and "two slopes" aspirations. In the rest of this chapter, only aspirations well fitted by the modified SLS model are analyzed.

4.2.3   Measurement of apparent properties

In order to measure the mechanical properties of the PSM along the AP axis, a series of aspirations in three different regions of the same PSM was carried out. We defined these regions as we did in chapter 3: anterior PSM, medial PSM and posterior PSM. As the typical critical pressure ΔP_c for pipette diameters ranging from 30 μm to 50 μm was around 200 Pa, the applied pressure ΔP varied between 250 Pa and 600 Pa. The same step of pressure was successively applied to the three regions in a random order. A representative example is shown Figure 4.11, for which the fitted parameters δ and $\dot{L}_\infty$ exhibit a graded profile along the axis, whereas τ_c and β do not show any particular profile.

In order to calculate elasticity and viscosity from these fitted parameters, relations 4.16 must be verified. To do so, as shown in Figure 4.5, a solution is to keep ΔP_c constant and vary ΔP. This requires to keep constant the pipette radius R_p, the tension γ and the local curvature κ_d. R_p can easily be controlled. However, we cannot assume that surface tension is constant in all explants and we noticed that the local curvature varied between different explants. Therefore the only solution to keep all these parameters constant is to carry out a series of successive aspirations of the same explant. However, each aspiration leads to an extensive rearrangement of the tissue, so it would be a very strong and unrealistic assumption to consider that aspirations will not alter the mechanical properties of the tissue. In addition, it has been previously shown that aspirations could lead to an active response of the tissue (Guevorkian et al., 2010, Guevorkian et al., 2011). Consequently, in order to verify relations 4.16 and thus calculate elasticity and viscosity, ΔP_c must be measured for each aspiration.

Before measuring ΔP_c, we first assumed that in the range of pressure we used, the linearity of relations 4.16 was verified. In this way, we could normalize the fitted parameters by the pressure to calculate apparent mechanical properties (without
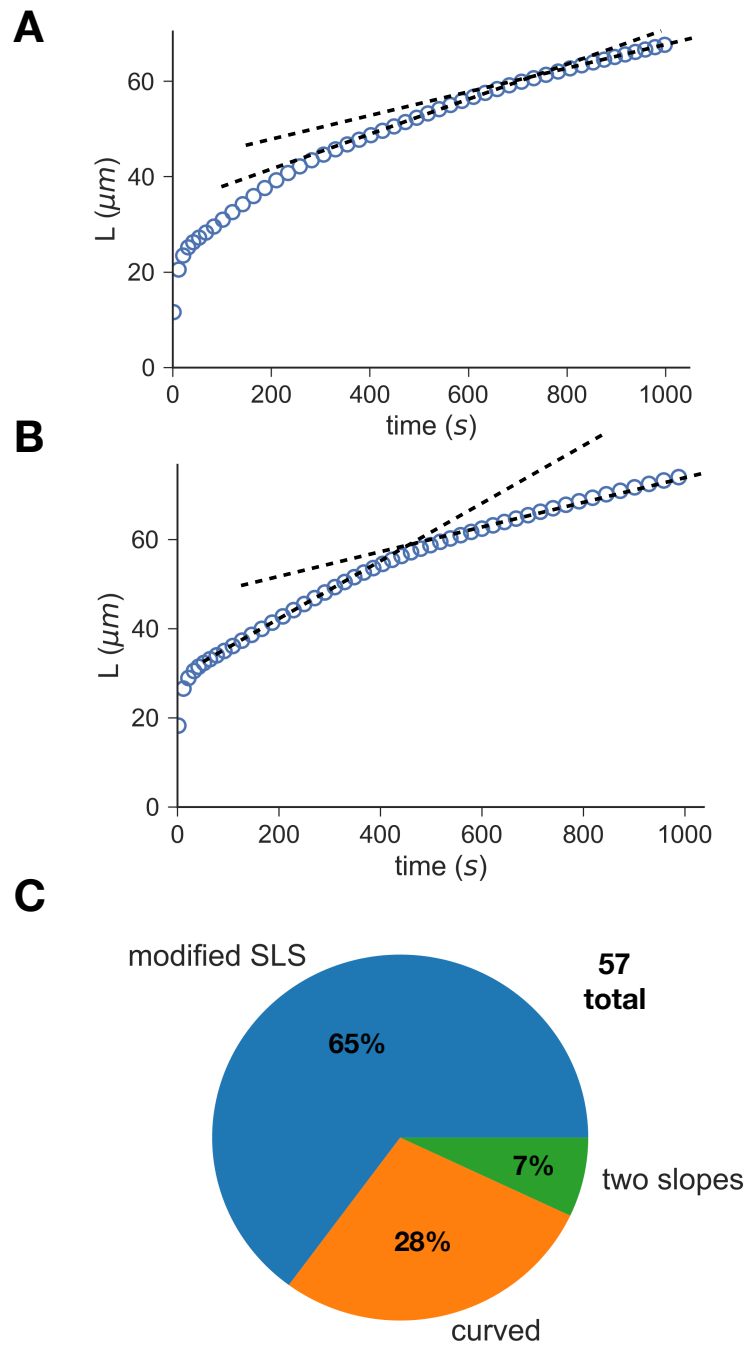
FIGURE 4.10 – Various kinds of aspiration curves. **A**: "Curved" shape aspiration for a posterior explant with $\Delta P = 588$ Pa. **B**: "Two slopes" shape aspiration for a posterior explant with $\Delta P = 588$ Pa. The dashed lines show the tangents to the curve at different times. **C**: Statistics of the different kinds of curve shapes.
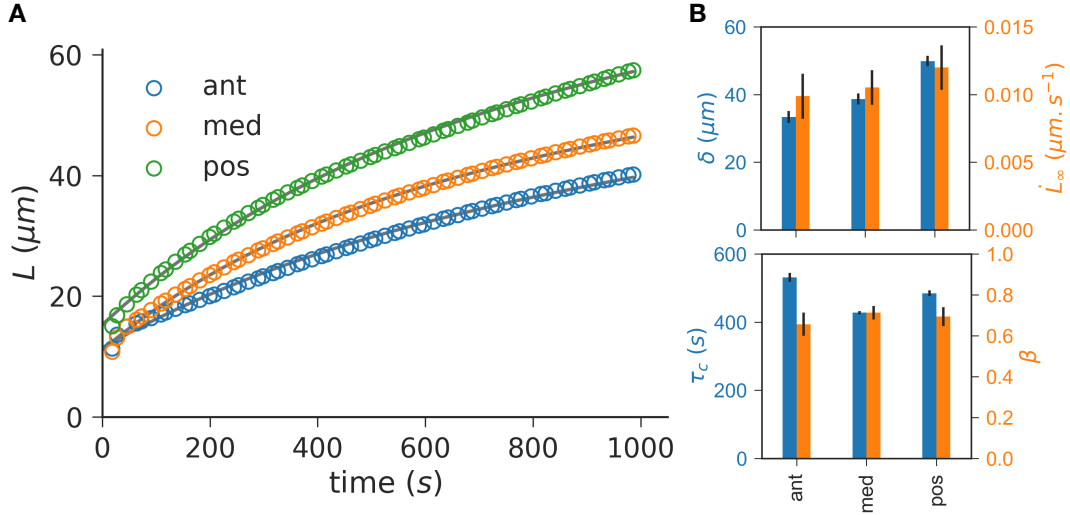
FIGURE 4.11 – Example of a series of aspirations on a PSM along the anteroposterior axis. **A**: Aspiration curves for $\Delta P = 294$ Pa and $R_p = 18.6$ µm. Circle: tracked data points of the kymograph. Solid line: modified SLS fit. (ant: anterior, med: medial, pos: posterior). **B**: Fitted parameters for each curve.

TABLE 4.1 – Apparent mechanical properties of pancreatin dissected explants (mean and standard deviation).

	Anterior	**Medial**	**Posterior**
E_{app} (Pa)	280 ± 102	243 ± 150	201 ± 96
η_{app} (kPa · s)	44.4 ± 16.3	47.6 ± 29.6	41.6 ± 17.2
τ_c (s)	251 ± 205	263 ± 156	263 ± 275
τ_t (s)	1740 ± 1153	2536 ± 1656	2379 ± 1599

removing the effect of surface tension). We define two apparent properties respectively homogeneous to an elasticity and to a viscosity:

$$\begin{cases} E_{app} & = \dfrac{R_p \Delta P}{\delta} \\ \eta_{app} & = \dfrac{R_p \Delta P}{3\pi \dot{L}_\infty} \end{cases} \tag{4.22}$$

We calculated these properties independently for our two dissection methods collagenase and pancreatin (see Figure 4.12 and Tables 4.1, 4.2). For both datasets, apparent elasticity is fairly constant along the axis. There is a slight anteroposterior gradient for the pancreatin dataset, but it is not significant (Student's t-test between anterior and posterior regions: $p = 0.23$). However, there is a significant gradient of apparent viscosity for the collagenase dataset (Student's t-test between anterior and posterior regions: $p = 0.04$). The two characteristic times τ_c and τ_t exhibit flat profiles along the axis as well. We noticed a more striking difference between absolute values of the two datasets. Explants from the pancreatin dataset are on average softer and more viscous. This difference is especially significant in the posterior region (Student's t-test for E_{app}: $p = 0.007$, and for η_{app}: $p = 0.019$).

A part of the data dispersion might come from the non-constant contribution

TABLE 4.2 – Apparent mechanical properties of collagenase dissected explants (mean and standard deviation).

	Anterior	**Medial**	**Posterior**
E_{app} (Pa)	329 ± 54	339 ± 123	313 ± 89
η_{app}(kPa $\cdot$ s)	36.9 ± 11.7	35.5 ± 8.3	27.1 ± 8.6
τ_c (s)	133 ± 84	162 ± 102	143 ± 42
τ_t (s)	1096 ± 414	1105 ± 404	869 ± 344
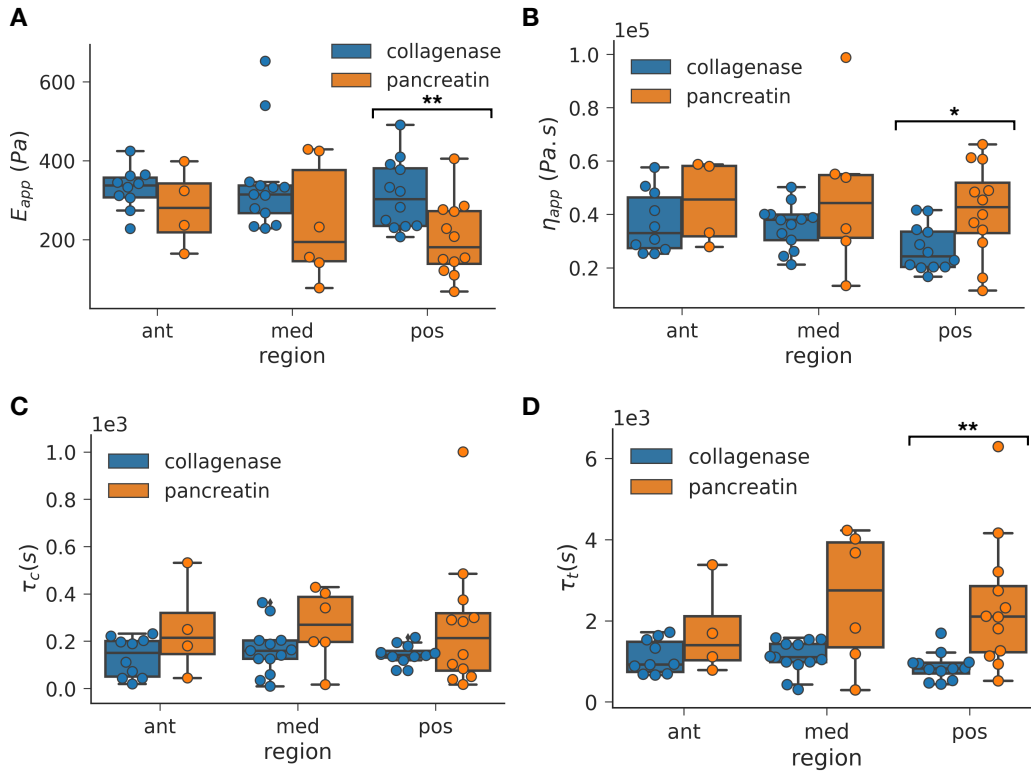
FIGURE 4.12 – Apparent mechanical properties along the anteroposterior axis for the pancreatin and collagenase datasets. **A**: Apparent elasticity. **B**: Apparent viscosity. **C**: Elastic regime typical time. **D**: Tissue relaxation time. Anterior explant (ant), medial explant (med), posterior explant (pos). Student's t-test p-value p: $\star$: $p < 0.05$, $\star\star$: $p < 0.01$.

of tension to the apparent properties. Another part might be due to an important inter-embryonic variability which has often been reported in measurements of embryonic mechanical properties (Von Dassow and Davidson, 2009). To investigate the dispersion in inter-embryonic data, we plotted the mechanical properties for individual PSMs. We present pairwise measurements for each PSM for which we had exploitable measurements both in anterior and posterior regions (see Figure 4.13 A, B). In this way, we could show that absolute values are variable between embryos but there is a consistent profile in individual embryos. We noticed that the PSM was almost always stiffer (n=8/10) and more viscous (n=9/10) in anterior than posterior for both datasets. Thereby, the anterior region is on average 30% stiffer and 85% more viscous than the posterior within the same embryo. Figure 4.13 C presents differences between the anterior and posterior properties normalized by the posterior value. We define $\Delta_{AP}E_{app} = \frac{E_{app}^{ant} - E_{app}^{pos}}{E_{app}^{pos}}$, where E_{app}^{ant} and E_{app}^{pos} are E_{app} respectively in anterior and posterior regions. Similarly, $\Delta_{AP}\eta_{app} = \frac{\eta_{app}^{ant} - \eta_{app}^{pos}}{\eta_{app}^{pos}}$.

4.2.4 Tension measurement

Explant curvature measurement

We then decided to measure surface tension to calculate bulk properties. As presented before the tension γ is related to ΔP_c, the pipette radius R_p and the local curvature κ_d. The latter can be rewritten $\kappa_d = \frac{2}{R_d}$ in the case of a spherical drop of radius R_d (relation 4.9). However, our PSM explants did not have a spherical geometry. Before dissection, PSMs have a cylinder shape in anterior which flattens towards the posterior region. After dissection, the posterior region rapidly rounds up, as shown in chapter 3. After a few dozens of minutes in culture, full PSM explants adopt a pear shape, with a thicker posterior region. Thus, the explants present two curvatures: an in-plane curvature and an out-of-plane curvature. The in-plane (horizontal plane) curvature can be measured by regular transmitted microscopy. The out-of-plane curvature can be measured by an orthogonal section along the vertical axis (see Figure 4.14). Regarding smaller explants, as they round up faster than a full PSM, they quickly adopt a shape with a larger in-plane curvature than the full PSMs. As a result, we can rewrite 4.9 taking into account the explant geometry:

$$\gamma = \frac{\Delta P_c}{\frac{2}{R_p} - \kappa_d} = \frac{\Delta P_c}{\frac{2}{R_p} - \left(\frac{1}{R_{in}} + \frac{1}{R_{out}} \right)} \tag{4.23}$$

where R_{in} and R_{out} are respectively the in-plane and out-of-plane radii of curvature. Note that relation 4.23 is a generalization of relation 4.9, as for a sphere $R_{in} = R_{out} = R_d$. For a true cylinder of radius R_c, $R_{in} = \infty$ and $R_{out} = R_c$, hence $\gamma = \frac{\Delta P_c}{\frac{2}{R_p} - \frac{1}{R_c}}$.

Practically, R_{in} could be measured for each aspiration by manually fitting an arc of circle along the explant spot of aspiration. However, R_{out} was not easily accessible. Thereby, we used average values of R_{out} that we measured by confocal microscopy:

$$\begin{cases} R_{out} &= 50 \text{ µm for anterior explants} \\ R_{out} &= 55 \text{ µm for medial explants} \\ R_{out} &= 60 \text{ µm for posterior explants} \end{cases} \tag{4.24}$$

As $R_p \sim 20$ µm, the local curvature is not negligible. Even for a true cylinder, not taking into account the out-of-plane curvature would underestimate tension by 20% (for $R_{out} \sim 50$ µm).
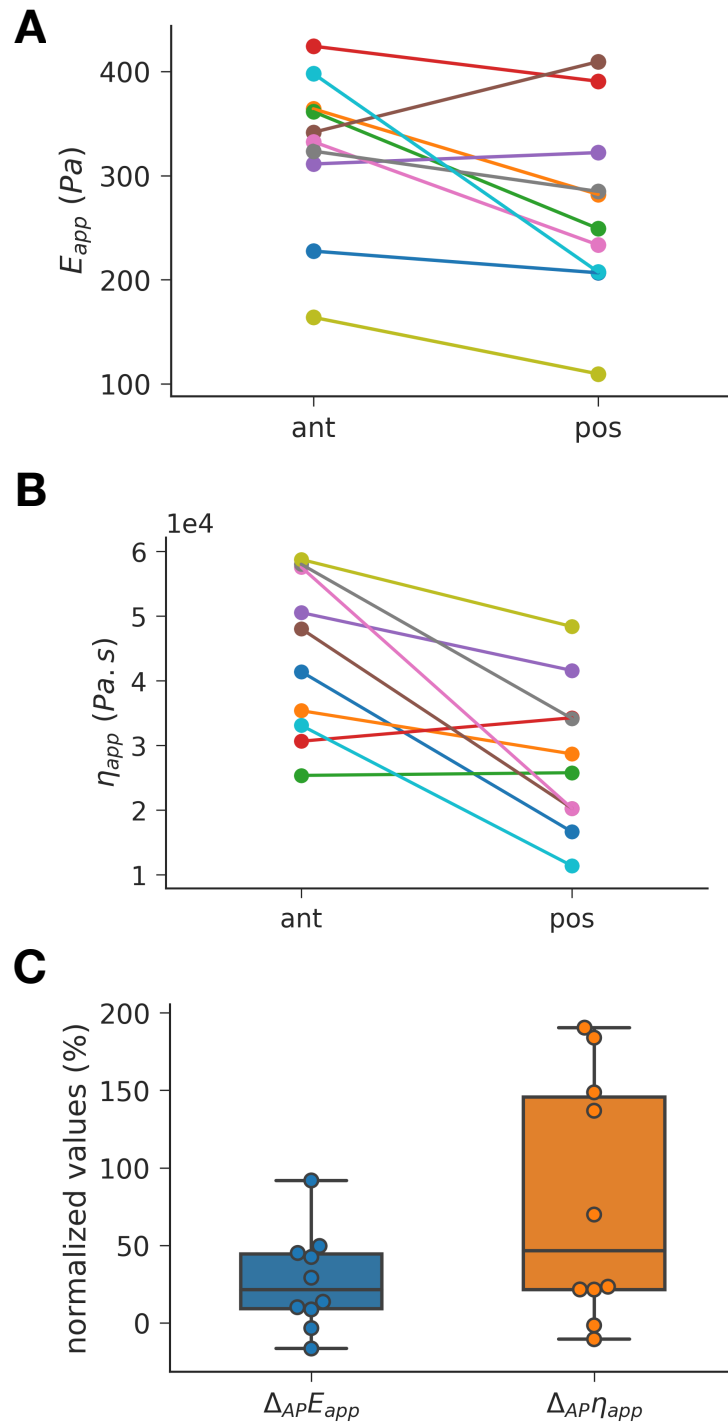
FIGURE 4.13 – Apparent mechanical properties gradient. Apparent elasticity (**A**) and apparent viscosity (**B**) pair measurements within the same PSM, for both collagenase and pancreatin dissected explants. Each color represents one PSM (same color code between panels **A** and **B**). **C**: Pairwise difference (anterior property - posterior property) scaled by the posterior property.
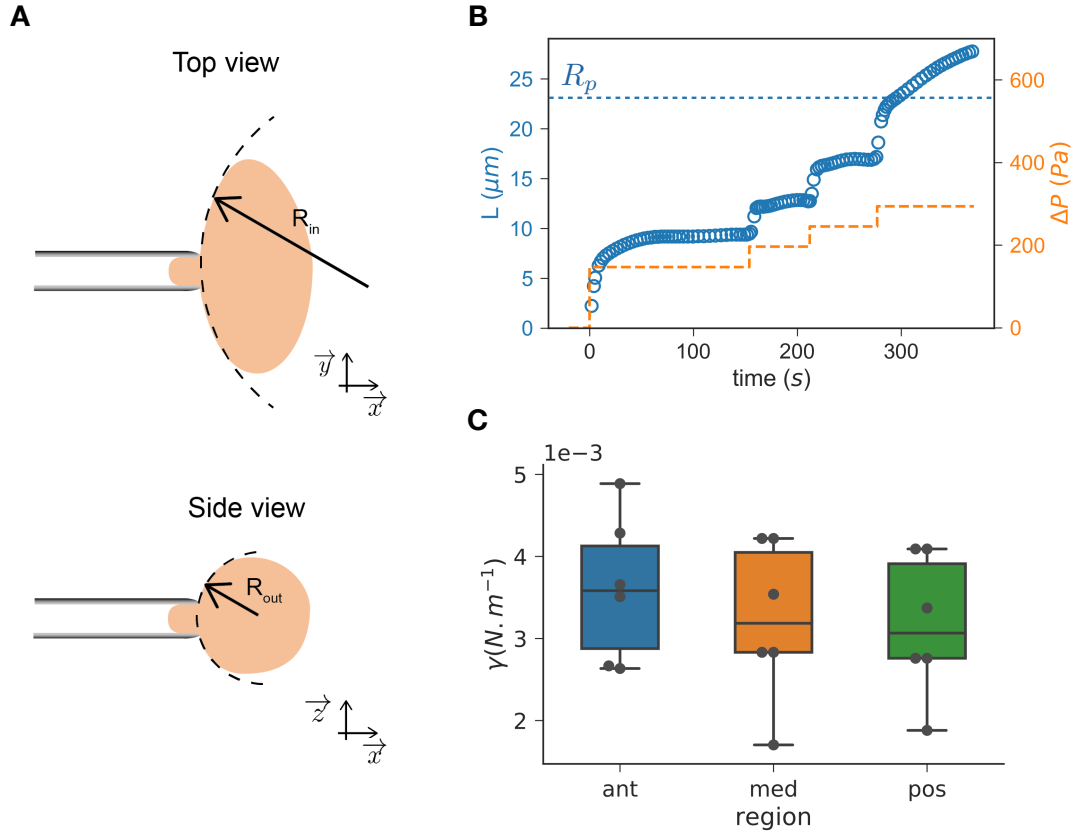
FIGURE 4.14 – Surface tension measurement. **A**: Schematic of the local explant curvature. R_{in}: radius of the in-plane curvature, R_{out}: radius of the out-of-plane curvature. $\vec{x}$ and $\vec{y}$ define the microscope horizontal plane and $\vec{z}$ defines the vertical direction. **B**: Direct measurement of ΔP_c by 50 Pa incremental steps of pressure. Note the tissue starts flowing when $L \geq R_p$ ($R_p = 23$ μm). **C**: Surface tension measured by the direct method on collagenase dissected explants.

Direct measurement of the critical pressure

As introduced above (see section 4.1.1), the critical pressure ΔP_c can be measured in three different ways:

- a direct measurement based on its definition: ΔP_c is the pressure at which the aspirated material starts flowing into the pipette as soon as the radius of curvature in the pipette is larger than R_p;

- a calculation based on fitted parameters of an aspiration and a successive retraction (see relations 4.17 and 4.18);

- a linear regression of the fitted parameters with respect to the applied pressure, *only if* ΔP_c can be assumed to be constant (see Figure 4.5).

Unfortunately, the latter method is challenging, as we cannot *a priori* assume surface tension to be constant during successive aspirations, nor can we prepare explants with the exact same local curvature. For these reasons, we only used the first two methods.

To carry out the direct measurement method, we applied successive steps of pressure on collagenase dissected explants (see Figure 4.14 B). For each step, we monitored the advancement of the tongue during 100-200 s to make sure its length was saturating at $L < R_p$, as the viscoelastic time τ_c ranges from 30 to 200 s. Then, we measured the pressure when the tongue started to flow and L is slightly larger than R_p. With the measured ΔP_c value, we could calculate the corresponding surface tension γ using formula 4.23. We saw that anterior explants exhibited a slightly higher surface tension (3.6 ± 0.9 mN $\cdot$ m^{-1}) than the medial and posterior explants (respectively 3.2 ± 1.0 mN $\cdot$ m^{-1} and 3.2 ± 0.9 mN $\cdot$ m^{-1}). However, the difference was not statistically significant (p-value of the Student's t-test between anterior and posterior regions: 0.39).

The direct measurement method is a relatively straightforward way of measuring ΔP_c, even though it is not very precise. ΔP_c precision is limited by the incremental steps (50 Pa). It corresponds to roughly a 0.5 mN $\cdot$ m^{-1} precision for our orders of magnitude of R_p and κ_d. Moreover, distinguishing a saturating tongue from a weakly flowing one was not always clear. A more important problem was that this measurement could not be coupled with a subsequent measurement of bulk properties. The explant having been already aspirated, we considered that its mechanical properties could have been altered by the surface tension measurement.

Fitted parameters-based calculation of the critical pressure

In theory, the fitted parameters-based calculation can lead to a more precise value of ΔP_c, as a continuous range of pressure can be calculated. Conversely, the direct method only yields a discrete range of pressure (in practice by steps of 50 Pa). In addition, the fitted parameters-based calculation offers the possibility of measuring ΔP_c and the bulk properties at the same time. Unfortunately, we experienced some difficulties with the retraction experiments.

Firstly, we noticed that after aspirations of full PSMs, explants were very often falling to the bottom of the dish as soon as the pressure was set back to zero. As a result, the aspirated tongue was pulled out of the pipette at a much higher rate than it would be with the sole contribution of surface tension. Secondly, as the PSM is a mesenchymal tissue, an important cell-cell rearrangement often happened during the aspiration, which led to a less coherent tongue during the retraction. Therefore
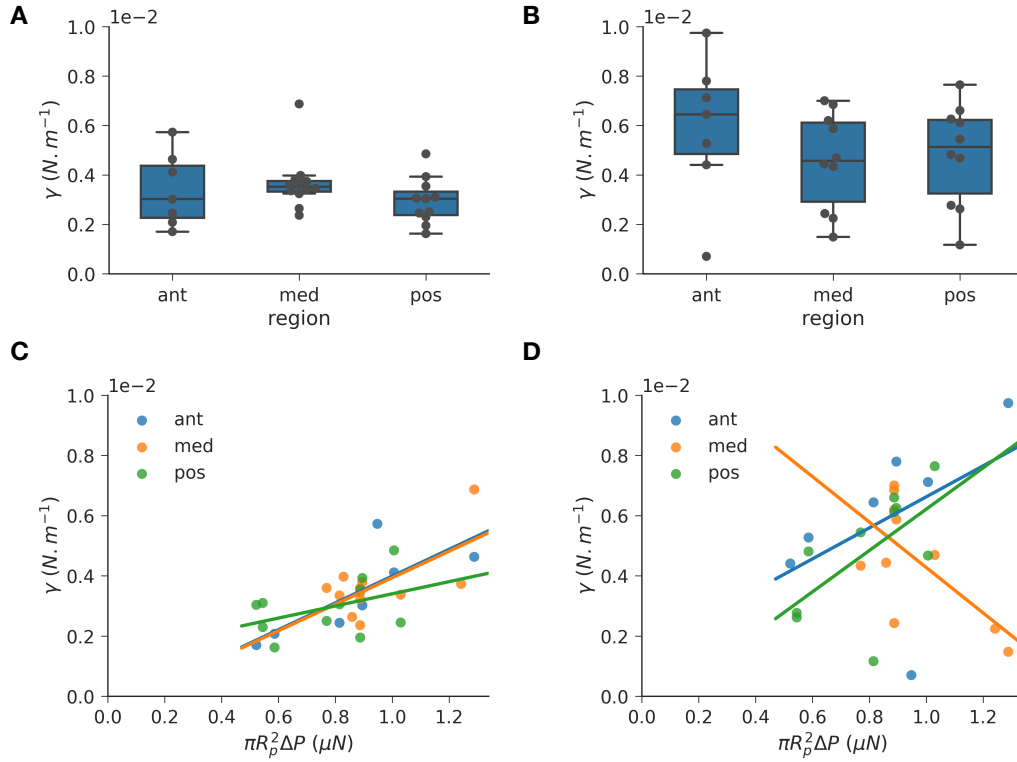
FIGURE 4.15 – Fitted parameters-based calculation of surface tension. Tension along the AP axis (**A**, **B**). Tension with respect to the aspiration force for the collagenase dataset only (**C**, **D**). **A**, **C**: δ-method. **B**, **D**: $\dot{L}_\infty$-method.

tracking the tongue edge was even less precise during the retraction. For these reasons, no aspiration from the full PSM explant dataset (also the pancreatin dataset) was exploitable. Only a limited subset of the smaller explant dataset (also the collagenase dataset) showed exploitable retractions.

Regarding the exploitable retractions, ΔP_c can be computed by two distinct formula: 4.17 (referred to as the δ-method) and 4.18 (referred to as the $\dot{L}_\infty$-method). Figure 4.15 and Table 4.3 show that the δ-method gives similar values as the direct method, despite a wider dispersion. The $\dot{L}_\infty$-method yields even more noisy results with higher absolute values. This might come from the fact that the flow was accelerated by the explant partially falling off the pipette. In particular, the anterior tension seems higher than the medial and posterior ones (even though there is no statically significant difference).

As reported for cellular explants, we observed a linear dependency of surface tension measured by the δ-method and $\dot{L}_\infty$-method on the aspiration force (see Figures 4.15 C, D). However, we did not consider the linear correlation reliable enough to estimate by extrapolation the tension value at rest. Indeed, the best correlation coefficient for the anterior region with the δ-method is $R^2 = 0.61$. The correlation confidence is even lower for the $\dot{L}_\infty$-method, showing again the great dispersion of the data. As a result, we do not use data from $\dot{L}_\infty$-method in the rest of this thesis.

TABLE 4.3 – Collagenase dissected explants surface tension along the anteroposterior axis (mean and standard deviation).

	Anterior	Medial	Posterior
direct method (mN $\cdot$ m^{-1})	3.6 ± 0.9	3.2 ± 1.0	3.2 ± 0.9
δ-method (mN $\cdot$ m^{-1})	3.4 ± 1.5	3.7 ± 1.1	2.9 ± 0.9
$\dot{L}_\infty$-method (mN $\cdot$ m^{-1})	5.9 ± 2.9	3.8 ± 2.5	4.4 ± 2.4

TABLE 4.4 – Collagenase dissected explants elasticity (mean and standard deviation).

	Anterior	Medial	Posterior
using $\langle \gamma_0 \rangle$ (Pa)	204.0 ± 47.5	219.0 ± 73.6	184.6 ± 57.9
δ-method (Pa)	193.2 ± 55.5	202.5 ± 69.3	189.0 ± 38.4

4.2.5 Measurement of Young's modulus and viscosity

We next used the measured values of ΔP_c to compute the bulk mechanical properties E and η, by two methods: *(i)* from average values of surface tension, *(ii)* from the fitted parameters-based calculation method.

(i) For each explant, we calculated ΔP_c from the average value of the measured tensions with the direct method $\langle \gamma_0 \rangle$. We then calculated E and η for each explant as shown in Figure 4.16 A, C and Tables 4.4, 4.5, 4.6.
This calculation suffered from an important limitation. $\langle \gamma_0 \rangle$ corresponds to the surface tension at rest. But surface tension seems to depend on the applied pressure (see Figure 4.15 C, D). As a result, the tension contribution might be underestimated, especially for greater aspiration pressures. One solution would be to use the linear relations between γ and the force of aspiration showed in Figure 4.15 C, D, in order to calculate the apparent surface tension for each aspiration. However, as the linear regression errors were not negligible, we did not choose this solution. Therefore, this method might underestimate ΔP_c and so overestimate E and η.

(ii) We also directly calculated E and η with the ΔP_c measured with the δ-method (see Figure 4.16 B, D and Tables 4.4, 4.5). In theory, this method should be more precise than using average values of tension, as it uses the apparent value of ΔP_c for each explant. However, as it was shown above, this method has its own sources of imprecision and only a limited subset of aspirations could be used.

We could apply the direct method using the same value $\langle \gamma_0 \rangle$ to both the pancreatin and the collagenase dataset. However, the δ-method could be used only on the collagenase dataset, as we did not have any exploitable retraction for the pancreatin dataset.
Regarding the collagenase dataset, the direct method and the δ-method yield similar orders of magnitude of surface tension. In consequence, elasticity and viscosity

TABLE 4.5 – Collagenase dissected explants viscosity (mean and standard deviation).

	Anterior	Medial	Posterior
using $\langle \gamma_0 \rangle$ (kPa $\cdot$ s)	22.6 ± 7.3	23.1 ± 5.6	16.3 ± 6.6
δ-method (kPa $\cdot$ s)	23.1 ± 9.0	21.3 ± 5.7	16.9 ± 7.1

TABLE 4.6 – Pancreatin dissected explants bulk properties using $\langle \gamma_0 \rangle$ values (mean and standard deviation).

	Anterior	Medial	Posterior
E (Pa)	64.1 ± 62.3	66.4 ± 90.4	59.6 ± 50.7
η (kPa $\cdot$ s)	10.9 ± 11.6	11.3 ± 9.4	10.4 ± 9.4

data are also similar. Elasticity exhibits a flat pattern along the axis with an order of magnitude of 200 Pa. On the contrary, as observed for apparent viscosity, viscosity shows a significant gradient (Student's t-test between anterior and posterior: $p = 0.04$) with an order of magnitude 16 kPa $\cdot$ s (in posterior) and 23 kPa $\cdot$ s (in anterior).

We next compared the two datasets. The orders of magnitude of both elasticity and viscosity are lower for pancreatin dissected explants (significantly regarding elasticity). We previously showed that apparent elasticity was slightly lower for pancreatin dissected explants but apparent viscosity was slightly *higher*. The fact that the difference between apparent and bulk properties is higher for the pancreatin dataset suggests that bulk properties' contribution to apparent properties is lower in pancreatin dissected explants. However, this result potentially reveals an experimental artifact as surface tension was measured only with collagenase dissected explants.

To further assess the reliability of the measured properties, we investigated the linearity of the scaled fitted parameters δ / R_p and $\dot{L}_\infty / R_p$ with respect to the applied stress $\Delta P - \Delta P_c$. As presented in Figure 4.5, this relation should be linear and have a zero y-intercept. Some regions seem to show a linear correlation with y-intercept close to zero. Even though the linearity seems to be verified in some cases, the data show an important inter-embryo dispersion that prevents us from systematically verifying the linearity of relations 4.16 (see Figure 4.17).

As for the apparent mechanical properties, we plotted the PSM individual properties to remove inter-embryonic variability. We noticed the same anteroposterior gradient. Individual PSMs are stiffer in anterior than posterior by $16 \pm 27\%$ (using $\langle \gamma_0 \rangle$ values) and by $20 \pm 17\%$ (δ-method), and more viscous in anterior than posterior by $70 \pm 80\%$ (using $\langle \gamma_0 \rangle$ values) and by $94 \pm 106\%$ (δ-method) (see Figure 4.18).

4.2.6 Measurement of the mechanical properties of blebbistatin-treated explants

We also studied the effect of blebbistatin on the mechanical properties of the PSM. As it is an inhibitor of the actomyosin network contractility, we expected to notice a non-negligible effect on the mechanical properties. To do so, explants were
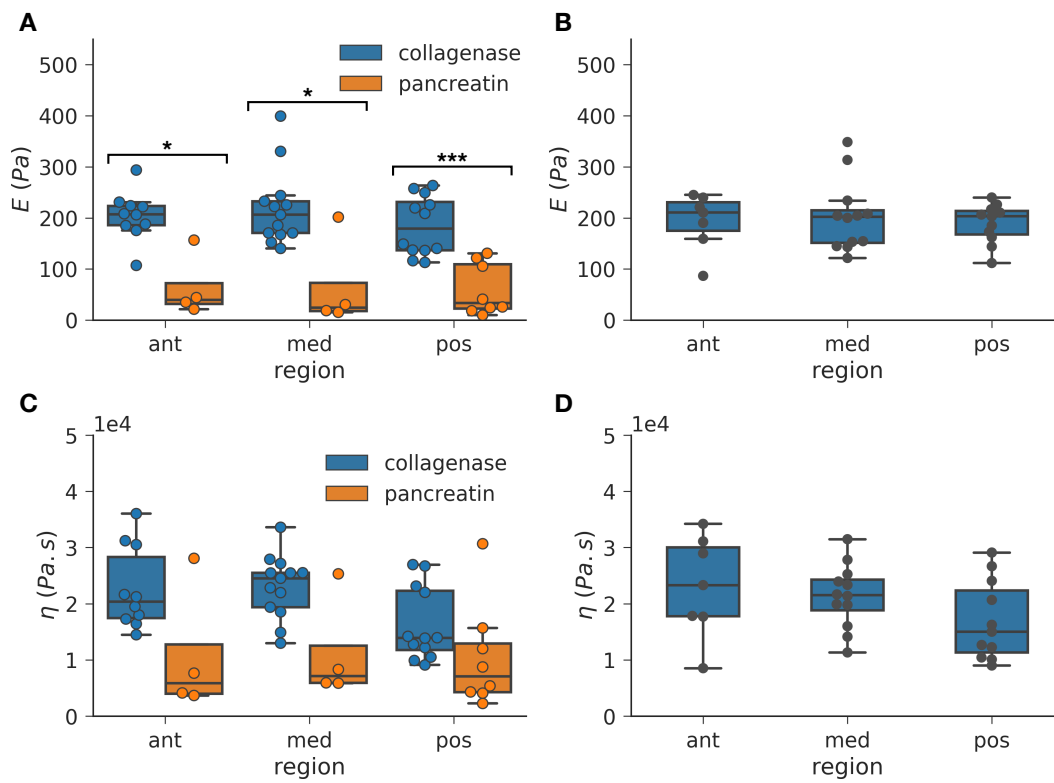
FIGURE 4.16 – Bulk elasticity (**A**, **B**) and viscosity (**C**, **D**) along the anteroposterior axis. Bulk properties calculated using: $\langle \gamma_0 \rangle$ (**A**, **C**), the δ-method (**B**, **D**). Student's t-test p-value p: $\star$: $p < 0.05$, $\star\star\star$: $p < 10^{-4}$.
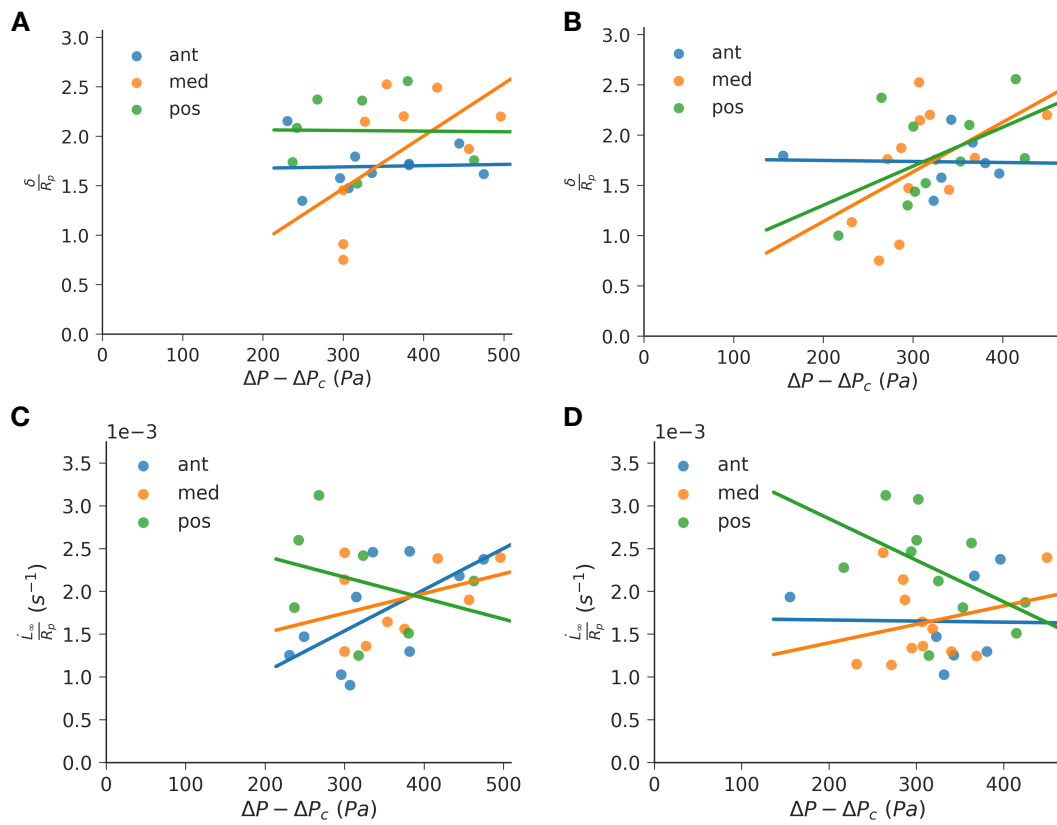
FIGURE 4.17 – Bulk elasticity (**A**, **B**) and viscosity (**C**, **D**) with respect to the applied stress for the collagenase dataset. Bulk properties calculated using: $\langle \gamma_0 \rangle$ (**A**, **C**), the δ-method (**B**, **D**).
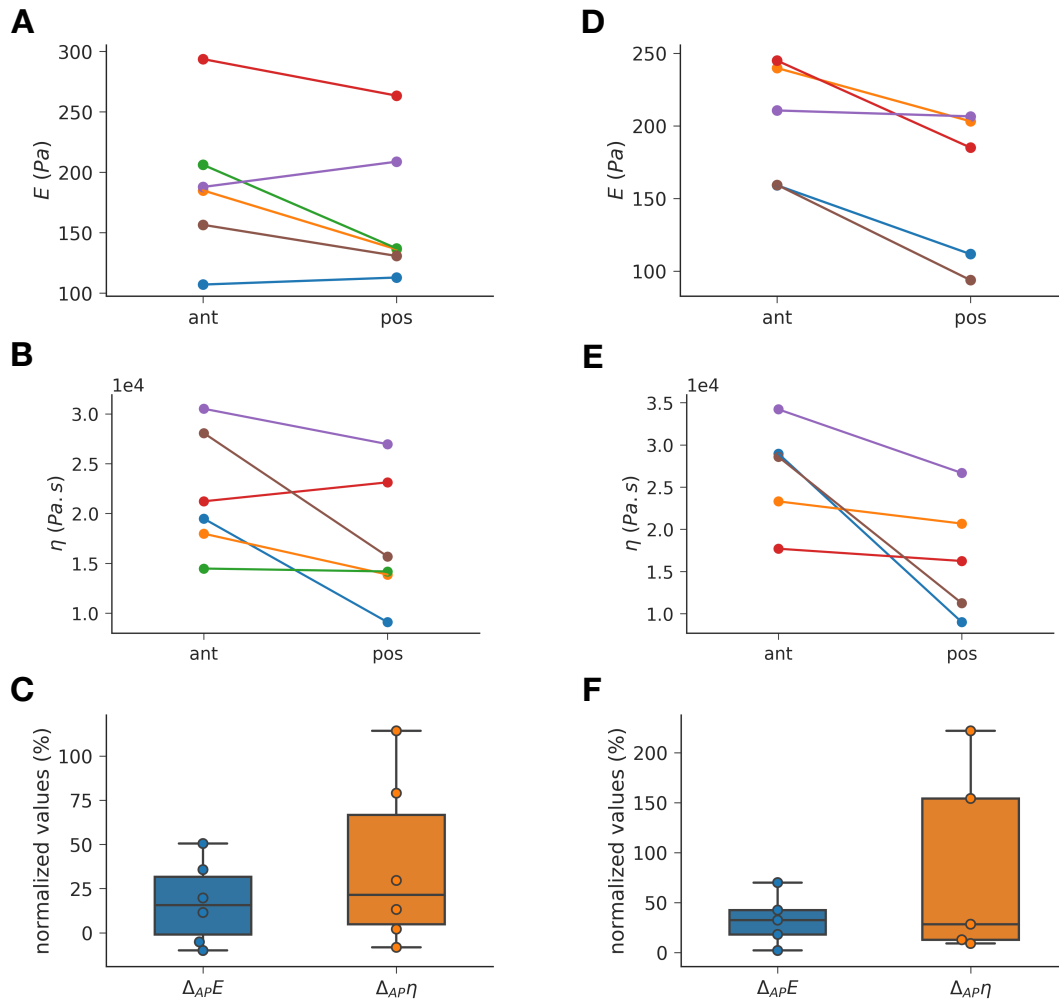
FIGURE 4.18 – Bulk elasticity (**A**, **D**) and viscosity (**B**, **E**) gradient between anterior and posterior regions. Each color represents one PSM (same color code between respectively panels **A** and **B**, panels **D** and **E**). **C**, **F**: Pairwise difference (anterior property - posterior property) scaled by the posterior property. Bulk properties calculated using: $\langle \gamma_0 \rangle$ (**A**, **B**, **C**) for both collagenase and pancreatin dissected explants, the δ-method (**D**, **E**, **F**) for collagenase dissected explants only.
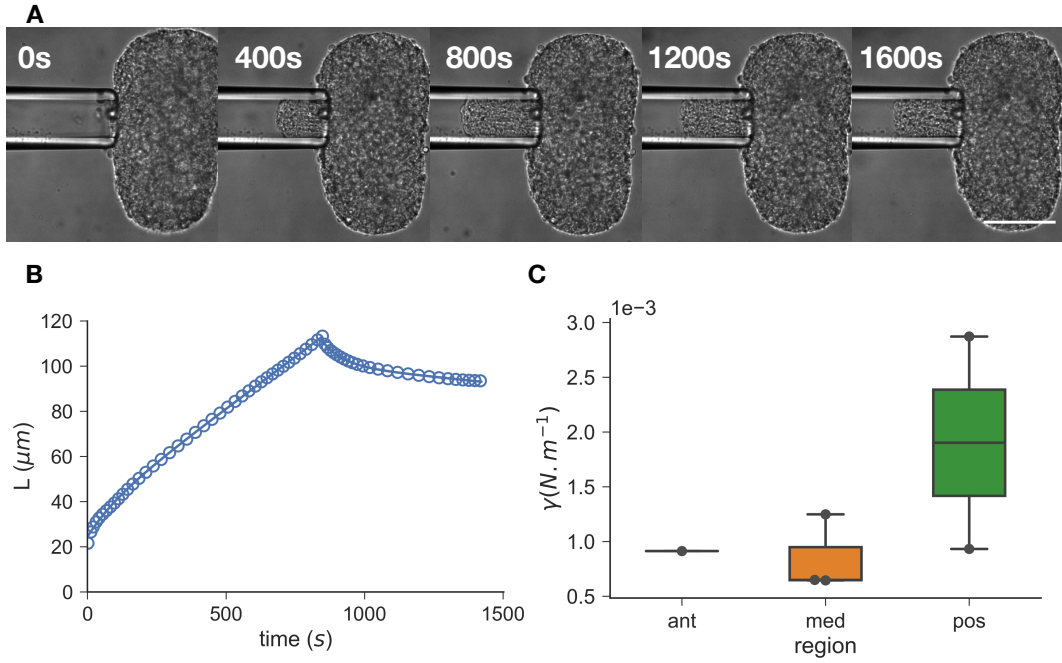
FIGURE 4.19 – Aspiration of blebbistatin treated explants. **A**: Series of snapshots of an aspiration and retraction (starting at 900s) of a medial region explant at 294 Pa. Scale bar: 100 µm. **B**: Aspiration dynamics of the same explant. Solid line: modified SLS fit. **C**: $\dot{L}_\infty$-based measurement of surface tension.

dissected (following the collagenase-based protocol) and incubated in 20 µM blebbistatin (in DMEM-F12 with 10% FBS) at 37 °C and 7.5 % of CO_2 for one hour. They were subsequently transferred to the aspiration dish and aspiration experiments as presented above were carried out. As we already noticed during the rounding experiments in Chapter 3, the blebbistatin treated explants present a much smoother surface due to the absence of protrusive activity. We also noticed that the effect of the blebbistatin was quickly reversible. Indeed, if explants were transferred to a control medium after one hour of incubation in blebbistatin, we could see the protrusive activity starting again inside the pipette and the explant contracting inside the pipette after 10 min (see Movie 8).

At comparable aspiration pressures, the aspiration rate was strikingly higher than the control explants. Moreover, the retraction was extremely slow. This suggests that the critical pressure ΔP_c is much lower in the blebbistatin treated explants. In this case, the retraction rate being slow, the $\dot{L}_\infty$-based measurement of surface tension gave much more reliable results. Surface tension was a 4.5-fold lower than the one of control explants, which was confirmed by tension direct measurements that yield an average surface tension of 0.72 ± 0.26 mN $\cdot$ m^{-1}. To control the effect of the prior incubation and of DMSO (from the blebbistatin solution), we also aspirated explants after 1-hour of incubation at 37 °C and 7.5 % of CO_2 with 20 µM of DMSO. No significant difference with non-treated explants without incubation was found.

As the dispersion of the bulk properties is greater than tension data, a much greater number of aspirations would be required to be conclusive. Despite the strong limitation of our dataset, the orders of magnitude of our preliminary data suggest that elasticity is not really affected by the blebbistatin treatment, whereas viscosity seems to be reduced by a 4-fold change in anterior, a 3-fold in medial and 50% in
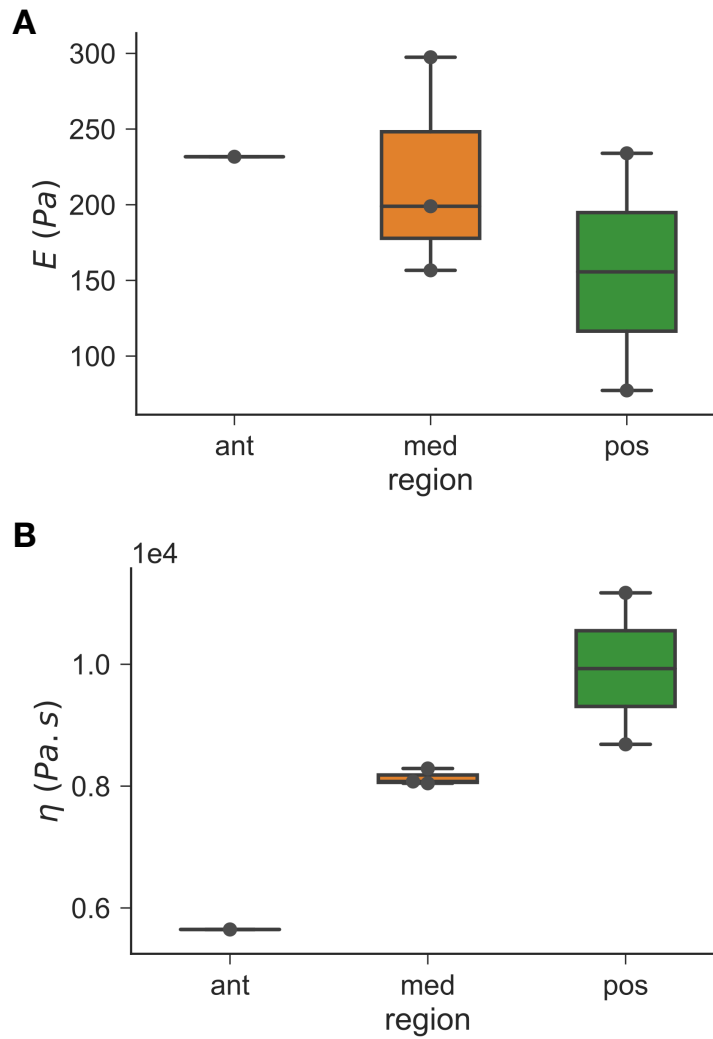
FIGURE 4.20 – Bulk elasticity (**A**) and viscosity (**B**) along the AP axis of blebbistatin treated explants.

posterior.

Conclusion

In this section, we presented a first approach to measure PSM elasticity, viscosity and surface tension independently along the AP axis using dissected explants. We had to face a high inter-embryonic dispersion making it difficult to verify the linearity of the stress-strain relation. While it was challenging to show a trend along the AP axis when all embryos were pooled together, patterns in individual embryos suggest there is clear viscoelastic gradient along the AP axis. Our protocol of dissection of explants was clearly challenging the mechanical properties of the PSM as we were using ECM-digesting enzymes and the tissues were taken out of their physiological environment. In addition, the mapping of the PSM was quite coarse as it was divided in three main regions. Thus, we devised another approach to tackle these limitations.

4.3 Mechanical properties of tissues *in vivo*

We used another approach to perform micropipette aspiration on the chicken embryo. We tried a less invasive method than dissecting out PSM explants. We developed a protocol to aspirate embryonic tissues, either the PSM or the neural tube (NT), inside the living embryo. This technique allowed us to precisely map the spots of aspiration, to keep the tissues in conditions closer to the physiological ones, and to avoid enzyme digestion during the dissection.

4.3.1 Sample preparation and setup

Several challenges had to be overcome to carry out pipette aspiration *in vivo*:

1. accessing the tissue to be aspirated and image the pipette;

2. being sure to aspirate only the correct tissue;

3. preparing the tissue so it can freely flow as it should not stick to another tissue which would perturb its flow;

4. immobilizing the tissue during the aspiration.

The simplest way of accessing the PSM is to lift open the ectoderm, which means aspirating the PSM from the dorsal side. Because the pipette needs to be parallel and close to the bottom of the dish (to be in the focal plane of the objective), the plane of the embryo would need to be vertical (to be orthogonal to the pipette). We cut away the extra-embryonic tissues and held the embryonic tissues vertical by gluing them to a coverslip, using a surgical glue (see Figure 4.21 A). However, the density of the superimposed tissues made it impossible to image the spot of aspiration. Therefore we found it extremely challenging to aspirate from the dorsal side of the embryo.

We favored another approach, which consisted in aspirating the PSM from its lateral side. The NT was cut away from the PSM as shown in Figure 4.21 B, C. The lateral side of the PSM flanking the NT was then accessible. Next, we removed completely the ectoderm because the PSM is indistinguishable from both the ectoderm and the endoderm by wide-field microscopy. Although we tried to remove the endoderm as well, the sole connection of the PSM with the lateral plate was too weak to keep the PSM intact. Instead, we decided to keep the PSM supported by the endoderm which was labeled by local injection of DiI (a membrane lipophilic dye). In this way, the monolayer of the endoderm could be distinguished from the mesoderm by bringing the fluorescence into the focal plane (see Figure 4.23 B). This method was adapted to alternatively aspirate the NT, by removing the PSM and the somites flanking the NT (see Figure 4.21 D, E).

In order to maintain the embryo hydration and keep it at 37 °C, the dissected embryo was transferred to DMEM-F12 with 10% FBS at 37 °C. However, once dissected, the embryo could not be manipulated by the classical filter paper ring technique (Chapman et al., 2001), which prevents the embryo from curling into a dense mass of tissues by maintaining it under tension. We tried to glue the embryo (using a physiological surgical glue) to the bottom of the dish to keep it flat and under tension. But, as the embryonic tissues are extremely fragile, movements of the culture
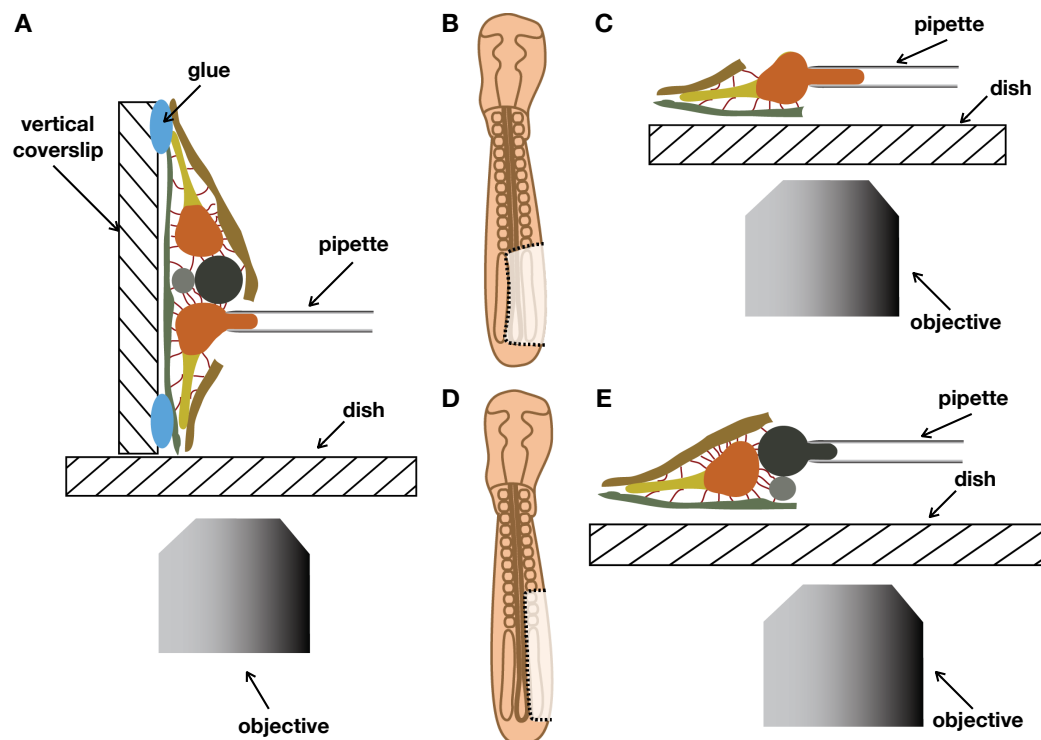
FIGURE 4.21 – . Schematics of the sample preparation for *in vivo* aspiration. **A**: Aspiration of the PSM from the dorsal side. Aspiration of the PSM from the lateral side (**B**, **C**). **B**: Top view of the dissection to access the PSM. **C**: Side view of the *in vivo* aspiration of the PSM. Aspiration of the NT from the lateral side (**D**, **E**). **D**: Top view of the dissection to access the NT. **E**: Side view of the *in vivo* aspiration of the NT. Tissue legend: brown: ectoderm, orange: PSM, yellow: lateral plate, black: NT, gray: notochord, green: endoderm.
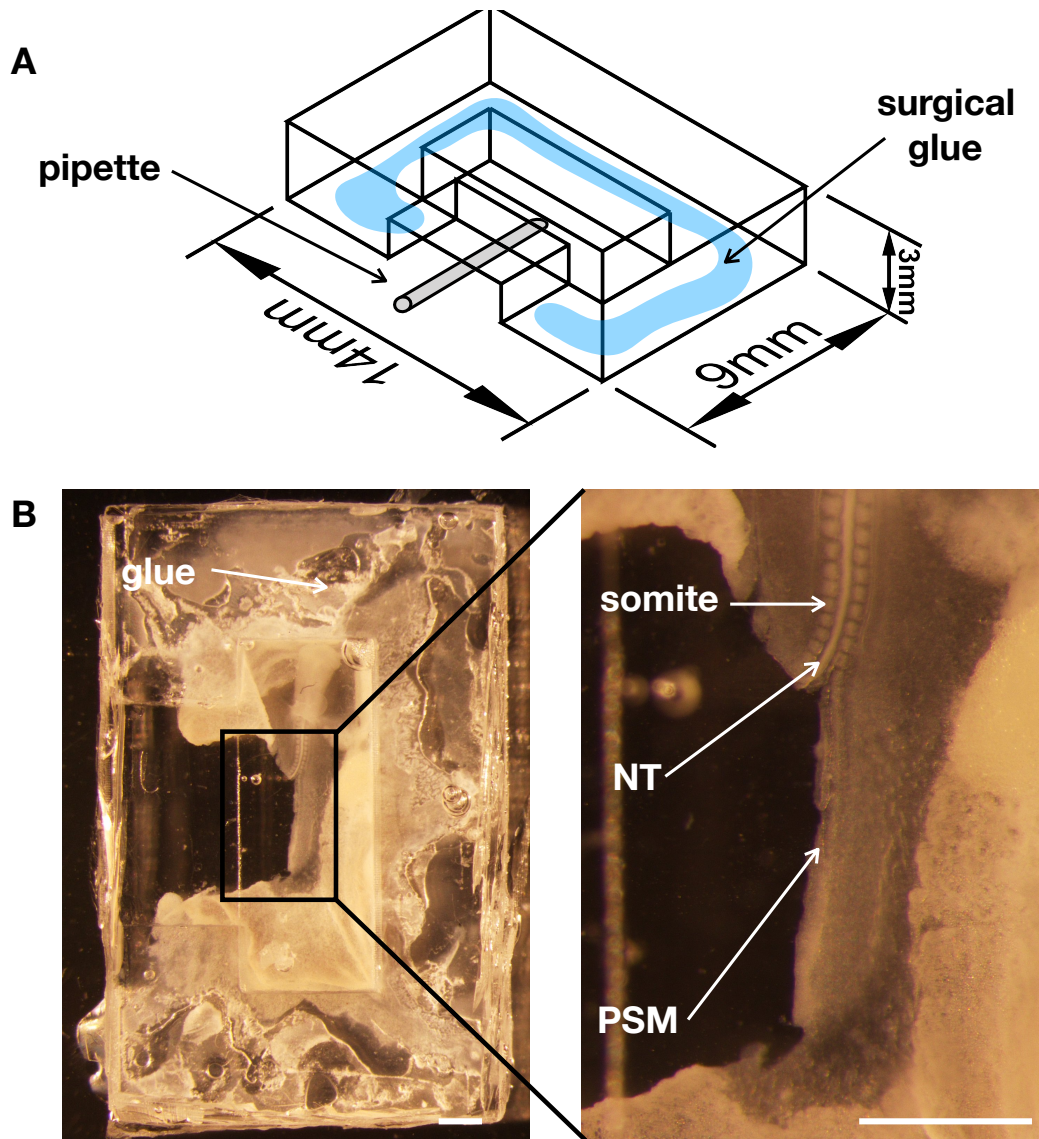
FIGURE 4.22 – PDMS chamber for *in vivo* aspiration. **A**: Schematic of the PDMS chamber. **B**: Top view of the PDMS chamber with glued embryo. Scale bars: 1 mm.

medium would tear it apart. To solve this issue, we designed a polydimethylsiloxane (PDMS) chamber to immobilize the embryo and protect it from any flow within the dish. We fabricated a 3D-printed mold to produce such a PDMS chamber (see Figure 4.22 A). A small opening (5×1.5 mm^2) was used to access the tissues with the pipette. The embryo was held still by gluing the extra-embryonic tissues between the bottom of the dish and the walls of the chamber, by means of physiological surgical glue (see Figure 4.22 B). Similarly to the explant aspiration, a thin layer of mineral oil was added on top of the medium to prevent any evaporation.

Once in the confined environment of the chamber, the tissues stayed flat and could be aspirated. The NT being a large tissue, it was easily distinguished from the other tissues. The neurectoderm flanking the NT is dense, enabling easy detection of the border between the two tissues and certainty that only the NT was aspirated (see Figure 4.23 A). Conversely, when we aspirated the PSM, the tissue thickness being smaller, the endoderm was always very close to the pipette opening. For this reason,
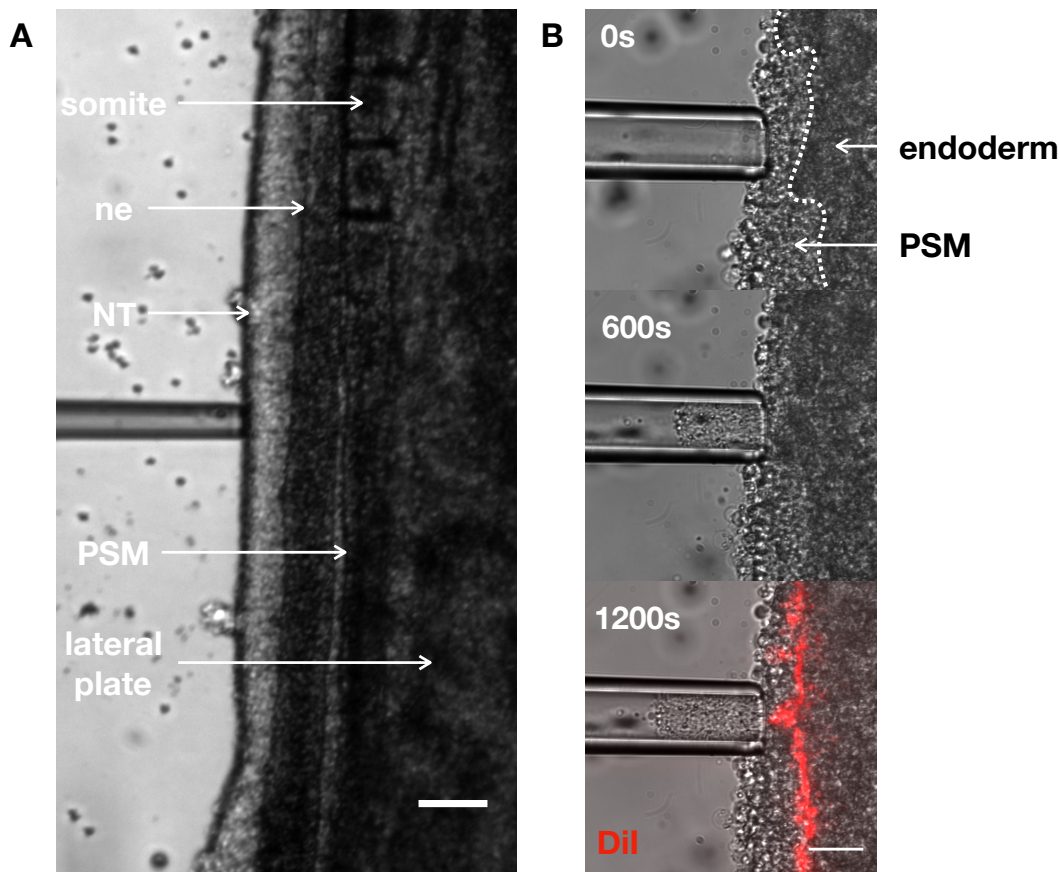
FIGURE 4.23 – *In vivo* aspirations. **A**: Aspiration of a NT. ne: neurectoderm. Scale bar: 100 µm. **B**: Snapshots of an aspiration of a PSM (medial region) at 294 Pa. Top panel: the dotted line outlines the boundary between the endoderm and the PSM. Lower panel: DiI fluorescence in red: no endoderm cells was aspirated. Scale bar: 50 µm.

we always monitored the DiI-stained tissue to ensure no aspiration of the endoderm occurred (see Figure 4.23 B).

We had to face another unexpected challenge. The tissue often slowly drifted along a specific direction at a velocity scale comparable to the aspiration rate. This slow movement was presumably a consequence of the dissection. The amplitude and the direction of this large-scale movement were unpredictable. As a result, some aspirations were exploitable as the movement was negligible, but an important number of experiments were impossible to carry out because the movement was displacing the tissue during the aspiration. This issue was extremely challenging to solve. The only solution would have been to isolate the aspirating tissue from the rest of the embryo which was precisely the explant experiment presented in the previous section. Thus, we coped with this problem by discarding any experiment for which the movement impacted the aspiration. Precisely, we measured the position of the region of aspiration before the aspiration and after the retraction. If the region of aspiration had drifted more than 10 µm during the aspiration, we discarded the aspiration.

TABLE 4.7 – *In vivo* mechanical properties along the PSM (mean and standard deviation).

	Anterior	Medial	Posterior
E_{app} (Pa)	241.5 ± 107.5	159.1 ± 85.6	132.4 ± 37.4
η_{app} (kPa $\cdot$ s)	21.0 ± 6.1	20.8 ± 8.6	15.7 ± 5.6
E (Pa)	71.1 ± 35.4	37.9 ± 27.0	39.4 ± 20.3
η (kPa $\cdot$ s)	6.4 ± 2.9	7.5 ± 4.9	4.4 ± 3.1

4.3.2 Measurement of *in vivo* viscoelasticity along the presomitic mesoderm

Despite the strong limitation of the drifting movement, we obtained a substantial number of exploitable results. An important advantage of the *in vivo* technique is that the aspiration position can be precisely measured as the whole body configuration can be imaged (see Figure 4.24 A). Therefore, we could plot the mechanical properties with respect to the distance away from the last formed somite. We observed a graded profile of apparent elasticity along individual PSM but not for apparent viscosity (see Figures 4.24 B, C). To compare these data with explants data, we pooled our measurements along the axis in three regions and noticed lower orders of magnitude (see Figures 4.24 D, E). We were not able to measure the *in vivo* surface tension, as a very few retractions were exploitable and the direct method was challenging because the PSM was not plugging the pipette for low aspiration pressures. As a result, in order to calculate the bulk properties we used the average value of surface tension we had measured by the direct method on explants $\langle \gamma_0 \rangle$. Figure 4.25 shows that elasticity along individual PSMs also shows a graded profile. However, both elasticity and viscosity are significantly lower than the explant properties. For instance, the anterior PSM elasticity was in the order of 70 Pa (instead of 200 Pa for collagenase dissected explants).

In summary, we measured PSM properties *in vivo* with a lower order of magnitude and an anteroposterior gradient of elasticity. However, we did not see any viscosity profile because of the dispersion of the data. This higher dispersion and softer properties can be explained by several reasons. First, the non-enzymatic dissection often resulted in a damaged PSM. It is, therefore, possible the dissection weakened the tissue. Second, PSM being physically connected to the rest of the embryonic body was not free to move. Consequently, it is possible that the pipette opening was not perfectly plugged by the tissue, which would affect the aspiration flow.

4.3.3 Measurement of *in vivo* viscoelasticity along the neural tube

The same method was successfully implemented on the NT. We first noticed that it was a stiffer tissue than the PSM, as we had to apply greater pressures (typically 600 - 800 Pa) for comparable deformations. We also observed smoother aspiration curves (see Figure 4.26 and Movies 9, 10). In addition, the NT is a longer tissue than the PSM, thus we could explore a greater part of the AP axis: we also aspirated regions anterior to the last formed somite. To measure the position along the axis, we kept the reference point as the last formed somite. We, therefore, note as positive the distance to the last somite towards the posterior end, and as negative towards the
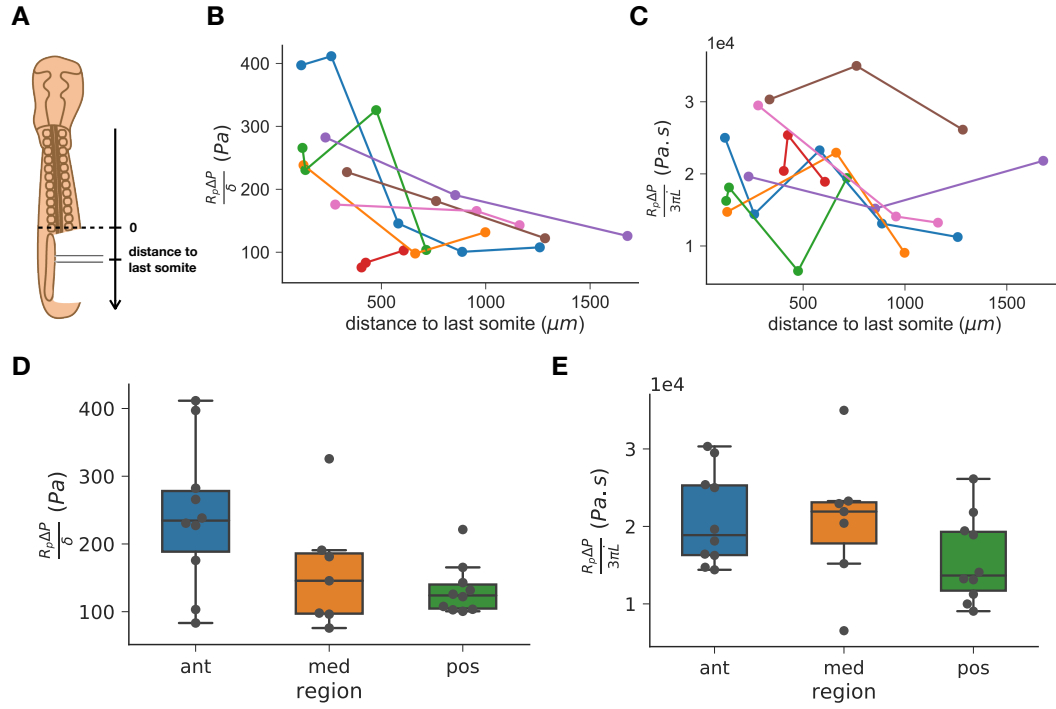
FIGURE 4.24 – *In vivo* PSM apparent properties. **A**: Schematic of aspiration position measurement. Gradient along individual PSMs of apparent elasticity (**B**) and apparent viscosity (**C**). Each color represents one PSM. Apparent elasticity (**D**) and apparent viscosity (**E**) pooled by regions (ant: anterior, med: medial, pos: posterior).

anterior end (see Figure 4.26 A).

We measured a more regular graded profile of apparent properties along the NT than along the PSM. Both data along individual NTs and pooled data by regions exhibit a significant anteroposterior gradient (see Figure 4.27 and Table 4.8).

Our dataset of NT surface tension measured by the direct method was extremely limited because of the aforementioned challenges we faced with this method *in vivo*. Regarding the δ-method, we measured a flat pattern of tension between the NT facing somitic region and the NT facing the medial PSM region (see Figure 4.28 A). Surface tension also depended on the aspiration force (see Figure 4.28 B).

In order to calculate the bulk properties, we used the average value of tension measured from our limited dataset obtained with the direct method $\langle \gamma_0 \rangle = 2.4\,\mathrm{mN} \cdot \mathrm{m}^{-1}$. Even though this average value measurement was not extremely reliable, we used it as a first approximation to calculate the bulk properties. Furthermore, as the contribution of surface tension is less important in the NT than in the PSM, the potential error on the bulk stress calculation is less important. Indeed, regarding the PSM we typically had the bulk stress $\Delta P - \Delta P_c \approx 200$ Pa, with $\Delta P_c \approx 200$ Pa, while for NT we had $\Delta P - \Delta P_c \approx 500$ Pa, with $\Delta P_c \approx 200$ Pa.

Both elasticity and viscosity show a significant graded pattern along the axis, for both individual NTs and data pooled by regions (see Figure 4.29 and Table 4.8). For instance, the NT facing the somitic region is significantly stiffer (556.5 ± 328.2 Pa) than the NT facing the medial PSM region (278.9 ± 146.7) and the NT facing the posterior PSM region (208.3 ± 171.7), the Student t-test p-values being respectively 0.013 and 0.004.
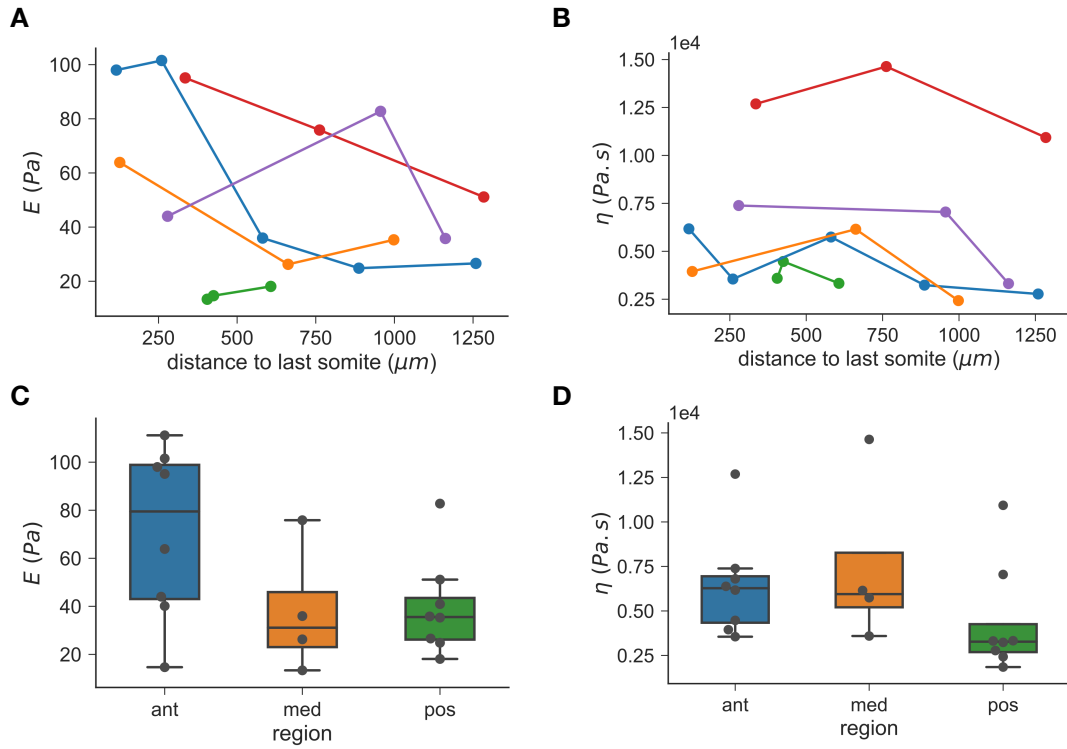
FIGURE 4.25 – *In vivo* PSM bulk properties. Gradient along individual PSMs of bulk elasticity (**A**) and bulk viscosity (**B**) calculated using $\langle \gamma_0 \rangle$. Each color represents one PSM. Bulk elasticity (**C**) and bulk viscosity (**D**) pooled by regions (ant: anterior, med: medial, pos: posterior).

TABLE 4.8 – *In vivo* mechanical properties along the neural tube (mean and standard deviation).

	Somite region	Anterior PSM	Medium PSM	Posterior PSM
E_{app} (Pa)	864.9 ± 446.8	530.5 ± 128.6	446.3 ± 134.7	378.4 ± 192.9
η_{app} (kPa · s)	55.8 ± 30.2	46.5 ± 21.8	31.2 ± 14.5	20.9 ± 7.6
E (Pa)	556.5 ± 328.2	337.6 ± 140.1	274.0 ± 152.9	208.3 ± 171.7
η (kPa · s)	35.8 ± 23.9	30.6 ± 17.7	19.9 ± 12.7	9.6 ± 4.6
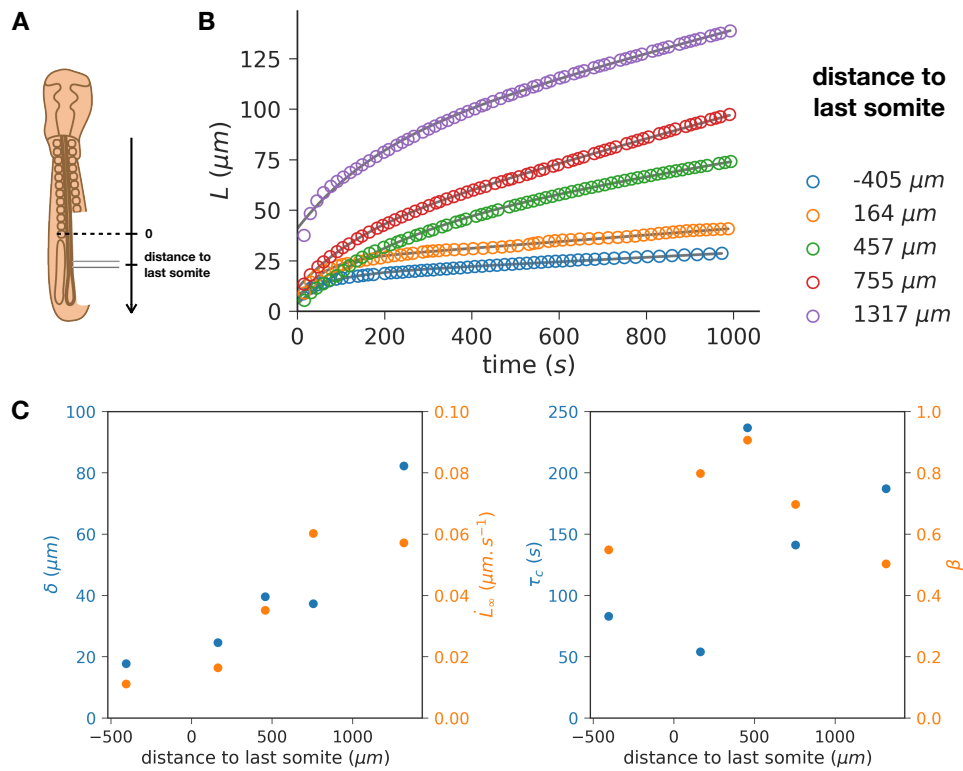
FIGURE 4.26 – Example of a series of *in vivo* aspirations of a NT along the anteroposterior axis. **A**: Schematic of aspiration position measurement. **B**: Aspiration curves for $\Delta P = 784$ Pa and $R_p = 15$ µm. Circle: tracked data points of the kymograph. Solid line: modified SLS fit. **C**: Fitted parameters for each curve.
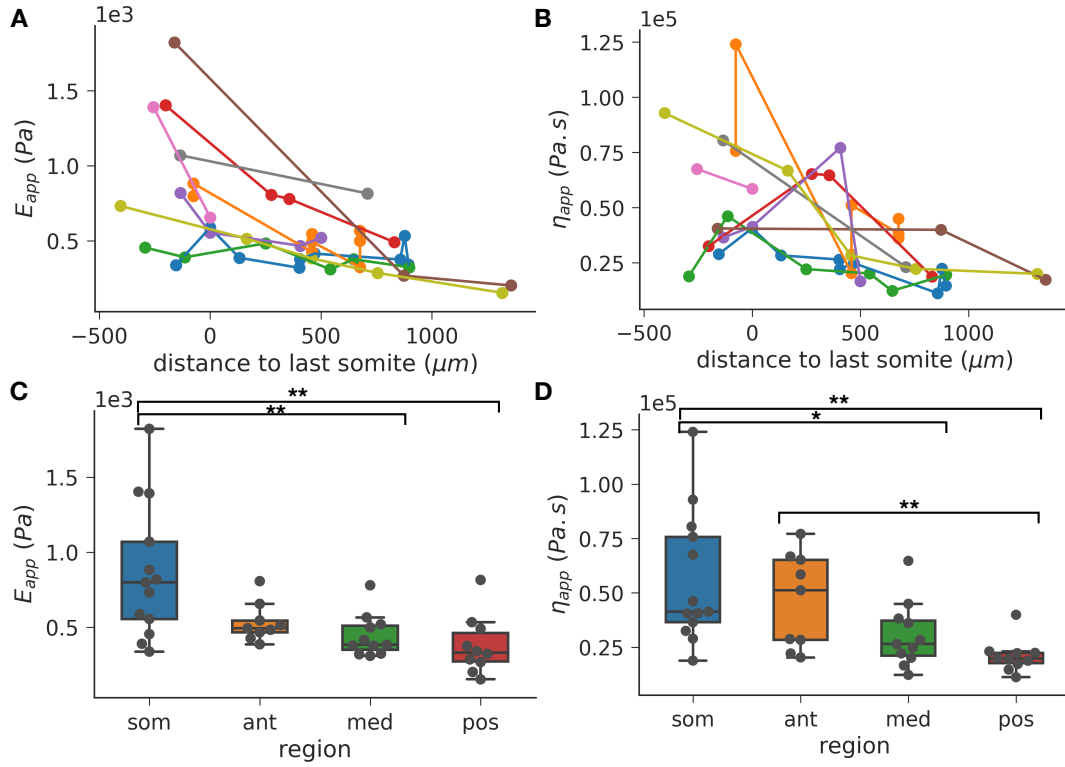
FIGURE 4.27 – *In vivo* NT apparent properties. Gradient along individual NTs of apparent elasticity (**A**) and apparent viscosity (**B**). Each color represents one NT. Apparent elasticity (**C**) and apparent viscosity (**D**) pooled by regions (som: somitic region, ant: anterior PSM region, med: medial PSM region, pos: posterior PSM region). Student's t-test p-value p: $\star$: $p < 0.05$, $\star\star$: $p < 0.01$.
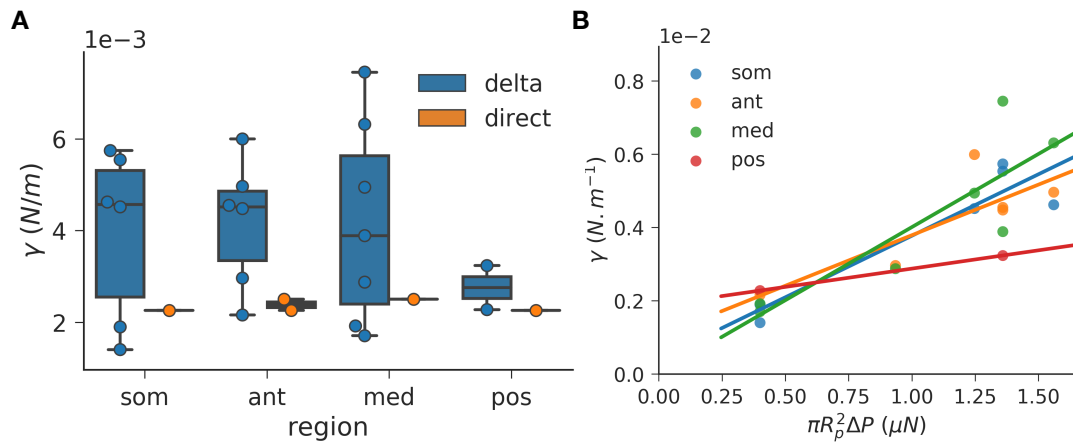
FIGURE 4.28 – *In vivo* NT surface tension. **A**: Surface tension along the axis measured by the direct method and the δ-method. **B**: Surface tension measured by δ-method with respect to the aspiration force.
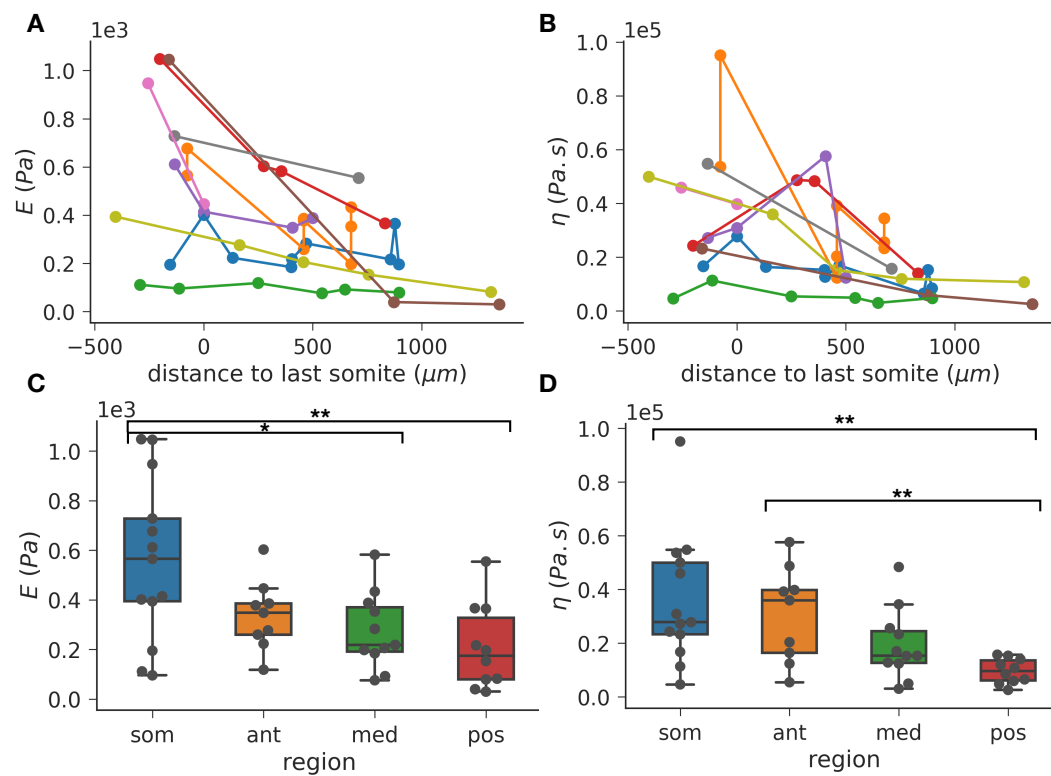
FIGURE 4.29 – *In vivo* NT bulk properties. Gradient along individual NTs of bulk elasticity (**A**) and bulk viscosity (**B**) calculated calculated using $\langle \gamma_0 \rangle$. Each color represents one NT. Bulk elasticity (**C**) and bulk viscosity (**D**) pooled by regions (som: somitic region, ant: anterior PSM region, med: medial PSM region, pos: posterior PSM region). Each color represents one NT. Student's t-test p-value p: $\star$: $p < 0.05$, $\star\star$: $p < 0.01$.

4.4   Comparison of the neural tube and the presomitic mesoderm

Finally, we decided to compare the mechanical properties of the NT with the PSM in order to address the PSM confinement hypothesis assumed by the random cell motility model. A few aspirations on NT explants were tried but as the NT is a large tissue, we faced the same issue we had with full PSMs: explants easily fell out, thus it was challenging to plug the end of the pipette. For this reason, we compared the NT *in vivo* dataset with the collagenase dissected PSM explant dataset. The collagenase dataset was larger and showed the stiffest values (compared to pancreatin dissected explants and *in vivo* PSMs). Thus, if there is a difference with the NT, the difference will be even larger with the other datasets. Figure 4.30 shows that the anterior PSM is significantly softer than the neighboring NT (Student's t-test p-value $p = 0.017$). The medial PSM is slightly softer but not significantly. However, the posterior PSM and NT exhibit comparable stiffnesses. Viscosity does not show a major difference between the two tissues, except for the posterior region: surprisingly, the PSM is more viscous than the neighboring NT. This difference could be explained by the fact that during *in vivo* measurements the posterior limit cannot be easily identified. As a result, regions even more posterior to the region dissected for the explant dataset might have been aspirated. In this case, posterior values from explants and *in vivo* measurements might be comparable.

Our data partially confirm the assumption of the random motility gradient model in which the PSM is confined medio-laterally by the lateral plate and the NT. Unsuccessful measurements on lateral plate explants were carried out. Indeed, the lateral plate flat geometry did not allow correct aspirations to be performed.

4.5   Conclusion

In this chapter, we presented the first elasticity, viscosity and surface tension profile along the AP axis for both the PSM and the NT in the chicken embryo. The PSM is roughly 3 times softer, 10 times less viscous and has a 2-fold lower surface tension than murine sarcoma (S180) cell line explants measured by the same technique (Guevorkian et al., 2010).

Surface tension was measured by several methods. On average, chicken PSM exhibits higher surface tension ($\gamma \approx 3\ \mathrm{mN \cdot m^{-1}}$) than zebrafish mesendoderm aggregates ($\gamma \approx 0.4\ \mathrm{mN \cdot m^{-1}}$, Schötz et al., 2008) but slightly lower tension than epithelial aggregates ($\gamma \approx 4.5\ \mathrm{mN \cdot m^{-1}}$, Stirbat et al., 2013a). We also noticed a dependency of surface tension to the aspiration force, suggesting a potential active response.

Chicken PSM is stiffer ($E \approx 200\ \mathrm{Pa}$) than *Xenopus* embryonic tissues at a similar stage (from 20 to 80 Pa) (Zhou et al., 2009). Importantly, Zhou et al. measured that the PSM was the stiffest tissue. However, because the authors measured the elastic properties before the neural tube closure, we cannot compare our NT data directly with theirs. In the chicken, the higher stiffness of the NT compared to the PSM confirmed that we can assume the PSM to be laterally confined by the NT, in the anterior region at least. However, the stiffness might be underestimated in the NT, as the posterior region was less well defined with the *in vivo* technique. Interestingly, while no pattern of elasticity along PSMs can be observed because of an important inter-embryonic dispersion, there is a clear AP gradient of elasticity within individual embryos. Furthermore, PSM dissected by collagenase are significantly stiffer than
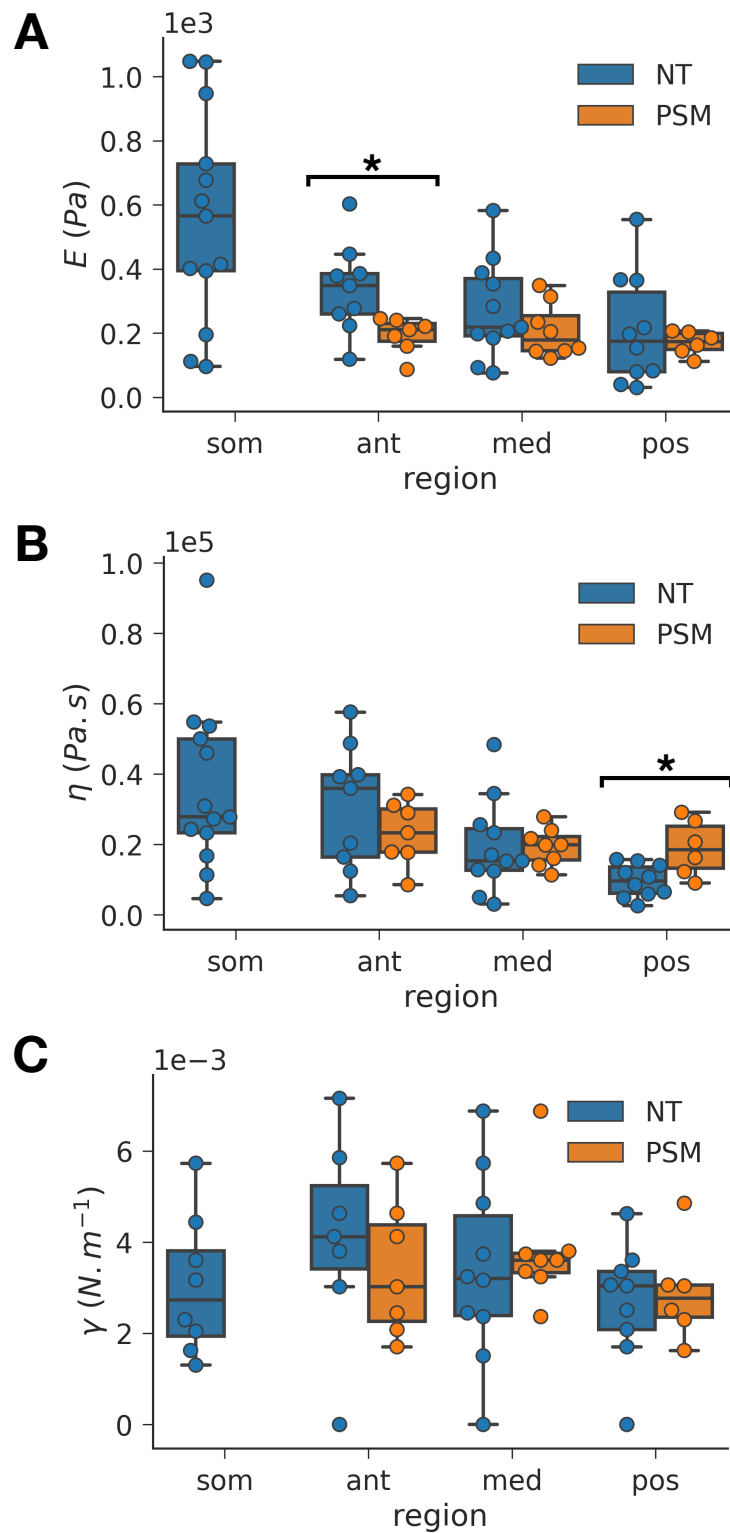
FIGURE 4.30 – Comparison of the PSM and the NT properties. **A**: Bulk elasticity along the AP axis using mean values of tension. **B** Bulk viscosity along the AP axis using mean values of tension. **C**: Surface tension along the AP axis using δ-based measurement of ΔP_c. Student's t-test p-value p: $\star$: $p < 0.05$.

pancreatin dissected explants. This result highlights the potential role of fibronectin in PSM stiffness. This result would imply another difference with *Xenopus* tissues for which the ECM has been shown to have a limited impact on mechanical properties (Zhou et al., 2009).

Finally, viscosity exhibits a clear gradient along the PSM. The average viscosity (20 kPa · s) is in the same order of magnitude than viscosity of zebrafish embryonic tissues, which has been measured by a combination of fusion experiments and tension measurements (Schötz et al., 2008). Chicken PSM viscosity is however 30 times lower than viscosity in epithelial cell aggregates (620 kPa · s, Stirbat et al., 2013a).

We had to face an important dispersion of the data which might be explained by several limitations and challenges:

- The PSM is a mesenchymal tissue with a low cell density and a high protrusive activity. Its low density made it difficult to dissect and could lead to variable mechanical states after dissection. In addition, the tissue could lose its cohesiveness during the aspiration making it difficult to analyze. Its high protrusive activity makes its interface rough and difficult to track.

- We faced in a third of the aspirations, a different kind of dynamics that could not be fitted by our model.

- Because of alteration during the aspiration or the explant falling off from the tip of the pipette, the retractions were extremely difficult to analyze. This issue prevented us from having a systematic measurement of ΔP_c which would have given us a better measurement of surface tension and the bulk properties.

- We might also face an inherent high inter-embryonic variability, as previously reported in *Xenopus* (Von Dassow and Davidson, 2009).

Despite these limitations, we were able to show that individual PSMs exhibit graded anteroposterior viscoelastic properties, which could be explained by the pattern of ECM, cellular density and cell motility along the axis. More experiments are needed to investigate the impact of these various factors.

In order to compare the results of this Chapter with the mechanical properties presented in Chapter 3, we also computed the viscocapillary velocity from aspiration data (see Table 4.9). We saw an important discrepancy, especially in anterior explants, with a 45-fold difference. This might be explained by the fact that the aspiration technique probes different mechanical properties. While the rounding experiment measures mechanical properties at rest, the pipette experiment actively pulls on the tissue. If there is an active response of the tissue, the apparent surface tension could be increased. Also if the tissue is partially damaged by the aspiration, the apparent viscosity could be smaller. These two effects taken together would lead to a higher viscocapillary velocity. Another explanation could be that the rounding data are less accurate in the anterior region (where the discrepancy is the largest) as the somite cleft formation perturbed the rounding process.

In order to have another estimate of PSM viscosity, we calculated it using the pipette tension data and the rounding data. This value of viscosity is likely to reflect more the viscous property at rest. Indeed, this calculation used tension data from the direct method for which the active response should be minimal and rounding data which depend on the tissue rearrangement timescale. Thus, we calculated viscosity

TABLE 4.9 – Viscocapillary velocity along the PSM (mean and standard deviation).

	Anterior	Medial	Posterior
pipette data ($\mu m \cdot min^{-1}$)	9.56 ± 3.90	8.31 ± 3.29	11.78 ± 5.81
rounding data ($\mu m \cdot min^{-1}$)	0.21 ± 0.08	0.91 ± 0.44	1.56 ± 0.53
fold change	45.5	9.1	7.6

along the axis to be: $\eta = 1.0 \times 10^6 \pm 6.5 \times 10^5$ Pa $\cdot$ s in anterior PSM, $\eta = 2.1 \times 10^5 \pm 1.7 \times 10^5$ Pa $\cdot$ s in medial PSM and $\eta = 1.2 \times 10^5 \pm 7.6 \times 10^4$ Pa $\cdot$ s in posterior PSM. This calculation yields a value in the anterior region which is in the range of the most viscous epithelial tissues. This suggests that the viscocapillary velocity might have been underestimated. However, the posterior region is a 2-fold less viscous than epithelial explants (Guevorkian et al., 2010), which seems reasonable.

Chapter 5

Stress production during anteroposterior axis elongation

The second aim of this Ph.D. thesis is to measure the force production by the elongating axis in order to assess the PSM contribution to elongation. Our theoretical model predicts that the PSM can produce up to 1.3 Pa of pushing stress and the resisting stress of the posterior boundary is about ~ 1mPa (Regev et al., 2017). The stress exerted by the PSM cells should, therefore, be able to propel the growth of the axis. However, this theoretical prediction still needs experimental validation. Is the PSM capable of exerting such a stress? If so, this pushing force needs to be integrated into a multi-tissue model to understand how it can drive elongation of the whole body. As presented in Figure 2.7, several models can be envisioned to explain the coordination of the tissues during growth. To investigate the relevance of each of these models, two questions must be answered:

- What is the contribution of the PSM to the total force production, *i.e.* what it the proportion of the force exerted by the two PSMs with respect to the total body elongation force?

- How is the putative pushing force of the PSM transmitted to the neighboring tissues in order to drive the whole body extension?

We can simplify the process of caudal growth by considering only the pushing force exerted by the axial tissues (neural tube and notochord) f_{ax} and the pushing force exerted by the PSM f_{PSM}. We neglect the ectoderm as it should not exert large forces because of its limited cross section. Besides, Bénazéraf et al., 2017 showed that the lateral plate and the endoderm extend at a lower rate than other tissues, so they should not exert pushing forces. Considering there are two PSMs in an embryo, the total force of elongation f_{total} should read:

$$f_{total} = 2f_{PSM} + f_{ax} \tag{5.1}$$

Following the hypothesis in which PSMs exert all the pushing forces and the axial tissues are dragged in some way (Figure 2.7 A), $f_{ax} \approx 0$ and $f_{PSM} \approx \frac{f_{total}}{2}$. In the hypothesis in which the axial tissues exert important forces (even though it depends on the PSM activity, see Figure 2.7 B), no special relation between f_{total}, f_{PSM} and f_{ax} can be predicted. However, if the axial tissues have an autonomous growth but cannot exert enough forces in the absence of the PSM (Figure 2.7 C), we should measure that $f_{ax} \ll 2f_{PSM}$. Consequently, measuring the ratio $\frac{2f_{PSM}}{f_{total}}$ should give us more insight on the most probable elongation model.

We, therefore, designed two experiments: *(i)* a measurement of the force produced by the whole embryonic body *in vivo* (f_{total}), *(ii)* a measurement of the force produced by an isolated PSM *in vitro* (f_{PSM}).

5.1   Measurement of stress production *in vivo*

In order to measure the force associated with a uniaxial extension, we decided to use a cantilever force sensor. A cantilever force sensor is an elongated structure (beam or fiber) which has been calibrated to measure the force applied to bend it. There is a range in which the deflection at its tip is proportional to the applied force. As the embryo is flat and it can be cultured horizontally under a microscope, we decided to design a cantilever that could be inserted vertically and which tip could be imaged within the embryo (see Figure 5.1).
Technically, the measured force depends on the area of the force sensor: a larger force sensor probes a higher force for a given stress. Therefore, measuring the stress production by normalizing the force by the probe area is more relevant. Furthermore, measuring the instantaneous stress exerted by a growing tissue is challenging as it requires to monitor the tissue growth and to automatically displace the force sensor accordingly. Consequently, as a first approach, we decided to measure the stalling stress, *i.e.* the maximum stress a tissue can produce.

Inserting a cantilever at the end of an elongating embryo requires to culture the embryo in an open environment. Indeed, the cantilever base needs to be fixed with respect to the elongation movement. As such, it has to be held from outside the embryo. We, therefore, decided to bring it in contact with the embryo by means of a micromanipulator. As classical embryo culture takes place in a sealed dish (EC culture, Chapman et al., 2001), we had to devise a novel culture method. In addition, we fabricated custom soft cantilevers to match the embryonic properties and allow a good imaging.

5.1.1   Embryo culture in open environment

A standard culture method has been proposed by Chapman et al., 2001. Early embryos (up to 3 days old) can be cultured on a gel-based substrate. The embryo is collected by placing a ring of filter paper onto the extra-embryonic tissue and by subsequently removing the embryo (attached to the filter paper) from the yolk surface. It can then be deposited on a bacto-agar gel containing thin albumen and glucose, and then cultured at 37°C in a sealed dish preventing the embryo from drying. The gel clarity allows microscopy imaging to be performed during its development. However, if the dish is not sealed, the embryo hydration cannot be maintained longer than a few minutes. In addition, the embryo surface could not be kept at 37°C, as evaporation (which dissipates heat) takes place in a very thin layer of fluid above the embryo. We, therefore, developed alternative methods to the EC culture method.

Liquid culture

The most straightforward method to prevent hydration was to immerse the embryo in a liquid environment and to cover the medium with a layer of mineral oil preventing any evaporation (see Figure 5.1 A). To do so, we cultured the embryo in a DMEM-F12 medium (equivalent to the one introduced by Oginuma et al., 2017). We first noticed difficulties with the embryo stability. Indeed, in classical EC culture,
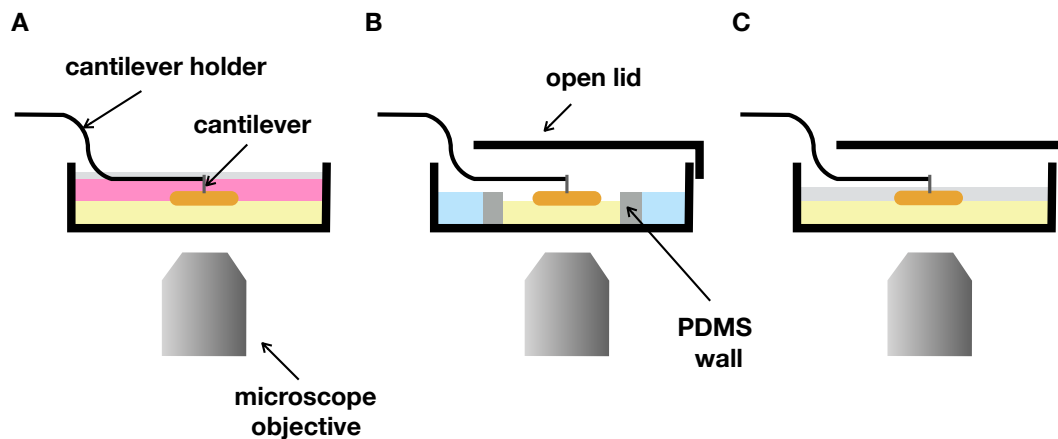
FIGURE 5.1 – Culture methods in open environment. **A** : liquid culture. **B**: Hydrated EC culture. **C**: Oil-covered EC culture. Light gray: mineral oil, pink: DMEM, orange: embryo, yellow: EC culture gel, blue: PBS.

the embryo sticks to the filter paper. However, in a liquid environment, the extra-embryonic tissues quickly detach from the filter ring. We, therefore, sandwiched the extra-embryonic tissues between two rings of filter paper. This improved the embryo stability, but it was not optimal compared to the EC culture. Indeed, the embryo could be drifting, which was an important issue since we want to measure only movements due to elongation. Furthermore, development in a liquid medium was abnormal, as it was shown by Oginuma et al., 2017. Elongation rate quickly decreases to about a third of the normal rate under liquid culture. This was a major concern as the elongation force might have been impacted by the elongation rate decrease. Altogether, the difficulties introduced by the liquid culture method made it unsuitable for a force measurement.

Hydrated EC culture

We next turned to a modification of the EC culture. We designed a dish allowing to keep hydration for a longer duration in an open environment (see Figure 5.1 B). We made a custom Petri dish with a small opening in the lid for the cantilever insertion, and two fluid reservoirs keeping the moisture in the environment longer. The reservoirs were made by stripes of PDMS making a separation between the EC culture gel and a zone filled with PBS. On top of the dish and the micromanipulator holding the cantilever, a custom insulation box was designed to reduce the temperature and moisture loss. In this situation, the hydration could be kept for 3-4 hours, and the temperature at the surface was kept close to 35°C. This method was not ideal but allowed short-term experiments. However, not abolishing evaporation led to unexpected difficulties. We noticed that our custom mica cantilever (see below) underwent bending movements when placed above an evaporating environment (presumably because of condensation at its surface). We, therefore, considered this method was not suitable either.
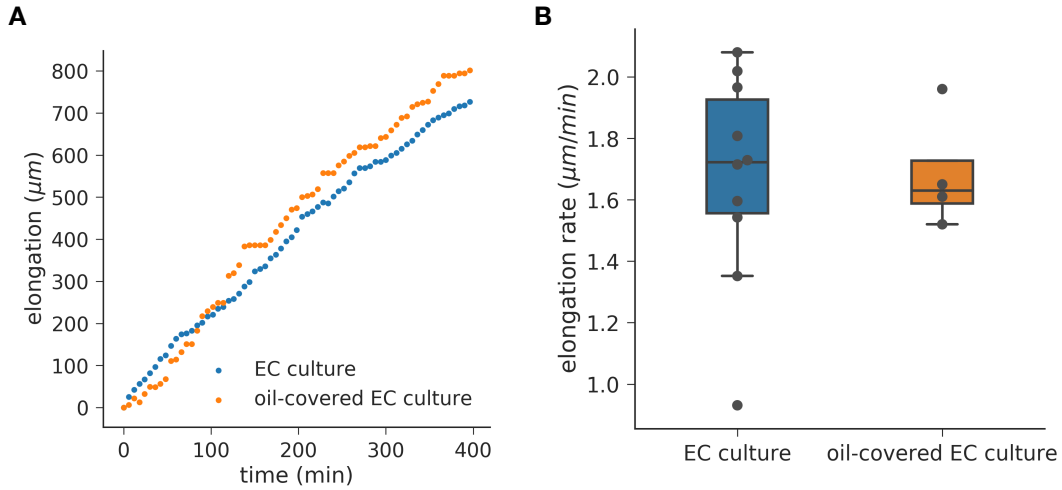
FIGURE 5.2 – Elongation during oil-covered EC culture. Comparison of elongation (**A**) and elongation rate (**B**) for EC culture and oil-covered EC culture.

Oil-covered EC culture

Surprisingly, simply covering a classical EC culture with a layer of mineral oil (see Figure 5.1 C) did not affect embryonic development. Indeed, we could not notice any developmental defect after culturing the embryo for typically 12 hours. We validated that the speed of elongation was comparable to classical EC culture (see Figure 5.2).

5.1.2 Cantilever fabrication and calibration

In collaboration with L. Mahadevan's laboratory, we tried two strategies to fabricate cantilevers which have to follow two requirements: *(i)* having a stiffness compatible with embryonic force production, *(ii)* offering a good imaging of the embryo as it would cast a shadow onto the embryo.

Mica cantilever

We first designed a rectangular mica cantilever (see Figure 5.3 A). Mica is a stratified mineral that can be thinned down by iteratively removing mineral sheets. In this way, the cantilever stiffness can be theoretically easily controlled as it depends on the cube of its length and thickness. For a rectangular beam of length ℓ, thickness t, width w, Young's modulus E, the bending stiffness k writes:

$$k = E\frac{wt^3}{4\ell^3} \tag{5.2}$$

Therefore, as the Young's modulus of mica is $E \approx 10^{11}$ Pa, we estimated $k \approx 2.5$ mN $\cdot$ m^{-1} for $\ell = 1$ mm, $t = 1$ μm and $w = 100$ μm, which is in the same order of magnitude as previous studies on *Xenopus* (Moore et al., 1995). However, mica cantilevers were challenging to thin down below 20 μm of thickness, as they became extremely brittle. At this thickness, fabricating a cantilever of a couple of millimeters long should lead to minimal stiffness of 0.1 N $\cdot$ m^{-1}. We confirmed this estimate by calibration. To calibrate a mica cantilever, we put its tip in contact with the tip of a force sensor under an inverted microscope and monitored the two deflections
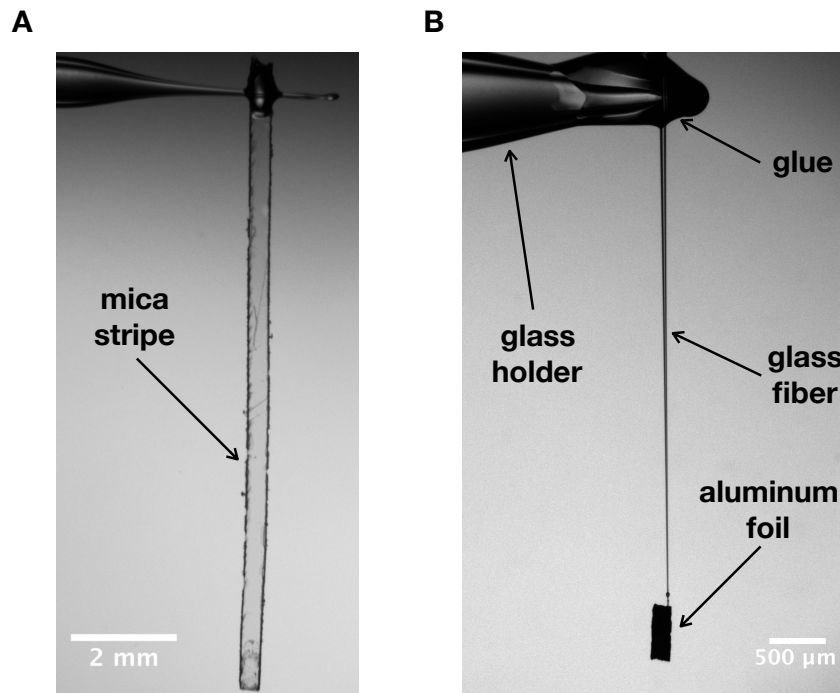
FIGURE 5.3 – Mica cantilever (**A**) and glass fiber cantilever (**B**).

(see Figure 5.4 A). The force sensor is a glass rod of bending stiffness $0.58 \, \text{N} \cdot \text{m}^{-1}$, which was calibrated by hanging small weights at its tip (see materials and methods section 7.4). We could then plot the force-deflection curve of the mica cantilever (see Figure 5.4 B) and measure its stiffness. We fabricated several mica cantilevers but we never could reach a bending stiffness lower than $0.1 \, \text{N} \cdot \text{m}^{-1}$.

We next tried to measure force production with these mica cantilevers. We could not observe any cantilever deflection even with the softest cantilevers. The protocol leading to this measurement will be presented in detail below (see section 5.1.3). In addition, we saw that the tissue was torn by the cantilever as the embryo was elongating, suggesting that the mica cantilevers were too stiff to be deflected (see Figure 5.5). For this reason, we decided to try a new fabrication method.

Glass fiber cantilever

We next turned to a strategy allowing to precisely control the width of our cantilever. To do so, we used pulled glass rods. When glass rods are pulled, the section of the rod can be considered conical towards its end and the tip is extremely thin (submicron). Therefore, the stiffness can be varied by severing the end of the rod at various lengths. To do so, we melted the tip using a microforge. This technique allowed us to precisely monitor the tip diameter as it melts. We typically used rods with tips of 2-3 μm of diameter. We then glued a rectangle of aluminum foil at the tip in order to probe areas at the tissular scale (see Figure 5.3 B). The aluminum probe was typically 500 μm long, 150 μm wide and 25 μm thick. The probe was glued to the rod tip under a microscope by approaching the rod tip, that was previously soaked in a UV polymerizing glue. The cantilever was subsequently glued to a holder made of a pulled glass capillary, so the base of the cantilever was as fine and transparent as

A

B
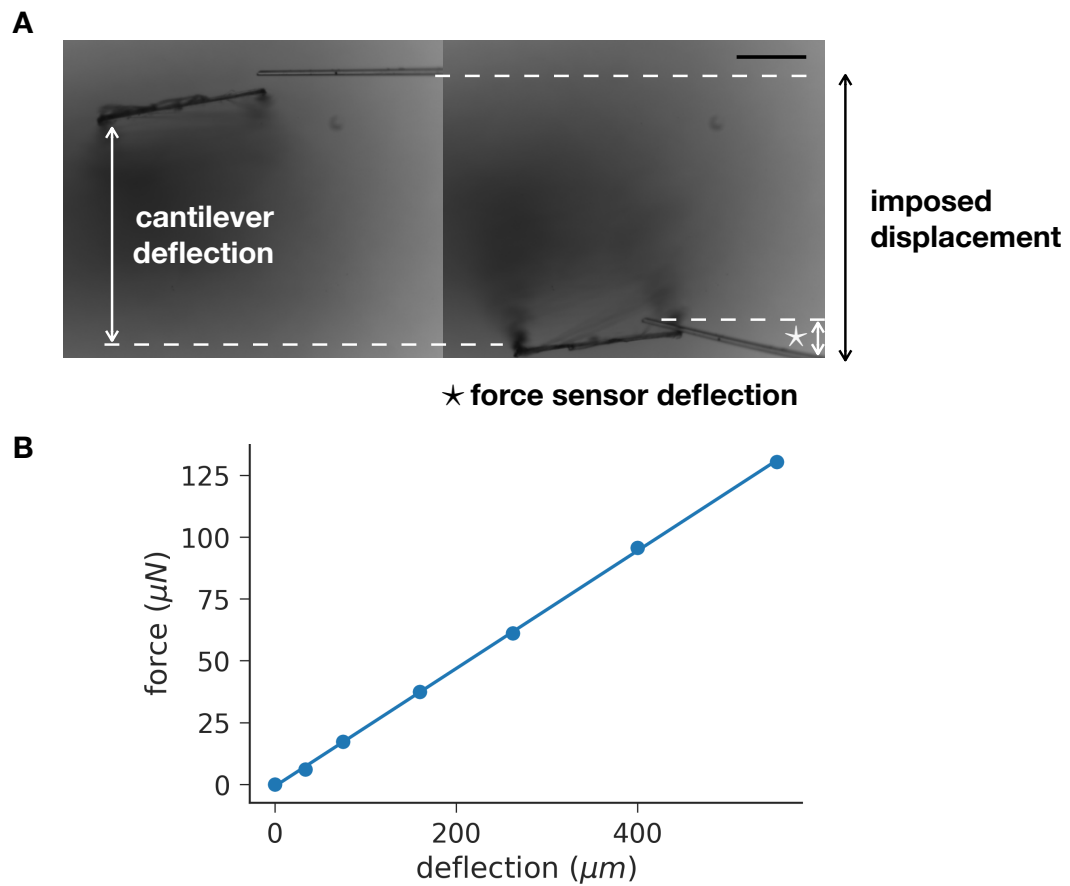
FIGURE 5.4 – Mica cantilever calibration. **A**: Snapshots of a deflection experiment (left picture: before deflection, right picture: deflected). Scale bar: 250 µm. **B**: Force-deflection curve. Linear regression yields a stiffness of $0.24 \, \text{N} \cdot \text{m}^{-1}$.
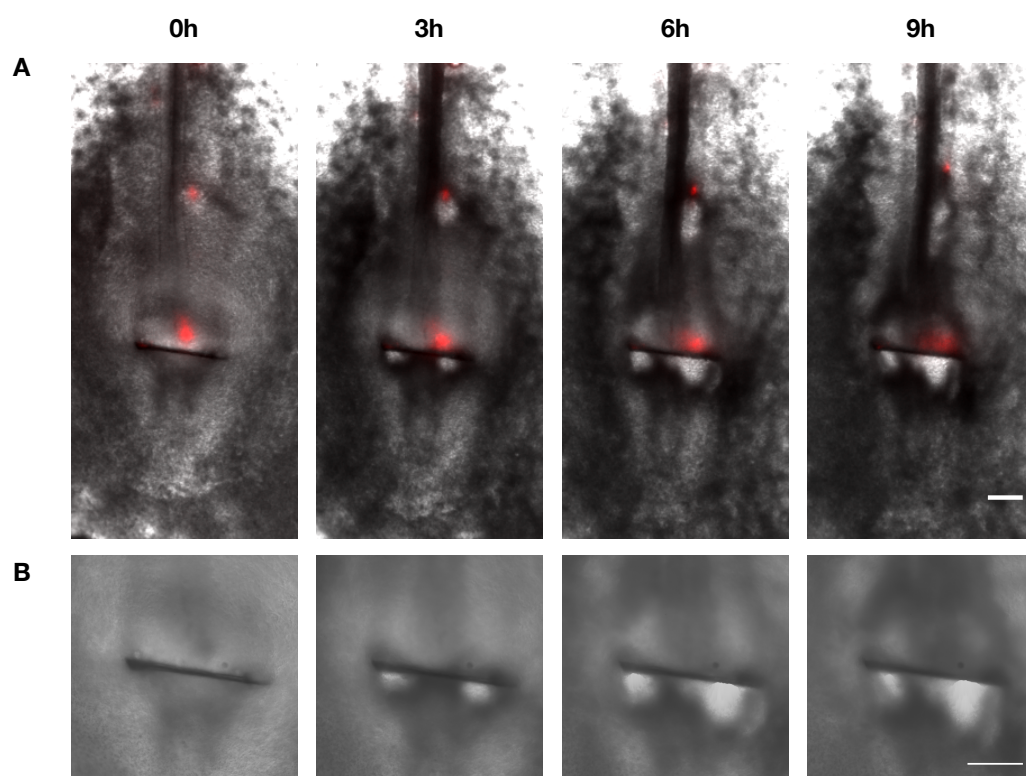
FIGURE 5.5 – *In vivo* insertion of a mica cantilever. Snapshots of an elongation movie at low magnification (**A**) and high magnification (**B**). Red: spot of DiI injected prior to experiment. Scale bars: 200 μm

possible. In this way, we reduced the shadow cast over the region of the cantilever insertion.

Once fabricated, the challenge was to calibrate these cantilevers. As they did not have regular geometries, and the glue at the tip could change their stiffness, we could not rely on any theoretical calculation. The contact method with a force sensor we used for the mica cantilever was not conceivable as the force sensor was several orders of magnitude stiffer. Indeed, we could not produce softer force sensors using the hanging weights calibration, as it would have required masses below the scale precision (milligram). We, therefore, used a direct method based on the resonant frequency of the cantilever which depends on its mass and its stiffness.
If we assume that all the mass is concentrated within the aluminum probe, the resonant frequency $f^\star$ is related to the stiffness k and the probe mass m (which is calculated using the volume of the probe and the aluminum density):

$$f^\star = \frac{1}{2\pi}\sqrt{\frac{k}{m}} \tag{5.3}$$

The assumption that all the mass is concentrated in the aluminum probe is reasonable since its volume is about 3 orders of magnitude larger than the rod, and both have similar densities ($\rho_{borosilicate} = 2230 \, \text{kg} \cdot \text{m}^{-3}$ and $\rho_{aluminum} = 2700 \, \text{kg} \cdot \text{m}^{-3}$).

The resonant frequency of the rod was measured by filming the oscillations of the cantilever with a high-speed camera (at 8,000 frames per second) after a perturbation (a gentle blow) (see Figure 5.6 A and Movie 11). The oscillations were tracked using a skeletonized kymograph of the movie (using the Fiji software) which yielded the coordinates of the tip of the cantilever over time (see Figure 5.6 B). The resonant frequency was then extracted by Fourier transform after smoothing the deflection data by moving average subtraction (see Figure 5.6 C). However, this technique did not allow us to explore the linearity range of the cantilever, as a force-displacement calibration would have.

In this way, we fabricated aluminum cantilevers with stiffness ranging from 1 to 100 $\text{mN} \cdot \text{m}^{-1}$.

5.1.3 Measurement of embryo stalling stress

In order to measure the stalling stress, we vertically inserted an aluminum cantilever in the posterior region of the embryo and monitored its deflection over time.

Measurement procedure

We envisioned a potential pitfall to our cantilever-based measurement of the posterior movements. As the cantilever is deflected, its resistance to the movement could make the embryo slip towards the anterior. In this case, the posterior pushing force would have been converted into an anterior force. To tackle this issue, we tried to force the embryo to elongate only posteriorly by blocking any anterior movement. To do so, we thrust a U-shape pin over the midline structures in the somitic region (see Figure 5.7). However, the anterior movements could not be blocked in this way, and the somites were sliding under the pin. We also tried more stringent blockages by cutting the embryo along the ML axis in the somitic region and inserting an aluminum foil based wall. These harsher treatments all led to the death of the embryo
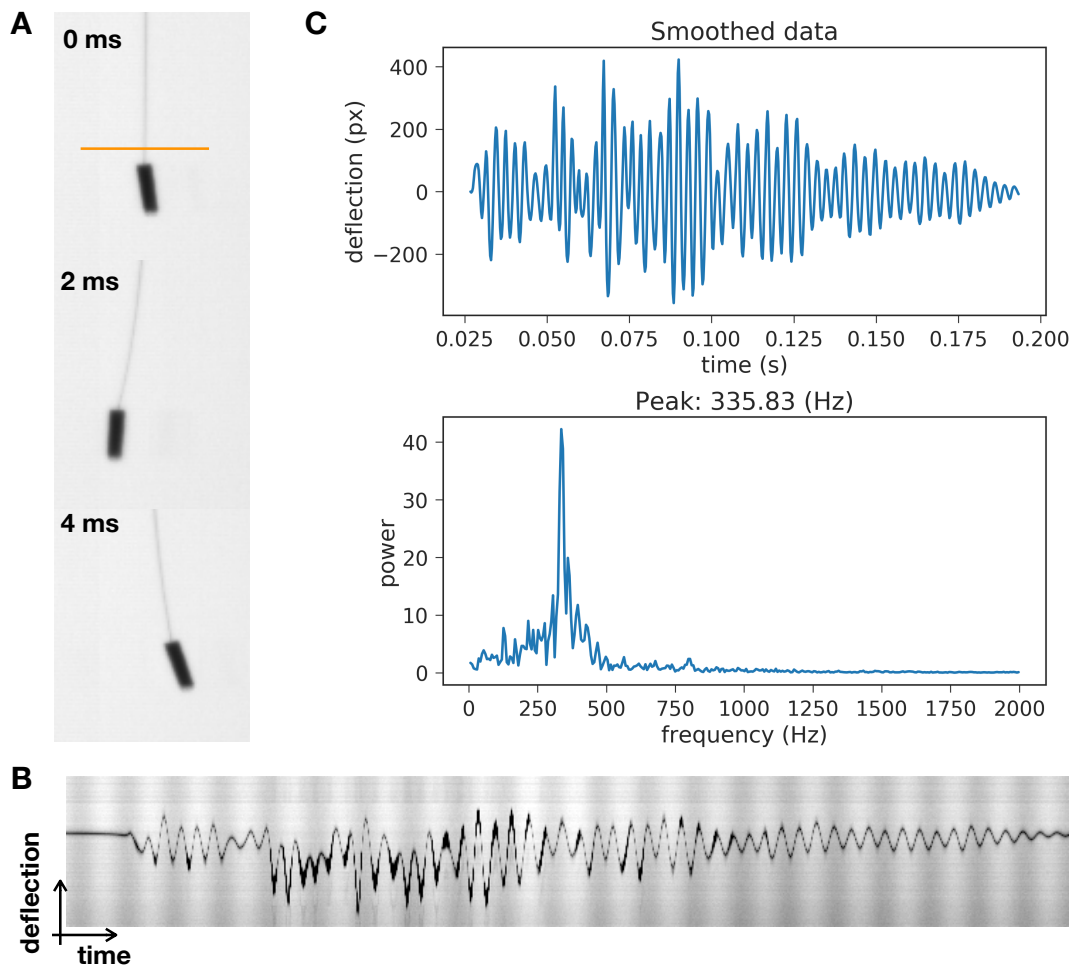
FIGURE 5.6 – Calibration of a glass rod cantilever. **A**: Snapshots of a high speed camera movie during oscillations of the cantilever. **B**: Kymograph along the orange line (top panel of **A**). **C**: Top panel: smoothed deflection data by moving average subtraction. Bottom panel: power spectrum obtained by Fourier transform.
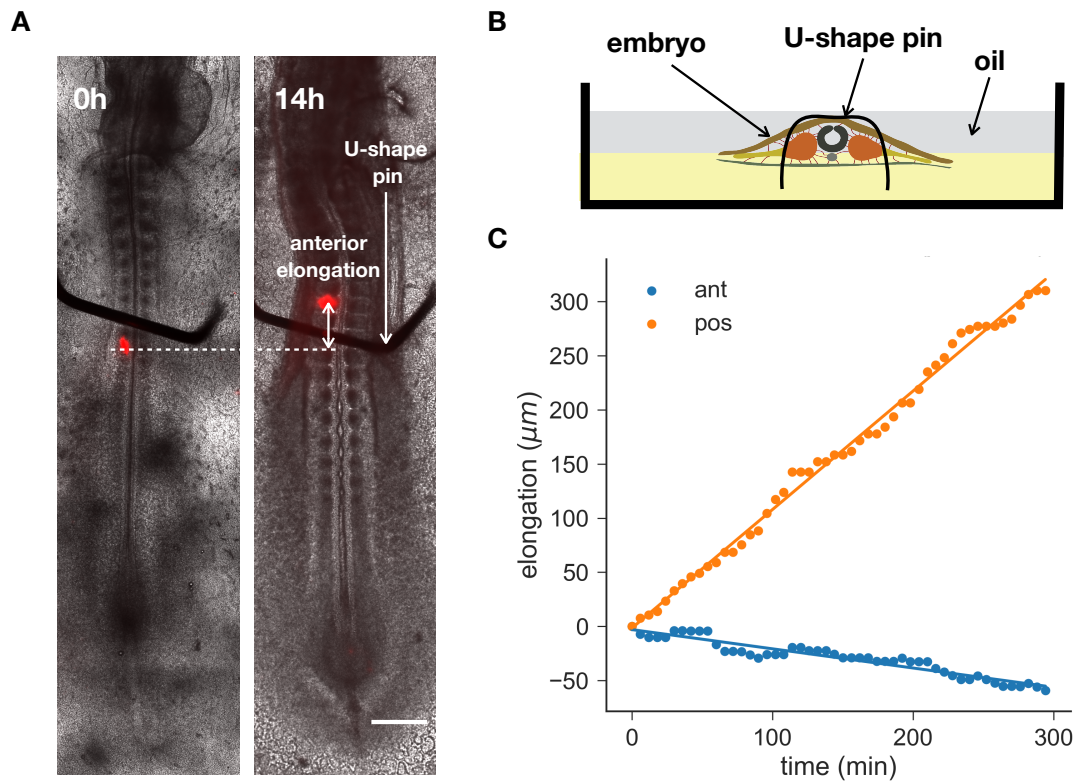
FIGURE 5.7 – Anterior movements during elongation. **A**: Snapshot before and after an elongation with U-shape pin. Red: spots of DiI injected prior to the experiment. Scale bar: 500 μm. **B**: Schematic of the U-shape pin insertion (side view). **C**: Elongation along AP axis of the posterior end and the anterior end, in the referential of the pin. Posterior movements are defined as positive and anterior movements as negative.

or highly impaired development. It seemed, therefore, challenging to force the embryo to elongate only posteriorly. In addition, as it was presented above, when a very stiff wall (like a mica cantilever) is inserted in the tail, the posterior movements are not arrested but the tissue flows around and is torn. This suggests that a posterior blockage cannot be converted into an anterior force all along the AP axis. For these reasons, we decided to measure only the posterior force without preventing any anterior movements.

We monitored the embryonic elongation speed in parallel, so we could assess the impact of the measurement on the embryo. To do so, we had to have at the same time a wide field of view of the whole embryo and a zoomed view on the cantilever region. Wide fields of view are usually obtained by stitching together high-resolution microscopy images over large regions of the embryo. It requires to move the microscope stage to different locations. However, the base of the cantilever does not move with the stage (as the micromanipulator cannot be fixed on the stage). As a result, moving the stage would have introduced relative movements with respect to the cantilever. Such movements would have most likely broken the cantilever or torn the embryo. A prerequisite of this measurement was, therefore, to keep the microscope stage fixed. We thus imaged the embryo axis with a wide field objective (2.5X, numerical aperture 0.07) while the cantilever was imaged with a higher resolution objective (10X, numerical aperture 0.3). We identified two limitations to using a 2.5X

objective. First, due to its small numerical aperture, the wide field image quality was notably lower than classical microscopy imaging. This was a strong limitation, as we routinely manually track visual features along the axis to measure the elongation (last formed somite and the Hensen's node). In addition, fluorescently labeled nuclei cannot be resolved with such a resolution. Consequently, no cell motility measurement is possible with a 2.5X objective. Secondly, even though the field of view was wider, it did not allow us to image the whole body. It did not encompass more than the 2-3 last formed pairs of somites. So, when the somites moved anteriorly during the elongation, they were going out of the field of view, which prevented us from tracking the elongation for a long time. On top of these difficulties, the cantilever cast a shadow over its insertion region which further decreases the imaging quality.

To tackle these imaging issues, we made visual landmarks by injecting small spots of DiI (a lipophilic fluorescent dye). These fluorescent spots are extremely bright and could be easily tracked. We injected DiI in the posterior region and in the anterior PSM, so that when the last formed somites went out of the field of view, we could track other anterior landmarks allowing us to measure the anterior movements (see Figure 5.8 and Movies 12, 13).

For a typical stress measurement experiment, a 12-somite embryo was placed under an inverted microscope after DiI labeling. A layer of mineral oil was then added on top. It was left equilibrating for an hour, due to adjustment of the system to the temperature. Elongation was then monitored without any cantilever for a duration of 2 hours so the elongation speed without any constraint could be measured. The cantilever was then inserted on the ventral side (so its deflection was not impaired by the vitelline membrane) and the deflection and elongation were monitored for typically 12 hours (overnight).

Elongation and stalling stress measurement

Cantilevers of different stiffness were used to measure the stress production during elongation. Depending on the cantilever stiffness k, the deflection dynamics varied:

- for $k > 50 \, \mathrm{mN \cdot m^{-1}}$, there was no deflection and the cantilever acted as a stiff wall (like in the case of mica cantilevers);

- for soft cantilevers ($k \sim 1 \, \mathrm{mN \cdot m^{-1}}$), the deflection was linear over time and did not seem to perturb the elongation (see Figure 5.9 A);

- for cantilevers of intermediate stiffness ($k \sim 10 \, \mathrm{mN \cdot m^{-1}}$), the deflection was saturating after some time and a maximum stress could be measured (see Figure 5.9 B, C).

We first analyzed the impact of the stress measurement on the elongation rate. The elongation rate is measured by linear regression of the axis length over time. The axis length is measured by tracking the movement of the anterior spot of DiI with respect to the Hensen's node.

We noticed that the elongation rate decreases upon cantilever insertion. We define the elongation rate reduction $\Delta r = r_0 - r$, where r_0 is the elongation rate prior to cantilever insertion and r the elongation rate during stress measurement. We noticed that on average $\Delta r = 0.54 \pm 0.51 \, \mathrm{\mu m \cdot min^{-1}}$. However, Δr does not depend on
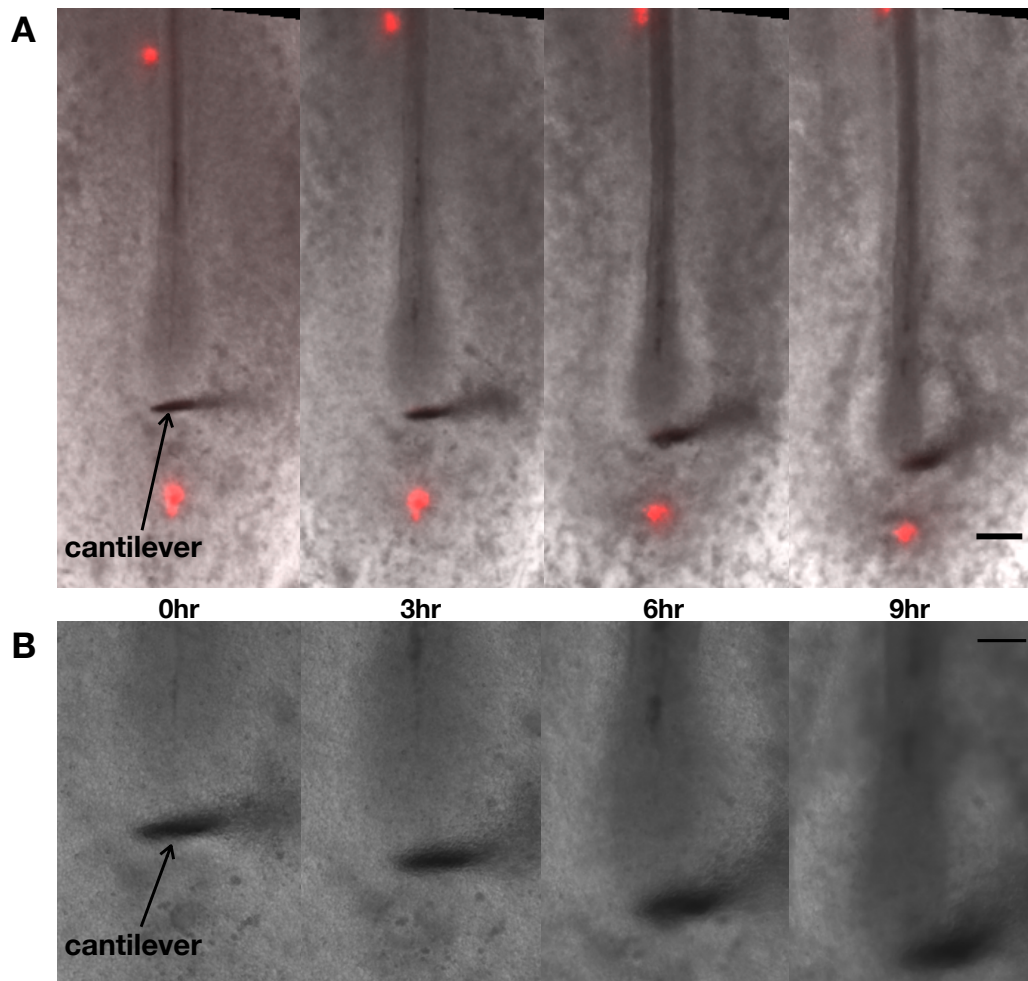
FIGURE 5.8 – Stress production measurement. Snapshots of an elongation with a cantilever inserted in the posterior region, wide field of view of the axis (**A**) and zoom on the cantilever (**B**). Red dots: DiI landmarks. Scale bars: 200 µm (**A**) and 100 µm (**B**).
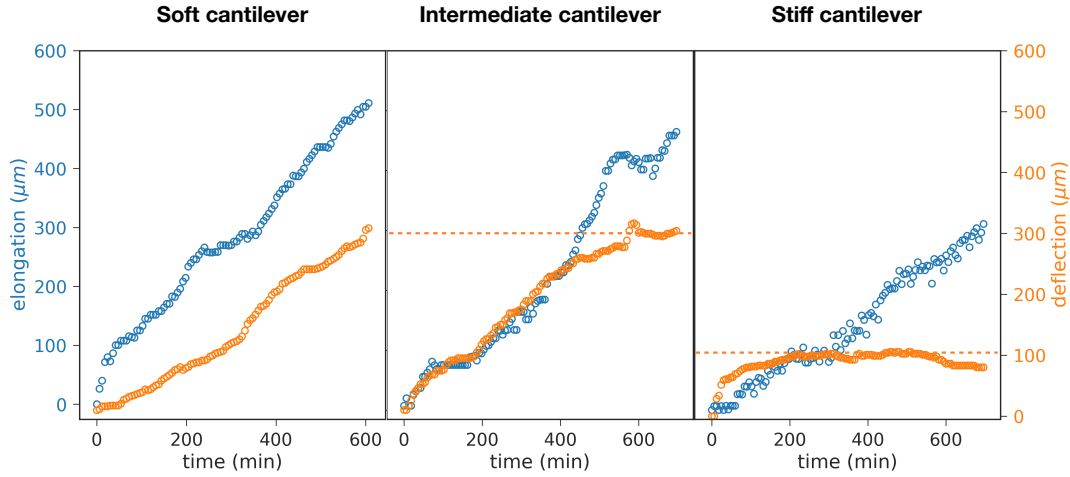
FIGURE 5.9 – Axis elongation and cantilever deflection for three embryos with various cantilever stiffnesses k. Left panel: soft cantilever, $k = 2$ mN $\cdot$ m^{-1}. Center panel: intermediate stiffness, $k = 7$ mN $\cdot$ m^{-1}. Right panel: stiff cantilever, $k = 17$ mN $\cdot$ m^{-1}. Dash lines indicate deflection plateaus.

the cantilever stiffness (see Figure 5.10 A)

We next analyzed the stalling stress measurements. To do so, we measured the deflection plateau of saturating experiments. We discarded experiments for which the deflection was negligible (with extremely stiff cantilevers) because the measurement would have been too noisy. Consequently, we considered only experiments with a minimal deflection plateau of 30 μm (larger than the thickness of the probe). Measuring the deflection plateau gave us directly the stalling force. In order to get the stress, we estimated the area of contact between the probe and the tissue. To do so, we brought the probe in contact with the surface of the endoderm and we focused the focal plane on the tip of the probe. Contact could be noticed by observing a slight movement of the tissue. We then inserted the cantilever down to the ectoderm and measured the difference between the two focal planes. The insertion depth was typically between 70 and 90 μm, which is coherent with the known thickness of the embryo. The area of contact was then the product of the probe width (which is imaged by microscopy, typically 250 μm) and the estimated insertion depth. Thus, the typical contact area was 20,000 μm^2.
The stalling stress was on average 114.1 ± 26.4 Pa. We observed a weak dependency of the stalling stress with respect to elongation rate prior to cantilever insertion r_0 and elongation rate r (see Figure 5.10 B, C). Both exhibit poor linear correlations (respectively $R^2 = 0.15$ and $R^2 = 0.05$). We also noticed that embryos generate greater stress when stiffer cantilevers were used (a better linear correlation was observed, $R^2 = 0.69$, see Figure 5.10 D). This result parallels the stress production accommodation that was noticed in *Xenopus* dorsal explants (Zhou et al., 2015).

In summary, we have presented a first set of measurements of stress production during axis elongation in the chicken embryo. The maximum stress the whole axis can produce is on average 114 Pa. Interestingly, this stress is in the same order of magnitude as the posterior tissue stiffness, which means it can generate substantial deformation. In order to better understand the role of the PSM in this stress production, its individual contribution must be assessed.
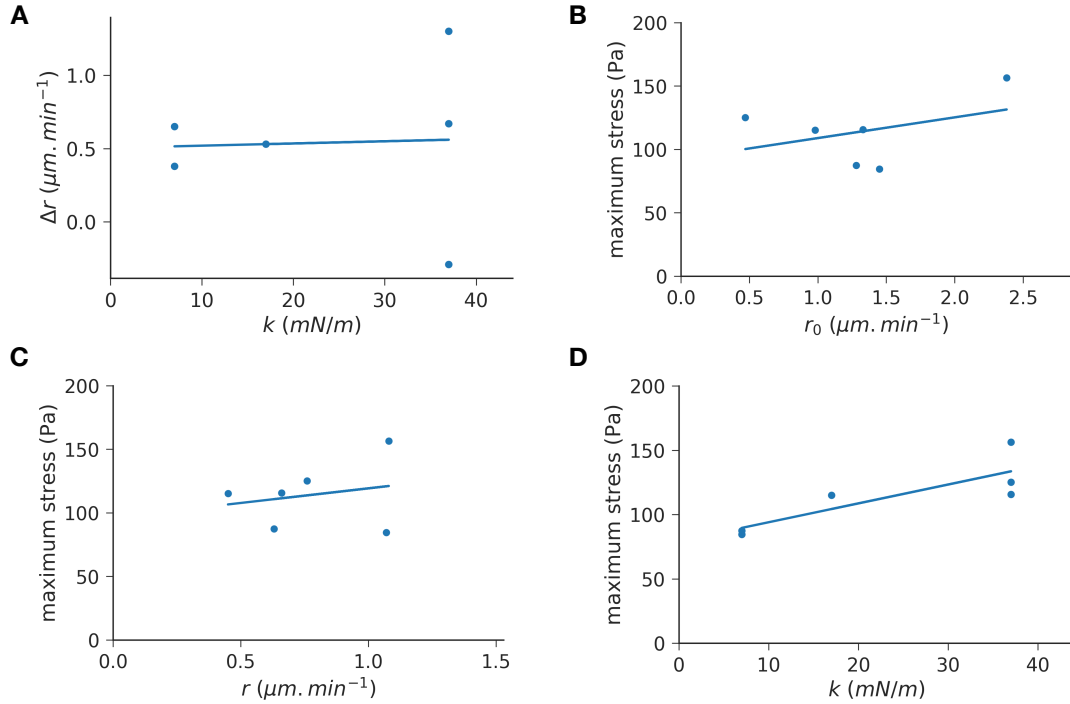
FIGURE 5.10 – Maximum stress production. **A**: Elongation rate decrease upon cantilever insertion. Maximum stress production with regard to prior elongation rate (**B**), elongation rate (**C**), cantilever stiffness (**D**). Solid lines: linear regression.

5.2 Measurement of the presomitic mesoderm stress production *in vitro*

In order to measure the force production of the PSM alone, we needed to isolate it from the rest of the embryo. However, as shown in Chapter 3, when PSM explants are dissected out of the embryo and cultured, they deform to a typical pear shape (as the posterior round up more than the anterior). Therefore, without the confinement of its neighboring tissues, the potential PSM extension cannot be monitored. Consequently, we decided to mimic the PSM confinement by using PDMS microchannels. To do so, we devised a design allowing us to, first, monitor PSM extension and the cellular movements and, second, measure stress production by an isolated PSM.

5.2.1 Microchannels preparation

We microfabricated an array of PDMS channels, closed on top by a glass coverslip. The detailed protocol of microfabrication of the channel mold is presented in materials and methods (Chapter 7) but we quickly review it here. We designed our array of channels to be of variable widths: 3 series of 4 channels of respectively 60, 75 and 90 µm, so we could try different confinements (see Figure 5.11). A larger channel (1 mm wide) around the array of microchannels was designed to leave room for manipulation of the PSM during insertion in the channel. A 150 µm thick sheet of commercially available photosensitive resin (SUEX) was laminated onto a silicon wafer. The resin was UV-exposed following our design and then developed. The resulting resin mold was used to produce PDMS microchannels.
The array of microchannels was subsequently closed on top by a glass coverslip. The

FIGURE 5.11 – Microchannels array fabrication. Schematic of the microchannels array in top view (**A**) and zoomed side view (**B**). **C**: Picture of the microchannels array. Scale bar: 250 μm.

edge of the coverslip was positioned at the edge of the array of microchannels so an opening was left to slide the PSM in. In order to reduce adhesion of 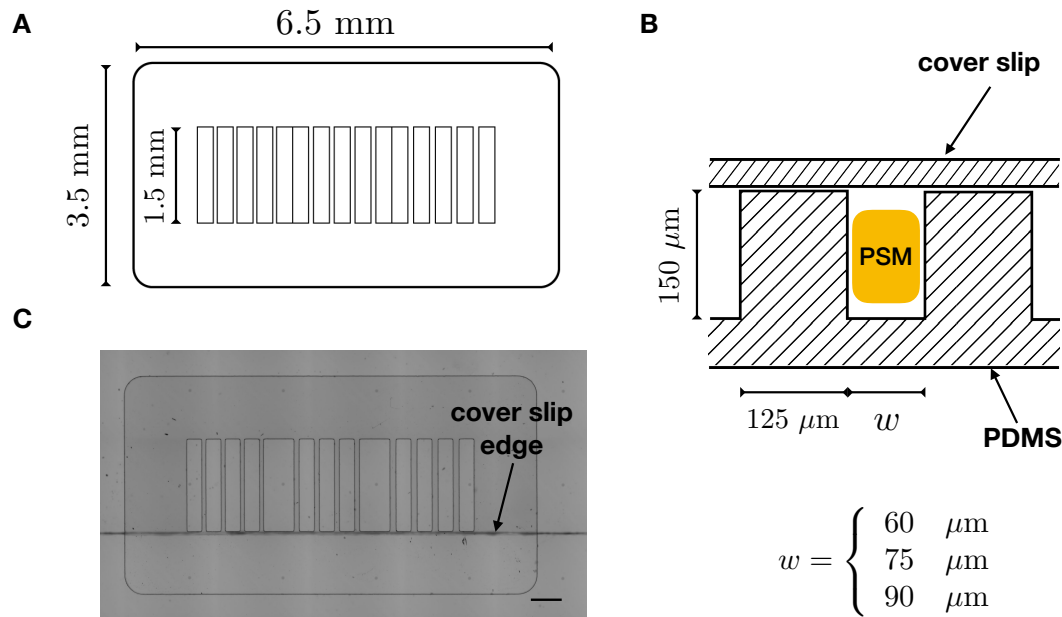the PSM cells to the coverslip, the coverslip was coated with a 0.3 mg/mL PEG-PLL solution (in 10 mM HEPES) for 1 hour. The coating solution was injected by removing air bubbles in the microchannel using a vacuum chamber. The channels were then rinsed with PBS and incubated with DMEM-F12 supplemented by 10% FBS at 37°C and 7.5% CO_2 before adding PSM explants.

5.2.2 Elongation of presomitic mesoderm explants in microchannels

We first wanted to investigate if PSM explants are able to elongate when isolated from the embryo. To do so, we dissected out PSM explants from 12 to 14-somite stage embryos, using the collagenase-based protocol presented section 3.2.1. PSM explants were subsequently carefully slid into the microchannels. The microchannel array was next placed under an inverted microscope at 37°C and 7.5% CO_2 and typically imaged overnight.

We first observed that PSM explants were viable for about 10 hours and were able to produce up to 4 somites (see Figure 5.12 A and Movie 14). Therefore we considered that our culture protocol was suitable. We next noticed that because of the low adhesion with the PDMS wall, explants had a tendency of sliding along the channel, especially towards the anterior end. We attributed this behavior to the fact that posterior PSM rounds up faster than anterior PSM and, therefore, gets compressed by the walls before the anterior end. When the posterior end is compressed by the walls, the anterior end is not and it slides. Therefore, there is an anterior-ward slippage. Finally, we noticed that when a PSM slid out of the channel, it would start rounding at its free extremity and it would pull on the rest of the PSM (see Figure 5.13 A). This behavior is similar to the retraction phase during a pipette aspiration experiment, the surface tension pulls on the rest of the tissue to eventually form a sphere. As the size of the free spherical end grows the pulling force increases, as it

was shown in analogous experiments on oil slug capillary extraction (Piroird et al., 2011).

We next characterized the PSM structure after confined elongation. After a 6-hour elongation, PSM explants were fixed by means of 4% paraformaldehyde (PFA) within the microchannel. When we removed them from the microchannels, we could observe the explants had taken the whole available volume and exhibited the channel parallelepiped shape. We observed that the filamentous actin (F-actin) was enriched at the location of somite formation (see Figure 5.13 B). The PSM displayed in Figure 5.13 B was fixed after undergoing an aforementioned channel extraction and rounding of its extremity, hence its rounded shape in the posterior region. We could observe that the F-actin network was developed in the rounding posterior region, suggesting an important mechanical activity. We also investigated the expression of the chicken homolog of Mesogenin1 (Msgn1), CMESPO. Msgn1 is a marker of PSM differentiation. It exhibits a graded expression along the PSM (strong expression in the posterior region, and repressed in the anterior). We could see that the CMESPO positive cells were restricted to the posterior-most region after 6 hours in a channel (see Figure 5.13 B), suggesting that a large part of the PSM differentiated during the culture within the channel.

We next analyzed the elongation dynamics. We first observed a contraction of the tissue during 1-2 hours that we attributed to the tissue filling the available volume around it. After, the contraction phase, we could see an expansion phase during which the length of the explant ℓ increases at a linear rate for a variable time of 2-6 hours and then saturates. We measured the elongation ratio defined as the difference between the maximal PSM length ℓ_{max} and its minimal length ℓ_{min} (at the end of the contraction phase), normalized by the minimal length: $\frac{\ell_{max}-\ell_{min}}{\ell_{min}}$. On average PSM explants extends by $19.3 \pm 10.3\%$ (see Figure 5.14 A and Table 5.1)
In order to identify the region responsible for this elongation, we monitored the elongation on PSM halves. We noticed that posterior regions elongated significantly more than anterior regions (Student's t-test p-value=0.016). Therefore, PSM extension is predominantly driven by posterior growth, which correlates with the key role of posterior PSM demonstrated *in vivo* (Bénazéraf et al., 2010, Bénazéraf et al., 2017).

We next studied the elongation rate during the linear growth phase (see Figure 5.14 B and Table 5.2). Surprisingly, no significant difference could be noticed between regions. However, the dispersion of the elongation rate would require a higher statistical power to be conclusive. Indeed, more data are needed regarding PSM halves (anterior: $n = 3$, posterior: $n = 4$). On average PSMs elongate at 0.39 ± 0.17 μm/ min, which is about a quarter of the embryo elongation rate. While different regions elongate at the same rate, the aforementioned difference in total elongation can be explained by a longer duration of elongation in the posterior region.

We next investigated the role of the FGF8/MAPK gradient in elongation by monitoring the growth of explants cultured with a MAPK inhibitor PD0325901. We observed that elongation was impaired in a dose-dependent fashion upon PD0325901 treatment. Inhibition by 2 μM PD0325901 led to an elongation of full PSMs of $7.9 \pm 6.7\%$, whereas elongation was almost abolished upon a 10 μM treatment. Moreover, a similar pattern of greater elongation in the posterior region was kept, with posterior halves elongating by $28.1 \pm 7.0\%$ upon 2 μM treatment. Elongation speed

A

B
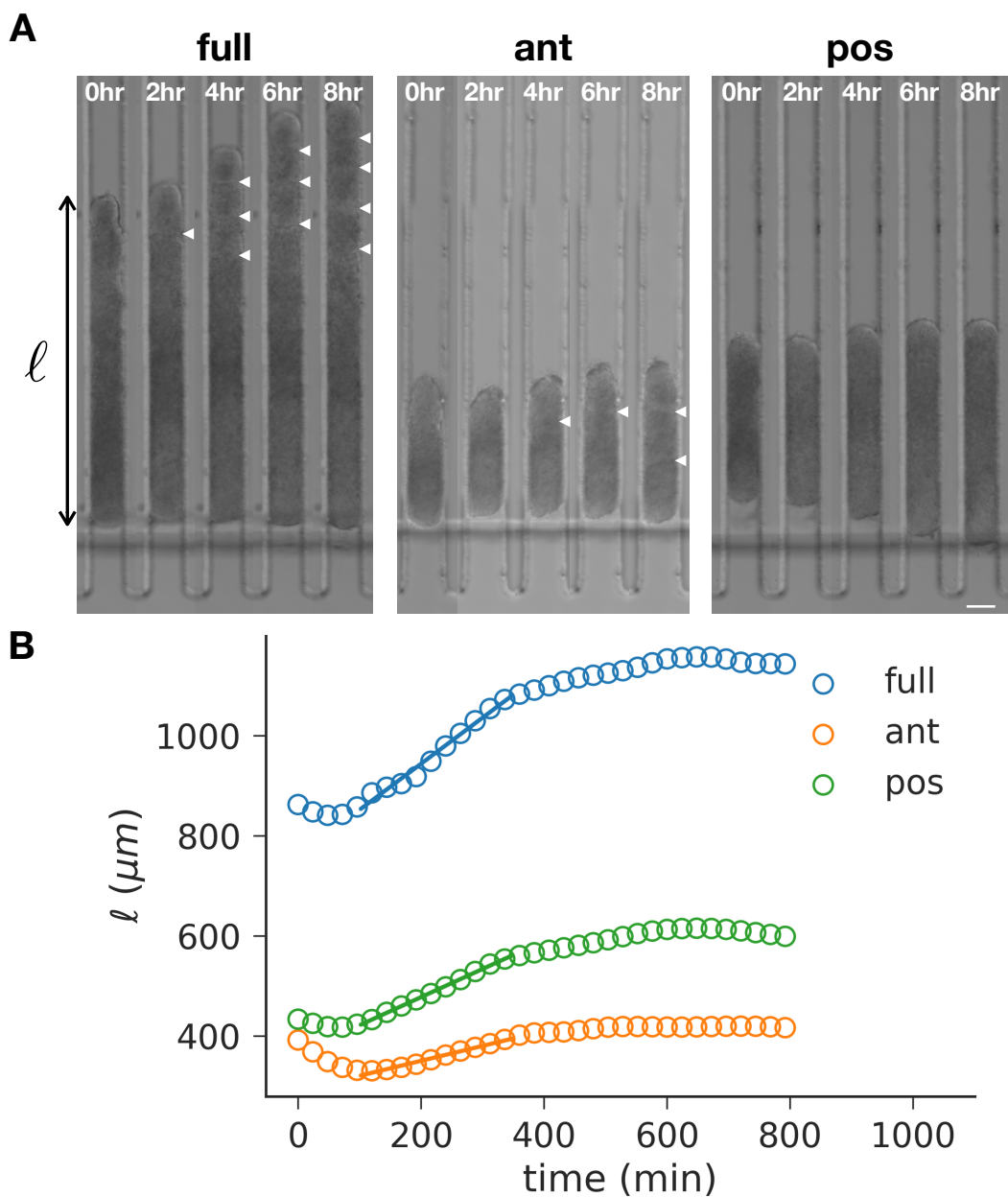
FIGURE 5.12 – Elongation of isolated PSM explants. **A**: Snapshots during explant elongations (full: full PSM explant, ant: anterior half of a PSM explant, pos: posterior half of a PSM explant). Scale bar: 75 µm. White arrow heads indicate inter-somitic clefts. Anterior ends are up. **B**: Explant length over time.

TABLE 5.1 – PSM explant elongation ratio (mean and standard deviation).

	Full PSM	Anterior PSM	Posterior PSM
control (%)	19.3 ± 10.2	16.1 ± 11.1	56.5 ± 13.8
2 µM PD0325901 (%)	7.9 ± 6.7	5.0 ± 4.4	28.1 ± 7.0
10 µM PD0325901 (%)	2.2 ± 4.0	8.4 ± 3.7	18.6 ± 7.4
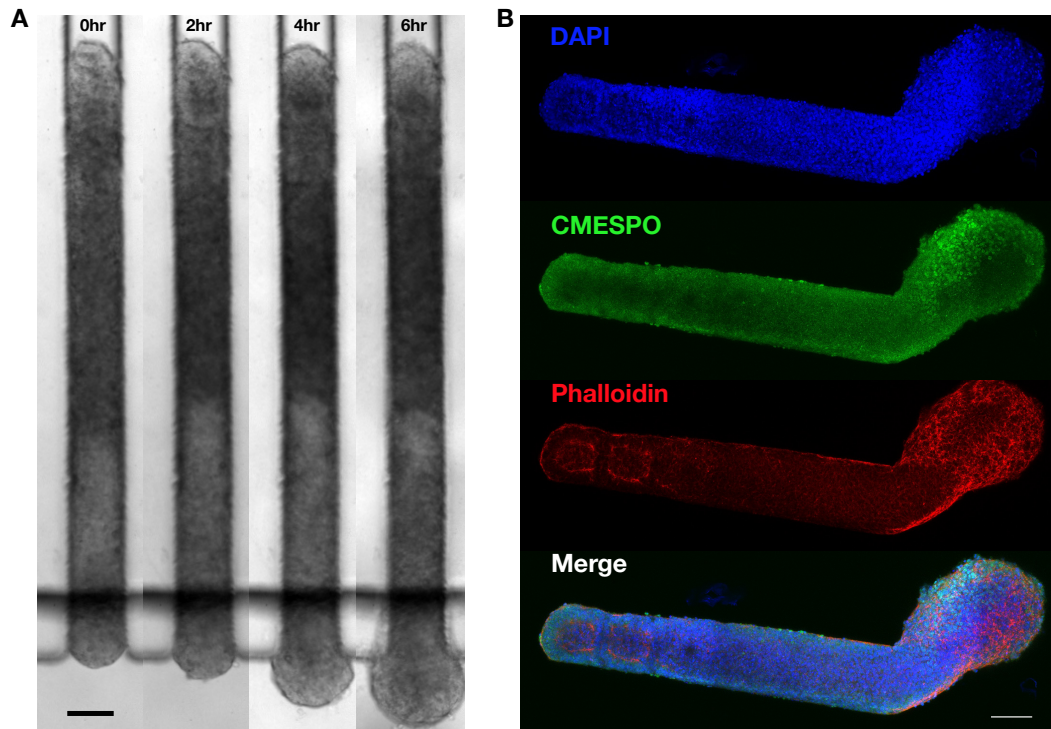
FIGURE 5.13 – Structure of PSM explant after elongation. **A**: Snapshots during a surface tension driven extraction of a full PSM explant from a microchannel. Scale bar: 75 μm. **B**: Structure of a PSM explant after a 6-hour elongation. Maximum projection of a confocal stack. Scale bar: 100 μm. Anterior is left, posterior is right.
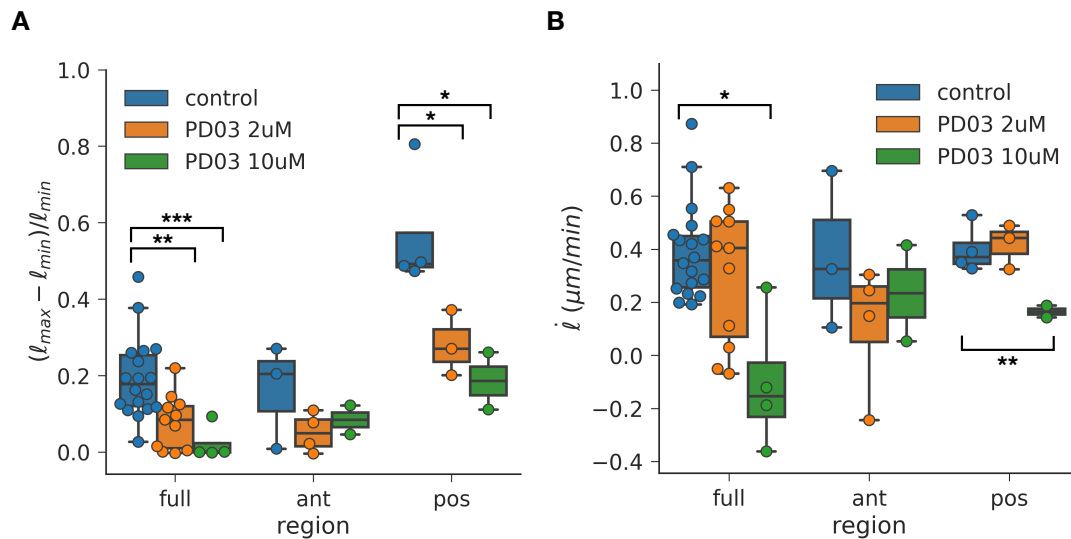
FIGURE 5.14 – Elongation ratio (**A**) and elongation rate (**B**) of isolated PSM explants (full: full PSM explant, ant: anterior half of a PSM explant, pos: posterior half of a PSM explant). P-value p of Student's t-test between culture conditions (PD03 abbreviates for PD0325901): $\star$: $p < 0.05$, $\star\star$: $p < 0.01$, $\star\star\star$: $p < 0.001$. If not indicated, $p > 0.05$.

TABLE 5.2 – PSM explant elongation rate (mean and standard deviation).

	Full PSM	Anterior PSM	Posterior PSM
control ($\mu m \cdot min^{-1}$)	0.39 ± 0.17	0.37 ± 0.24	0.39 ± 0.07
2 μM PD0325901 ($\mu m \cdot min^{-1}$)	0.30 ± 0.24	0.11 ± 0.21	0.41 ± 0.06
10 μM PD0325901 ($\mu m \cdot min^{-1}$)	-0.10 ± 0.22	0.23 ± 0.18	0.16 ± 0.02

was not significantly different upon 2 µM treatment but the elongation duration was reduced, explaining the difference in total elongation. However, 10 µM treatment led to significantly slower elongations. The PSM was often constricting, yielding a negative elongation rate. The posterior region kept elongating but at drastically reduced pace compared to control explants.

In summary, we showed that PSM explants are able to elongate when confined by a stiffer environment in a similar geometry as *in vivo*. A major part of this elongation arises from the posterior region. In addition, PSM elongation depends on FGF8/MAPK activity. FGF8/MAPK controls in particular cell motility, which has been shown to be directly linked to embryo elongation *in vivo*. The role of motility *in vitro* is addressed in the following section.

5.2.3 Motility of the presomitic cells in microchannels

We next measured the motility profile along the PSM, to check if the motility gradient observed *in vivo* (Bénazéraf et al., 2010) is maintained *in vitro*. To do so, we mosaically labeled cell nuclei by electroporating PSM progenitors with an H2B-RFP construct. Cell movements were monitored by wide-field fluorescent microscopy. Therefore, movements in the vertical direction (dorso-ventral axis) could not be measured. We restricted our analysis to 2D movements. Cell nuclei were automatically segmented and tracked using the Fiji plugin Mosaic (Sbalzarini and Koumoutsakos, 2005).

To analyze cell trajectories, we wrote a custom visualization and analysis Python-based toolkit. This toolkit can also be used for 3D trajectories, as it was developed to analyze cell movements in the primitive streak (see other projects in Appendix C.1). This toolkit offers flexibility to visualize trajectories depending on several criteria, in particular, it can be used to back-track regions and draw fate maps. It also offers the ability to draw velocity maps, compaction-expansion maps, and cell fluxes through a surface.

Since a non-negligible slippage of the PSM within the channel was observed, the movement of the PSM anterior end was subtracted from each cell trajectory. We observed unexpected tissular flow in the posterior region, exhibiting rotating movements. On the PSM sides, cells exhibit directional movements towards the posterior end, they rotate at the PSM end and move towards the anterior in the middle of the PSM (see Figure 5.15 and Movie 15). We highlighted these movements by plotting the instantaneous velocity along the $\overrightarrow{y}$ axis (AP axis) v_y. Cells at the periphery exhibit posterior movements ($v_y > 0$), whereas cells in the middle show anterior movements ($v_y < 0$). This kind of trajectories has never been observed *in vivo*. We hypothesized it might be due to the lack of adhesive interface between the PDMS
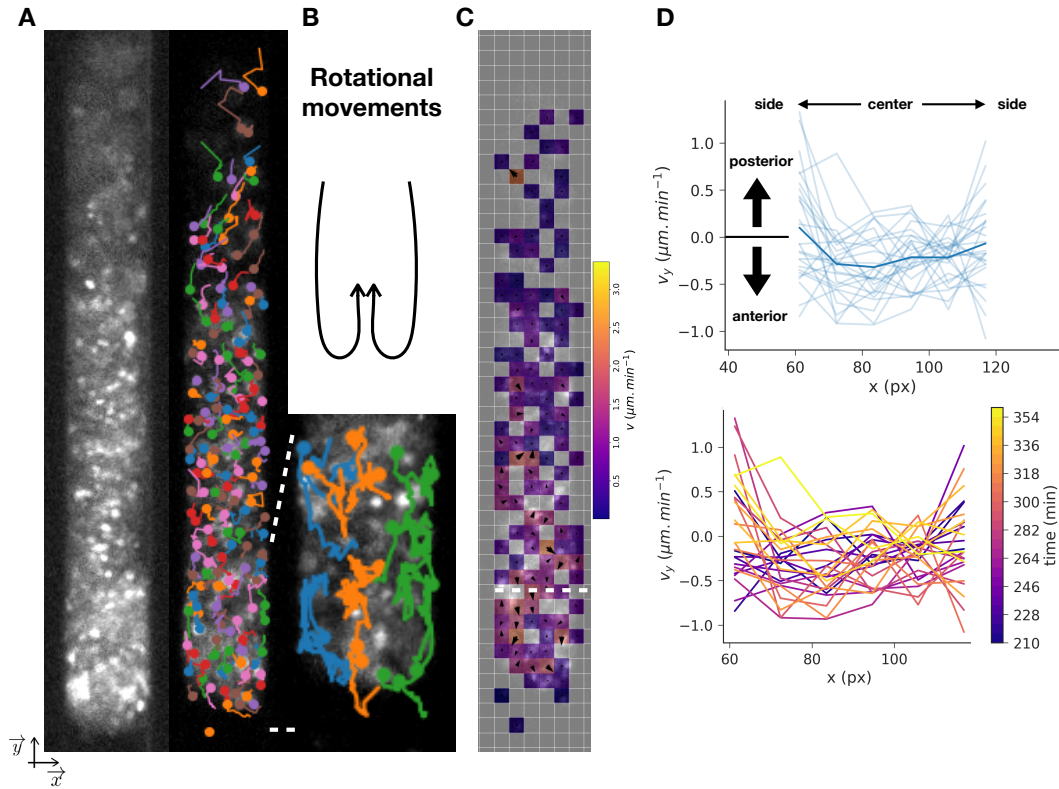
FIGURE 5.15 – Cellular movements within an isolated PSM. **A**: Cell tracking in the PSM. Left panel: H2B-RFP electroporated PSM. Right panel: tracked cells trajectories. **B**: Rotational movements in the posterior region. Top panel: schematic of the rotational movements. Bottom panel: zoom on the trajectories of the posterior regions. 3 groups of cells are highlighted: cells against the left wall (blue), cells in the middle (orange), cells against the right wall (green). **C**: Instantaneous velocity map of the PSM. **D**: Velocity component along $\overrightarrow{y}$ axis (AP axis) v_y along over time and along the section of the PSM. The section along the $\overrightarrow{x}$ axis (ML axis) is shown as a dashed line in **C**. Positive v_y are defined as posterior movements, and negative v_y are defined as anterior movements. Top panel: individual profiles over time are in light blue, time average profile in deep blue. Bottom panel: individual profiles over time are color coded.
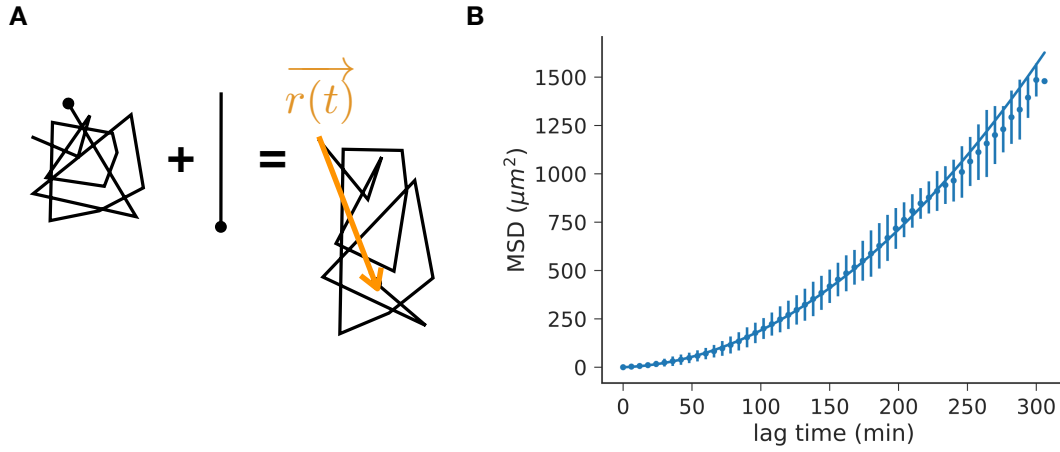
FIGURE 5.16 – Mean squared displacement of a diffusing cell within a flow. **A**: Schematic of the trajectory of a diffusing cell within a flow. **B**: Mean squared displacement of cell with respect of lag time. Points are average for each lag time. Error bars show standard deviation for each lag time. Solid line: fit by Equation 5.4 weighed by invert of standard deviation, yielding $D = 0.06 \ \mu m^2 \cdot min^{-1}$ and $\langle v \rangle = 0.13 \ \mu m \cdot min^{-1}$

walls and the PSM, but more investigation needs to be conducted.

In order to analyze the profile of cell motility along the PSM, we measured the cell diffusion coefficient. To do so, we calculated the mean squared displacement (MSD) $\langle \Delta r^2(t) \rangle$ using the lag time method. For each interval of time (lag time), we calculated the squared displacement between any time of the trajectory separated by such a lag time and averaged the squared displacements. The number of calculated squared displacements decreases, thus the statistic deteriorates, as the lag time increases.

We assumed the cell movements could be described by a 2D random walk of diffusion coefficient D, within a directional flow $\langle v \rangle$ (see Figure 5.16 A). The mean squared displacement is then written:

$$\langle \Delta r^2(t) \rangle = 4Dt + \langle v \rangle^2 t^2 \tag{5.4}$$

We calculated the MSD for all trajectories longer than 15 frames (1.5 hours) and fitted it with Equation 5.4 weighing each lag time with the invert of the associated standard deviation, so larger lag times (with lower statistics) have a smaller impact on the fit (see Figure 5.16 B).

We next plotted the fitted parameters D and $\langle v \rangle$ along the AP axis (see Figure 5.17 A, B). The position of every trajectory along the axis was defined as its mean position over time. We noticed an important dispersion of the data which did not allow us to observe the same AP gradients that were measured *in vivo*. However, the absolute values are in the same order of magnitude. We also remarked that both the diffusion and the flow velocity decreases over time. We averaged both quantities over the AP axis and over different time windows during elongation and saw that the averages decreased over time (see Figure 5.17 C, D). We also compared these quantities for control explants and explants treated with 2 μM PD0325901 (see Figure 5.18). We observed a decrease of diffusion during the high diffusion phase (4
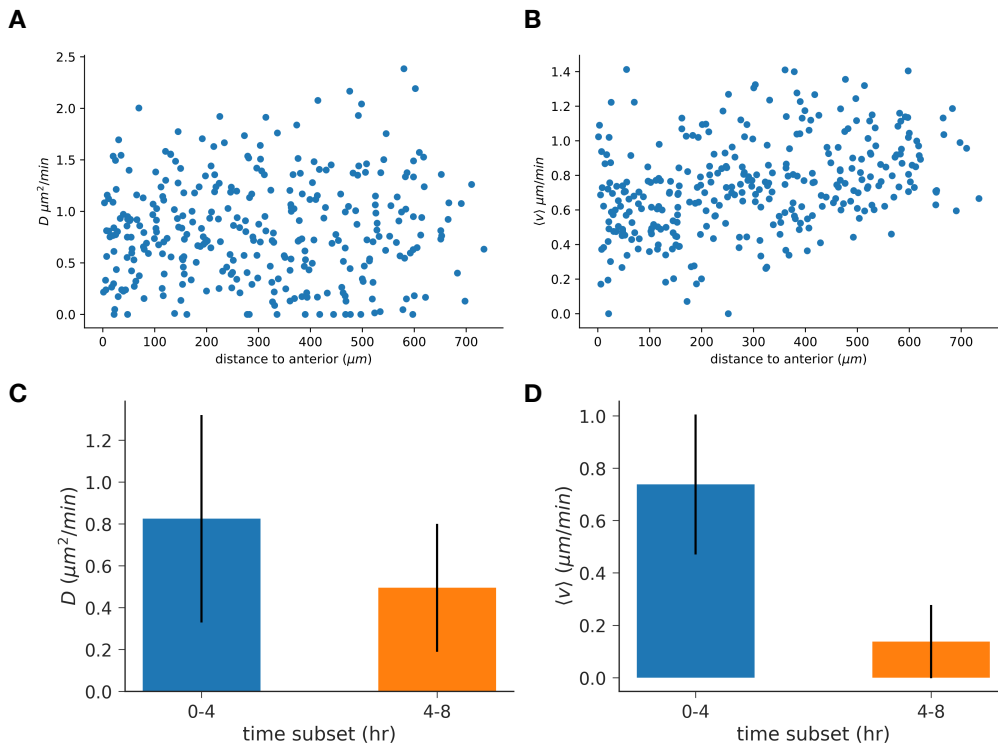
FIGURE 5.17 – Motility profile along the AP axis of an explant. **A**: Diffusion profile along the AP axis. **B**: Flow velocity profile along the AP axis. **C**: Mean diffusion along the AP axis over two periods of elongation (first 4 hours and subsequent 4 hours). Error bars show standard deviation. **D**: Mean flow velocity along the AP axis over two periods of elongation (first 4 hours and subsequent 4 hours). Error bars show standard deviation.

first hours) upon MAPK inhibition, although this decrease was not statistically significant. We also measured the gradient along the AP axis by linear regression over the AP profile. Despite the wide dispersion of the data shown 5.17, the slope was always positive indicating a slight but significative AP gradient. We also observed a decrease in the diffusion gradient during the high diffusion phase (4 first hours) upon MAPK inhibition but this decrease was not significant either.
We attributed the important dispersion of the data to the poor quality of our tracking. Indeed, in contrast with *in vivo* data in which the embryo is mostly flat and trajectories seldom cross, the geometry of the microchannels (deeper than the wide) complicates the tracking. In such a geometry, cells very often cross which can lead to erroneous trajectories.

In summary, we showed that cell motility exhibited unexpected patterns within the microchannels. The origin of such patterns remains to be elucidated. In particular, the role of adhesion needs to be investigated by coating the channels with fibronectin for instance. Furthermore, even though the quality of our tracking did not offer us the ability to investigate the cell motility gradient within the channels, we could observe the effect of FGF8 inhibition on cell motility.

FIGURE 5.18 – Effect of FGF8 on motility. Mean along the AP axis of diffusion (**A**) and flow velocity (**B**), and gradient along the AP axis of diffusion (**C**) and flow velocity (**D**) for control explants and explants treated with 2 µM PD0325901 (PD03). Each data points is the mean over an explant. Data are measured over 4-hour periods of elongation.
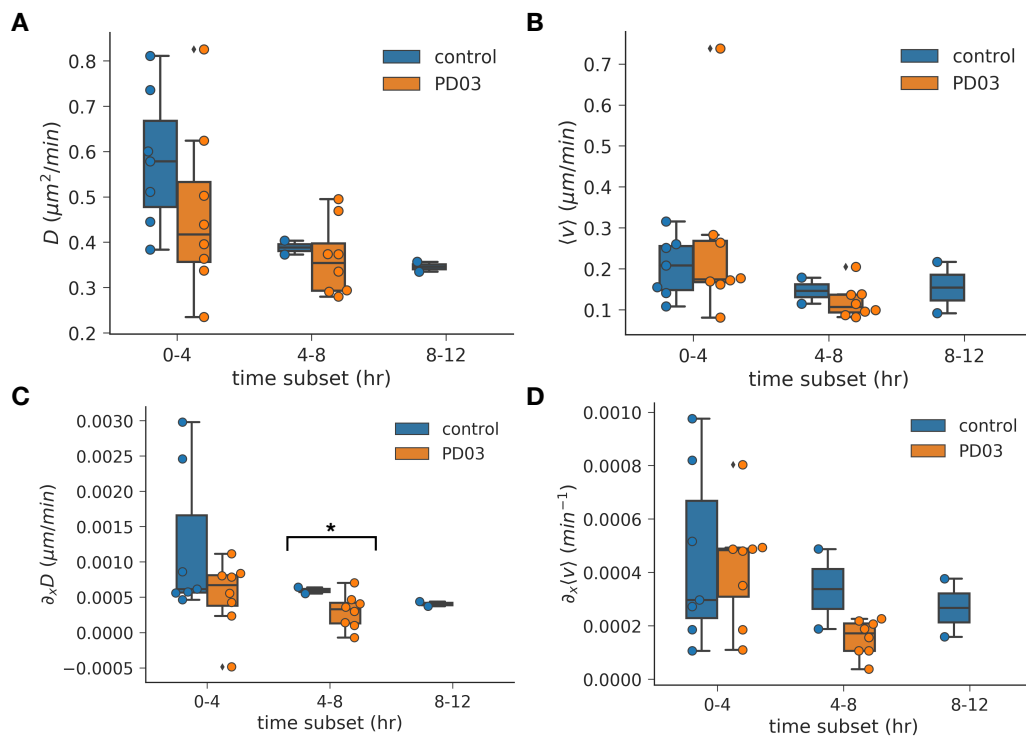
5.2.4 Elongation force of confined presomitic mesoderm

We finally measured the elongation force produced by an elongating PSM. As anterior slippage would have impaired the measurement, the anterior end of the PSM was blocked by a piece of PDMS (see Figure 5.19 A and Movie 16). The PDMS plug was smaller than the channel so the channel was not clogged and normal medium diffusion could take place. A cantilever was subsequently placed at the other end of the channel, towards which the posterior PSM end was growing. As the PSM grew out of the channel it deflected the cantilever. We observed the deflection over time and noticed a maximum deflection indicating that the stalling force was reached (see Figure 5.19 B). The corresponding stalling stress was 9.1 Pa, which is larger than the instantaneous stress production predicted by Regev et al., 2017, and 10-fold lower than the embryo stalling force. Furthermore, we can hypothesize this measurement underestimated the real stalling stress as the measurement was not optimal. The cantilever was wider than the channel width and could not be placed inside the channel. As a result, when the deflection happened, the PSM went out of the channel where it was not confined anymore. We can hypothesize the lack of confinement reduced the pushing force along the AP axis.

5.3 Conclusion

We have shown that elongation of the AP axis in the chicken embryo can produce up to 114 Pa and an isolated PSM maximum stress production is 9 Pa. Although the measurement of isolated PSM stress production is preliminary ($n = 1$) and might be underestimated, we can give a first estimate of the ratio $\frac{2f_{PSM}}{f_{total}}$. If we assume that stress production is homogeneous across tissues, the stalling force is proportional to the stalling stress. Therefore, the force ratio is equal to the stress ratio, and we can calculate that $\frac{2f_{PSM}}{f_{total}} = 0.16$. As a result, we have shown that the contribution of the two PSMs to the stalling force is about 16%. Nonetheless, this modest contribution to the stalling force should not be interpreted as a minor contribution to axis elongation. First, it is possible that the *in vitro* culture conditions affect the force production of the PSM. Second, as it will be discussed in Chapter 6, the magnitude of the stalling stress depends both on the mechanical properties and the stress production.

Besides, we have developed a platform to study cell motility in isolated PSM explants and its relation with growth. We showed that isolated PSM explants under ML confinement elongate by about 19% over the course of roughly 6-8 hours. This elongation is driven by an important elongation of the posterior half (about 57%). Although the protocol remains to be improved in order to allow a better cell tracking, preliminary results show that there is a slight AP gradient of cell motility that can be modulated by FGF8/MAPK activity.
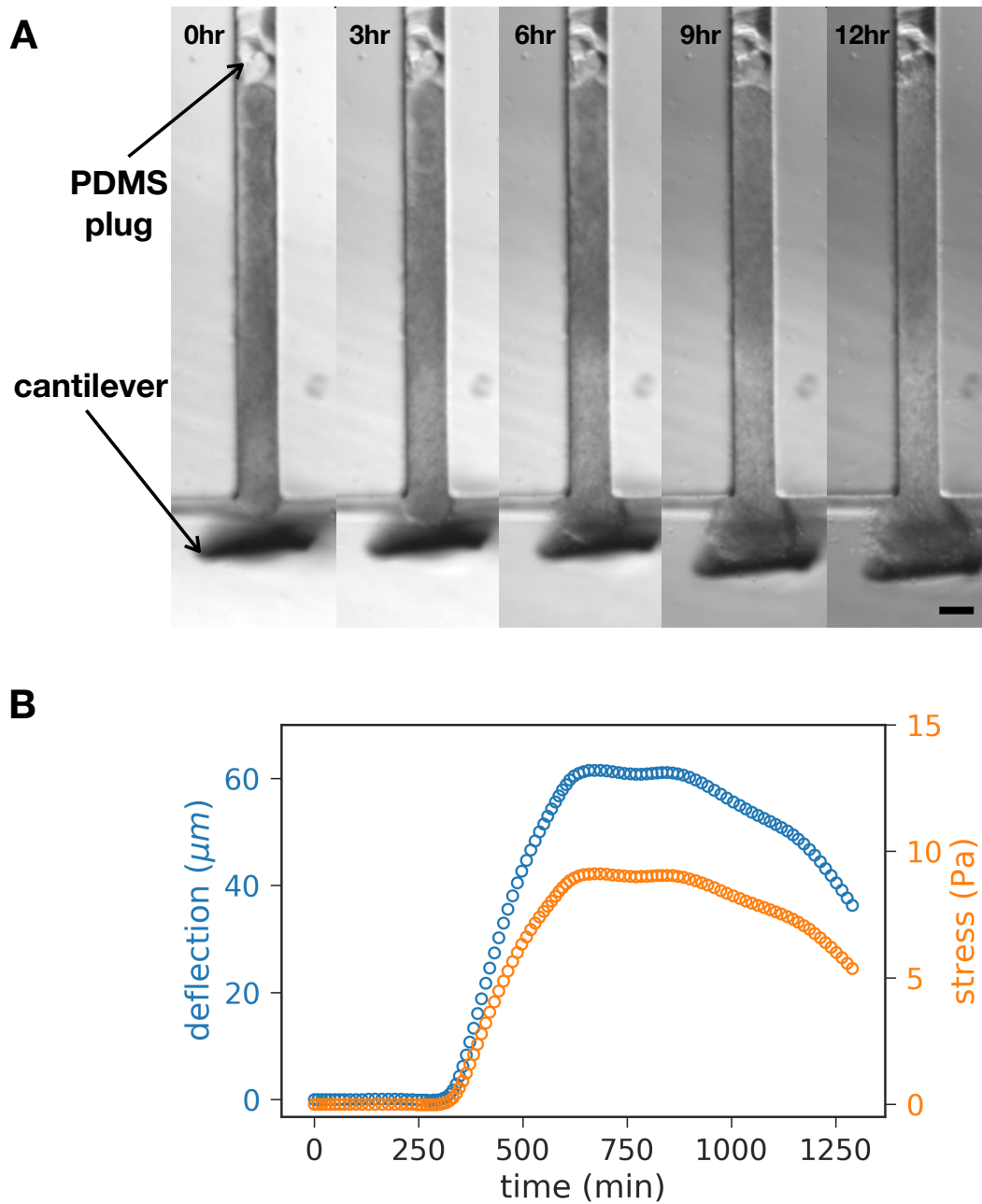
FIGURE 5.19 – PSM explant stress production over time. **A**: Snapshots during an elongation of a full PSM explant deflecting a cantilever. Scale bar: 75 µm. **B**: Deflection and stress measurement over time.

Chapter 6

Discussion

In this Ph.D. thesis, we have reported the first measurements, to our knowledge, of the profile of mechanical properties along the AP axis (aim 1) and stress production during axis elongation (aim 2) in the chicken embryo. To tackle the first aim, we adapted previously described biophysical techniques to the chicken PSM and NT. In contrast, we had to develop a new experimental system in order to address the second aim. As a result, several results from the second aim remain at a preliminary phase and require more development. In this chapter, we discuss the main results reported in this thesis and present potential perspectives to the project.

6.1 Aim 1: mechanical properties measurement along the anteroposterior axis

We reported mechanical properties measurements using two distinct methods: monitoring explants rounding and fusion (Chapter 3) and pipette aspiration (Chapter 4). These methods rely on the assumption that tissues obey continuum mechanics laws. If we exclude some pathological situations in which tissues lost their cohesiveness after challenging dissections, we found that this assumption could be verified. The methods we used measure different quantities: viscocapillary velocity (rounding and fusion), and elasticity, viscosity and surface tension (pipette aspiration). Viscocapillary velocity is the ratio of surface tension over viscosity. So, these methods can be compared and used in complementarity. For instance, surface tension, respectively viscosity, measured by pipette aspiration can be used to calculate viscosity, respectively surface tension, out of the viscocapillary velocity value. We observed some discrepancy between data measured by these two methods. We discuss here potential explanations for this discrepancy.

6.1.1 Results summary and discussion

Anteroposterior gradient of mechanical properties

Rounding and fusion data show a clear gradient of mechanical properties along the AP axis. There is a 7.4 fold difference in viscocapillary velocity between anterior and posterior explants. However, pipette aspiration data do not show such a clear behavior. There is only a 1.2 fold difference in viscocapillary velocity calculated from aspiration data. This flatter gradient might be explained by important inter-embryonic variability in the pipette aspiration data. This variability could indeed conceal a potentially steeper gradient because of an insufficient statistical power with respect to the magnitude of the dispersion. In addition to inter-embryonic variability, there is also a variability in the gradient along individual PSMs. We almost always observed a clear gradient of elasticity and viscosity along individual PSMs.

However, there is a wide dispersion in the slope of this gradient. The viscosity gradient varies from 0 to 2 fold ($\langle \gamma_0 \rangle$-based calculation) and from 0 to 3 fold (δ-method calculation).

The pipette data variability might originate from several sources of error:

- Tissue preparation
  Dissecting a mesenchymal tissue like the PSM is a challenging step. Its low cell density and its lack of epithelial boundary (except for the anterior region) make it difficult to isolate from the rest of the embryo. The mechanical state of the tissue can, therefore, be altered by the dissection step. Both rounding and aspiration experiments relies on dissection, but the quality of dissection is expected to impact more significantly aspiration experiments. Pipette aspiration requires a smooth surface and a non-porous tissue so that the pipette is plugged by the tissue. If after the dissection, the tissue surface is rough or if it has been torn, it is challenging to completely plugged the pipette. We verified that the PSM was a non-porous tissue by monitoring the flow inside the pipette (using micron-sized beads as flow trackers). We observed that the flow was fully arrested as soon as the explant was held at the pipette opening by a low suction pressure. We also observed damaged explants which lost their cohesiveness during the aspiration. In these cases, we could detect a flow as cells were flowing away from the tongue. We discarded these experiments. Nonetheless, we cannot exclude that there were intermediate situations between healthy and damaged tissues for which a slight porosity was not detectable but affected the data.

- Analysis procedure
  We experienced difficulties to measure the length of the aspirated tongue. The edge of the tongue was not well defined because of an important protrusive activity. Also, the aforementioned variability of mechanical state could result in a tongue of variable cohesiveness. Therefore, we sometimes monitored aspiration dynamics which were not as regular as required for a correct fitting procedure. As a result, an important subset of our aspirations (a third) could not be fitted by our mechanical model. Within the analyzed aspirations, it is possible that we had intermediate situations between well-fitted curves and obvious ill-fitted curves for which non-negligible fitting errors led to measured parameters variability.

- Non-linear effect
  Because of the dispersion of the data, we could not verify the linearity of the elasticity and viscosity relations (relations 4.16). Thus, if non-linear effects exist at some pressure regime, we were not able to evidence it.

- Bulk properties calculation cumulates two sources of error
  Furthermore, elasticity and viscosity are calculated by removing the contribution of surface tension to the apparent properties. Therefore, bulk properties are the results of two distinct measurements, for each one of which an experimental error is associated. Regarding bulk properties calculated using the retraction data, the poor quality of many retractions was likely to result in an important error. Conversely, bulk properties using the average tension value $\langle \gamma_0 \rangle$, an error comes from the tension measurement and another error comes from the fact that tension varies with the aspiration force, which was not corrected.

The variability of aspiration data can partially explain the discrepancy with rounding data. However, even in the most extreme situations, we never observed a 7-fold difference in viscosity between the anterior and posterior regions. Thus, as surface tension shows a roughly constant profile along the axis, we never observed such a steep gradient of viscocapillary velocity either. Consequently, an additional explanation must be proposed.

Our surface tension data might be the most reliable data of the properties measured by aspiration. Indeed, two distinct methods (the direct method and the δ-method) yield similar orders of magnitude. Moreover, the direct method does not rely on any fitting procedure, it is, therefore, more simple and can be expected to give more robust data. Furthermore, measured tension is in the same range of previously measured tension (Guevorkian et al., 2010, Stirbat et al., 2013a). In contrast, experimental investigation of tissular viscosity remains scarce. So it is more difficult to evaluate our confidence in our viscosity data.

For this reason, we combine our surface tension data (from aspiration experiments) with our viscocapillary data (from rounding experiment) to calculate another estimate of viscosity. Logically, this other estimate also highlights the discrepancy between the two methods. This second estimate yields a viscosity in the medial region in the same order of magnitude of epithelial cellular aggregate measured by aspiration ($\eta \approx 2 \times 10^5$ Pa $\cdot$ s, Guevorkian et al., 2010), and twice less viscous in the posterior region. However, we observed extremely viscous properties in the anterior PSM ($\eta \approx 10^6$ Pa $\cdot$ s). This is comparable with the most viscous tissues measured by this method (for instance, aggregates of chicken 9-day embryonic retina cells, $\eta \approx 4 \times 10^6$ Pa $\cdot$ s, Mombach et al., 2005). It seems unlikely that a non-fully epithelialized tissue exhibits such a high viscosity. We can, thus, hypothesize that the somitic cleft formation perturbed the measurement. Indeed, we fitted the rounding dynamics only after the end of the failure of the cleft formation, which resulted in significantly longer experiments (8-10 hours instead of 1-3 hours for the posterior region). As such, it is possible we measure properties of a tissue in which differentiation continued and which is not comparable to the anterior PSM anymore. Another explanation could be that the anterior PSM is at the limit between liquid and solid behaviors. As shown in Figure 3.7, we observed that, when fusing, individual anterior explants kept their shape for a long time (5 hours) before fusing and rounding. This might indicate that at first anterior explants behave more as a solid and eventually become more liquid-like. On the contrary, in the case of pipette aspirations, anterior explants have a liquid behavior on the short timescales (15-30 min). This contrast might be suggesting the existence of a yield stress. A yield stress is the minimal stress below which the system is jammed and behave as a solid and, above which it flows like a liquid (Bonn et al., 2017). Yield stress has been proposed to play an important role in development of embryonic tissue (Bi et al., 2016). If so, both methods would measure different properties.

In summary, uncertainties in the aspiration data in general and on rounding data in anterior explants in particular, do not allow us to fully explain the observed discrepancy. However, while the absolute value of viscosity remains to be confirmed to explain this discrepancy, it appears that a gradient along the AP axis is present. Interestingly, this viscosity gradient parallels the gradient of cell motility, cell density and ECM assembly. The individual roles of these three properties in viscosity remain to be studied in detail.

Effects of actomyosin contractility and extracellular matrix

Another striking result of our investigation of PSM mechanical properties was the effect of the inhibition of actomyosin contractility. Blebbistatin-treated explants exhibited a significantly reduced surface tension (by a 4.5 fold). In anterior PSM, blebbistatin treatment resulted in a moderate, but significant, increase of viscocapillary velocity (about 33% increase). This increase might be due to the absence of the somite generation in blebbistatin-treated explants (see Figure 3.5). However, it did not lead to any significant change of viscocapillary velocity in medial and posterior regions. This means that the surface tension reduction should be compensated by a reduction of viscosity to a similar extent. Our preliminary aspiration results indicate indeed a viscosity reduction in the same order of magnitude as the tension decrease (a 3-fold decrease in medial PSM). Regarding elasticity, surprisingly blebbistatin treatment did not result in any change. In *Xenopus*, actomyosin contractility has been shown to control tissue stiffening during development (Zhou et al., 2009). In this study, tissue stiffness was measured by compression assays. This technique does not offer the possibility of uncoupling surface and bulk properties. Therefore, if mechanical properties are conserved between amphibians and chicken embryos, we can hypothesize that the reported stiffening in *Xenopus* was due to a surface tension increase.

In the same study, Zhou et al. showed that the ECM did not have a significant effect on the mechanical properties. The authors measured that mechanical properties were left unchanged in embryos in which fibronectin assembly was inhibited by morpholino injection. This is in sharp contrast with our aspiration experiments in which PSM explants were dissected with pancreatin which digests a wide range of ECM molecules including fibronectin. In this case, both apparent and bulk elasticities were significantly reduced compared to collagenase dissected explants. More experiments are needed to demonstrate the role of fibronectin in this elasticity reduction. Indeed, we cannot exclude that the observed difference is a consequence of the dissection protocols which altered differentially the mechanical properties.

Effect of cell motility on mechanical properties

As cell motility is a key parameter of chicken embryo elongation, we investigated the role of cell motility on mechanical properties. The connection between cell motility and mechanical properties remains unclear. A greater cell motility could actively fluidize (*i.e.* reduce viscosity) by promoting cell-cell exchange. Conversely, one can envision that a high motile activity requires a high cytoskeleton contractility which might resist an external stress. Therefore, two opposite outcomes to a high cell motility can be hypothesized. To date, the role of motility in tissue viscosity remains open to question.

We investigated this issue by measuring the effect of actomyosin contractility inhibition and FGF8/MAPK inhibition. As discussed above, actomyosin contractility inhibition by blebbistatin treatment both resulted in a surface tension reduction and a viscosity reduction. However, this condition does not allow us to uncouple the effect of cell motility and actomyosin contractility. For this reason, we also studied the effect of FGF8/MAPK inhibition using PD0325901. It resulted in a reduction of viscocapillary velocity, which would imply a viscosity increase if surface tension is kept constant. Such a viscosity increase would parallel the previously reported reduction of cell motility upon FGF8/MAPK inhibition. Unfortunately, we cannot test

this hypothesis as we did not measure the effect of PD0325901 treatment on surface tension by aspiration.

6.1.2 Perspectives

Investigating the discrepancy between rounding and aspiration data

Even if we exclude the anterior PSM where the discrepancy between our two methods might be amplified by the somitic cleft formation, the discrepancy is about one order of magnitude in the rest of the PSM. We can envision two strategies to reconcile the two methods. First, we should measure viscosity and surface tension by other methods. Parallel plate compression could be carried out on explant after leaving them to round up, as this technique requires spherical tissues. Regarding tissue viscosity, to our knowledge, no other technique offers the possibility of measuring viscosity uncoupled from surface tension.

Second, to date, no systematic comparison of rounding and fusion experiments with other methods has been carried out. These methods have been used in complementarity: viscocapillary velocity has been combined with surface tension measurements to estimate viscosity (Schötz et al., 2008, Douezan and Brochard-Wyart, 2012, Stirbat et al., 2013a). However, the same system has not been measured by several methods to verify that it exhibits the same viscocapillary velocity. For instance, we also calculated there was a roughly 10-fold discrepancy between viscocapillary values of aggregates of murine sarcoma (S180) cell lines calculated with aspiration data ($v_p \approx 1.8\ \mu m \cdot min^{-1}$, Guevorkian et al., 2010) and values of the same cell line aggregates measured by fusion ($v_p \approx 0.16\ \mu m \cdot min^{-1}$, Douezan and Brochard-Wyart, 2012). Therefore, it seems important to investigate this discrepancy with systems less prone to sample variability, such as aggregates of cell lines.

Third, if the discrepancy is the result of an active response of the tissue to the technique, the nature of this response should be elucidated. Is the cell-cell exchange mechanism identical during a rounding experiment and an aspiration? One can hypothesize that in a rounding experiment, cell-cell exchange happens by cell active movements, whereas cells are passively displaced by the external stress during an aspiration experiment. Therefore, the role of cell motility should be different in both experiments. It is also possible that pipette aspiration fluidizes the tissue. In this case, a non-linearity between the measured viscous slope and the aspiration pressure should be measured. We could not verify this hypothesis as our the inter-embryonic variability was too large to accurately test the linearity of relations 4.16.

Studying the effect of FGF8/MAPK inhibition on surface tension

The effect of FGF8/MAPK inhibition on viscocapillary velocity remains challenging to interpret as no surface tension and viscosity measurement are carried out in such conditions. Therefore, pipette experiments on PD0325901 treated explants must be conducted.

Studying the effects of cell motility, cell density and ECM assembly

The respective roles of cell motility, cell density, ECM assembly and cytoskeleton in tissue mechanics remain unclear. We have shown that actomyosin contractility is involved in surface tension and viscosity but not elasticity. These results need to be reproduced with a higher statistical power. To further evidence the role of contractility, nocodazole, a drug increasing cell contractility (Brevier et al., 2007), could be

used to see if both surface tension and viscosity are increased.

In order to better describe the role of motility during these measurements, cell nuclei can be marked by electroporation prior to experiments so that cells can be tracked during rounding and aspiration experiments. However, as presented in Chapter 5, nuclei tracking can be challenging when the sample is thick. Therefore, 3D tracking by confocal imaging should be carried out for the rounding experiment. However, monitoring aspiration by confocal imaging is more challenging because of the required time resolution.

Conclusion

We have reported the profile of mechanical properties along the PSM and the NT in the chicken embryo. We have demonstrated the existence of an AP gradient in parallel to the previously reported cell density gradient, ECM assembly gradient and cell motility gradient downstream of an FGF8/MAPK gradient. Although more detailed investigations are required, we have shown that cell motility and ECM assembly play important roles in mechanical properties. We also experienced a non-negligible discrepancy between our two methods. This discrepancy should be placed in perspective with the current lack of experimental comparison of these different techniques in other biological systems.

6.2   Aim 2: stress production during anteroposterior axis elongation

In Chapter 6, we presented a first set of measurements of stress production by the AP axis in the chicken embryo. We developed a culture method and a cantilever system to measure the elongation force *in vivo* in parallel to the elongation rate. We discuss below our confidence in these results and the relevance of these measurements to the elongation mechanism. Besides, we fabricated a microchannel array to investigate the growth dynamics of isolated PSM explants. We showed that, if confined mediolaterally, isolated explants could undergo extension. Furthermore, this extension is predominantly driven by posterior PSM. We have also reported preliminary results of cell motility within our microchannels. We will discuss improvements and future directions to this experimental investigation.

6.2.1   Results summary and discussion

Stress measurement

We measured stress production *in vivo* by means of a cantilever. Our cantilever was calibrated by only one method (resonant frequency measurement). The measured bending stiffness cannot be compared to any theoretical prediction because of the cantilever complex geometry. Moreover, this method does not provide us with the linearity range of the cantilever. As such, we cannot estimate the range of deflection for which the linear relation between force and deflection is valid. We have tried to calibrate our cantilevers by measuring force-displacement curves by AFM. However, the large fluctuations of the cantilever tip resulted in very noisy measurements.

In addition to this uncertainty, the cantilever manual fabrication led to a high variability of the cantilever stiffness and quality. The control over the cantilever stiffness was poor because of the gluing step that could modify the stiffness to a large extent.

As a result, we had to fabricate a large number of cantilevers, calibrate them and then choose those who exhibited the desired stiffness. Furthermore, very soft cantilevers were characterized by a very fine tip and, therefore, a smaller contact area to glue the aluminum probe. Consequently, these cantilevers were very fragile and often broke.

Stalling stress and elongation mechanism

We have measured a moderate contribution of the PSM to the total stalling stress (16%). This should not be interpreted as a minor role of the PSM in elongation. Indeed, the stalling stress is controlled by instantaneous stress production, which might depend on the resistance to elongation (active response), and tissue stiffness. For instance, if a soft tissue exerts an important stress when it grows, it might buckle when the resistance to its growth increases. Therefore, it is possible that the PSM produces an important instantaneous stress which pushes forward the PSM posterior boundary. However, as it is a soft tissue it cannot sustain large resisting stress. On the other hand, axial tissues which are stiffer can sustain large resisting stress, hence the large stalling stress, but they might not be able to produce an important instantaneous stress to push the posterior boundary. To test these hypotheses, the instantaneous stress and the axial autonomous growth must be evaluated. Furthermore, it is possible that the PSM force production is impaired *in vitro*.

PSM explants autonomous elongation

An important result of this Ph.D. was the autonomous elongation of isolated PSM explants. We have shown that full PSM explants elongate by about 19% and this growth mostly originates from the posterior region which grows by about 57%. The importance of the posterior region is in agreement with previous results demonstrating its involvement in the elongation rate (Bénazéraf et al., 2010) and its volume expansion (Bénazéraf et al., 2017). Furthermore, we have shown that this elongation is FGF8/MAPK dependent, which is also in agreement with previous *in vivo* studies. However, isolated tissues might be more sensitive to cell death, as it has been shown that axial tissues inhibited apoptosis in somites (Sanders and Parker, 2001). For this reason, cell viability needs to be controlled in more detail to verify that elongation inhibition upon PD0325901 treatment is not caused by a more important cell death. To do so, we have tried to monitor cell viability using calcein AM, which is a cell viability fluorescent dye. Calcein fluorescence is activated in living cells only. However, we observed that calcein fluorescence was rapidly bleached, thus we could not follow cell viability over time. Adding pulses of calcein was not optimal, as penetration in channels was not homogeneous (only cells close to the channel opening were stained). Therefore, a more reliable assay needs to be conducted.

Cell motility in isolated explants

We have presented preliminary results of cell tracking within microchannels. We have seen unexpected rotating movements within the posterior region which were never reported *in vivo*. We can hypothesize that these movements originate from the tissue interface generated by dissection. As this interface deforms to minimize the area to volume ratio, it can generate large-scale movements. It would, therefore, be interesting to investigate if modifying the interface properties by changing the wall adhesion, for instance, can control these rotating movements. It would also

be worth understanding how PSM cell random motility can generate such collective movement patterns. While understanding the origin of these movements is an interesting problem, it seems to be an experimental artifact which makes the investigation of the random motility gradient challenging. For these reasons, it would be valuable to be able to control these movements, so random diffusion closer to the *in vivo* situation can be studied.

Besides, because of the important depth of the channel, cell trajectories very often crossed. As a result, even manually, it was extremely difficult to track cells for a long time. Therefore, this issue will not be solved by improved image analysis but better image acquisition strategies must be devised.

6.2.2   Perspectives

Developing a new cantilever

We need to devise a new strategy for fabricating cantilevers. First, a more reliable method of fabrication should be devised. Second, a parallelepiped geometry would be preferable in order to use classical beam theory in order to predict its bending stiffness. And finally, its dimensions should be easily controlled so it can be scaled down and used inside microchannels.

Measuring elongation of isolated axial tissues

In order to further test the validity of different mechanisms of elongation, each tissue contribution to elongation has to be assessed. To do so, our microchannel array seems to be a powerful platform. By adapting channels width to tissue specific-dimensions, the autonomous elongation of various tissues could be measured. Importantly, it seems necessary to investigate if the notochord and the NT are capable of autonomous elongation. If so, their stress production should be measured as well, using our cantilever system.

Investigating cell viability

To control cell viability during explant elongation under different treatments, a systematic TUNNEL assay should be performed to estimate cell apoptosis.

Investigating cell movements

Several features of cell motility within microchannels have to be investigated. A pre-requisite to any further cell motility measurement is improving cell tracking. This can be achieved by two different strategies: either monitoring cell movements by confocal 3D imaging or reducing the channel depth to confine cells in a thinner plane. The two strategies can be combined to obtained high-quality tracking.

Next, it seems important to elucidate the origin of the rotating movements observed in the posterior region. These movements were never reported *in vivo*, as a result, we should verify that no experimental important artifact is involved. To tackle this problem, several questions should be answered. Are these movements, bulk movements or autonomous cell migration? Imaging the ECM movements by fibronectin labeling (as in Zamir et al., 2006, Bénazéraf et al., 2010) would be a way of addressing this question. Are these movements the consequence of generating a tissue-medium interface after dissection? If so, coating the PDMS walls with fibronectin would be

a way of modifying the tissue interface. Fibronectin coating should also prevent explant slippage along the channel, which would simplify the analysis.

These improvements should yield better measurements of the diffusion coefficient and the local flow velocity along the PSM. As such, the impact of FGF8/MAPK loss and gain of function on elongation and the cell motility gradient will be investigated in more details. For the moment, only the loss of function by PD0325901 treatment has been carried out. It needs to be complemented by electroporation of a dominant-negative version of the FGF receptor (FGFR1dn). Regarding gain of function experiment, electroporation of a constitutive FGF8 construct will be carried out. In particular, it will be interesting to see if FGF8 overexpression also results in a reduced elongation *in vitro*.

Investigating volume growth

We have reported that PSM explants take the full available volume in a channel, which also highlights the PSM liquid behavior. Consequently, the tissue volume must increase as it elongates. Understanding this volume growth is key. Does it originate from proliferation, cellular growth or interstitial volume growth (*i.e.* cell density lowering)? To address this question, one must investigate the contribution of these different processes. The impact of cell division inhibition on elongation by aphidicolin treatment should be evaluated. Unlike many cell division inhibitors, aphidicolin does not target cytoskeleton but it is a cell cycle inhibitor, which is important since cell motility is involved in elongation. In order to test the role of cell growth, suspended microchannel resonator (SMR) can be used to measure cell mass and cell volume (Godin et al., 2010). In collaboration with S. Manalis' laboratory, we have already conducted preliminary SMR experiments with PSM cells yielding a mean cell mass of 1.0 ng and a mean cell volume 0.9 pL. Comparing SMR measurements after PSM dissection with PSM after growth in microchannel could be a way of measuring if there are any cell mass and volume gain. Finally, staining the interstitial medium with fluorescent dextran could give interesting measurements of any potential volume gain in the interstitial space.

Measuring cell motility mediated stress production

In order to experimentally verify the stress predicted by the theoretical random cell motility model, we need to assess the instantaneous stress produced by cell motility. One strategy could be to use a gel sensor like in Zhou et al., 2015. A posterior PSM explant could be embedded in such a calibrated gel and cell motility could be controlled in various ways. We could then be able to correlate volume expansion with modification of cell motility. For instance, we could benefit from the rapid reversibility of blebbistatin by embedding blebbistatin treated explants in a gel. Then, we would remove the blebbistatin treatment and monitor the potential subsequent volume increase due to cell motility. By monitoring cell motility and gel deformation, cell-mediated stress production could be measured.

6.3 Conclusion

We report an analysis of the mechanical properties along the PSM and the NT in the chicken embryo. Our elasticity data allowed us to partially validate the mediolateral confinement hypothesis of the random cell motility theoretical model (Regev et al., 2017). Despite a persisting uncertainty on the absolute value of viscosity, the

measured profile of viscous properties will be important to refine the theoretical model predictions. Although mechanistic details remain to be characterized, we have demonstrated that autonomous PSM elongation was possible and was driven by its posterior region. Measurements of instantaneous stress production by different tissues are needed to better describe the multi-tissue model of elongation. Nonetheless, it seems that axial tissues are capable of undergoing larger resisting stress than the paraxial tissues. To account for the key role of the PSM, we can envision an incremental growth mechanism: *(i)* the high PSM cell activity produces a pushing stress which displaces the posterior boundary, then *(ii)* the axial tissues have space to grow and maintain the embryo elongated by their stiffness. In the future, investigating the autonomous growth and stress production of different tissues will allow testing the various elongation models.

Chapter 7

Materials and methods

7.1 Dissection and culture

Dissection

PSM explants and dissected embryos were collected by harvesting embryos at stage HH11 (12-14 somites). Wild-type eggs were incubated for roughly 40 hours at 37°C, 65% humidity (the precise time of incubation depends on eggs batches and needed to be often adapted to match the desired stage). Embryos were harvested by cutting a circle around the *area opaca* and by transferring the embryo to a PBS solution to rinse it. Next, the embryo was transferred to a dissection dish in a PBS solution without Ca^{2+}, Mg^{2+} cations (pancreatin protocol) or with Ca^{2+}, Mg^{2+} cations (collagenase protocol). Embryos were pinned down and dissected using enzymes (explants) or no enzyme (for *in vivo* aspirations).

For explants dissection using enzymes, we used either pancreatin (Sigma diluted in PBS at 25 mg/mL in PBS) or collagenase type IV (Thermo Fisher Scientific diluted in PBS at 1 mg/mL in PBS). Pancreatin was used for 1 minute and then inactivated by FBS. Collagenase was used for 10 minutes. Dissection was carried out by means of pulled glass rods. Solid borosilicate rods (1 mm of diameter, Sutter instrument) were pulled using a P97 filament-based pipette puller (Sutter instrument) and severed to yield roughly a 10 µm tip.

For *in vivo* aspiration, the ectoderm and the separation of the PSM with the NT was carried out using pulled glass rods. The NT was cut using tungsten needles. The extraembryonic tissues were cut using fine scissors.

Embryo elongation

Embryo culture presented in Chapter 5 was carried out by harvesting 10-somite stage embryos using the filter paper technique described by Chapman et al., 2001. They were then either cultured ventral side up using the regular EC culture technique (Chapman et al., 2001) or our modified EC culture (during cantilever experiments). Regarding our modified protocol, we added a layer of mineral oil (Sigma) previously warmed to 37°C. DiI staining was carried out by injecting a solution of DiI (Vybrant Multicolor cell-labeling kit, Invitrogen) by means of a glass needle.

Tissue culture and treatments

The culture medium for explant culture and embryo during *in vivo* aspirations consisted of DMEM-F12 (Life Technologies) supplemented with 10% FBS (VWR) and 1% penicillin-streptomycin (2mM L-Glutamine, 100U Penicillin, 100 µg/ml Streptomycin). (-)-Blebbistatin (Sigma) stock solution was prepared by resuspending it in DMSO at 25 mM. It was then diluted in culture medium at 20 µM. PD0325901

(AXON MEDCHEM BV) stock solution was prepared by resuspending it in DMSO at 10 mM. It was then diluted in culture medium at 2 or 10 µM. Evaporation was suppressed by adding a layer of mineral oil (Sigma) at the surface of the culture.

For rounding and fusion experiments, explants were cultured on LabTek dishes coated with 0.3 mg/ml PEG-PLL (PolyEthyleneGlycol-PolyLysin, PLL(20)-g[3.5]-PEG(2), SuSoS) in HEPES 10 mM for 1 hour. LabTek dishes were then rinsed twice with PBS and incubated with culture medium at 37°C and 7.5% CO_2 for one hour prior to adding explants.

For microchannels experiments, the PDMS microchannel array was placed in a 60 mm Petri dish. Microchannels were closed by a glass coverslip. Next, they were saturated with a PBS solution and gas was removed using a vacuum chamber. Microchannels were then coated with PEG-PLL by vigorously pipetting a 0.3 mg/ml PEG-PLL solution to replace water. After one hour of coating, the PEG-PLL solution was washed away by PBS. The microchannel array was then incubated with culture medium at 37°C and 7.5% CO_2 for one hour prior to adding explants. Explants were carefully slid into the channel by means of a fine glass rod.

For the PSM force measurement in a microchannel, CO_2 could not be controlled because of the cantilever insertion. The culture medium was therefore supplemented with HEPES 10 mM.

Electroporation

Chicken embryos were electroporated *in ovo* at stage HH5. Eggs were windowed and a pCAGG-H2B-RFP plasmid solution (described by Denans et al., 2015) at 1 $\mu g \cdot \mu L^{-1}$ final concentration and fast green (FCF 0.4 $mg \cdot mL^{-1}$, Sigma) was microinjected into the space between the vitelline membrane and the epiblast. Electroporations were carried out by placing a cathode below the embryo in the yolk and fine tip anode on the primitive streak at 70-80% of its total length away from its posterior end. Five successive squared pulses of 12V for 50 ms were produced using a BTX ECM 830 electroporator. Eggs were then taped to seal the opening and re-incubated for 24 hours.

7.2 Microscopy

Rounding, fusion and microchannels experiments

Rounding, fusion and microchannels experiments were carried out on a computer controlled, wide-field inverted microscope (Zeiss Axioobserver Z1) equipped with a motorized stage and EMCCD camera (Evolve Photometrics). Explants were imaged by stitching together images (Zen 2 software stitching function) acquired with a 10X objective (EC Plan-Neofluar, numerical aperture=0.3). The acquisition rate used was 10 frames per hour (6 min between frames). When fluorescence was used (DiI, or H2B-RFP electroporated PSM), an HXP 120 C light source with a filter cube (excitation 565/30, emission 620/60) were used. Temperature and CO_2 were maintained respectively at 37°C and 7.5% by means of a Pecon TempController 2000-2 and a Pecon CO_2Controller 2000 (except for the PSM force measurement in a microchannel for which only the temperature was controlled).

Aspiration experiments

Aspiration dynamics was imaged on a computer controlled, wide-field inverted microscope (Zeiss Axioobserver Z1) equipped with an EMCCD camera (Evolve Photometrics). Images were acquired with a 20X objective (LD Plan-Neofluar, numerical aperture=0.4). The acquisition rate varied over experiments from 4 frames per minute (15 s between frames) to 30 frames per minute (2 s between frames).

Embryo elongation time-lapse

For regular EC culture experiments, embryo were cultured in a custom 6-well (one per embryo) sealed chamber and imaged on a microscope using a custom built time-lapse station (Bénazéraf et al., 2010). We used a computer controlled, wide-field epifluorescent microscope (Leica DMR) workstation, equipped with a motorized stage and cooled digital camera (QImaging Retiga 1300i). For each embryo, several images corresponding to different focal planes and different fields were captured at every single time-point. The acquisition rate used was 10 frames per hour (6 min between frames).

For modified EC culture experiments (force measurement), one embryo was cultured and imaged on a computer controlled, wide-field inverted microscope (Zeiss Axioobserver Z1) equipped with an EMCCD camera (Evolve Photometrics). At each frame, an image was acquired with a 2.5X objective (N-Achroplan, numerical aperture=0.07) and one image with a 10X objective (EC Plan-Neofluar, numerical aperture=0.3). The acquisition rate used was 10 frames per hour (6 min between frames). When fluorescence was used (DiI, or H2B-RFP electroporated PSM), an HXP 120 C light source with a filter cube (excitation 565/30, emission 620/60) were used.

Confocal microscopy

PSM explants were imaged by confocal microscopy on a Zeiss LSM780 confocal microscope using a 20X Plan-ACHROMAT (numerical aperture: 0.8) objective. A Z-stack was acquired with a 4 μm focal plane interval.

Immunohistochemistry

Explants were rinsed with PBS and fixed in fresh PBS, 4% PFA for 2 hours at room temperature. Then, they were rinsed in PBS and incubated for an hour in PBS, 0.1% Triton. Explants were rinsed three times in PBS and incubated in blocking solution (PBS, 0.1% Triton, horse serum 1%) for 45 minutes. Explants were then incubated overnight at 4°C with rabbit polyclonal anti-CMESPO antibody (Oginuma et al., 2017) (1:1000). Explants were then washed three times for 1 hour at room temperature in PBS, 0.1% Triton. Explants were blocked and secondary antibodies coupled with Alexa fluorophores (Life technologies) were incubated overnight at 4°C. Nuclear staining was performed with Hoechst33342 (1:1000, Life technologies). F-actin staining was performed with Phalloidin-Alexa 647 (1:50, Invitrogen). All immunostaining data were acquired using a Zeiss LSM780 confocal microscope using a 20X objective.
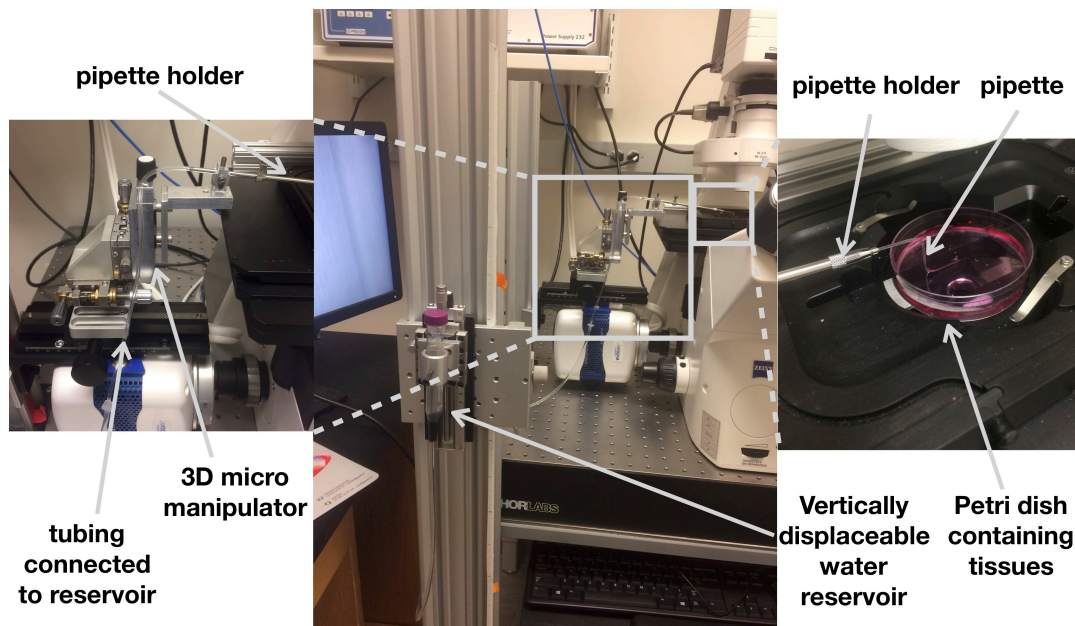
FIGURE 7.1 – Aspiration setup.

7.3 Micropipette aspiration setup

Pipettes were prepared by pulling 15 cm long borosilicate capillaries (outer diameter: 1 mm, inner diameter: 0.58 mm, Sutter Instruments), using a filament-based pipette puller (P-97 Sutter Instruments). We used pulling parameters to yield pipettes with almost parallel walls (parameters: 1 cycle P=500, HEAT=495, PULL=0, VEL=40, TIME=30). Pipettes tip was manually severed with a ceramic tile (Sutter Instruments) and, next, fire-polished using a microforge (MF-1, TPI). Pipettes were subsequently coated with a 0.3 mg/mL PEG-PLL in HEPES solution (10 mM) for 1 hour. Pipettes were then rinsed with double-distilled water.

Aspirations were conducted with a hydrostatically controlled pressure system (see Figure 7.1). A pipette was connected to a vertically displaceable water reservoir by means of a pipette holder (IM-H1, Narishige). The pipette holder was manipulated with a 3D micromanipulator (assembled using Velmex and Newport elements). The reservoir was displaced along a vertical rail (Newport and Thorlabs)

The oil calibration was carried out with a polybutene oil (poly(dimethylsiloxane), trimethylsiloxy-terminated, Cannon).

In vivo aspirations were carried out by fixing the dissected embryo in a PDMS chamber. The extra-embryonic tissues were glued with a surgical glue (Vetbond) between the chamber wall and the dish. The chamber was prepared by curing PDMS (10% curing agent, Sylgard 184) within a mold. The chamber mold was 3D printed using an Asiga Pico printer.

7.4 Cantilevers fabrication

Mica cantilever fabrication

Mica sheets were separated from thicker sheets (Ladd research industry) by iteratively removing mineral sheets by means of adhesive tape. When the desired thickness was reached ($\sim$ 20 µm) a stripe of approximately 2-3 mm long, 500 µm wide was cut using a scalpel blade. The mica stripe was glued to a holder made by a pulled pipette (used for its transparency and its fine tip), using a UV polymerizing glue (Bondic).

Force sensor calibration

We calibrated the bending stiffness of a pulled glass rod by measuring its deflection when a weight was hanged at different positions away from the tip (see Figure 7.2 A). We used masses ranging from 6 to 27 mg. We fitted the deflection profile by Equation B.5, which yielded the effective bending stiffness $\tilde{k}$ and the effective bending stiffness ℓ (order of magnitude) (see Figure 7.2 B). We then calculated the bending stiffness: $k = 578 \pm 11$ mN $\cdot$ m^{-1}. From the fitted deflection profile, we also extrapolated the deflection at the tip $\delta_0 = \delta(0)$, and performed a linear regression of the weight mg with respect to δ_0. This force-deflection profile was linear and yielded a similar value of the bending stiffness: $k = 577$ mN $\cdot$ m^{-1} (see Figure 7.2 C). Interestingly, the fitted parameters $\tilde{k}$, ℓ were useful to calculate a more precise value of the measured force when the rod was used as a force sensor, since the contact was not always exactly at its tip.

Mica cantilever calibration

The mica cantilever tip was brought to the microscope focal plane and held fixed by means of a 3D micromanipulator. The glass rod force sensor was fixed onto the microscope motorized stage. The imposed movement of the force sensor was measured using the stage positioning system. Before bringing the force sensor into contact with the cantilever, a few images at different positions were acquired to ensure the stage movements and the image positions yielded the same displacement. We then brought the force sensor into contact with the cantilever and measured the displacement of the tip. The difference between the tip displacement and the imposed displacement yielded the tip deflection, hence the force measurement.

Aluminum cantilever fabrication

Aluminum rectangular probes were produced by cutting rectangles (approximately 800 by 400 µm) into an aluminum foil (25 µm thick) using a scalpel blade. The aluminum probe was glued to a holder made by a pulled pipette (used for its transparency and its fine tip), using a UV polymerizing glue (Bondic).

Aluminum cantilever calibration

The cantilever movements were monitored using a Phantom v 7.3 fast camera at 8,000 frames per second. The cantilever fluctuation was recorded after excitation by a gentle blow. The base of the glass rod was tracked over time by drawing a kymograph along the orthogonal direction to the rod (see section 7.6). The kymograph was then skeletonized (using the "Skeletonized" function from Fiji software)
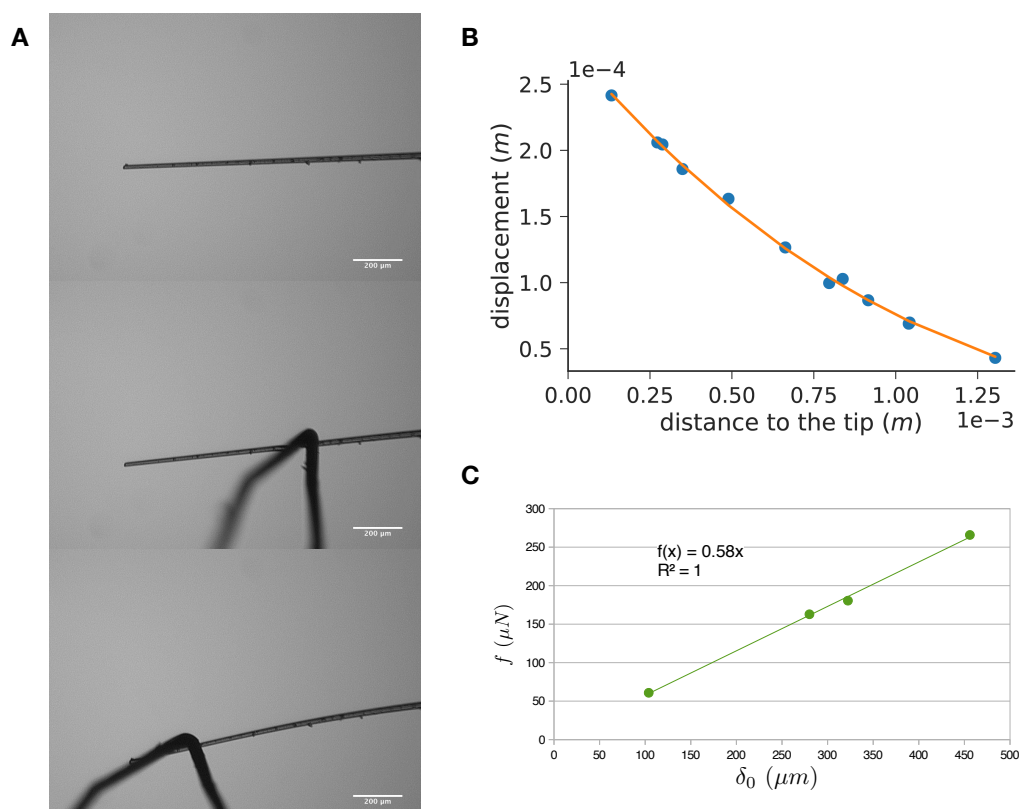
FIGURE 7.2 – Glass rod calibration. **A**: Snapshot of the rod deflection for a hanging weight at different positions. **B**: Deflection with respect to the weight distance to the tip, fitted by Equation B.5. **C**: Extrapolated deflection δ_0 with respect to the load.

to produce a one-pixel wide curve. Aberrant branches produced by the skeletonize algorithm were manually removed. The pixel positions on the image were converted into positions over time using the Python image analysis package Scikit-Image (Walt et al., 2014). Next, the position curve was smoothed by subtracting a rolling average (window size: 10 data points). The power spectrum of the fluctuation data was then computed by Fourier transform, using the Python package Scipy (Jones et al., 2001). The resonant peak was automatically detected as the spectrum maximum.

7.5 Microchannel fabrication

Channel mold fabrication

A resin master was microfabricated in a clean room in order to produce PDMS microchannels. Our photomask was designed using Autocad software and printed by Output city (`http://www.outputcity.com`). A commercial 150 μm thick sheet of epoxy photoresist (SUEX from DJ MicroLaminates `https://djmicrolaminates.com`) was laminated onto previously activated silicon wafer (diameter 76.2 mm, purchased from University Wafer `https://www.universitywafer.com`). Wafer activation was carried by heating a clean silicon wafer at 160°C for 20 min and then by O_2 plasma treatment for 20 min at 200 W. The SUEX sheet was laminated using a SKY 335R6 Laminating Machine. The laminated SUEX was next UV exposed (at 365 nm) for 3 min at 14.5 mW. The exposed SUEX was baked for 5 min at 65°C and 30 minutes at 80°C. The temperature was then ramped down (10°C every 5 min) to 20°C. The SUEX was then developed in SU-8 developer (face-up for 40 min, face-down for 40 min). The master was then silanized to reduced adhesion by placing it above tridecafluoro-tetrahydrooctyl-trichlorosilane left evaporating in a vacuum chamber for 20 min. Silane was cured at 150°C for 10 min.

PDMS channel preparation

Channels were prepared by pouring PDMS (10% curing agent, Sylgard 184) in the master. 15 g of PDMS was used to ensure the PDMS was not thicker than 2-3 mm as channels were used with an inverted microscope (limited working distance). Gas bubbles were removed in a vacuum chamber for 45 min. PDMS was cured at 150°C for 10 min.

7.6 Image analysis

Rounding analysis

The shape of rounding explants was automatically measured by segmenting their contour using the CellProfiler software (Carpenter et al., 2006). In brief, the following functions were subsequently applied to the images: smoothing, edge enhancement, intensity rescale, segmentation (using a minimum cross entropy algorithm), measurement of segmented objects' shape and size. The boundaries to the segmentation threshold were sometimes manually adjusted to improve inaccurate segmentation.

Fusion analysis

The fusion neck was manually measured using the line measurement tool from Fiji software.

Aspiration analysis

Aspiration dynamics was analyzed with Fiji software. The image was rotated to ensure the pipette was horizontal. A rectangular region of interest was drawn inside the pipette with its origin at the pipette tip. A kymograph along each horizontal line was generated with the "reslice" function. All kymographs were averaged using the "Z project" function. The tongue edge was hand-drawn using the polyline tool and the "fit spline" function. This procedure yielded a curve with an irregular time resolution because the "fit spline" function generates more data points in regions where the slope varies more. This could lead to fitting inaccuracies by giving more weight to some parts of the curve. We, therefore, regularized the time resolution using the frame rate by interpolating the curve by means of the `interp1d` function from the Python package Scipy (Jones et al., 2001).

Elongation and deflection analysis

Embryo elongation rate was measured by manually tracking landmarks at each end of the AP axis, using the "Manual Tracking" plugin from the Fiji software. In detail, in the anterior region, the position of either the last formed somite or a DiI spot in the anterior PSM (if the last formed somite was out of the field of view) was tracked over time. In the posterior region, the position of either the Hensen's node or a DiI spot in the progenitors' zone (if the image quality was too poor to distinguish the Hensen's node) was tracked over time. The distance between the two points was then calculated.

Cantilever deflection was measured by rotating the image so the deflection movement was vertical and by tracking the position of the cantilever along the vertical axis over time using the "Manual Tracking" plugin from the Fiji software.

The length of PSM explants in channel experiments was measured by drawing the edge of the two PSM ends on a kymograph. A kymograph along the channel axis was drawn using the same procedure as the aspiration analysis (see section 7.6). The positions of the two ends over time were also regularized (see aspiration analysis) using the frame rate. At each time step, the distance between was then calculated.

Cell tracking

Motility in microchannels was analyzed by automatically tracking the PSM cells by means of the Fiji Mosaic plugin (Sbalzarini and Koumoutsakos, 2005). Cell trajectories were visualized and analyzed using a custom Python-based toolkit (see C.1). In brief, the PSM slippage movement was measured by drawing a kymograph across the anterior edge. The slippage movement was subtracted from the cell trajectories.

7.7 Curve fitting

Linear regressions were performed using the `curve_fit` function from the Python package Scipy (Jones et al., 2001). Aspiration curves, MSD curves and glass rod deflection curves were fitted using the non-linear least-squared regression toolkit provided by the Python package LMFIT (Newville et al., 2014).

Appendix A

Supplementary movies

Movie 1

Rounding of anterior explant. Green solid line: segmented contour.

Movie 2

Rounding of medial explant. Green solid line: segmented contour.

Movie 3

Rounding of posterior explant. Green solid line: segmented contour.

Movie 4

Fusion of two anterior explants.

Movie 5

Fusion of two posterior explants.

Movie 6

Aspiration of an anterior explant. $\Delta P = 490$ Pa until $t = 2080$ s, then $\Delta P = 0$ Pa.

Movie 7

Aspiration of a posterior explant. $\Delta P = 490$ Pa until $t = 2004$ s, then $\Delta P = 0$ Pa.

Movie 8

Aspiration of an anterior explant incubated 1 hour in 20 µM blebbistatin prior to aspiration. Aspirated in a blebbistatin-deprived medium at $\Delta P = 686$ Pa until $t = 922$ s, then $\Delta P = 0$ Pa. Note the protrusive activity and the contraction of the tongue starting at roughly $t = 500$ s, indicating the rapid reversibility of the blebbistatin activity.

Movie 9

Neural tube aspiration *in vivo* in the PSM anterior region (90 µm posterior of the last formed somite). $\Delta P = 784$ Pa.

Movie 10

Neural tube aspiration *in vivo* in the PSM medial region (500 µm posterior of the last formed somite). $\Delta P = 784$ Pa.

Movie 11

Calibration of aluminum cantilever by resonant frequency measurement. 8000 frame per second.

Movie 12

Cantilever-based measurement of axis stress production. Cantilever stiffness $k = 35$ mN $\cdot$ m^{-1}. Left panel: 2.5X objective. Right panel: 10X objective.

Movie 13

Cantilever-based measurement of axis stress production. Cantilever stiffness $k = 7$ mN $\cdot$ m^{-1}. Left panel: 2.5X objective. Right panel: 10X objective.

Movie 14

PSM explants autonomous elongation within microchannels (width 75 µm). From left to right: full PSM, anterior half PSM, full PSM, posterior half PSM. Anterior is up.

Movie 15

Cell motility within a microchannel (width 75 µm). H2B-RFP electroporated PSM. Anterior is up. Note the posterior-most PSM does not exhibit any labeled cells. The intense cell mixing advects these cells to the medial region by then end of the movie.

Movie 16

Cantilever-based measurement of PSM explant stress production. Cantilever stiffness $k = 2$ mN $\cdot$ m^{-1}.

Appendix B

Mathematical appendix

B.1 Integration of the SLS model

We can write the equation that governs the relation between the strain ϵ of the SLS model and the applied stress σ:

$$\dot{\epsilon} + \frac{1}{\tau_c}\epsilon = \frac{1}{k_1 + k_2}\left(\frac{k_2}{\xi_c}\sigma + \dot{\sigma}\right) \tag{B.1}$$

where $\tau_c = \frac{\xi_c(k_1+k_2)}{k_1 k_2}$ and ξ_c, k_1, k_2 are defined Figure 4.3 A.

We integrate this equation for an instantaneous jump of stress, such as $\sigma = 0$ for $t < t_0$ and $\sigma = \sigma_0$ for $t \geq t_0$. Therefore, we can write the temporal derivative of the stress as $\dot{\sigma} = \sigma_0 \delta(t - t_0)$ where δ is the Dirac function.

By integrating B.1 with respect to time and by considering $\epsilon(t_0) = 0$, we have:

$$
\begin{aligned}
\epsilon(t) &= \epsilon(t_0)e^{-t/\tau_c} + \int_{t_0}^{t} \frac{1}{k_1 + k_2}\left(\frac{k_2}{\xi_c}\sigma + \dot{\sigma}\right)e^{(t'-t)/\tau_c}dt' \\
&= \frac{\sigma_0 \tau_c k_2}{(k_1 + k_2)\xi_c}\left(1 - e^{(t_0-t)/\tau_c}\right) + \frac{\sigma_0}{k_1 + k_2}e^{(t_0-t)/\tau_c}
\end{aligned}
$$

Simplifying using the expression of τ_c, we have:

$$\epsilon(t) = \frac{\sigma_0}{k_1}\left(1 - \frac{k_2}{k_1 + k_2}e^{(t_0-t)/\tau_c}\right) \tag{B.2}$$

B.2 Stiffness of a pulled rod

We fabricated a force sensor with a pulled glass rod. Its non-trivial geometry does not allow a direct calculation of its bending stiffness. However, we can write its dependency on its length with a geometrical pre-factor. For a rectangular beam of length ℓ, thickness t, width w, Young's modulus E, the bending stiffness k is given by:

$$k = E\frac{wt^3}{4\ell^3} \tag{B.3}$$

Regarding the pulled rod, its section varies along its length. The thick part of the rod is considerably stiffer than the rest and therefore can be approximated as being static. Only the tip is assumed to be in a bending mode. We note the length of this region ℓ (see Figure B.1 A). We approximate this region as a cylinder. Therefore, like a rectangular beam, its bending stiffness k is also a function of $1/\ell^3$. We can write:

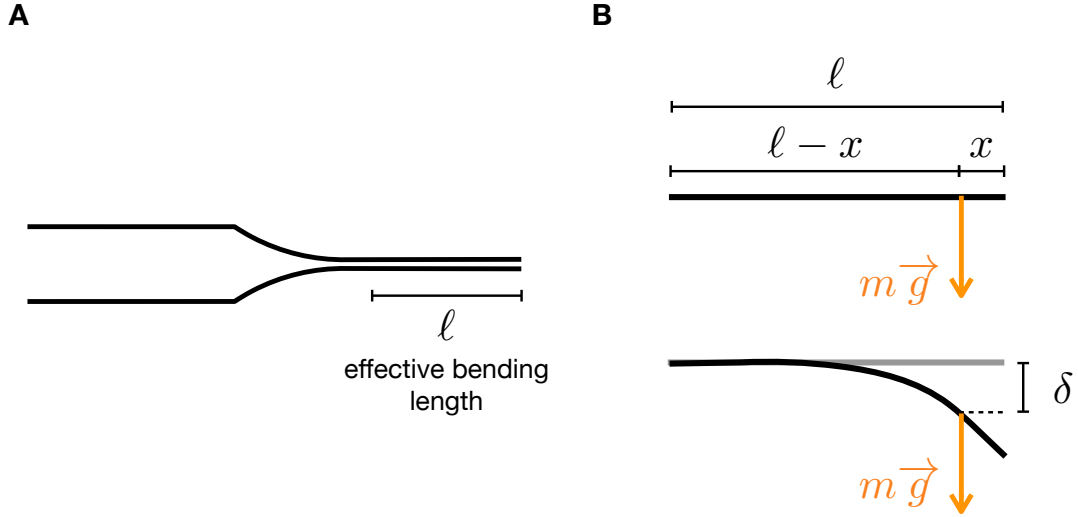$$k = \tilde{k}\frac{1}{\ell^3} \tag{B.4}$$

A

B

FIGURE B.1 – Schematic of a bending glass rod. **A**: Effective bending length of a pulled glass rod. **B**: Bending is function of the hanging mass position with respect to the tip x.

where $\tilde{k}$ is pre-factor depending on the cylinder section, the glass Young's modulus and any other irregularities introduced by our approximations.

If a force f is applied at the rod tip (like a hanging mass m). The rod bends with a deflection $\delta = \frac{f}{k} = \frac{mg}{k}$, where g is the gravitational constant. Note that this expression holds only if the rod is horizontal and we stay in the linear regime (small deflections). In practice, it can be challenging to hold a hanging mass exactly at the tip. It is, therefore, positioned at a distance x from the tip (see Figure B.1 B). The effective bending length is then $\ell - x$. Thus, using the bending stiffness relation B.4, the deflection measured at the position of the load reads:

$$\delta = \frac{mg}{k} = \frac{mg(\ell - x)^3}{\tilde{k}} \tag{B.5}$$

In this way, $\tilde{k}$ and ℓ can be fitted by measuring δ with hanging weights at different positions x.

Appendix C

Other projects

I have been involved in other projects during my Ph.D., which are briefly described here.

C.1   Analysis of the 3D cell trajectories in the primitive streak

An important side project during this Ph.D. was the development of a toolkit to visualize and analyze tracking data. Charlène Guillot generated high-quality 3D cell tracking during the regression of the primitive streak. Tracking softwares usually offer only basic visualization functions and rarely provide advanced analysis. When subtraction of a movement, compaction/expansion maps, polarization analysis, rotation analysis, etc. are needed custom codes are usually required (see for instance Lawton et al., 2013, Rozbicki et al., 2015 or Bénazéraf et al., 2017). I, therefore, developed an entirely Python-based toolkit. This toolkit does *not* perform any tracking. Its goal is to analyzed already tracked data and to provide visualization tools. It supports both 2D and 3D data.

This toolkit remains under development and is open-source: `https://github.com/amichaut/track_analysis`. It consists of 4 main methods:

- `cell_analysis`
  This method is a trajectory visualization tool. It allows plotting trajectories onto (or not) the microscopy images. If 3D data are provided, the trajectory depth is color-coded (see Figure C.1 A). It provides several filtering options: minimal trajectory length, trajectories over a subset of frames and trajectories within regions of interest (hand-drawn using a user-friendly graphical interface). Importantly the last filtering option offers the ability to perform fate maps. A subset of cells present in a region can be selected and their future trajectories imaged. Conversely, all cells present in a region can be back-tracked by plotting the trajectories that led them to this region.

- `map_analysis` This method plots various kinds of maps all based on the calculation of the velocity field. A grid of the desired resolution is used to average all cells within each block of the grid. The instantaneous velocity vector field can then be plotted. Maps of divergence (expansion/contraction), of the different velocity components along directions of space (v_x, v_y, v_z) and of velocity magnitude can be plotted (see Figures C.2 A, B).

- `avg_ROIs` This method offers a 2D visualization of the maps generated by `map_analysis`. Rectangular regions of interest can be hand-drawn onto the maps to plot the average of the map along the major axis of the region of interest. This function yields 2D profiles of the map (see Figures C.2C,D).
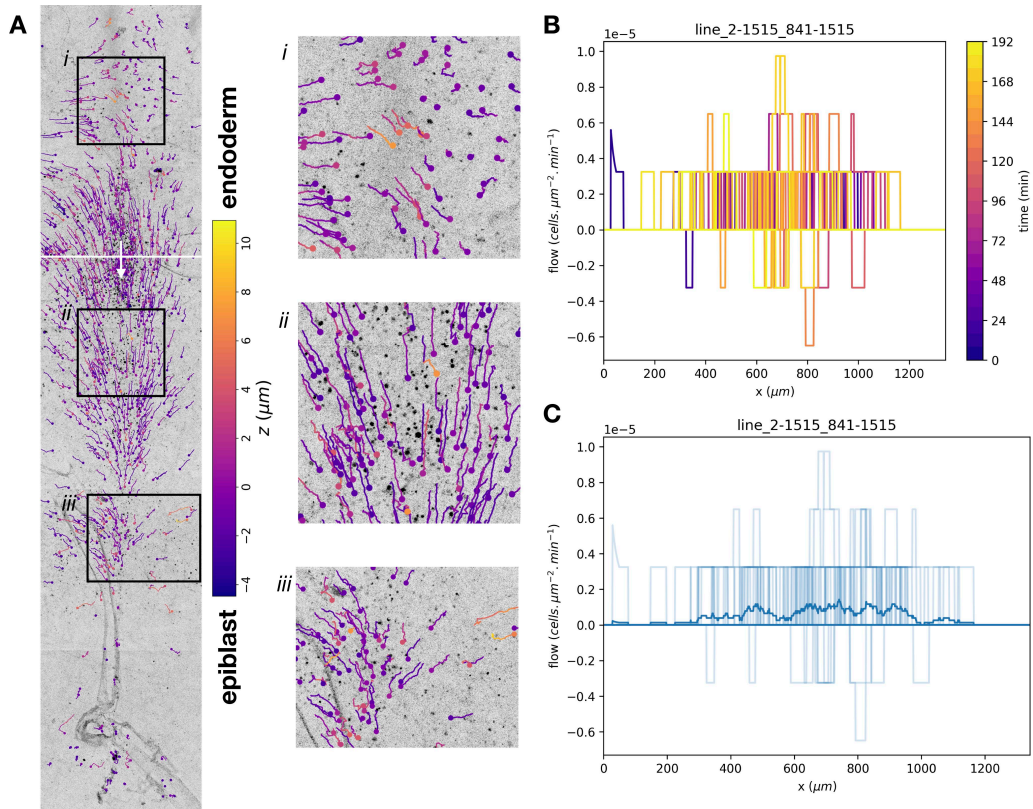
FIGURE C.1 – Trajectory analysis. **A**: Trajectories over 200 min. Squares labeled *i*, *ii*, *iii* define zooms presented in the right panels. Note trajectories becoming yellow are ingressing cells. Anterior is up, posterior is down. The surface $z = 0$ is defined as the mean z-position of all cells. $z < 0$ towards the epiblast, $z > 0$ towards the hypoblast. Cell flow through the vertical surface defined by the white line (and oriented by white arrow) panel **A**. Temporal evolution of the flow (**B**) and time average (**C**). Individual profiles are shown in transparency and time average as a solid line.

- `XY_flow` This method measures the flow of cells through a surface (for 3D data) or a line (for 2D data). A line is hand-drawn onto a microscopy image and is polarized to define the orientation of the measured flow (see Figures C.1 B, C).

A communication is in preparation:
Guillot, C., Michaut, A. and Pourquié, O. "Revisiting axis morphogenesis by understanding the unique dynamics of the Neuro-Mesodermal Progenitors"

C.2   Image analysis of brain asymmetry

I carried out image and statistical analysis on mice brain sections in order to investigate asymmetrical nuclei distribution in different cortical regions.

A communication is in preparation:
Rebagliati, M., Vilhais-Neto, G.C., Petiet, A., Lange, M., Michaut, A., Plassat, JL., Vermot, J., Riet F., Noblet, V., Laquerrière, P., Cussigh, D., Bedu, S., Dray, N., Sayed Gomaa, M., Simons, C., Meziane, H., Lehéricy, S., Bally-Cuif, L. and Pourquié, O. "WHHERE-dependant Retinoic Acid signaling controls brain asymmetry and handedness".
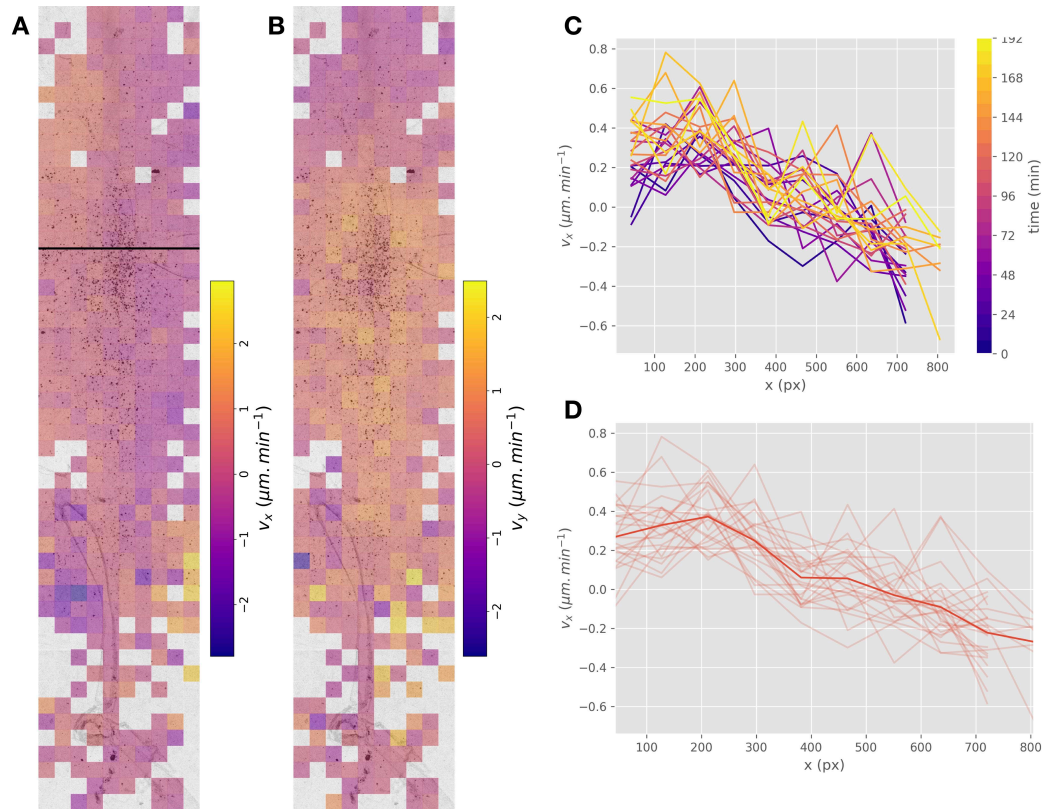
FIGURE C.2 – Map analysis. Maps of velocity components v_x (**A**, along the ML axis) and v_y (**B**, along the AP axis). Anterior is up, posterior is down. Postive values defines left to right displacements and anterior to posterior displacement. Average v_x profile along solid line panel **A**. Temporal evolution (**C**) and time average (**D**). Individual profiles are shown in transparency and time average as a solid line. Note the positive values (left to right movements) on the left part of the profile and the negative values (right to left movements) on the right part of the profile, indicating convergent movements towards the midline.

C.3   Science communication: *Ma thèse en 180 secondes*

Among other science communication projects (I founded the soft matter blog "Softbites" https://softbites.org/ and I am part of the science festival "taste of science" https://tasteofscience.org/), I was involved in a science communication event in direct relation with my Ph.D. I won the first American edition of the French-speaking competition *Ma thèse en 180 secondes*. This competition aims at summarizing a Ph.D. in 3 minutes for a lay audience. After winning this competition in the USA, I was qualified for the international final in Liège, Belgium in September 2017.

Appendix D

Extended French summary

D.1 Introduction

Les Vertébrés ont divergé des Céphalochordés par acquisition d'un squelette métamérisé. Les unités répétitives embryonnaires (appelées somites) du squelette axial se forment le long de l'axe antéro-postérieur (AP) puis se différencient en vertèbres. Les somites sont générés par une segmentation rythmique du mésoderme pré-somitique (PSM) de l'antérieur vers le postérieur (processus dénommé somitogenèse). Concomitamment à la somitogenèse, l'axe AP s'allonge. C'est au cours de ces processus que le plan d'organisation des Vertébrés est mis en place.

Afin d'étudier ce processus crucial, le poulet est un modèle animal approprié pour plusieurs raisons. Tout d'abord, à l'instar des Mammifères, les oiseaux sont des Amniotes et des Homéothermes. Les étapes précoces de leur développement sont grandement similaires. Ensuite, l'embryon de poulet se développe dans un œuf, ce qui le rend plus accessible que les embryons de Mammifères. De plus, durant la somitogenèse, l'embryon de poulet est relativement plat, ce qui facilite l'imagerie par microscopie et la culture sur de relativement longues durées. Enfin, les grandes dimensions de l'embryon de poulet (comparables à celles du Xénope) rendent sa manipulation physique plus aisée que celle de l'embryon de souris ou de poisson-zèbre (*Danio rerio*). En résumé, l'embryon de poulet est un Amniote dont les charactéristiques présentent un bon compromis pour l'imagerie et la manipulation physique. Pour cette raison, dans cette thèse, nous avons choisi l'embryon de poulet pour conduire une étude des propriétés mécaniques de l'embryon au cours de l'élongation de l'axe AP. Dans cette introduction, nous présentons les principales étapes du développement embryonnaire chez l'embryon de poulet et nous décrivons le modèle actuel expliquant le mécanisme d'élongation de l'axe AP durant la somitogenèse.

D.1.1 Aperçu du développement embryonnaire chez le poulet

Les premières divisions de la cellule-œuf se déroulent dans l'oviducte. Lorsque l'œuf est pondu, l'embryon est constitué d'un disque de 60 000 cellules (Eyal-Giladi and Kochav, 1976, Pokhrel et al., 2017), appelé blastoderme. Le disque est formé d'une unique couche de cellules (l'*area pellucida*), entourée d'un anneau sombre composé de plusieurs couches de cellules (l'*area opaca*). Du stade XI à XIII (de la table des stades précoces de Eyal-Giladi and Kochav, 1976), des cellules d'une zone plus dense de la zone postérieure de l'*area pellucida*, la zone postérieure marginale (PMZ), migrent vers l'antérieur pour former une deuxième couche de cellules, l'hypoblaste. La couche supérieure est appelée l'épiblaste et la cavité entre l'hypoblaste et l'épiblaste se nomme le blastocœle.

Après la formation des deux premiers feuillets embryonnaires, l'axe AP devient visible lors de la gastrulation. La gastrulation est le processus qui mène à la formation
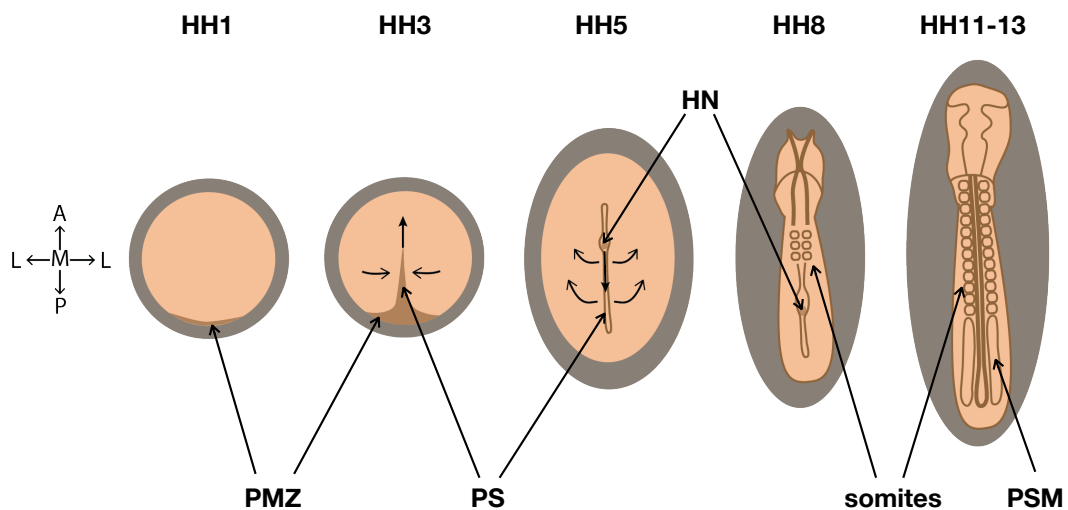
FIGURE D.1 – Schéma des stades précoces du développement embryonnaire chez le poulet. Gris : *area opaca*, beige : *area pellucida*. La polarité est donnée par les flèches sur la gauche : A : antérieur, P : postérieur, L : latéral, M : médian. PMZ : zone marginale postérieure, PS : ligne primitive, HN : nœud de Hensen, PSM : mésoderme présomitique. Les flèches indiquent les mouvements morphogénétiques. Les stades embryonnaires HH1, HH3, HH5, HH8, HH11-13 sont donnés par la table d'Hamburger-Hamilton (Hamburger and Hamilton, 1951).

des trois feuillets embryonnaires : l'ectoderme, le mésoderme et l'endoderme. Chez les Amniotes, la gastrulation se déroule le long d'une structure allongée le long de l'axe AP, appelée la ligne primitive (voir Figure D.1). Les cellules de l'épiblaste sont internalisées dans la région de la ligne primitive pour former l'endoderme et le mésoderme. La ligne primitive s'étend vers l'antérieur jusqu'au stade HH5 (Hamburger and Hamilton, 1951), puis régresse en initiant un mouvement postérieur de l'embryon. Dans l'axe, la plaque neurale et la notochorde sont alors formées dans la zone antérieure à la ligne primitive. Le tube neural est généré par plissement de la plaque neurale jusqu'à la neurulation secondaire (stade 27 somites). Les tissus axiaux sont flanqués du mésoderme paraxial composé d'une région segmentée (les somites) et d'une région non-segmentée (le PSM). Ces tissus dérivent de cellules progénitrices situées dans la zone postérieure de l'axe. Par conséquent, il y a un gradient de différenciation le long de l'axe AP, les cellules plus matures se trouvant vers la partie antérieure. Après quatre jours d'incubation, le mésoderme paraxial est totalement segmenté et les futurs organes continuent leur développement selon le plan d'organisation établi pendant la somitogenèse.

Les processus d'élongation de l'axe ont historiquement été étudiés chez le Xénope. Un mécanisme a été décrit comme étant un acteur majeur de l'élongation : la convergence extension (CE). La CE fait intervenir une contraction d'un tissu embryonnaire dans une direction et une extension selon la direction orthogonale. Ce processus aboutit à une déformation du tissu. Différents mécanismes de polarisation cellulaire ont été démontrés comme étant responsables de la contraction selon une direction (Keller et al., 2000). Cette contraction mène à l'intercalation des cellules au niveau de la zone centrale de la contraction et aboutit à l'extension du tissu
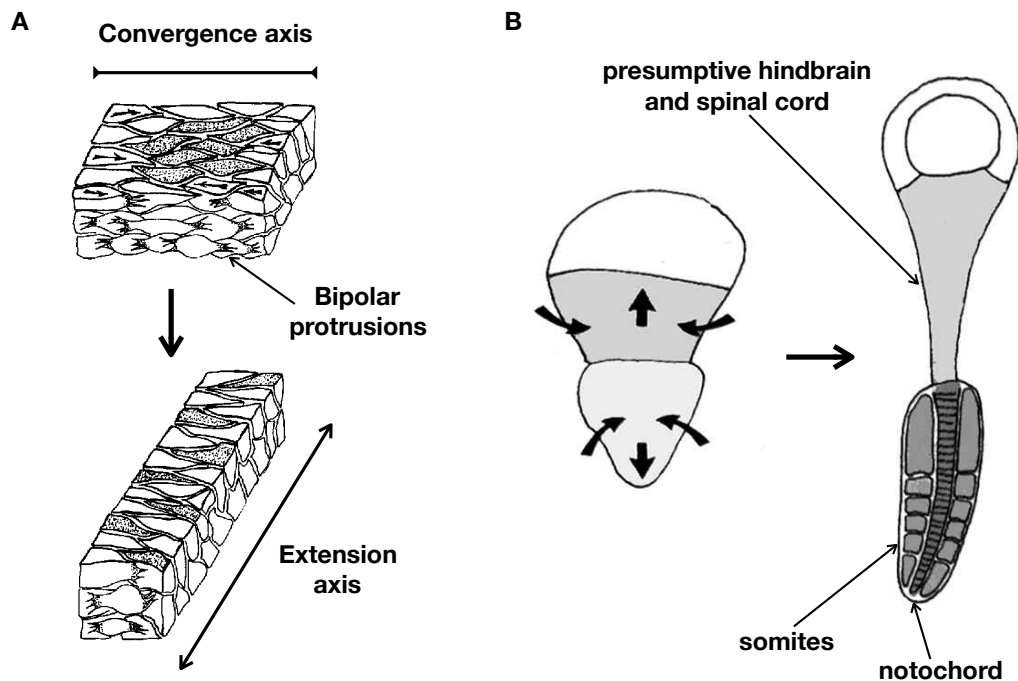
FIGURE D.2 – Schéma du mécanisme de convergence extension adapté de Keller et al., 2000. **A** : Convergence extension médiée par l'intercalation cellulaire. **B** : Élongation d'un explant de mésoderme de Xénope par convergence extension.

(voir Figure D.2). La CE médiée par l'intercalation des cellules est impliquée dans l'extension de la gastrula de Xénope (Keller et al., 2000), l'extension de l'axe AP du poisson-zèbre (Steventon et al., 2016), l'extension de l'axe AP de la souris (Yen et al., 2009, Williams et al., 2014), ainsi que lors de l'extension de la ligne primitive chez le poulet (Voiculescu et al., 2007, Rozbicki et al., 2015). Durant la somitogenèse chez l'embryon de poulet, une importante convergence selon l'axe médio-latéral est observée jusqu'au stade 10 somites. En revanche, l'élongation de l'axe AP se poursuit ensuite sans intervention d'une convergence selon l'axe médio-latéral. La CE ne peut donc pas totalement expliquer l'élongation de l'embryon de poulet. Un autre mécanisme basé sur la motilité cellulaire a été récemment proposé.

D.1.2 Rôle du mésoderme pré-somitique dans l'élongation du poulet

Chez l'embryon de poulet, un mécanisme original impliquant le profil de motilité cellulaire le long du PSM a récemment été proposé pour expliquer l'élongation de l'axe AP (Bénazéraf et al., 2010). Les auteurs ont montré que le PSM postérieur est essentiel à l'élongation de l'axe. Il avait été démontré précédemment qu'un gradient de Wnt et FGF8 le long du PSM contrôlait l'élongation (Delfini et al., 2005). Bénazéraf et al., 2010 ont pour leur part établi que le gradient de FGF8 était à l'origine d'un gradient de motilité cellulaire au sein du PSM. Les cellules du PSM ne présentent pas de migration directionnelle par rapport à leur environnement local mais des mouvements aléatoires. L'amplitude de ces mouvements aléatoires est graduée le long de l'axe : une forte motilité dans la région postérieure (associée à une faible densité
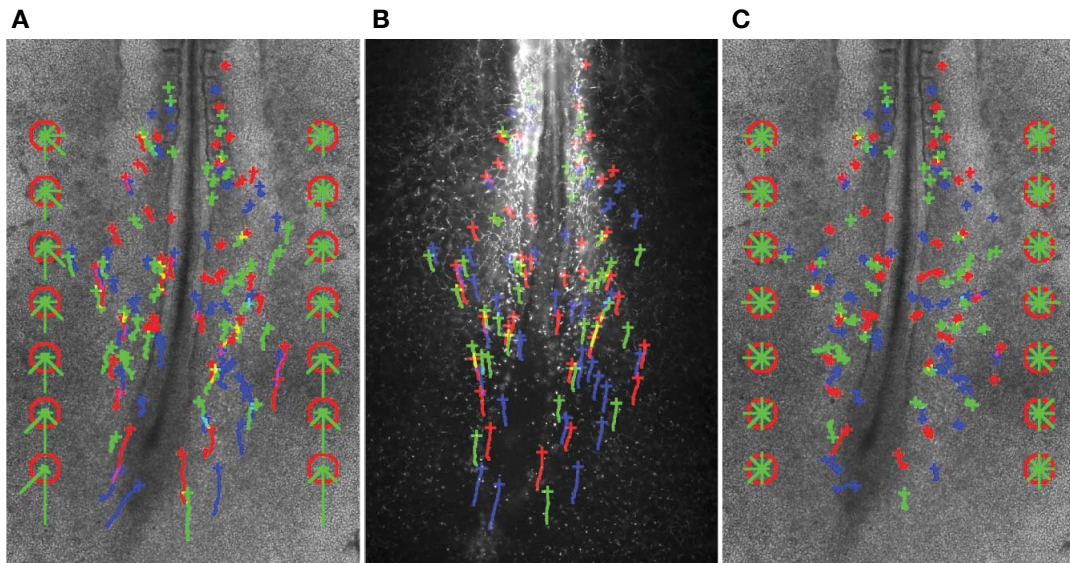
FIGURE D.3 – Mouvements cellulaires et de la matrice extracellulaire le long de l'axe (adapté de Bénazéraf et al., 2010). **A** : Trajectoires de cellules individuelles et directionalité moyenne. **B** : Mouvements de la matrice extracellulaire. **C** : Trajectoires cellulaires par rapport à la matrice extracellulaire.
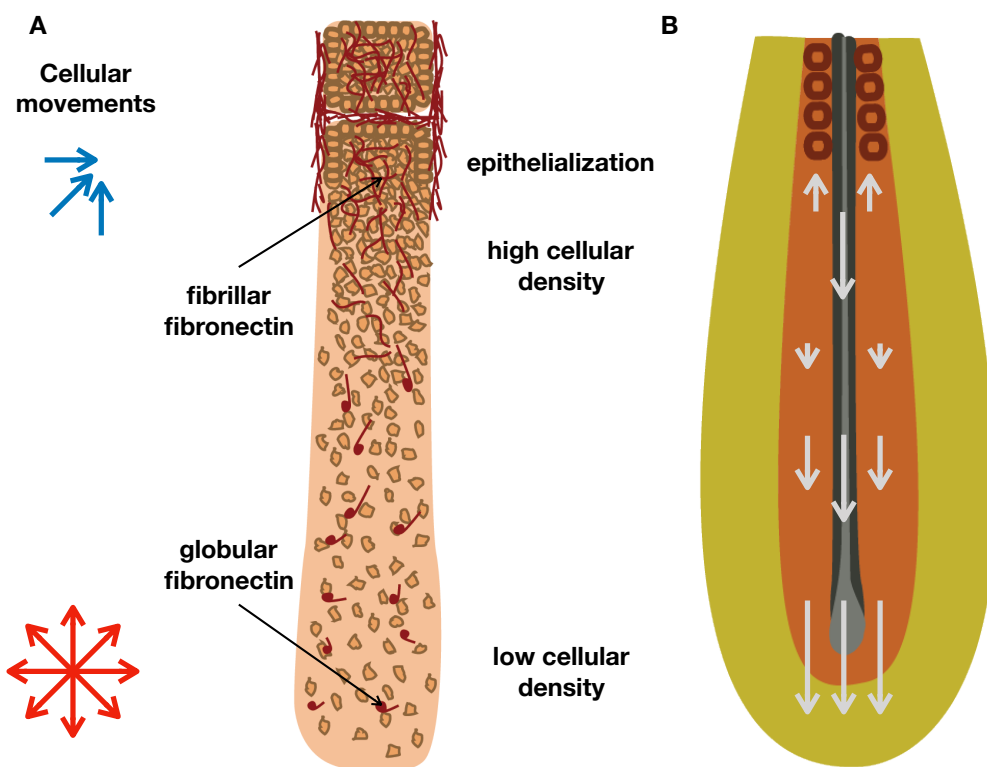

FIGURE D.4 – Schéma des mouvements cellulaires et tissulaires. **A** : Densité et mouvements cellulaires le long de l'axe. **B** : Mouvements tissulaires relatifs. Les flèches représentent la composante AP de la vitesse par rapport au dernier somite formé.
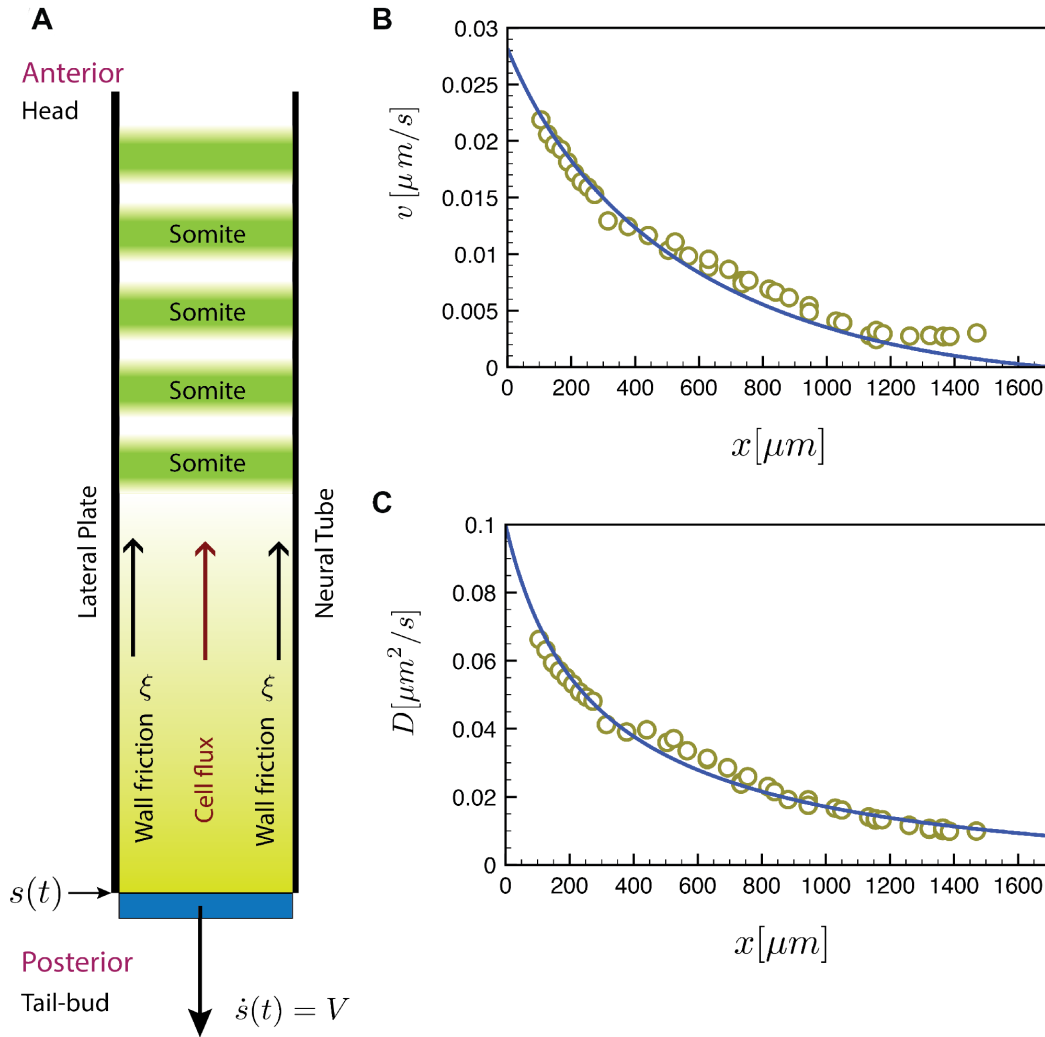
FIGURE D.5 – Modèle continu de motilité aléatoire (adapté de Regev et al., 2017). **A** : Schéma du modèle continu. Mesures expérimentales de la vitesse du flot (**B**) et diffusivité cellulaire (**C**) le long de l'axe.

cellulaire) et une faible motilité dans la région antérieure (associée à une plus forte densité cellulaire) ont été décrites (voir Figures D.3 et D.4). Le gradient de motilité cellulaire est essentiel à l'élongation. De plus, la prolifération et l'injection de cellules progénitrices ne semblent pas être cruciales pour la bonne élongation de l'axe, du moins à court terme. Il a par ailleurs été démontré que le gradient de motilité le long de l'axe était relié à un gradient métabolique et un gradient de pH intracellulaire et extracellulaire (Oginuma et al., 2017). Une haute activité glycolytique et une acidité extracellulaire plus importante dans le PSM postérieur ont été observées. Des altérations de ces différents gradients mènent à des défauts d'élongation qui sont également corrélés à une altération du gradient de motilité cellulaire. En résumé, le gradient de motilité cellulaire au sein du PSM semble crucial à l'élongation.

Pour expliquer le rôle du gradient de motilité aléatoire, Bénazéraf et al., 2010 ont proposé que le gradient de motilité entrainait un mouvement aléatoire biaisé des cellules vers l'extrémité postérieure. La forte motilité postérieure exercerait une pression déformant la limite postérieure de l'embryon. Ce modèle a été développé de manière quantitative grâce à une description continue du PSM (Regev et al., 2017).

Le PSM est alors considéré comme un fluide actif confiné médio-latéralement par des bords rigides (voir Figure D.5). Le modèle théorique requiert plusieurs grandeurs physiques estimées à partir de mesures expérimentales. En particulier, le modèle considère une viscosité constante le long du PSM $\eta \approx 10^4$ (ordre de grandeur issu de mesures préliminaires par aspiration par micropipette). Le modèle prédit en particulier la pression exercée par le PSM postérieur ($\alpha \rho_0 \approx 1.3$ Pa) et la contrainte de la limite postérieure résistant l'avancée du PSM ($F \approx 1.5$ mPa).

Afin de vérifier la validité du modèle, ses hypothèses (en particulier, le confinement médio-latéral du PSM) et les grandeurs physiques mesurées (en particulier la viscosité) doivent être étudiées expérimentalement. À ce jour, seules des données d'élasticité moyenne de la totalité de l'embryon ont été rapportées (Agero et al., 2010). De plus, il est nécessaire de comparer les prédictions de pression produite par le PSM avec des données expérimentales. De ce fait, dans cette thèse, nous présentons tout d'abord des mesures de propriétés mécaniques des tissus le long de l'axe AP grâce à deux techniques. Premièrement, nous mesurons la vitesse visco-capillaire le long du PSM par des expériences d'arrondissement et de fusion d'explants. Deuxièmement, nous mesurons la tension de surface, l'élasticité et la viscosité du PSM et du tube neural. Enfin, nous mesurons la pression produite par, d'une part, l'embryon et, d'autre part, le PSM isolé lors de l'élongation.

D.2 Propriétés visco-capillaires du mésoderme pré-somitique le long de l'axe antéro-postérieur

Afin d'étudier les propriétés mécaniques du PSM nous avons employé une première approche consistant à mesurer le ratio de tension de surface sur viscosité : la vitesse visco-capillaire. Nous utilisons deux expériences basées sur les propriétés liquides du PSM à long terme. Un explant de PSM en culture a tendance à minimiser son rapport surface sur volume en formant une sphère. Ce processus est mené par la tension de surface et résisté par la viscosité. Les dynamiques d'arrondissement d'un explant non-sphérique ou de fusion de deux explants pour former une sphère plus large sont donc dictées par un rapport de tension de surface sur viscosité. En particulier, si un tissu s'arrondissant est considéré comme un ellipsoïde de révolution, sa dynamique d'arrondissement peut-être décrite par l'évolution temporelle de son rapport d'aspect a/b, où a et b sont respectivement les longueurs des axes majeur et mineur (voir Figure D.6 A). Le rapport d'aspect suit une décroissance exponentielle (Gordon et al., 1972) :

$$\frac{a(t)}{b(t)} - 1 = \left(\frac{a_0}{b_0} - 1\right) \exp\left(\frac{-t}{\tau}\right) \tag{D.1}$$

où $a_0 = a(0)$, $b_0 = b(0)$ et le temps typique de décroissance τ est donné par :

$$\tau = \alpha \frac{\eta}{\gamma} R_f \tag{D.2}$$

avec le préfacteur numérique $\alpha \approx 0.95$, η la viscosité du tissu, γ la tension de surface et R_f le rayon final du tissu. La vitesse visco-capillaire $v_p = \frac{\gamma}{\eta}$ peut alors être mesurée par régression de l'évolution temporelle.

La vitesse visco-capillaire peut également être estimée en mesurant la vitesse de croissance du contact entre deux sphéroïdes de rayon initial R_0 fusionnant. D'après
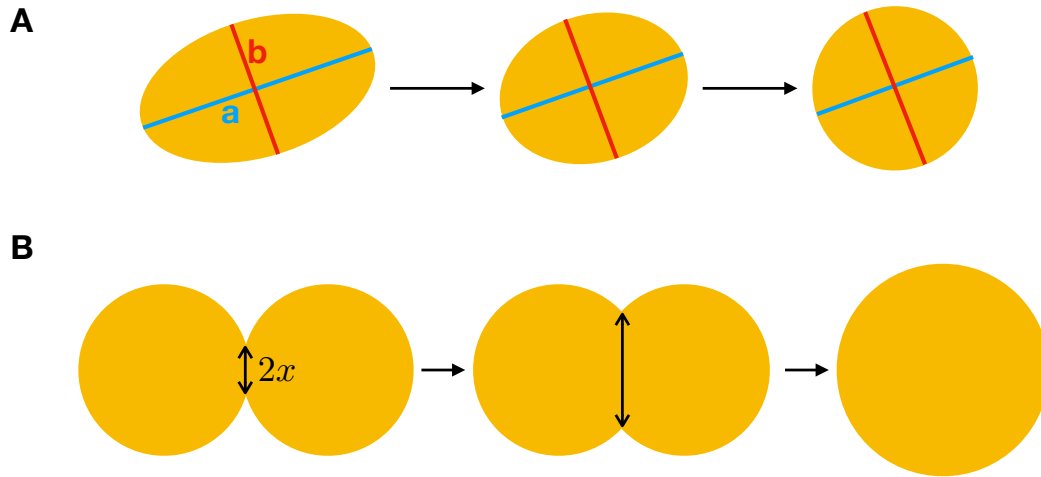
A

B

FIGURE D.6 – Schéma des expériences d'arrondissement et de fusion.
A : Expérience d'arrondissement. Un explant sous la forme d'un ellip-
soïde de révolution d'axe majeur a et axe mineur b s'arrondit au cours
du temps. **B** : Expérience de fusion. Deux sphéroïdes fusionnent via
un contact de rayon x qui croit au court du temps.

la théorie de Frenkel, 1945, le carré du rayon du contact x^2 croît linéairement à temps
courts (voir Figure D.6 B). Ainsi :

$$x^2 = \frac{R_0 \gamma}{\eta} t. \tag{D.3}$$

Nous avons observé une différence claire de dynamique d'arrondissement et de
fusion le long de l'axe. La Figure D.7 montre qu'un explant antérieur s'arrondit net-
tement plus lentement qu'un explant postérieur. Les expériences d'arrondissement
et de fusion aboutissent aux mêmes ordres de grandeur de vitesse visco-capillaire
(voir Figure D.8), avec un facteur 7 de différence entre les régions antérieure et
postérieure. Nous avons également étudié l'influence de la motilité cellulaire sur
la vitesse visco-capillaire en traitant les explants de deux manières différentes. Nous
avons utilisé un inhibiteur de la phosphorylation de la myosine (la blebbistatin) et
un inhibiteur de la voie FGF8/MAPK (le PD0325901). L'effet de ces traitements sur
la vitesse visco-capillaire aboutit à une modification non-triviale du profil de vitesse
visco-capillaire le long de l'axe. En antérieur, v_p est augmentée et en postérieur v_p est
diminuée (dans le cas du PD0325901) ou inchangée (dans le cas de la blebbistatin). Il
est probable que la blebbistatin impacte à la fois la tension de surface et la viscosité
dans la mesure où elle inhibe la contractilité cellulaire. Ce résultat peut donc être ex-
pliqué par une diminution équivalente de la viscosité et de la tension de surface en
postérieur. En antérieur, l'augmentation est probablement due à la diminution d'un
artefact expérimental présent dans les explants contrôles (formation de la fissure so-
mitique). Dans le cas de l'inhibition de FGF8/MAPK, il est plus difficile d'anticiper
l'impact sur la tension de surface, de ce fait l'interprétation est moins aisée.
En résumé, nous avons mis en évidence un gradient clair de propriétés mécaniques
du PSM le long de l'axe AP. Ce gradient doit être mis en regard avec les gradients de
motilité cellulaire et de densité cellulaire. Les perturbations de la motilité cellulaire
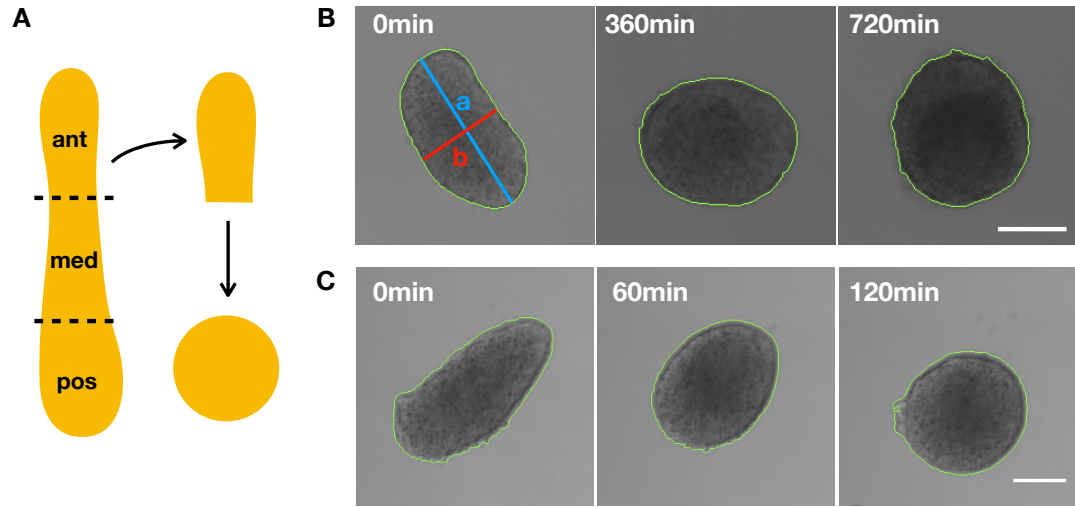aboutissent à une modification des propriétés mécaniques.

FIGURE D.7 – Dynamique d'arrondissement. **A** : Schéma de dissection d'un explant. Clichés de microscopie pendant l'arrondissement d'un explant antérieur (**B**) et postérieur (**C**). Échelles : 100 μm.
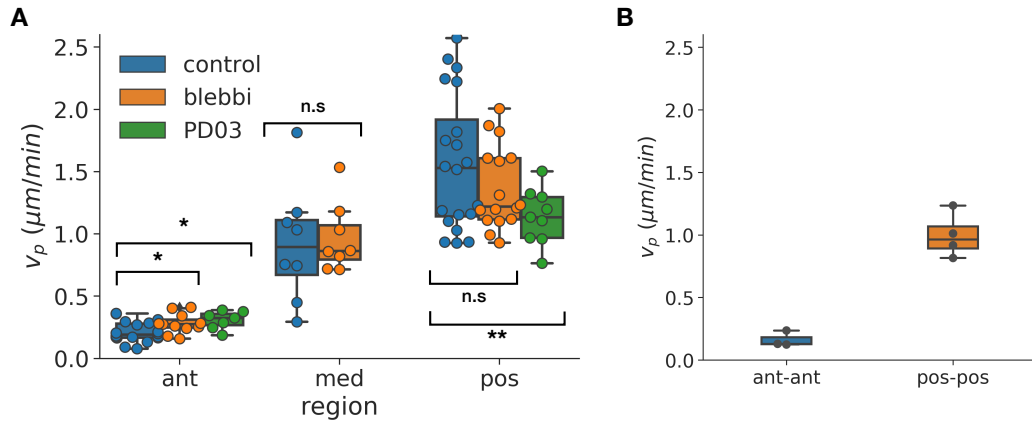

FIGURE D.8 – Vitesse visco-capillaire le long de l'axe antéro-postérieur. **A** : Vitesse visco-capillaire mesurée par arrondissement d'explants de différentes régions (ant : antérieur, med : médian, pos : postérieur) pour différentes conditions (blebbi : blebbistatin 20 μM, PD03 : PD0325901 2 μM). **B** : Vitesse visco-capillaire mesurée par fusion de paires d'explants antérieurs (ant-ant) et de paires d'explants postérieurs (pos-pos).
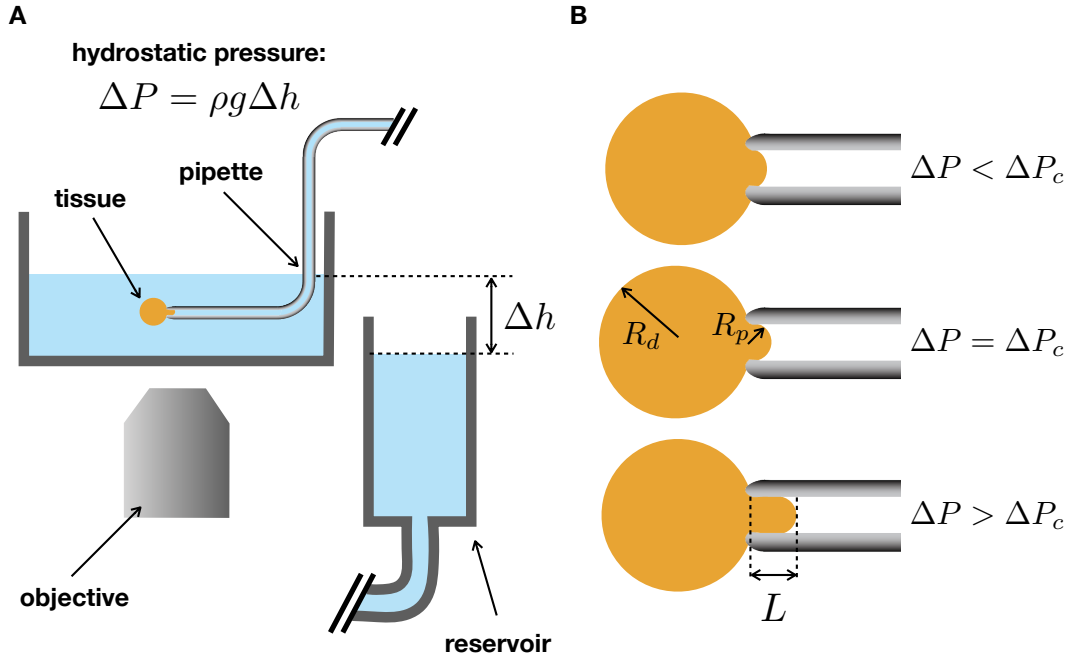
FIGURE D.9 – Principe d'aspiration par micropipette. **A** : Schéma d'un montage d'aspiration. **B** : Schéma d'une goutte visqueuse aspirée sous différents régimes de pression : $\Delta P < \Delta P_c$: la courbure dans la pipette augmente avec la pression, $\Delta P = \Delta P_c$: la courbure dans la pipette est maximale ($2/R_p$), $\Delta P > \Delta P_c$: la courbure dans la pipette reste constante et la goutte flue dans la pipette.

D.3 Propriétés visco-élastiques des tissus axiaux et paraxiaux le long de l'axe antéro-postérieur

Afin de mesurer indépendamment la tension de surface, la viscosité et l'élasticité, nous avons réalisé des mesures d'aspiration par micropipette. Cette technique consiste à observer la dynamique d'aspiration et de rétraction d'un fragment de tissu soumis à une pression d'aspiration (voir Figure D.9 A). Cette technique permet de découpler les propriétés surfaciques et volumiques. La tension de surface est à l'origine d'une pression critique ΔP_c en dessous de laquelle la contribution de la tension de surface domine l'aspiration et au-delà de laquelle le tissu flue dans la pipette (voir Figure D.9 B). Lorsqu'un explant de PSM est aspiré à une pression supérieure à cette pression critique, il flue avec une dynamique caractéristique d'un solide visco-élastique à temps courts et d'un liquide à temps longs. Nous avons donc modélisé la rhéologie du PSM par une modification du *Standard Linear Solid model* en rajoutant un élément visqueux en série. La dynamique d'aspiration à la suite d'un saut de pression suit donc l'équation suivante :

$$L(t) = \delta \left(1 - \beta e^{-t/\tau_c} \right) + \dot{L}_\infty t \tag{D.4}$$

où L est la longueur de la langue de tissu aspiré (voir Figure D.10 A), δ l'amplitude de la déformation élastique, $\dot{L}_\infty$ le taux du flot visqueux, β un paramètre contrôlant l'instantanéité de la réponse élastique et τ_c le temps caractéristique du régime élastique. En pratique, des explants de différentes régions du PSM sont aspirés et les paramètres du modèle rhéologique sont calculés par régression (voir Figure D.10 B, C).
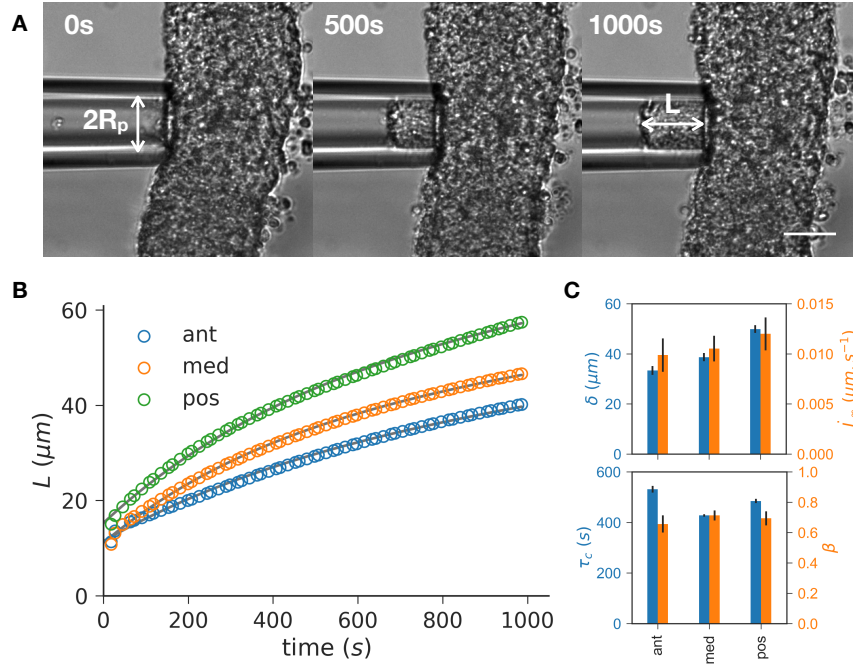
FIGURE D.10 – Exemple d'aspiration d'explants de PSM. **A** : Extraits d'un film d'aspiration. Échelle : 50 µm. **B** : Dynamique d'aspiration le long de l'axe (ant : antérieur, med : médian, pos : postérieur). **C** : Paramètres de régression.

La dynamique d'aspiration dépend à la fois de la tension de surface et des propriétés volumiques (élasticité et viscosité). Nous séparons ces contributions en mesurant la tension de surface, en déterminant la pression critique ΔP_c par augmentation itérative de la pression (voir Figure D.11 A). En effet, la tension de surface γ est reliée à la pression critique par :

$$\gamma = \frac{\Delta P_c}{\frac{2}{R_p} - \kappa_d}$$ (D.5)

où R_p est le rayon de la pipette et κ_d est la courbure locale de l'explant.

L'élasticité et la viscosité peuvent être ensuite calculées en soustrayant la contribution de la tension à la réponse :

$$\begin{cases} E &= \frac{R_p(\Delta P - \Delta P_c)}{\delta} \\ \eta &= \frac{R_p(\Delta P - \Delta P_c)}{3\pi \dot{L}_\infty} \end{cases}$$ (D.6)

Nous avons mesuré un profil de tension de surface relativement constant le long de l'axe (voir Figure D.11 B). Quant aux propriétés volumiques, nous avons observé une nette différence entre des explants disséqués à l'aide de pancréatine (hydrolysant un large spectre de molécules de la matrice extra-cellulaire) et des explants disséqués à l'aide de collagénase (préservant en particulier la fibronectine.) Les explants disséqués par pancréatine sont clairement moins rigides et moins visqueux (voir Figure D.11 C, D). Nous avons observé une importante dispersion entre embryons. En revanche, à l'échelle de PSM individuels, nous avons systématiquement noté l'existence d'un gradient antéro-postérieur d'élasticité et de viscosité (antérieur plus rigide et plus visqueux).
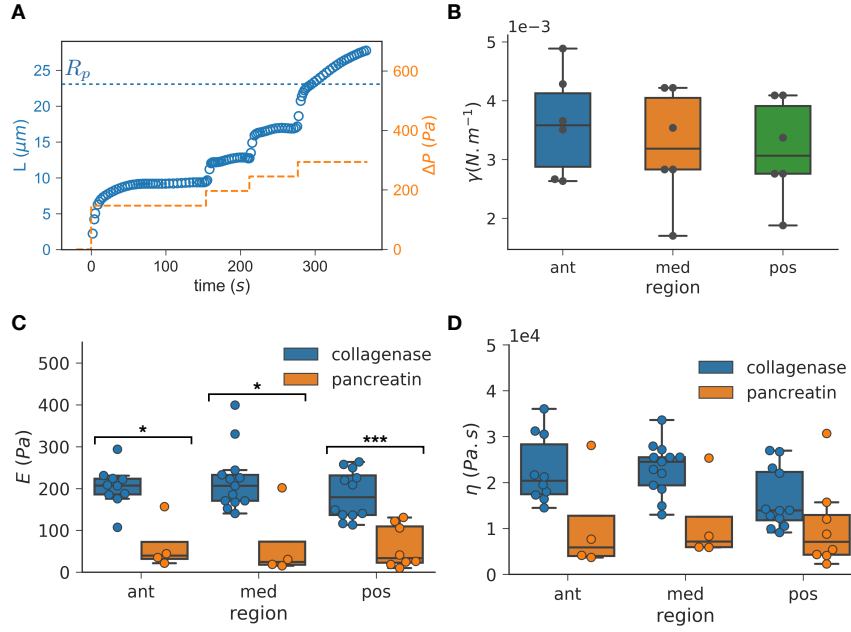
FIGURE D.11 – Tension de surface, élasticité et viscosité le long de l'axe. **A** : Mesure de ΔP_c. **B** : Tension de surface. **C** : Élasticité. **D** : Viscosité. ant : antérieur, med : médian, pos : postérieur. p-value p du t-test de Student : $\star$: $p < 0.05$, $\star\star$: $p < 0.01$.

Nous avons également mesuré les propriétés du tube neural. Le tube neural présente un gradient net d'élasticité le long de l'axe (voir Figure D.12). De plus dans les régions antérieures, il est significativement plus rigide que le PSM. Ce résultat nous permet de confirmer partiellement l'hypothèse de modèle de motilité aléatoire : le PSM est confiné latéralement par le tube neural.

Nous avons par ailleurs calculé la vitesse visco-capillaire avec les mesures de pipette. Une importante différence avec les expériences d'arrondissement et de fusion a alors été remarqué. Les données d'aspiration mènent à une vitesse visco-capillaire 45 fois plus importante en antérieur et 7 fois plus importante en postérieur que les données d'arrondissement. Cette différence pourrait être expliquée soit par une mesure d'un différent type de viscosité entre les deux expériences dans la mesure où
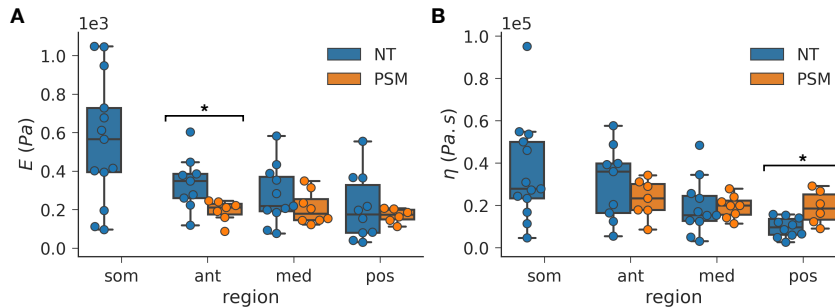
FIGURE D.12 – Comparaison des propriétés mécaniques du PSM et du tube neural. **A** : Élasticité. **B** : Viscosité. NT : tube neural. som : région somitique, ant : région du PSM antérieur, med : région du PSM médian, pos : région du PSM postérieur. p-value p du t-test de Student : $\star$: $p < 0.05$.

le temps caractéristique d'expérience sont nettement différents (quelques minutes pour l'aspiration et plusieurs heures pour l'arrondissement). Même si les deux méthodes de mesure des propriétés rhéologiques du PSM ne mènent pas à une même valeur, toutes deux mettent en évidence un gradient antéro-postérieur de propriétés mécaniques.

D.4 Pression générée par l'élongation de l'axe antéro-postérieur

Afin de tester notre modèle théorique nous avons souhaité mesurer la force générée par le PSM en particulier lors de l'élongation, pour la comparer à la pression prédite par le modèle. De plus, nous avons mesuré la force produite par la totalité de l'embryon pour évaluer la contribution du PSM à l'élongation. Pour cela, nous avons fabriqué un senseur de force (*cantilever*) à l'aide d'une fibre de verre étirée et d'un feuillet d'aluminium (voir Figure D.13 A). Nous avons également mis au point une méthode de culture permettant d'insérer le senseur de force pendant la croissance de l'embryon. La raideur du senseur de force a été calibrée par mesure de sa fréquence de résonance à l'aide d'une caméra à haute vitesse.
Nous avons mesuré la force maximale que pouvait générer un embryon lors de la croissance. Lorsque le *cantilever* est inséré dans l'embryon, il est défléchi au cours de la croissance et sa résistance augmente. En fonction de la raideur du *cantilever*, un plateau de déflection apparaît au cours du temps, ce qui signale que la force maximale que l'embryon peut produire est atteinte. Pour les *cantilevers* souples ($\sim$ 1-5 mN $\cdot$ m^{-1}), la force maximale n'est pas atteinte, alors que pour des raideurs plus élevées ($\sim$ 10-20 mN $\cdot$ m^{-1}), la force maximale est atteinte plus ou moins rapidement (voir Figure D.13 B, C). La force mesurée par le *cantilever* dépend de la surface de contact. Nous avons donc mesuré la pression maximale produite par l'embryon en divisant par l'aire de contact. L'embryon développe une pression maximale d'environ 120 Pa, ce qui est dans les mêmes ordres de grandeurs que l'élasticité des tissus embryonnaires. Ceci suggère que l'embryon développe des pressions suffisantes pour déformer son environnement.

Dans le but de mesurer la contribution du seul PSM à l'élongation de l'embryon, nous avons développé un système de microcanaux mimant le confinement medio-latéral du PSM. Des explants de PSM sont introduits dans des canaux de PDMS fermés par une lamelle de verre (voir Figure D.14). Nous avons observé que le PSM est capable de s'allonger de manière autonome, en l'absence des tissus adjacents, durant 6-8 heures. En moyenne, un PSM s'allonge de 19%. Cette croissance est principalement menée par la moitié postérieure du PSM qui quant à elle s'allonge de 57% en moyenne (voir Figure D.15). De plus, l'inhibition de la voie FGF8/MAPK par PD0325901 aboutit à une diminution de l'élongation de l'explant. Par ailleurs, nous avons aussi mesuré que la pression maximale que pouvait générer un PSM confiné dans un microcanal était de 9 Pa.

En résumé, nous avons démontré que le PSM est capable d'élongation de manière autonome et que cette élongation est menée par la région postérieure. Nous avons également pu estimer la contribution du PSM à la force maximale que peut développer l'embryon. Cette contribution est relativement modeste (16%), cependant ce résultat ne doit pas être interprété comme une contribution mineure du PSM au mécanisme d'élongation. En effet, il est possible que le PSM isolé de l'embryon développe une force moindre. Ensuite, la force maximale d'élongation dépend à la
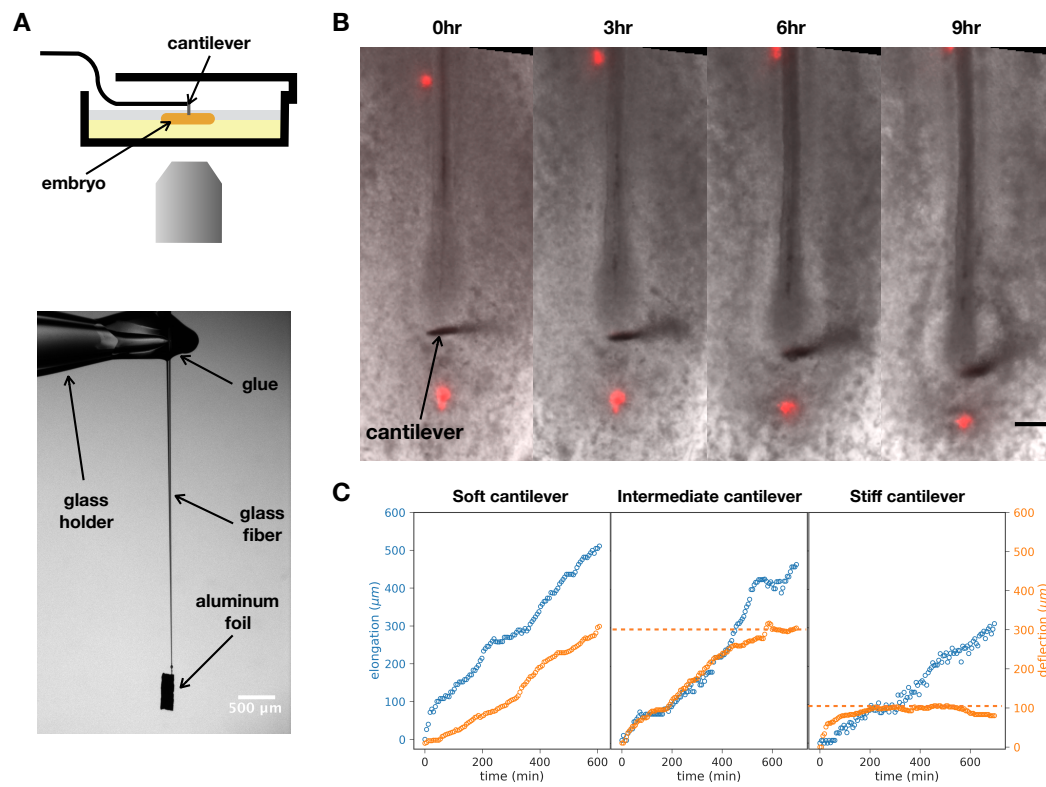
FIGURE D.13 – Mesure de la force d'élongation *in vivo*. **A** : Montage expérimental. **B** : Déflection du senseur de force au cours de l'élongation. **C** : Mesure de l'élongation et de la déflection pour différentes raideurs de senseur de force.
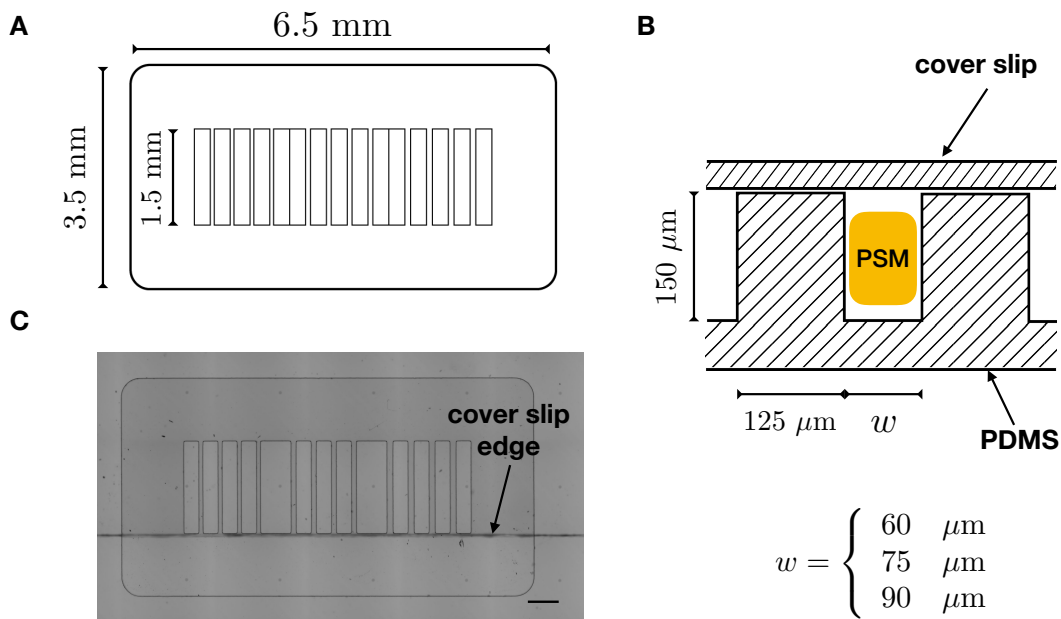

FIGURE D.14 – Fabrication de microcanaux. Schéma de la série de microcanaux vue du dessus (**A**) et vue de côté (**B**). **C** : Cliché de microscopie de la série de microcanaux. Échelle : 250 µm.
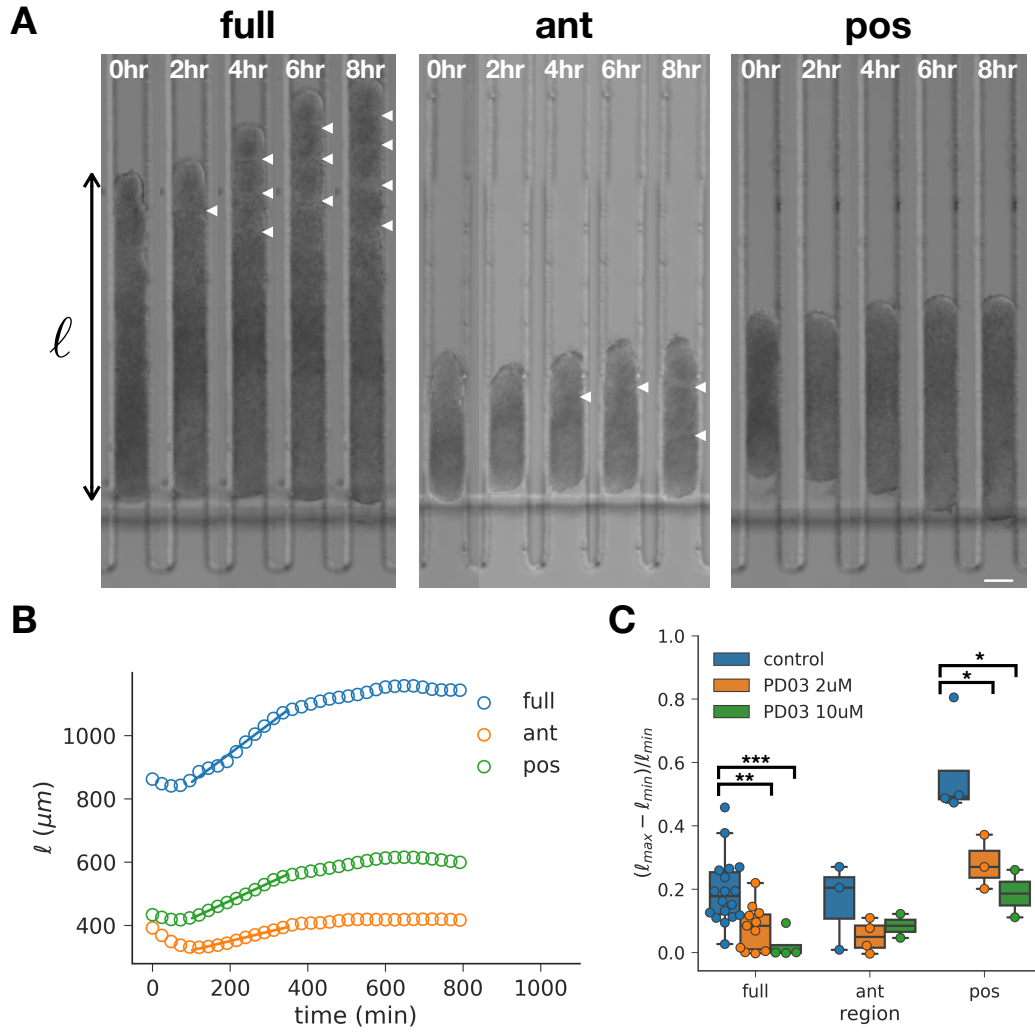
FIGURE D.15 – Élongation autonome de PSM confinés dans des microcanaux. **A** : Série de clichés de microscopie au cours d'une élongation pour un PSM entier, une moitié antérieure et une moitié postérieure. **B** : Évolution temporelle de la longueur d'un explant confiné pour un PSM entier, une moitié antérieure et une moitié postérieure. **C** : Élongation sous différentes condition (contrôle, 2 µM PD0325901, 10 µM PD0325901) pour PSM entiers, moitiés antérieures et moitiés postérieures. p-value p du t-test de Student : $\star$: $p < 0.05$, $\star\star$: $p < 0.01$, $\star\star\star$: $p < 0.001$.

fois de production de force instantanée et des propriétés mécaniques des tissus. Il est donc possible que le PSM étant un tissu mou ne puisse pas développer une force maximale importante. Cependant, *in vivo*, la résistance à l'élongation est potentiellement largement inférieure à cette force maximale, ce qui expliquerait que le PSM soit tout de même moteur.

D.5   Conclusion et discussion

Dans cette thèse, nous avons étudié le profil de propriétés mécaniques le long de l'axe AP ainsi que la génération de force par différents tissus lors de l'élongation, chez l'embryon de poulet. Les propriétés mécaniques ont été mesurées en appliquant à l'embryon de poulet des méthodes existantes, alors qu'un nouveau système expérimental a été développé pour mesurer la force d'élongation.

Les deux méthodes que nous avons utilisées (arrondissement et microaspiration) pour mesurer les propriétés mécaniques ont mis en évidence l'existence d'un gradient antéro-postérieur. Cependant, les deux méthodes mènent à des valeurs absolues différentes. De plus, les expériences d'arrondissement conduisent à un gradient bien plus important que les expériences d'aspiration. Cet écart peut être expliqué de trois façons. Premièrement, il est probable que la puissance statistique de nos mesures soit trop faible par rapport à l'importante dispersion des données (particulièrement dans le cas des aspirations par micropipette). Deuxièmement, il est possible que les deux techniques mesurent des propriétés réellement différentes. En effet, les tissus biologiques étant des matériaux actifs, ils peuvent répondre de manière différente en fonction du type de mesure. Les expériences d'arrondissement et de pipette se déroulent à des temps caractéristiques distincts (respectivement plusieurs heures et quelques minutes). La viscosité mesurée peut donc être différente en fonction des processus en jeu. Enfin, une vérification systématique que ces différentes méthodes aboutissent à des résultats similaires n'a pas encore été réalisée sur des systèmes biologiques plus reproductibles (comme des aggrégats de lignées de cellules). La théorie sur laquelle ces méthodes sont basées est encore donc à vérifier plus en détails.

Nous avons montré que le PSM était capable de s'allonger de manière autonome. En particulier, la région postérieure qui a été précédemment décrite comme clé vis à vis de l'élongation *in vivo*, est la région principalement responsable de l'élongation du PSM isolé. Nous avons également développé un système de mesure de force d'élongation. Comme première approche, nous avons mesuré la contribution du PSM à la force maximale que peut développer l'embryon. Cependant, cette grandeur est différente de la force associée avec la motilité cellulaire prédite par le modèle théorique. Cette force reste à être mesurée dans le futur. De plus, afin de préciser le modèle d'élongation, l'élongation autonome des tissus axiaux et leur force d'élongation doivent être également mesurées.

Bibliography

Adams, D S, R Keller, and M a Koehl (1990). "The mechanics of notochord elongation, straightening and stiffening in the embryo of Xenopus laevis." In : *Development (Cambridge, England)* 110.1, pp. 115–30. ISSN : 0950-1991. DOI : `10.1093/icb/40.1.53`. URL : `http://www.ncbi.nlm.nih.gov/pubmed/2081454`.

Agero, Ubirajara, James a Glazier, and Michael Hosek (2010). "Bulk elastic properties of chicken embryos during somitogenesis." In : *Biomedical engineering online* 9.1, p. 19. ISSN : 1475-925X. DOI : `10.1186/1475-925X-9-19`. URL : `http://biomedical-engineering-online.biomedcentral.com/articles/10.1186/1475-925X-9-19http://www.ncbi.nlm.nih.gov/pubmed/20353597http://www.pubmedcentral.nih.gov/articlerender.fcgi?artid=PMC3212891`.

Alev, Cantas, Yuping Wu, Yukiko Nakaya, and Guojun Sheng (2013). "Decoupling of amniote gastrulation and streak formation reveals a morphogenetic unity in vertebrate mesoderm induction". In : *Development* 140.13, pp. 2691–2696. ISSN : 0950-1991. DOI : `10.1242/dev.094318`. URL : `http://dev.biologists.org/lookup/doi/10.1242/dev.094318`.

Aoki, Takahira, Toshiro Ohashi, Takeo Matsumoto, and Masaaki Sato (1997). "The pipette aspiration applied to the local stiffness measurement of soft tissues". In : *Annals of Biomedical Engineering* 25.3, pp. 581–587. ISSN : 0090-6964. DOI : `10.1007/BF02684197`. URL : `http://link.springer.com/10.1007/BF02684197`.

Balland, Martial, Nicolas Desprat, Delphine Icard, Sophie Féréol, Atef Asnacios, Julien Browaeys, Sylvie Hénon, and François Gallet (2006). "Power laws in microrheology experiments on living cells : Comparative analysis and modeling." In : *Physical review. E, Statistical, nonlinear, and soft matter physics* 74.2 Pt 1, p. 021911. ISSN : 1539-3755. DOI : `10.1103/PhysRevE.74.021911`. arXiv : `0603211 [physics]`. URL : `http://www.ncbi.nlm.nih.gov/pubmed/17025476`.

Bambardekar, Kapil, Raphaël Clément, Olivier Blanc, Claire Chardès, and Pierre-François Lenne (2015). "Direct laser manipulation reveals the mechanics of cell contacts in vivo". In : *Proceedings of the National Academy of Sciences* 112.5, pp. 1416–1421. ISSN : 0027-8424. DOI : `10.1073/pnas.1418732112`. URL : `http://www.pnas.org/lookup/doi/10.1073/pnas.1418732112`.

Beauzamy, Léna, Julien Derr, and Arezki Boudaoud (2015). "Quantifying Hydrostatic Pressure in Plant Cells by Using Indentation with an Atomic Force Microscope". In : *Biophysical Journal* 108.10, pp. 2448–2456. ISSN : 00063495. DOI : `10.1016/j.bpj.2015.03.035`. URL : `http://linkinghub.elsevier.com/retrieve/pii/S0006349515002969`.

Bénazéraf, Bertrand and Olivier Pourquié (2013). "Formation and Segmentation of the Vertebrate Body Axis". In : *Annual Review of Cell and Developmental Biology* 29.1, pp. 1–26. ISSN : 1081-0706. DOI : `10.1146/annurev-cellbio-101011-155703`. URL : `http://www.ncbi.nlm.nih.gov/pubmed/23808844http://www.annualreviews.org/doi/abs/10.1146/annurev-cellbio-101011-155703http://www.annualreviews.org/doi/10.1146/annurev-cellbio-101011-155703`.

Bénazéraf, Bertrand, Paul François, Ruth E Baker, Nicolas Denans, Charles D Little, and Olivier Pourquié (2010). "A random cell motility gradient downstream of

FGF controls elongation of an amniote embryo." In : *Nature* 466.7303, pp. 248–52. ISSN : 1476-4687. DOI : 10.1038/nature09151. URL : http://www.pubmedcentral.nih.gov/articlerender.fcgi?artid=3118990{\&}tool=pmcentrez{\&}rendertype=abstracthttp://www.ncbi.nlm.nih.gov/pubmed/20613841http://www.pubmedcentral.nih.gov/articlerender.fcgi?artid=PMC3118990.

Bénazéraf, Bertrand, Mathias Beaupeux, Martin Tchernookov, Allison Wallingford, Tasha Salisbury, Amelia Shirtz, Andrew Shirtz, David Huss, Olivier Pourquié, Paul François, and Rusty Lansford (2017). "Multiscale quantification of tissue behavior during amniote embryo axis elongation". In : *Development* August, dev.150557. ISSN : 0950-1991. DOI : 10.1242/dev.150557. URL : http://dev.biologists.org/lookup/doi/10.1242/dev.150557.

Benham-Pyle, Blair W., Beth L. Pruitt, and W. James Nelson (2015). "Cell adhesion. Mechanical strain induces E-cadherin-dependent Yap1 and β-catenin activation to drive cell cycle entry." In : *Science (New York, N.Y.)* 348.6238, pp. 1024–7. ISSN : 1095-9203. DOI : 10.1126/science.aaa4559. URL : http://www.ncbi.nlm.nih.gov/pubmed/26023140http://www.pubmedcentral.nih.gov/articlerender.fcgi?artid=PMC4572847.

Bertocchini, Federica and Claudio D. Stern (2002). "The hypoblast of the chick embryo positions the primitive streak by antagonizing nodal signaling." In : *Developmental cell* 3.5, pp. 735–44. ISSN : 1534-5807. DOI : 10.1016/S1534-5807(02)00318-0. URL : http://www.ncbi.nlm.nih.gov/pubmed/12431379.

Bi, Dapeng, Xingbo Yang, M. Cristina Marchetti, and M. Lisa Manning (2016). "Motility-driven glass and jamming transitions in biological tissues." In : *Physical review. X* 6.2, pp. 1–13. ISSN : 2160-3308. DOI : 10.1103/PhysRevX.6.021011. arXiv : 1509.06578. URL : http://www.ncbi.nlm.nih.gov/pubmed/28966874http://www.pubmedcentral.nih.gov/articlerender.fcgi?artid=PMC5619672.

Bonazzi, Daria, Valentina Lo Schiavo, Silke Machata, Ilyas Djafer-Cherif, Pierre Nivoit, Valeria Manriquez, Hirokazu Tanimoto, Julien Husson, Nelly Henry, Hugues Chaté, Raphael Voituriez, and Guillaume Duménil (2018). "Intermittent Pili-Mediated Forces Fluidize Neisseria meningitidis Aggregates Promoting Vascular Colonization." In : *Cell* 174.1, 143–155.e16. ISSN : 1097-4172. DOI : 10.1016/j.cell.2018.04.010. URL : http://www.ncbi.nlm.nih.gov/pubmed/29779947.

Bonn, Daniel, Morton M. Denn, Ludovic Berthier, Thibaut Divoux, and Sébastien Manneville (2017). "Yield stress materials in soft condensed matter". In : *Reviews of Modern Physics* 89.3, p. 035005. ISSN : 0034-6861. DOI : 10.1103/RevModPhys.89.035005. arXiv : 1502.05281. URL : https://link.aps.org/doi/10.1103/RevModPhys.89.035005.

Bonnet, Isabelle, Philippe Marcq, Floris Bosveld, Luc Fetler, Yohanns Bellaïche, and François Graner (2012). "Mechanical state, material properties and continuous description of an epithelial tissue." In : *Journal of the Royal Society, Interface / the Royal Society* 9.75, pp. 2614–23. ISSN : 1742-5662. DOI : 10.1098/rsif.2012.0263. URL : http://www.pubmedcentral.nih.gov/articlerender.fcgi?artid=3427523{\&}tool=pmcentrez{\&}rendertype=abstract.

Brevier, Julien, Marcel Vallade, and Daniel Riveline (2007). "Force-extension relationship of cell-cell contacts." In : *Physical review letters* 98.26, p. 268101. ISSN : 0031-9007. DOI : 10.1103/PhysRevLett.98.268101. URL : http://www.ncbi.nlm.nih.gov/pubmed/17678130.

Brodland, G. Wayne (2002). "The Differential Interfacial Tension Hypothesis (DITH) : a comprehensive theory for the self-rearrangement of embryonic cells and tissues." In : *Journal of biomechanical engineering* 124.2, pp. 188–97. ISSN : 0148-0731. DOI : 10.1115/1.1449491. URL : http://biomechanical.asmedigitalcollection.

asme.org/article.aspx?doi=10.1115/1.1449491http://www.ncbi.nlm.nih.gov/pubmed/12002128.

Brodland, G. Wayne and Helen H Chen (2000). "The mechanics of heterotypic cell aggregates : insights from computer simulations." In : *Journal of biomechanical engineering* 122.4, pp. 402–7. ISSN : 0148-0731. DOI : 10.1115/1.1288205. URL : http://www.ncbi.nlm.nih.gov/pubmed/11036564.

Brodland, G Wayne, Jim H Veldhuis, Steven Kim, Matthew Perrone, David Mashburn, and Shane Hutson (2014). "CellFIT : A Cellular Force-Inference Toolkit Using Curvilinear Cell Boundaries". In : 9.6. DOI : 10.1371/journal.pone.0099116.

Campàs, Otger, Tadanori Mammoto, Sean Hasso, Ralph a Sperling, Daniel O'Connell, Ashley G Bischof, Richard Maas, David a Weitz, L Mahadevan, and Donald E Ingber (2013). "Quantifying cell-generated mechanical forces within living embryonic tissues." In : *Nature methods* December. ISSN : 1548-7105. DOI : 10.1038/nmeth.2761. URL : http://www.ncbi.nlm.nih.gov/pubmed/24317254.

Campinho, Pedro, Martin Behrndt, Jonas Ranft, Thomas Risler, Nicolas Minc, and Carl-Philipp Heisenberg (2013). "Tension-oriented cell divisions limit anisotropic tissue tension in epithelial spreading during zebrafish epiboly." In : *Nature cell biology* 15.12, pp. 1405–14. ISSN : 1476-4679. DOI : 10.1038/ncb2869. arXiv : 1505.01642. URL : http://dx.doi.org/10.1038/ncb2869http://www.ncbi.nlm.nih.gov/pubmed/24212092.

Carpenter, Anne E, Thouis R Jones, Michael R Lamprecht, Colin Clarke, In Han Kang, Ola Friman, David A Guertin, Joo Han Chang, Robert A Lindquist, Jason Moffat, Polina Golland, and David M Sabatini (2006). "CellProfiler : image analysis software for identifying and quantifying cell phenotypes." In : *Genome biology* 7.10, R100. ISSN : 1474-760X. DOI : 10.1186/gb-2006-7-10-r100. arXiv : 1201.3109. URL : http://genomebiology.biomedcentral.com/articles/10.1186/gb-2006-7-10-r100http://arxiv.org/abs/1201.3109http://www.ncbi.nlm.nih.gov/pubmed/17076895http://www.pubmedcentral.nih.gov/articlerender.fcgi?artid=PMC1794559.

Chal, Jérôme, Charlène Guillot, and Olivier Pourquié (2016). "PAPC couples the Segmentation Clock to somite morphogenesis by regulating N-cadherin dependent adhesion". In : *bioRxiv* January. ISSN : 1098-6596. DOI : doi/10.1242/dev.143974. arXiv : arXiv:1011.1669v3.

Chapman, Susan C., Jérôme Collignon, Gary C. Schoenwolf, and Andrew Lumsden (2001). "Improved method for chick whole-embryo culture using a filter paper carrier." In : *Developmental dynamics : an official publication of the American Association of Anatomists* 220.3, pp. 284–9. ISSN : 1058-8388. DOI : 10.1002/1097-0177(20010301)220:3<284::AID-DVDY1102>3.0.CO;2-5. URL : http://doi.wiley.com/10.1002/1097-0177(20010301)220:3{\%}3C284::AID-DVDY1102{\%}3E3.0.CO;2-5http://www.ncbi.nlm.nih.gov/pubmed/11241836.

Charrier, J B, M A Teillet, F Lapointe, and N M Le Douarin (1999). "Defining subregions of Hensen's node essential for caudalward movement, midline development and cell survival." In : *Development (Cambridge, England)* 126.21, pp. 4771–83. ISSN : 0950-1991. URL : http://www.ncbi.nlm.nih.gov/entrez/query.fcgi?cmd=Retrieve{\&}db=PubMed{\&}dopt=Citation{\&}list{_}uids=10518494http://www.ncbi.nlm.nih.gov/pubmed/10518494.

Chevalier, Nicolas R, Elodie Gazguez, Sylvie Dufour, and Vincent Fleury (2016). "Measuring the micromechanical properties of embryonic tissues". In : *Methods* 94, pp. 120–128. ISSN : 10462023. DOI : 10.1016/j.ymeth.2015.08.001. URL : http://dx.doi.org/10.1016/j.ymeth.2015.08.001http://linkinghub.elsevier.com/retrieve/pii/S1046202315300396.

Chuai, Manli and Cornelis J. Weijer (2008). "The Mechanisms Underlying Primitive Streak Formation in the Chick Embryo". In : *Current Topics in Developmental Biology* 81.07, pp. 135–156. ISSN : 00702153. DOI : 10.1016/S0070-2153(07)81004-0.

Chuai, Manli, Wei Zeng, Xuesong Yang, Veronika Boychenko, James A. Glazier, and Cornelis J. Weijer (2006). "Cell movement during chick primitive streak formation". In : *Developmental Biology* 296.1, pp. 137–149. ISSN : 00121606. DOI : 10.1016/j.ydbio.2006.04.451. arXiv : NIHMS150003. URL : http://linkinghub.elsevier.com/retrieve/pii/S0012160606007299.

Cui, Cheng, Xuesong Yang, Manli Chuai, James a. Glazier, and Cornelis J. Weijer (2005). "Analysis of tissue flow patterns during primitive streak formation in the chick embryo". In : *Developmental Biology* 284, pp. 37–47. ISSN : 00121606. DOI : 10.1016/j.ydbio.2005.04.021.

Dagan, Zeev, Sheldon Weinbaum, and Robert Pfeffer (1982). "An infinite-series solution for the creeping motion through an orifice of finite length". In : *Journal of Fluid Mechanics* 115.-1, p. 505. ISSN : 0022-1120. DOI : 10.1017/S0022112082000883.

Dassow, Michelangelo von, James a. Strother, and Lance a. Davidson (2010). "Surprisingly simple mechanical behavior of a complex embryonic tissue". In : *PLoS ONE* 5.12. ISSN : 19326203. DOI : 10.1371/journal.pone.0015359. arXiv : 78650833739.

Davidson, Bruce P., Simon J. Kinder, Kirsten Steiner, Gary C. Schoenwolf, and Patrick P.L. Tam (1999). "Impact of node ablation on the morphogenesis of the body axis and the lateral asymmetry of the mouse embryo during early organogenesis." In : *Developmental biology* 211.1, pp. 11–26. ISSN : 0012-1606. DOI : 10.1006/dbio.1999.9276. URL : http://www.ncbi.nlm.nih.gov/pubmed/10373301.

Davidson, Lance and Ray Keller (2007). "Measuring Mechanical Properties of Embryos and Embryonic Tissues". In : *Methods in Cell Biology*. Vol. 83. 07, pp. 425–439. ISBN : 0123705002. DOI : 10.1016/S0091-679X(07)83018-4. URL : http://linkinghub.elsevier.com/retrieve/pii/S0091679X07830184.

Delanoë-Ayari, H., J. P. Rieu, and M. Sano (2010). "4D Traction Force Microscopy Reveals Asymmetric Cortical Forces in Migrating Dictyostelium Cells". In : *Physical Review Letters* 105.24, p. 248103. ISSN : 0031-9007. DOI : 10.1103/PhysRevLett.105.248103. URL : http://link.aps.org/doi/10.1103/PhysRevLett.105.248103.

Delfini, Marie-Claire, Julien Dubrulle, Pascale Malapert, Jérôme Chal, and Olivier Pourquié (2005). "Control of the segmentation process by graded MAPK/ERK activation in the chick embryo." In : *Proceedings of the National Academy of Sciences of the United States of America* 102.32, pp. 11343–8. ISSN : 0027-8424. DOI : 10.1073/pnas.0502933102. URL : http://www.pnas.org/content/102/32/11343.shorthttp://www.ncbi.nlm.nih.gov/pubmed/16055560http://www.pubmedcentral.nih.gov/articlerender.fcgi?artid=PMC1183560.

Denans, Nicolas, Tadahiro Iimura, and Olivier Pourquié (2015). "Hox genes control vertebrate body elongation by collinear Wnt repression". In : *eLife* 4.4, pp. 1–33. ISSN : 2050-084X. DOI : 10.7554/eLife.04379. arXiv : arXiv:1011.1669v3. URL : http://elifesciences.org/lookup/doi/10.7554/eLife.04379.

Dias, Mark S. and Gary C. Schoenwolf (1990). "Formation of ectopic neurepithelium in chick blastoderms : Age-related capacities for induction and self-differentiation following transplantation of quail Hensen's nodes". In : *The Anatomical Record* 228.4, pp. 437–448. ISSN : 0003-276X. DOI : 10.1002/ar.1092280410. URL : http://doi.wiley.com/10.1002/ar.1092280410.

Douezan, Stéphane and Françoise Brochard-Wyart (2012). "Active diffusion-limited aggregation of cells". In : *Soft Matter* 8.3, p. 784. ISSN : 1744-683X. DOI : `10.1039/c1sm06399e`.

Dray, Nicolas, Andrew Lawton, Amitabha Nandi, Dörthe Jülich, Thierry Emonet, and Scott A. Holley (2013). "Cell-Fibronectin Interactions Propel Vertebrate Trunk Elongation via Tissue Mechanics". In : *Current Biology* 23.14, pp. 1335–1341. ISSN : 09609822. DOI : `10.1016/j.cub.2013.05.052`. URL : `http://linkinghub.elsevier.com/retrieve/pii/S0960982213006775`.

Duboule, D (1994). "Temporal colinearity and the phylotypic progression : a basis for the stability of a vertebrate Bauplan and the evolution of morphologies through heterochrony." In : *Development (Cambridge, England). Supplement* 42, pp. 135–42. ISSN : 09501991. DOI : `10.1007/SpringerReference_34725`. URL : `http://www.ncbi.nlm.nih.gov/pubmed/7579514`.

Ellis, Kathryn, Jennifer Bagwell, and Michel Bagnat (2013). "Notochord vacuoles are lysosome-related organelles that function in axis and spine morphogenesis." In : *The Journal of cell biology* 200.5, pp. 667–79. ISSN : 1540-8140. DOI : `10.1083/jcb.201212095`. URL : `http://www.ncbi.nlm.nih.gov/pubmed/23460678http://www.pubmedcentral.nih.gov/articlerender.fcgi?artid=PMC3587825`.

Eshelby, J. D. (1949). "Seminar on the Kinetics of Sintering (with discussions)". In : *Metals Trans.* 185.

Evans, E and A Yeung (1989). "Apparent viscosity and cortical tension of blood granulocytes determined by micropipet aspiration." In : *Biophysical journal* 56.1, pp. 151–60. ISSN : 0006-3495. DOI : `10.1016/S0006-3495(89)82660-8`. URL : `http://dx.doi.org/10.1016/S0006-3495(89)82660-8http://www.ncbi.nlm.nih.gov/pubmed/2752085http://www.pubmedcentral.nih.gov/articlerender.fcgi?artid=PMC1280460`.

Evans, E. A. (1973). "New membrane concept applied to the analysis of fluid shear- and micropipette-deformed red blood cells." In : *Biophysical journal* 13.9, pp. 941–54. ISSN : 0006-3495. DOI : `10.1016/S0006-3495(73)86036-9`. arXiv : `10/{\$}26.00 [978-1-4244-7903-0]`. URL : `http://www.scopus.com/inward/record.url?eid=2-s2.0-0015894192{\&}partnerID=tZOtx3y1http://www.ncbi.nlm.nih.gov/pubmed/4733701http://www.pubmedcentral.nih.gov/articlerender.fcgi?artid=PMC1484376`.

Eyal-Giladi, Hefzibah and Shimshon Kochav (1976). "From cleavage to primitive streak formation : a complementary normal table and a new look at the first stages of the development of the chick. I. General morphology." In : *Developmental biology* 49.2, pp. 321–37. ISSN : 0012-1606. DOI : `10.1016/0012-1606(80)90117-7`. URL : `http://www.ncbi.nlm.nih.gov/pubmed/944662`.

Fabry, Ben, Geoffrey N Maksym, James P Butler, Michael Glogauer, Daniel Navajas, and Jeffrey J Fredberg (2001). "Scaling the Microrheology of Living Cells". In : *Physical Review Letters* 87.14, p. 148102. ISSN : 0031-9007. DOI : `10.1103/PhysRevLett.87.148102`. URL : `https://link.aps.org/doi/10.1103/PhysRevLett.87.148102`.

Firmino, Joao, Didier Rocancourt, Mehdi Saadaoui, Chloé Moreau, and Jérôme Gros (2016). "Cell Division Drives Epithelial Cell Rearrangements during Gastrulation in Chick". In : *Developmental Cell* 36.3, pp. 249–261. ISSN : 18781551. DOI : `10.1016/j.devcel.2016.01.007`. URL : `http://dx.doi.org/10.1016/j.devcel.2016.01.007`.

Forgacs, G, R A Foty, Y Shafrir, and M S Steinberg (1998). "Viscoelastic properties of living embryonic tissues : a quantitative study." In : *Biophysical journal* 74.5,

pp. 2227–34. ISSN : 0006-3495. DOI : 10.1016/S0006-3495(98)77932-9. URL : http://www.sciencedirect.com/science/article/pii/S0006349598779329.

Foty, Ramsey A., Gabor Forgacs, Cathie M. Pfleger, and Malcolm S. Steinberg (1994). "Liquid properties of embryonic tissues : Measurement of interfacial tensions". In : *Physical Review Letters* 72.14, pp. 2298–2301. ISSN : 0031-9007. DOI : 10.1103/PhysRevLett.72.2298. URL : https://link.aps.org/doi/10.1103/PhysRevLett.72.2298.

Frenkel, Ja (1945). "Viscous flow of crystalline bodies under the action of surface tension". In : *J. Phys.(USS R)* 9.5, p. 385.

Gardner, David K (2015). "Lactate production by the mammalian blastocyst : manipulating the microenvironment for uterine implantation and invasion ?" In : *Bioessays* 37.4, pp. 364–371.

Godin, Michel, Francisco Feijó Delgado, Sungmin Son, William H Grover, Andrea K Bryan, Amit Tzur, Paul Jorgensen, Kris Payer, Alan D Grossman, Marc W Kirschner, and Scott R Manalis (2010). "Using buoyant mass to measure the growth of single cells". In : *Nature Methods* 7.5, pp. 387–390. ISSN : 1548-7091. DOI : 10.1038/nmeth.1452. URL : http://www.nature.com/doifinder/10.1038/nmeth.1452.

Gomez, Céline and Olivier Pourquié (2009). "Developmental control of segment numbers in vertebrates." In : *Journal of experimental zoology. Part B, Molecular and developmental evolution* 312.6, pp. 533–44. ISSN : 1552-5015. DOI : 10.1002/jez.b.21305. URL : http://www.ncbi.nlm.nih.gov/pubmed/19621429http://www.pubmedcentral.nih.gov/articlerender.fcgi?artid=PMC3094763.

Gomez, Céline, Ertuğrul M. Özbudak, Joshua Wunderlich, Diana Baumann, Julian Lewis, and Olivier Pourquié (2008). "Control of segment number in vertebrate embryos". In : *Nature* 454.7202, pp. 335–339. ISSN : 00280836. DOI : 10.1038/nature07020.

Gont, L K, H Steinbeisser, B Blumberg, and E M de Robertis (1993). "Tail formation as a continuation of gastrulation : the multiple cell populations of the Xenopus tailbud derive from the late blastopore lip." In : *Development (Cambridge, England)* 119.4, pp. 991–1004. ISSN : 0950-1991. URL : http://www.ncbi.nlm.nih.gov/pubmed/7916680.

Gordon, Richard, Narendra S. Goel, Malcolm S. Steinberg, and Lawrence L. Wiseman (1972). "A rheological mechanism sufficient to explain the kinetics of cell sorting." In : *Journal of theoretical biology* 37.1, pp. 43–73. ISSN : 0022-5193. DOI : 10.1016/0022-5193(72)90114-2. URL : http://www.ncbi.nlm.nih.gov/pubmed/4652421.

Graner, François and James A. Glazier (1992). "Simulation of biological cell sorting using a two-dimensional extended Potts model". In : *Physical Review Letters* 69.13, pp. 2013–2016. ISSN : 0031-9007. DOI : 10.1103/PhysRevLett.69.2013. arXiv : 0000135489. URL : https://link.aps.org/doi/10.1103/PhysRevLett.69.2013.

Gräper, Ludwig (1929). "Die Primitiventwicklung des Hühnchens nach stereokinematographischen Untersuchungen, kontrolliert durch vitale Farbmarkierung und verglichen mit der Entwicklung anderer Wirbeltiere". In : *Wilhelm Roux' Archiv für Entwicklungsmechanik der Organismen* 116.1, pp. 382–429. ISSN : 0949-944X. DOI : 10.1007/BF02145235. URL : http://link.springer.com/10.1007/BF02145235.

Grashoff, Carsten, Brenton D. Hoffman, Michael D. Brenner, Ruobo Zhou, Maddy Parsons, Michael T. Yang, Mark A. McLean, Stephen G. Sligar, Christopher S.

Chen, Taekjip Ha, and Martin A. Schwartz (2010). "Measuring mechanical tension across vinculin reveals regulation of focal adhesion dynamics." In : *Nature* 466.7303, pp. 263–6. ISSN : 1476-4687. DOI : 10.1038/nature09198. arXiv : NIHMS150003. URL : http://dx.doi.org/10.1038/nature09198http://www.ncbi.nlm.nih.gov/pubmed/20613844http://www.pubmedcentral.nih.gov/articlerender.fcgi?artid=PMC2901888.

Guevorkian, Karine, Marie-Josée Colbert, Mélanie Durth, Sylvie Dufour, and Françoise Brochard-Wyart (2010). "Aspiration of Biological Viscoelastic Drops". In : *Physical Review Letters* 104.21, p. 218101. ISSN : 0031-9007. DOI : 10.1103/PhysRevLett.104.218101. URL : http://link.aps.org/doi/10.1103/PhysRevLett.104.218101.

Guevorkian, Karine, David Gonzalez-Rodriguez, Camille Carlier, Sylvie Dufour, and Françoise Brochard-Wyart (2011). "Mechanosensitive shivering of model tissues under controlled aspiration." In : *Proceedings of the National Academy of Sciences of the United States of America* 108.33, pp. 13387–92. ISSN : 1091-6490. DOI : 10.1073/pnas.1105741108. URL : http://www.pubmedcentral.nih.gov/articlerender.fcgi?artid=3158194{\&}tool=pmcentrez{\&}rendertype=abstract.

Guo, Ming, Allen J. Ehrlicher, Mikkel H. Jensen, Malte Renz, Jeffrey R. Moore, Robert D. Goldman, Jennifer Lippincott-Schwartz, Frederick C. Mackintosh, and David A. Weitz (2014). "Probing the stochastic, motor-driven properties of the cytoplasm using force spectrum microscopy." In : *Cell* 158.4, pp. 822–832. ISSN : 1097-4172. DOI : 10.1016/j.cell.2014.06.051. arXiv : NIHMS150003. URL : http://dx.doi.org/10.1016/j.cell.2014.06.051http://www.ncbi.nlm.nih.gov/pubmed/25126787http://www.pubmedcentral.nih.gov/articlerender.fcgi?artid=PMC4183065.

Gupta, Mukund, Leyla Kocgozlu, Bibhu Ranjan Sarangi, Felix Margadant, Mohammed Ashraf, and Benoit Ladoux (2015). *Micropillar substrates : a tool for studying cell mechanobiology.* Vol. 125. Elsevier Ltd, pp. 289–308. ISBN : 9780128011034. DOI : 10.1016/bs.mcb.2014.10.009. URL : http://www.sciencedirect.com/science/article/pii/S0091679X14000107.

Hamburger, Viktor and Howard L. Hamilton (1951). "A series of normal stages in the development of the chick embryo". In : *Journal of Morphology* 88.1, pp. 49–92. ISSN : 0362-2525. DOI : 10.1002/jmor.1050880104. URL : http://doi.wiley.com/10.1002/jmor.1050880104.

Harris, Albert K. (1976). "Is Cell sorting caused by differences in the work of intercellular adhesion ? A critique of the Steinberg hypothesis." In : *Journal of theoretical biology* 61.2, pp. 267–85. ISSN : 0022-5193. DOI : 10.1016/0022-5193(76)90019-9. URL : http://www.ncbi.nlm.nih.gov/pubmed/985668.

Harris, Andrew R, Loic Peter, Julien Bellis, Buzz Baum, Alexandre J Kabla, and Guillaume T Charras (2012). "Characterizing the mechanics of cultured cell monolayers." In : *Proceedings of the National Academy of Sciences of the United States of America* 109.41, pp. 16449–54. ISSN : 1091-6490. DOI : 10.1073/pnas.1213301109. URL : http://www.pubmedcentral.nih.gov/articlerender.fcgi?artid=3478631{\&}tool=pmcentrez{\&}rendertype=abstract.

Hatada, Y and C D Stern (1994). "A fate map of the epiblast of the early chick embryo." In : *Development (Cambridge, England)* 120.10, pp. 2879–89. ISSN : 0950-1991. DOI : 7607078. URL : http://www.ncbi.nlm.nih.gov/pubmed/7607078.

Hayashi, Takashi and Richard W Carthew (2004). "Surface mechanics mediate pattern formation in the developing retina." In : *Nature* 431.7009, pp. 647–52. ISSN : 1476-4687. DOI : 10.1038/nature02952. URL : http://www.ncbi.nlm.nih.gov/pubmed/15470418.

Hochmuth, Robert M. (2000). "Micropipette aspiration of living cells". In : *Journal of Biomechanics* 33, pp. 15–22. ISSN : 00219290. DOI : 10.1016/S0021-9290(99)00175-X.

Iimura, Tadahiro and Olivier Pourquié (2006). "Collinear activation of Hoxb genes during gastrulation is linked to mesoderm cell ingression." In : *Nature* 442.7102, pp. 568–71. ISSN : 1476-4687. DOI : 10.1038/nature04838. URL : http://www.ncbi.nlm.nih.gov/pubmed/16760928.

Ishihara, S, K Sugimura, S J Cox, I Bonnet, Y Bellaïche, and F Graner (2013). "Comparative study of non-invasive force and stress inference methods in tissue." In : *The European physical journal. E, Soft matter* 36.4, p. 9859. ISSN : 1292-895X. DOI : 10.1140/epje/i2013-13045-8. URL : http://www.ncbi.nlm.nih.gov/pubmed/23615875.

Ishihara, Shuji and Kaoru Sugimura (2012). "Bayesian inference of force dynamics during morphogenesis." In : *Journal of theoretical biology* 313, pp. 201–11. ISSN : 1095-8541. DOI : 10.1016/j.jtbi.2012.08.017. URL : http://www.ncbi.nlm.nih.gov/pubmed/22939902.

Jones, Eric, Travis Oliphant, Pearu Peterson, et al. (2001). "SciPy : Open source scientific tools for Python". In : [Online ; accessed <today>]. URL : http://www.scipy.org/.

Jones, Wendy R., H P Ting-Beall, Greta M. Lee, Scott S. Kelley, Robert M. Hochmuth, and Farshid Guilak (1999). "Alterations in the Young's modulus and volumetric properties of chondrocytes isolated from normal and osteoarthritic human cartilage." In : *Journal of biomechanics* 32.2, pp. 119–27. ISSN : 0021-9290. DOI : 10.1016/S0021-9290(98)00166-3. URL : http://www.ncbi.nlm.nih.gov/pubmed/10052916.

Jouve, Caroline, Tadahiro Iimura, and Olivier Pourquié (2002). "Onset of the segmentation clock in the chick embryo : evidence for oscillations in the somite precursors in the primitive streak." In : *Development (Cambridge, England)* 129.5, pp. 1107–17. ISSN : 0950-1991. URL : http://www.ncbi.nlm.nih.gov/pubmed/11874907.

Käfer, Jos, Takashi Hayashi, Athanasius F M Marée, Richard W Carthew, and François Graner (2007). "Cell adhesion and cortex contractility determine cell patterning in the Drosophila retina." In : *Proceedings of the National Academy of Sciences of the United States of America* 104.47, pp. 18549–54. ISSN : 1091-6490. DOI : 10.1073/pnas.0704235104. URL : http://www.pubmedcentral.nih.gov/articlerender.fcgi?artid=2141814{\&}tool=pmcentrez{\&}rendertype=abstract.

Keller, R and M Danilchik (1988). "Regional expression, pattern and timing of convergence and extension during gastrulation of Xenopus laevis." In : *Development (Cambridge, England)* 103.1, pp. 193–209. ISSN : 0950-1991. URL : http://eutils.ncbi.nlm.nih.gov/entrez/eutils/elink.fcgi?dbfrom=pubmed{\&}id=3197629{\&}retmode=ref{\&}cmd=prlinks{\%}5Cnpapers2://publication/uuid/2A59ACFF-C630-4021-9D66-997D8DF3A2FBhttp://www.ncbi.nlm.nih.gov/pubmed/3197629.

Keller, R., Lance A. Davidson, A. Edlund, T. Elul, M. Ezin, D. Shook, and P. Skoglund (2000). "Mechanisms of convergence and extension by cell intercalation". In : *Philosophical Transactions of the Royal Society B : Biological Sciences* 355.1399, pp. 897–922. ISSN : 0962-8436. DOI : 10.1098/rstb.2000.0626. URL : http://rstb.royalsocietypublishing.org/cgi/doi/10.1098/rstb.2000.0626.

Keller, Ray (2006). "Mechanisms of elongation in embryogenesis." In : *Development (Cambridge, England)* 133.12, pp. 2291–302. ISSN : 0950-1991. DOI : 10.1242/dev.

02406. URL : http://dev.biologists.org/cgi/doi/10.1242/dev.02406http://www.ncbi.nlm.nih.gov/pubmed/16720874.

Koser, David E, Emad Moeendarbary, Janina Hanne, Stefanie Kuerten, and Kristian Franze (2015). "CNS cell distribution and axon orientation determine local spinal cord mechanical properties." In : *Biophysical journal* 108.9, pp. 2137–47. ISSN : 1542-0086. DOI : 10.1016/j.bpj.2015.03.039. URL : http://www.sciencedirect.com/science/article/pii/S0006349515003008.

Krens, S F Gabriel, Jim H Veldhuis, Vanessa Barone, Daniel Čapek, Jean-Léon Maître, G Wayne Brodland, and Carl-Philipp Heisenberg (2017). "Interstitial fluid osmolarity modulates the action of differential tissue surface tension in progenitor cell segregation during gastrulation." In : *Development (Cambridge, England)* 144.10, pp. 1798–1806. ISSN : 1477-9129. DOI : 10.1242/dev.144964. URL : http://rsbl.royalsocietypublishing.org/cgi/doi/10.1098/rsbl.2009.0501http://www.ncbi.nlm.nih.gov/pubmed/22344054http://www.ncbi.nlm.nih.gov/pubmed/28512197http://www.pubmedcentral.nih.gov/articlerender.fcgi?artid=PMC5450835.

Krieg, M, Y Arboleda-Estudillo, P-H Puech, J Käfer, F Graner, D J Müller, and C-P Heisenberg (2008). "Tensile forces govern germ-layer organization in zebrafish." In : *Nature cell biology* 10.4, pp. 429–36. ISSN : 1465-7392. DOI : 10.1038/ncb1705. arXiv : 43149088966. URL : http://www.ncbi.nlm.nih.gov/pubmed/18364700http://www.nature.com/doifinder/10.1038/ncb1705.

Lawson, Aaron and Gary C Schoenwolf (2003). "Epiblast and primitive-streak origins of the endoderm in the gastrulating chick embryo." In : *Development (Cambridge, England)* 130.15, pp. 3491–501. ISSN : 0950-1991. DOI : 10.1242/dev.00579. URL : http://www.ncbi.nlm.nih.gov/entrez/query.fcgi?cmd=Retrieve{\&}db=PubMed{\&}dopt=Citation{\&}list{_}uids=12810596http://www.ncbi.nlm.nih.gov/pubmed/12810596.

Lawton, Andrew K, Amitabha Nandi, Michael J Stulberg, Nicolas Dray, Michael W Sneddon, William Pontius, Thierry Emonet, and Scott a Holley (2013). "Regulated tissue fluidity steers zebrafish body elongation." In : *Development (Cambridge, England)* 140.3, pp. 573–82. ISSN : 1477-9129. DOI : 10.1242/dev.090381. URL : http://www.pubmedcentral.nih.gov/articlerender.fcgi?artid=3561786{\&}tool=pmcentrez{\&}rendertype=abstract.

Lutz, Hubert (1950). "Influence of the level of the section and the stage of incubation of the orientation of double embryos obtained experimentally in the duck". In : *Comptes rendus des séances de la Société de biologie et de ses filiales* 144.19-20, p. 1410.

Ma, Xiaoyan, Holley E Lynch, Peter C Scully, and M Shane Hutson (2009). "Probing embryonic tissue mechanics with laser hole drilling." In : *Physical biology* 6.3, p. 036004. ISSN : 1478-3975. DOI : 10.1088/1478-3975/6/3/036004. URL : http://www.ncbi.nlm.nih.gov/pubmed/19411738.

Maître, Jean-Léon, Ritsuya Niwayama, Hervé Turlier, François Nédélec, and Takashi Hiiragi (2015). "Pulsatile cell-autonomous contractility drives compaction in the mouse embryo." In : *Nature cell biology* 17.7, pp. 849–55. ISSN : 1476-4679. DOI : 10.1038/ncb3185. arXiv : 34547814216. URL : http://www.ncbi.nlm.nih.gov/pubmed/26075357.

Majkut, Stephanie, Timon Idema, Joe Swift, Christine Krieger, Andrea Liu, and Dennis E. Discher (2013). "Heart-Specific Stiffening in Early Embryos Parallels Matrix and Myosin Expression to Optimize Beating". In : *Current Biology* 23.23, pp. 2434–2439. ISSN : 09609822. DOI : 10.1016/j.cub.2013.10.057. URL : http://dx.doi.org/10.1016/j.cub.2013.10.057http://linkinghub.elsevier.com/retrieve/pii/S0960982213013328.

Marchetti, M. C., J. F. Joanny, S. Ramaswamy, T. B. Liverpool, J. Prost, Madan Rao, and R. Aditi Simha (2013). "Hydrodynamics of soft active matter". In : *Reviews of Modern Physics* 85.3, pp. 1143–1189. ISSN : 00346861. DOI : 10.1103/RevModPhys.85.1143. arXiv : 1207.2929.

Marmottant, Philippe, Abbas Mgharbel, Jos Käfer, Benjamin Audren, Jean-Paul Rieu, Jean-Claude Vial, Boudewijn van der Sanden, Athanasius F M Marée, François Graner, and Hélène Delanoë-Ayari (2009). "The role of fluctuations and stress on the effective viscosity of cell aggregates." In : *Proceedings of the National Academy of Sciences of the United States of America* 106.41, pp. 17271–5. ISSN : 1091-6490. DOI : 10.1073/pnas.0902085106. URL : http://www.pubmedcentral.nih.gov/articlerender.fcgi?artid=2765233{\&}tool=pmcentrez{\&}rendertype=abstract.

Martins, Gabriel G., Pedro Rifes, Rita Amaândio, Gabriela Rodrigues, Isabel Palmeirim, and Sólveig Thorsteinsdóttir (2009). "Dynamic 3D cell rearrangements guided by a fibronectin matrix underlie somitogenesis". In : *PLoS ONE* 4.10. ISSN : 19326203. DOI : 10.1371/journal.pone.0007429.

Mayer, Mirjam, Martin Depken, Justin S. Bois, Frank Jülicher, and Stephan W. Grill (2010). "Anisotropies in cortical tension reveal the physical basis of polarizing cortical flows." In : *Nature* 467.7315, pp. 617–21. ISSN : 1476-4687. DOI : 10.1038/nature09376. arXiv : 77957364208. URL : http://www.ncbi.nlm.nih.gov/pubmed/20852613.

Mohagheghian, Erfan, Junyu Luo, Junjian Chen, Gaurav Chaudhary, Junwei Chen, Jian Sun, Randy H. Ewoldt, and Ning Wang (2018). "Quantifying compressive forces between living cell layers and within tissues using elastic round microgels". In : *Nature Communications* 9.1, p. 1878. ISSN : 2041-1723. DOI : 10.1038/s41467-018-04245-1. URL : http://dx.doi.org/10.1038/s41467-018-04245-1http://www.nature.com/articles/s41467-018-04245-1.

Mombach, José C.M., Damien Robert, François Graner, Germain Gillet, Gilberto L. Thomas, Marco Idiart, and Jean-Paul Rieu (2005). "Rounding of aggregates of biological cells : Experiments and simulations". In : *Physica A : Statistical Mechanics and its Applications* 352.2-4, pp. 525–534. ISSN : 03784371. DOI : 10.1016/j.physa.2005.02.008. URL : http://linkinghub.elsevier.com/retrieve/pii/S0378437105001433.

Moore, S W, R E Keller, and M a Koehl (1995). "The dorsal involuting marginal zone stiffens anisotropically during its convergent extension in the gastrula of Xenopus laevis." In : *Development (Cambridge, England)* 121.10, pp. 3131–40. ISSN : 0950-1991. URL : http://www.ncbi.nlm.nih.gov/pubmed/7588048.

Needham, D and R M Hochmuth (1990). "Rapid flow of passive neutrophils into a 4 microns pipet and measurement of cytoplasmic viscosity." In : *Journal of biomechanical engineering* 112.3, pp. 269–76. ISSN : 0148-0731. DOI : 10.1115/1.2891184. URL : http://www.ncbi.nlm.nih.gov/pubmed/2214708.

Nerurkar, Nandan L., L. Mahadevan, and Clifford J. Tabin (2017). "BMP signaling controls buckling forces to modulate looping morphogenesis of the gut". In : *Proceedings of the National Academy of Sciences* 114.9, pp. 2277–2282. ISSN : 0027-8424. DOI : 10.1073/pnas.1700307114. URL : http://www.pnas.org/lookup/doi/10.1073/pnas.1700307114.

Newville, Matthew, Till Stensitzki, Daniel B. Allen, and Antonino Ingargiola (2014). "LMFIT : Non-Linear Least-Square Minimization and Curve-Fitting for Python". In : DOI : 10.5281/ZENODO.11813. URL : https://zenodo.org/record/11813.

Nishimura, Tamako, Hisao Honda, and Masatoshi Takeichi (2012). "Planar cell polarity links axes of spatial dynamics in neural-tube closure". In : *Cell* 149.5, pp. 1084–

1097. ISSN : 00928674. DOI : 10.1016/j.cell.2012.04.021. URL : http://dx.doi.org/10.1016/j.cell.2012.04.021.

Noordermeer, Daan and Denis Duboule (2013). "Chromatin architectures and Hox gene collinearity". In : *Current topics in developmental biology*. Vol. 104. Elsevier, pp. 113–148.

Oginuma, Masayuki, Philippe Moncuquet, Fengzhu Xiong, Edward Karoly, Jérôme Chal, Karine Guevorkian, and Olivier Pourquié (2017). "A Gradient of Glycolytic Activity Coordinates FGF and Wnt Signaling during Elongation of the Body Axis in Amniote Embryos." In : *Developmental cell* 40.4, 342–353.e10. ISSN : 1878-1551. DOI : 10.1016/j.devcel.2017.02.001. URL : http://www.ncbi.nlm.nih.gov/pubmed/28245921http://www.pubmedcentral.nih.gov/articlerender.fcgi?artid=PMC5403012.

O'Rahilly, R. and F. Müller (2003). "Somites, spinal Ganglia, and centra. Enumeration and interrelationships in staged human embryos, and implications for neural tube defects." In : *Cells, tissues, organs* 173.2, pp. 75–92. ISSN : 1422-6405. DOI : 10.1159/000068948. URL : http://www.ncbi.nlm.nih.gov/pubmed/12649586.

Palmeirim, Isabel, Domingos Henrique, David Ish-Horowicz, and Olivier Pourquié (1997). "Avian hairy Gene Expression Identifies a Molecular Clock Linked to Vertebrate Segmentation and Somitogenesis". In : *Cell* 91.5, pp. 639–648. ISSN : 00928674. DOI : 10.1016/S0092-8674(00)80451-1. URL : http://linkinghub.elsevier.com/retrieve/pii/S0092867400804511.

Palmeirim, Isabel, Julien Dubrulle, Domingos Henrique, D Ish-Horowicz, and O Pourquié (1998). "Uncoupling segmentation and somitogenesis in the chick presomitic mesoderm." In : *Developmental genetics* 23.1, pp. 77–85. ISSN : 0192-253X. DOI : 10.1002/(SICI)1520-6408(1998)23:1<77::AID-DVG8>3.0.CO;2-3. URL : http://onlinelibrary.wiley.com/doi/10.1002/(SICI)1520-6408(1998)23:1{\%}3C77::AID-DVG8{\%}3E3.0.CO;2-3/epdfhttp://www.ncbi.nlm.nih.gov/pubmed/9706696.

Phillips, H M and M S Steinberg (1969). "Equilibrium measurements of embryonic chick cell adhesiveness. I. Shape equilibrium in centrifugal fields." In : *Proceedings of the National Academy of Sciences of the United States of America* 64.1, pp. 121–7. ISSN : 0027-8424. URL : http://www.ncbi.nlm.nih.gov/pubmed/5262993http://www.pubmedcentral.nih.gov/articlerender.fcgi?artid=PMC286135.

Piroird, Keyvan, Christophe Clanet, and David Quéré (2011). "Capillary extraction." In : *Langmuir : the ACS journal of surfaces and colloids* 27.15, pp. 9396–402. ISSN : 1520-5827. DOI : 10.1021/la201490m. URL : http://pubs.acs.org/doi/abs/10.1021/la201490mhttp://www.ncbi.nlm.nih.gov/pubmed/21662237.

Plateau, Joseph Antoine Ferdinand (1873). *Statique expérimentale et théorique des liquides soumis aux seules forces moléculaires*. Vol. 2. Gauthier-Villars.

Pokhrel, N., E. Ben-Tal Cohen, O. Genin, D. Sela-Donenfeld, and Y. Cinnamon (2017). "Cellular and morphological characterization of blastoderms from freshly laid broiler eggs". In : *Poultry Science* 96.12, pp. 4399–4408. ISSN : 0032-5791. DOI : 10.3382/ps/pex242. URL : http://academic.oup.com/ps/article/96/12/4399/4349805.

Psychoyos, D and C D Stern (1996). "Fates and migratory routes of primitive streak cells in the chick embryo." In : *Development (Cambridge, England)* 122.5, pp. 1523–34. ISSN : 0950-1991. URL : http://www.ncbi.nlm.nih.gov/pubmed/8625839.

Raff, Rudolf A (1996). *The shape of life : genes, development, and the evolution of animal form*. University of Chicago Press.

Rauzi, Matteo, Pascale Verant, Thomas Lecuit, and Pierre-François Lenne (2008). "Nature and anisotropy of cortical forces orienting Drosophila tissue morphogenesis." In : *Nature cell biology* 10.12, pp. 1401–10. ISSN : 1476-4679. DOI : 10.1038/ncb1798. URL : http://www.ncbi.nlm.nih.gov/pubmed/18978783.

Regev, Ido, Karine Guevorkian, Olivier Pourquié, and L Mahadevan (2017). "Motility-gradient induced elongation of the vertebrate embryo". In : *bioRxiv*, pp. 1–11. DOI : http://dx.doi.org/10.1101/187443.

Rifes, P, L Carvalho, C Lopes, R P Andrade, G Rodrigues, I Palmeirim, and S Thorsteinsdottir (2007). "Redefining the role of ectoderm in somitogenesis : a player in the formation of the fibronectin matrix of presomitic mesoderm". In : *Development* 134.17, pp. 3155–3165. ISSN : 0950-1991. DOI : dev.003665[pii]10.1242/dev.003665. URL : http://www.ncbi.nlm.nih.gov/entrez/query.fcgi?cmd=Retrieve{\&}db=PubMed{\&}dopt=Citation{\&}list{_}uids=17670788{\%}5Cnhttp://dev.biologists.org/content/134/17/3155.full.pdf.

Rifes, Pedro and Sólveig Thorsteinsdóttir (2012). "Extracellular matrix assembly and 3D organization during paraxial mesoderm development in the chick embryo." In : *Developmental biology* 368.2, pp. 370–81. ISSN : 1095-564X. DOI : 10.1016/j.ydbio.2012.06.003. URL : http://www.ncbi.nlm.nih.gov/pubmed/22705477.

Rosenbluth, Michael J., Wilbur A. Lam, and Daniel A. Fletcher (2006). "Force microscopy of nonadherent cells : a comparison of leukemia cell deformability." In : *Biophysical journal* 90.8, pp. 2994–3003. ISSN : 0006-3495. DOI : 10.1529/biophysj.105.067496. URL : http://www.ncbi.nlm.nih.gov/pubmed/16443660http://www.pubmedcentral.nih.gov/articlerender.fcgi?artid=PMC1414579.

Rozbicki, Emil, Manli Chuai, Antti I Karjalainen, Feifei Song, Helen M Sang, René Martin, Hans-Joachim Knölker, Michael P MacDonald, and Cornelis J Weijer (2015). "Myosin-II-mediated cell shape changes and cell intercalation contribute to primitive streak formation". In : *Nature Cell Biology* 17.4, pp. 397–408. ISSN : 1465-7392. DOI : 10.1038/ncb3138. URL : http://www.nature.com/doifinder/10.1038/ncb3138.

Rudnick, Leslie R (2005). *Synthetics, mineral oils, and bio-based lubricants : chemistry and technology*. CRC press.

Sanders, E. J. and E. Parker (2001). "Ablation of axial structures activates apoptotic pathways in somite cells of the chick embryo." In : *Anatomy and embryology* 204.5, pp. 389–98. ISSN : 0340-2061. DOI : 10.1007/s004290100208. URL : http://www.ncbi.nlm.nih.gov/pubmed/11789986.

Sandersius, S. A., M. Chuai, C. J. Weijer, and T. J. Newman (2011). "A 'chemotactic dipole' mechanism for large-scale vortex motion during primitive streak formation in the chick embryo." In : *Physical biology* 8.4, p. 045008. ISSN : 1478-3975. DOI : 10.1088/1478-3975/8/4/045008. URL : http://www.ncbi.nlm.nih.gov/pubmed/21750368.

Savin, Thierry, Natasza A. Kurpios, Amy E. Shyer, Patricia Florescu, Haiyi Liang, L. Mahadevan, and Clifford J. Tabin (2011). "On the growth and form of the gut." In : *Nature* 476.7358, pp. 57–62. ISSN : 1476-4687. DOI : 10.1038/nature10277. arXiv : 79961136469. URL : http://dx.doi.org/10.1038/nature10277http://www.ncbi.nlm.nih.gov/pubmed/21814276http://www.pubmedcentral.nih.gov/articlerender.fcgi?artid=PMC3335276.

Sbalzarini, Ivo F and Petros Koumoutsakos (2005). "Feature point tracking and trajectory analysis for video imaging in cell biology". In : *Journal of structural biology* 151.2, pp. 182–195.

Schindelin, Johannes, Ignacio Arganda-Carreras, Erwin Frise, Verena Kaynig, Mark Longair, Tobias Pietzsch, Stephan Preibisch, Curtis Rueden, Stephan Saalfeld,

Benjamin Schmid, Jean-Yves Tinevez, Daniel James White, Volker Hartenstein, Kevin Eliceiri, Pavel Tomancak, and Albert Cardona (2012). "Fiji : an open-source platform for biological-image analysis." In : *Nature methods* 9.7, pp. 676–82. ISSN : 1548-7105. DOI : 10.1038/nmeth.2019. URL : http://dx.doi.org/10.1038/nmeth.2019http://10.0.4.14/nmeth.2019https://www.nature.com/articles/nmeth.2019{\#}supplementary-informationhttp://www.ncbi.nlm.nih.gov/pubmed/22743772http://www.pubmedcentral.nih.gov/articlerender.fcgi?artid=PMC3855844.

Schoenwolf, Gary C (1979). "Histological and ultrastructural observations of tail bud formation in the chick embryo." In : *The Anatomical record* 193.1, pp. 131–47. ISSN : 0003-276X. DOI : 10.1002/ar.1091930108. URL : http://www.ncbi.nlm.nih.gov/pubmed/760594.

Schötz, Eva-Maria, Rebecca D Burdine, Frank Jülicher, Malcolm S Steinberg, Carl-Philipp Heisenberg, and Ramsey a Foty (2008). "Quantitative differences in tissue surface tension influence zebrafish germ layer positioning." In : *HFSP journal* 2.1, pp. 42–56. ISSN : 1955-2068. DOI : 10.2976/1.2834817.

Seifert, Jessica R K and Marek Mlodzik (2007). "Frizzled/PCP signalling : a conserved mechanism regulating cell polarity and directed motility." In : *Nature reviews. Genetics* 8.2, pp. 126–38. ISSN : 1471-0056. DOI : 10.1038/nrg2042. URL : http://www.ncbi.nlm.nih.gov/pubmed/17230199.

Shih, J and S E Fraser (1996). "Characterizing the zebrafish organizer : microsurgical analysis at the early-shield stage." In : *Development (Cambridge, England)* 122.4, pp. 1313–22. ISSN : 0950-1991. URL : http://www.ncbi.nlm.nih.gov/pubmed/8620858.

Shook, David R, Eric M Kasprowicz, Lance A. Davidson, and Raymond Keller (2018). "Large, long range tensile forces drive convergence during Xenopus blastopore closure and body axis elongation". In : *eLife* 7, e26944. ISSN : 2050-084X. DOI : 10.7554/eLife.26944. arXiv : /dx.doi.org/10.1101/126201 [http:]. URL : https://elifesciences.org/articles/26944.

Shyer, Amy E, Tuomas Tallinen, Nandan L Nerurkar, Zhiyan Wei, Eun Seok Gil, David L Kaplan, Clifford J Tabin, and L Mahadevan (2013). "Villification : How the Gut Gets Its Villi". In :

Spemann, Hans and Hilde Mangold (1924). "Über induktion von Embryonalanlagen durch Implantation artfremder Organisatoren". In : *Archiv für mikroskopische Anatomie und Entwicklungsmechanik* 100.3-4, pp. 599–638.

Spratt, Nelson T. (1947). "Regression and shortening of the primitive streak in the explanted chick blastoderm". In : *Journal of Experimental Zoology* 104.1, pp. 69–100. ISSN : 0022-104X. DOI : 10.1002/jez.1401040105. URL : http://doi.wiley.com/10.1002/jez.1401040105.

Spratt, Nelson T. and Hermann Haas (1960). "Integrative mechanisms in development of the early chick blastoderm. I. Regulative potentiality of separated parts". In : *Journal of Experimental Zoology* 145.2, pp. 97–137. ISSN : 0022-104X. DOI : 10.1002/jez.1401450202. URL : http://doi.wiley.com/10.1002/jez.1401450202.

Steinberg, Malcolm S. (1970). "Does differential adhesion govern selfassembly processes in histogenesis ? Equilibrium configurations and the emergence of a hierarchy among populations of embryonic cells". In : *Journal of Experimental Zoology* 173.4, pp. 395–433. ISSN : 1097010X. DOI : 10.1002/jez.1401730406.

Steinwachs, Julian, Claus Metzner, Kai Skodzek, Nadine Lang, Ingo Thievessen, Christoph Mark, Stefan Münster, Katerina E Aifantis, and Ben Fabry (2016). "Three-dimensional force microscopy of cells in biopolymer networks." In : *Nature methods* 13.2, pp. 171–176. ISSN : 1548-7105. DOI : 10.1038/nmeth.3685. URL : http://dx.doi.org/10.1038/nmeth.3685.

Stern, Claudio (2004). *Gastrulation : from cells to embryo*. Cold Spring Harbor Press.

Steventon, Ben, Fernando Duarte, Ronan Lagadec, Sylvie Mazan, Jean-François Nicolas, and Estelle Hirsinger (2016). "Species-specific contribution of volumetric growth and tissue convergence to posterior body elongation in vertebrates." In : *Development (Cambridge, England)* 143.10, pp. 1732–41. ISSN : 1477-9129. DOI : 10.1242/dev.126375. URL : http://dev.biologists.org/lookup/doi/10.1242/dev.126375http://www.ncbi.nlm.nih.gov/pubmed/26989170.

Stirbat, Tomita Vasilica, Abbas Mgharbel, Selena Bodennec, Karine Ferri, Hichem C. Mertani, Jean-Paul Rieu, and Hélène Delanoë-Ayari (2013a). "Fine Tuning of Tissues' Viscosity and Surface Tension through Contractility Suggests a New Role for α-Catenin". In : *PLoS ONE* 8.2. Ed. by Carl-Philipp Heisenberg, e52554. ISSN : 1932-6203. DOI : 10.1371/journal.pone.0052554. URL : http://dx.plos.org/10.1371/journal.pone.0052554.

Stirbat, Tomita Vasilica, Sham Tlili, Thibault Houver, Jean-paul Rieu, Catherine Barentin, and Hélène Delanoë-Ayari (2013b). "Multicellular aggregates : a model system for tissue rheology". In : *The European Physical Journal E* 36.8, p. 84. ISSN : 1292-8941. DOI : 10.1140/epje/i2013-13084-1. URL : http://link.springer.com/10.1140/epje/i2013-13084-1.

Storey, K G, J M Crossley, E M De Robertis, W E Norris, and C D Stern (1992). "Neural induction and regionalisation in the chick embryo." In : *Development (Cambridge, England)* 114.3, pp. 729–41. ISSN : 0950-1991. URL : http://www.ncbi.nlm.nih.gov/pubmed/1618139.

Sugimura, K., P.-F. Lenne, and F. Graner (2016). "Measuring forces and stresses in situ in living tissues". In : *Development* 143.2, pp. 186–196. ISSN : 0950-1991. DOI : 10.1242/dev.119776. URL : http://dev.biologists.org/cgi/doi/10.1242/dev.119776.

Tada, M. and C.-P. Heisenberg (2012). "Convergent extension : using collective cell migration and cell intercalation to shape embryos". In : *Development* 139.21, pp. 3897–3904. ISSN : 0950-1991. DOI : 10.1242/dev.073007. URL : http://dev.biologists.org/cgi/doi/10.1242/dev.073007.

Theret, D. P., M. J. Levesque, M. Sato, R. M. Nerem, and L. T. Wheeler (1988). "The application of a homogeneous half-space model in the analysis of endothelial cell micropipette measurements." In : *Journal of biomechanical engineering* 110.3, pp. 190–9. ISSN : 0148-0731. DOI : 10.1115/1.3108430. URL : http://biomechanical.asmedigitalcollection.asme.org/article.aspx?articleid=1397916http://www.ncbi.nlm.nih.gov/pubmed/3172738.

Thompson, D'Arcy Wentworth (1942). *On growth and form.* Cambridge Univ. Press.

Townes, Philip L. and Johannes Holtfreter (1955). "Directed movements and selective adhesion of embryonic amphibian cells". In : *Journal of Experimental Zoology* 128.1, pp. 53–120. ISSN : 0022-104X. DOI : 10.1002/jez.1401280105. URL : http://doi.wiley.com/10.1002/jez.1401280105.

Trepat, Xavier, Michael R. Wasserman, Thomas E. Angelini, Emil Millet, David A. Weitz, James P. Butler, and Jeffrey J. Fredberg (2009). "Physical forces during collective cell migration". In : *Nature Physics* 5.6, pp. 426–430. ISSN : 1745-2473. DOI : 10.1038/nphys1269. URL : http://www.scopus.com/inward/record.url?eid=2-s2.0-67650227472{\&}partnerID=tZOtx3y1.

Varner, V. D., D. a. Voronov, and L. a. Taber (2010). "Mechanics of head fold formation : investigating tissue-level forces during early development". In : *Development* 137.22, pp. 3801–3811. ISSN : 0950-1991. DOI : `10.1242/dev.054387`. URL : `http://dev.biologists.org/cgi/doi/10.1242/dev.054387`.

Voiculescu, Octavian, Federica Bertocchini, Lewis Wolpert, Ray E. Keller, and Claudio D. Stern (2007). "The amniote primitive streak is defined by epithelial cell intercalation before gastrulation". In : *Nature* 449.7165, pp. 1049–1052. ISSN : 0028-0836. DOI : `10.1038/nature06211`. URL : `http://www.nature.com/doifinder/10.1038/nature06211`.

Voiculescu, Octavian, Lawrence Bodenstein, I. Lau Jun, and Claudio D. Stern (2014). "Local cell interactions and self-amplifying individual cell ingression drive amniote gastrulation". In : *eLife* 2014.3, pp. 1–26. ISSN : 2050084X. DOI : `10.7554/eLife.01817`.

Von Dassow, Michelangelo and Lance A. Davidson (2009). "Natural variation in embryo mechanics : Gastrulation in Xenopus laevis is highly robust to variation in tissue stiffness". In : *Developmental Dynamics* 238.1, pp. 2–18. ISSN : 10588388. DOI : `10.1002/dvdy.21809`. arXiv : `NIHMS150003`.

Walt, Stefan Van der, Johannes L Schönberger, Juan Nunez-Iglesias, François Boulogne, Joshua D Warner, Neil Yager, Emmanuelle Gouillart, and Tony Yu (2014). "scikit-image : image processing in Python". In : *PeerJ* 2, e453.

Wei, Y and T Mikawa (2000). "Formation of the avian primitive streak from spatially restricted blastoderm : evidence for polarized cell division in the elongating streak." In : *Development (Cambridge, England)* 127.1, pp. 87–96. ISSN : 0950-1991. URL : `http://www.ncbi.nlm.nih.gov/pubmed/10654603`.

Wetzel, Robert (1929). "Untersuchungen am Hühnchen. Die Entwicklung des Keims Während der Ersten Beiden Bruttage". In : *Untersuchungen am Hühnchen : Die Entwicklung des Keims während der ersten beiden Bruttage*. Berlin, Heidelberg : Springer Berlin Heidelberg, pp. 188–321. ISBN : 978-3-662-40980-0. DOI : `10.1007/978-3-662-40980-0_1`. URL : `https://doi.org/10.1007/978-3-662-40980-0{\_}1`.

Williams, Margot, Carol Burdsal, Ammasi Periasamy, Mark Lewandoski, and Ann Sutherland (2012). "Mouse primitive streak forms in situ by initiation of epithelial to mesenchymal transition without migration of a cell population." In : *Developmental dynamics : an official publication of the American Association of Anatomists* 241.2, pp. 270–83. ISSN : 1097-0177. DOI : `10.1002/dvdy.23711`. arXiv : `NIHMS150003`. URL : `http://www.ncbi.nlm.nih.gov/pubmed/22170865http://www.pubmedcentral.nih.gov/articlerender.fcgi?artid=PMC3266444`.

Williams, Margot, Weiwei Yen, Xiaowei Lu, and Ann Sutherland (2014). "Distinct Apical and Basolateral Mechanisms Drive Planar Cell Polarity-Dependent Convergent Extension of the Mouse Neural Plate". In : *Developmental Cell* 29.1, pp. 34–46. ISSN : 15345807. DOI : `10.1016/j.devcel.2014.02.007`. arXiv : `NIHMS150003`. URL : `http://dx.doi.org/10.1016/j.devcel.2014.02.007http://www.ncbi.nlm.nih.gov/pubmed/24703875http://www.pubmedcentral.nih.gov/articlerender.fcgi?artid=PMC4120093http://linkinghub.elsevier.com/retrieve/pii/S1534580714001002`.

Yanez, Livia Z., Jinnuo Han, Barry B. Behr, Renee A. Reijo Pera, and David B. Camarillo (2016). "Human oocyte developmental potential is predicted by mechanical properties within hours after fertilization". In : *Nature Communications* 7, p. 10809. ISSN : 2041-1723. DOI : `10.1038/ncomms10809`. URL : `http://www.nature.com/doifinder/10.1038/ncomms10809`.

Yen, W. W., M. Williams, A. Periasamy, M. Conaway, C. Burdsal, R. Keller, X. Lu, and A. Sutherland (2009). "PTK7 is essential for polarized cell motility and convergent extension during mouse gastrulation". In : *Development* 136.12, pp. 2039–2048. ISSN : 0950-1991. DOI : 10.1242/dev.030601. URL : http://dev.biologists.org/cgi/doi/10.1242/dev.030601http://www.ncbi.nlm.nih.gov/pubmed/28245921http://www.pubmedcentral.nih.gov/articlerender.fcgi?artid=PMC5403012.

Yeung, a and E Evans (1989). "Cortical shell-liquid core model for passive flow of liquid-like spherical cells into micropipets." In : *Biophysical journal* 56.1, pp. 139–149. ISSN : 00063495. DOI : 10.1016/S0006-3495(89)82659-1. URL : http://dx.doi.org/10.1016/S0006-3495(89)82659-1.

Zamir, Evan a. and Larry a. Taber (2004). "On the Effects of Residual Stress in Microindentation Tests of Soft Tissue Structures". In : *Journal of Biomechanical Engineering* 126.2, p. 276. ISSN : 01480731. DOI : 10.1115/1.1695573. URL : http://biomechanical.asmedigitalcollection.asme.org/article.aspx?articleid=1411646.

Zamir, Evan a, András Czirók, Cheng Cui, Charles D Little, and Brenda J Rongish (2006). "Mesodermal cell displacements during avian gastrulation are due to both individual cell-autonomous and convective tissue movements." In : *Proceedings of the National Academy of Sciences of the United States of America* 103.52, pp. 19806–19811. ISSN : 0027-8424. DOI : 10.1073/pnas.0606100103.

Zamir, Evan a., Brenda J. Rongish, and Charles D. Little (2008). "The ECM Moves during Primitive Streak FormationComputation of ECM Versus Cellular Motion". In : *PLoS Biology* 6.10. Ed. by Brigid Hogan, e247. ISSN : 1545-7885. DOI : 10.1371/journal.pbio.0060247. URL : http://dx.plos.org/10.1371/journal.pbio.0060247.

Zhang, Lixia, Christina Kendrick, Dörthe Jülich, and Scott A. Holley (2008). "Cell cycle progression is required for zebrafish somite morphogenesis but not segmentation clock function." In : *Development (Cambridge, England)* 135.12, pp. 2065–70. ISSN : 0950-1991. DOI : 10.1242/dev.022673. URL : http://dev.biologists.org/cgi/doi/10.1242/dev.022673http://www.ncbi.nlm.nih.gov/pubmed/18480162http://www.pubmedcentral.nih.gov/articlerender.fcgi?artid=PMC2923836.

Zhou, J., S. Pal, S. Maiti, and L. a. Davidson (2015). "Force production and mechanical accommodation during convergent extension". In : *Development* 142.4, pp. 692–701. ISSN : 0950-1991. DOI : 10.1242/dev.116533. URL : http://dev.biologists.org/cgi/doi/10.1242/dev.116533.

Zhou, Jian, Hye Young Kim, and Lance A. Davidson (2009). "Actomyosin stiffens the vertebrate embryo during crucial stages of elongation and neural tube closure". In : *Development* 136.4, pp. 677–688. ISSN : 0950-1991. DOI : 10.1242/dev.026211. URL : http://dev.biologists.org/cgi/doi/10.1242/dev.026211.

Arthur MICHAUT

Biomécanique de l'élongation de l'axe antéro-postérieur chez l'embryon de poulet

Résumé

Chez les Vertébrés, le plan d'organisation du corps est mis en place lors de l'élongation de l'axe antéro-postérieur. L'importance du mésoderme pré-somitique (PSM) dans l'élongation a précédemment été démontrée chez l'embryon de poulet. Il a été proposé qu'un gradient de motilité cellulaire aléatoire, contrôlé par un gradient de morphogène, était nécessaire à l'élongation de l'axe. À ce jour, les interactions entre un profil de signalisation moléculaire bien connu et un mécanisme physique d'élongation restent à explorer. En particulier, plusieurs questions de mécanique doivent être étudiées. Tout d'abord, un gradient de motilité cellulaire peut-il provoquer l'extension du PSM ? Ensuite, la force générée par l'extension du PSM peut-elle être à l'origine de l'élongation de l'axe ? Enfin, comment l'extension du PSM est-elle couplée mécaniquement à l'élongation des autres tissus ?

Pour répondre à ces questions, une meilleure description des propriétés mécaniques des tissus embryonnaires est nécessaire. De plus, afin d'estimer la contribution des différents tissus au processus d'élongation, une analyse quantitative de la production de force de ces tissus est essentielle. Dans cette thèse de doctorat, nous présentons le profil des propriétés visco-élastiques du PSM et du tube neural le long de l'axe. Nous démontrons également que des PSM isolés sont capables de s'allonger de manière autonome et nous mesurons leur contribution à la force totale d'élongation.

Mots-clés : élongation embryonnaire, mésoderme pré-somitique, propriétés mécaniques, production de force

Résumé en anglais

In vertebrates, the elongation of the anteroposterior axis is a crucial step during embryonic development as it results in the establishment of the basic body plan. A previous study highlighted the importance of the presomitic mesoderm (PSM) in elongation and showed that a gradient of random cell motility along the anteroposterior axis is necessary for proper elongation of the chicken embryo. It was proposed that a gradient of random cell motility, downstream of a morphogen gradient, drives axis extension. To date, the potential interaction between well-established molecular signaling and physical mechanisms involved in axis elongation remains largely unexplored. In particular, several mechanical questions need to be addressed. First, can the cell motility gradient lead to PSM extension? Second, is the force generated by PSM extension capable of promoting axis elongation? Third, how is PSM extension mechanically coupled with the elongation of all embryonic tissues?

In order to tackle these questions, a better description of the mechanical properties of the embryonic tissues is required. Moreover, to assess specific tissues' contribution to elongation, a quantitative analysis of their force production is needed. In this Ph.D. thesis, we measure how the viscoelastic properties of both the PSM and the neural tube vary along the anteroposterior axis. We also demonstrate that isolated PSM explants are capable of autonomous elongation and we measure their contribution to the total force production in the embryo.

Keywords: embryonic elongation, presomitic mesoderm, mechanical properties, force production